Effect of shell closure N = 50 and N = 82 on the structure of very neutron-rich nuclei produced at ALTO : measurements of neutron emission probabilities and half lives of nuclei at astrophysical r-processes path

Dmitry Testov

Institut de Physique Nucléaire

CNRS - UNIVERSITÉ PARIS SUD

17 Janvier 2014 IPNO-T-13-07

Thèse
Présentée par

TESTOV Dmitry

Pour obtenir le grade de Docteur ès Sciences
De l'Université Paris Sud

Effect of shell closure N = 50 and N = 82 on the structure of very neutron-rich nuclei produced at ALTO. Measurements of neutron emission probabilities and half lives of nuclei at astrophysical r-process path.

UNIVERSITE PARIS-SUD

ÉCOLE DOCTORALE : *Particules, Noyaux et Cosmos*
Institut de Physique Nucléaire d'Orsay

DISCIPLINE Physique Nucléaire

THÈSE DE DOCTORAT

soutenue le 17/01/2014

par

Dmitry TESTOV

Effect of shell closure N = 50 and N = 82 on the structure of very neutron-rich nuclei produced at ALTO. Measurements of neutron emission probabilities and half lives of nuclei at astrophysical r-process path.

Directeur de thèse :	Fadi IBRAHIM	Directeur de Recherche, CNRS, IPN Orsay
Co-directeur de thèse :	David Verney	Charge de Recherche, CNRS, IPN Orsay
Composition du jury :		
Président du jury :	Elias KHAN	Professeur, Universite Paris Sud
Rapporteurs :	Stéphane GREVY	Charge de Recherche, CNRS, CENBG
Bordeaux		
	Jeff Allen WINGER	Professor, Mississippi State University
Examinateurs :	Ari JOKINEN	Professor, University of Jyväskylä, Finland
	Marek LEWITOWICZ	Directeur Adjoint du GANIL, Caen
	David VERNEY	Charge de Recherche, CNRS, IPN Orsay

Remerciements

Je suis très heureux d'avoir soutenu la thèse à l'IPN Orsay. Mon projet, qui a été terminé dans le cadre de ma thèse, était si grand si complexe que je ne l'aurais jamais réussi sans aide inestimable de mes collègues ici en France et en Russie. C'est avec plaisir que je présente dans ce manuscrit les résultats de notre travail en collaboration.

Je voudrais remercier la directrice adjointe de l'IN2P3 Mme Dominique Guillemaud-Mueller ainsi que le directeur de l'IPN M. Faiçal Azaiez et le directeur du FLNR (JINR) M. Sergey Dmitriev de m'avoir permis de mener ma thèse dans l'Institut de Physique Nucléaire d'Orsay.

Je voudrais remercier sincèrement les responsables de la collaboration №0674 IN2P3-JINR (Dubna) – le directeur de la division de la recherche du CNRS M. Fadi Ibrahim et le responsable du groupe *,,Ractions avec des noyaux légèrs radioactifs et stables"* de JINR M. Yuri Penionzhkevich d'avoir proposé le sujet de ma thèse.

Je remercie chaleureusement mon co-directeur de la thèse M. David Verney qui a passé son HDR deux mois avant ma soutenance. Donc j'étais le premier étudiant soutenu sous son HDR. Merci David pour ta patience, ta disponibilité et ta crédibilité ainsi que pour ton grand enthousiasme et tes efforts à comprendre la langue Française je parlais!

Je tiens à remercier les membres de mon jury M. Ari Jokinen, M. Elias Khan, M. Marek Lewitowicz ainsi que mes rapporteurs M. Stèphane Grévy et M. Jeff Alen Winger d'avoir patiemment lu ma thèse ainsi que pour les discussions que nous avons pu avoir pendant la soutenance.

C'est avec plaisir que je remercie le groupe NESTER - Noyaux Exotiques STructure et Réactions (NESTER) qui m'a bien accueilli pendants toutes ces années. C'était grâce aux chercheurs de NESTER que j'ai appris le français. Évidemment, grâce à eux j'ai appris l'habitude de se délecter du repas du CESFO - le plus on parle le plus le repas est dlicieux.

Je remercie Brigitte Roussière pour tous les conseils excellents et pour toutes les réunions de dpouillement de données qu'on faisait régulièrement. Aussi merci de m'avoir encouragé de travailler sur l'argent (Ag). Merci à Iulian Stefan, Daisuke Susuki, Megumi Niikura. Merci Iolanda Matea, pour ton détecteur GeFoc29 que tu m'as consacré! Merci à Sebastien Ancelin pour la bande de transports des isotopes qui marchait toujours! Ta voiture blanche garée devant ma fenêtre m'apportait toujours l'espoir pour l'avenir! Je voudrais remercier Serge Franchoo et Ruohong Li! Grâce au laser que vous avez installé nous avons obtenu de très bons résultats! Également je dis merci aux ex-doctorants du groupe Karolina Kolos, Mathieu Ferraton et Matthieu Lebois.

Je voudrais également dire merci à Guillaume Mavilla avec qui nous avons fait 300m d'emballage plastique de câbles de TETRA. Je remercie Guillaume d'avoir pris des photos de ma soutenance, de les avoir effacées et puis de les avoir retrouvées dans la corbeille de son ordinateur. Je voudrais aussi remercier Luc Petizon qui a corrigé ces photos)). Merci Luc de m'avoir montré les descentes techniques est très jolis pistes pour VTT, côté Fontainebleau. Comme, Luc, m'a dit:"Si en plus tu te casse ta figure Fadi me tuera...". Évidement, Luc, je t'ai sauvé la vie, ...(!).

Je tiens à remercier John Wilson et Elena Kuznetsova pour les discussion de simulation MCNP; Julien Bettane qui a préparé tous les dessins techniques; ainsi que l'ensemble de l'équipe R&D. Je suis très reconnaissant à NGUYEN-Kim Kane, sans qui aucun manip n'aura jamais été possible. Je dis merci à Laure-Amélie Couturie qui m'a sauvé la vie plusieurs fois en informatique. Merci, Pascale Guyonvarch de m'avoir guidé dans l'administration française.

L'une des phrases françaises que j'ai vite apprise pendant ma thèse assez profondément c'était le "dégât de l'eau". C'était plus que la guerre! Je suis très reconnaissant à tous les ingénieurs et techniciens du Tandem qui se battaient dure, pour que ALTO tourne super bien de façon à réussir les manips! Tout d'abord je remercie Said Abdelhakim et les ingnieurs et techniciens avec qui je travaillais le plus: Croizet Hervé (merci pour tes leçons de pilotage de faisceau), Semsoum Alain (pour plusieurs affaires techniques), Bzyl Harold, Corbin Thony (pour les électrons), merci Raynaud Mark pour ta patience d'avoir fait des nombreux validations de badge d'accès de nos collègues russes! Et merci à vous tous pour la photo prise pour le cadre "My new family", vous êtes tous dans la famille de mon détecteur TETRA!

Merci à Laurence Berthier qui m'a aidé à s'installer, quand, au début de la thèse, j'étais sur mes béquilles. Merci à Gaubert-Rosier Céline d'être toujours optimiste. Je te souhaite, Celine, bon courage pour apprendre l'anglais. Merci à Pascale Pichot, je n'oublierai jamais ta salade!

Je souhaiterais remercier l'expert mondial en détecteurs remplis en ^{3}He M. Evgeny Sokol pour d'avoir répondu à toutes mes questions et sa disponibilité pour me donner des conseils. Également je remercie M. Vladimir Smirnov d'avoir terminé excellemment le système électronique pour le détecteur. Je dis merci à la secrétaire du groupe Mme Zinaida Pokrovskaj au JINR.

Merci à ma famille: Я хотел бы выразить благодарность свому отцу, он научил меня любить физику, и своей маме, которая всегда поддерживала меня в моих стремлениях бытъ учёным. Так же я благодарю моих бабушек Лилю и Люду, дедушку Юру и Валю за то что вы есть у нас! Моя докторская степень ваша

заслуга! Спасибо двум мои самым близким людям - моей сестре Дине и её мужу Максиму...

Je voudrais remercier ma petite amie Vera qui m'encourageais beaucoup. Je te remercie, Vera, pour le monde magique de la musique que tu m'as ouvert à Paris. Un fois dans en automne, en la soirée grise et triste ,,Lulu" d'Alban Berg nous a réunis .

Merci à Chantal Briançon, le Terminateur-1. Depuis deux ans quand j'étais le Terminateur-2 on a passé quelques moments inoubliable à l'Hôpital Antoine-Béclére. Donc je voudrais remercie Dr Philippe Cottin et Dr Nasser Mebtouche qui m'on réparé. Merci Chantal à toi, tu es devenu ma grande mère français!

Grâce à ma thèse j'ai fait beaucoup de connaissances extraordinaires ici, en France. Les amis qui pilotent le télescope Hubble, transportent des souris blanches en RER B, travaillent au mois Aout parce que c'est le saison des amours chez abeilles, qui décrivent le bozon Higgs, entranent l'équipe junior de foot d'Orsay-Bures, construisent les cryomodules où les détecteur de neutrons de fission... Merci à tous mes amis pour tous les projets (parfois un peu méchants) que nous avons réalisés ensemble (souvenez-vous la piscine)! Merci à l'équipe de ma colocation Giannis, Leonid et Anrey!

À la fin je souhaite très bon courage (et espoir) à tous les étudiants qui viendront faire leur thèse sur ALTO.

Abstract

Nowadays we are all witnesses to a competition between facilities in different countries to study unknown regions of neutron rich nuclei. Much effort is devoted to understand the role of neutron excess and its influence on nuclei in the vicinity of closed neutron shells whose structure is not yet fully studied. One of the means to investigate nuclear structure is in β-decay. Once a nucleus is proven to exist, its β-decay properties, such as $T_{1/2}$ and P_n (probability of β-delayed neutron emission), which are relatively easy to measure, can provide the first hints on the nuclear structure. For an r-process site ,,waiting points" (nuclei on closed neutron shells) have significant effects on the r-process dynamics and the abundance distribution. The actual site and the astrophysical conditions under which the nuclear synthesis takes place are still not known with certainty — since r-process nuclei are difficult to produce and to study experimentally, input parameters for r-process calculations are mostly derived from theoretical models. As it has been seen lately, most of the theories have failed to reproduce newly measured data sets near shell closures. With new experimental data already (or shortly) available theoretical approaches can be adjusted. Since β-delayed neutron emission becomes significant if not the dominating decaying channel for neutron-rich nuclei far from stability, usage of a proper neutron detector to study their properties is indispensable. To conduct the appropriate investigations, in the frame of the present thesis, in close collaboration with JINR (Dubna) a new detection system was constructed. It consists of 80 ^{3}He-filled counters, $4\pi\beta$ detector and a HPGe in order to measure simultaneously β, γ and neutron activities. The development of such a detection system, currently installed at the ALTO ISOL facility, was the first objective of the thesis. Then during two experimental campaigns conducted to investigate β-decay properties of neutron-rich nuclei in the neighborhood of N=50, N=82 the workability of the newly produced detection system was proven. In the vicinity of ^{78}Ni: half-lives and probability of β-delayed neutron emission for ^{80,82,83,84}Ga were measured. Furthermore, we were the first to observe the structure of ^{81,82}Ge via β-neutron gated γ spectra. Thanks to the neutron detection channel the absolute intensities of β-decay were proposed for the first time. In the vicinity of ^{132}Sn the half lives of ^{123,124,125}Ag and ^{127,128}In was measured. For the first time the β-delayed neutron emission was observed for ^{126}Cd, with its P_n value also measured. Based on the data obtained we come to the conclusion that to figure out the relative contribution of allowed and forbidden decays more theoretical efforts should be done crossing the N=50 shell. Whereas in the vicinity of N=82 shell more experimental challenge is required.

Keywords: *ISOL technique, photofission, radioactivity, laser ion source, magic numbers, nuclear structure, neutron detectors, MCNP simulations, β-decay, neutron emission, astrophysical r-process*

Contents

This thesis is dedicated to my father, who taught to love physics,
and to my mother who encouraged me to become a scientist...

Chapter 1

Introduction

Contents

1.1 Beta decay of neutron rich nuclei. Neutron emission.

It is known that there are about 300 stable nuclear species located in the chart of nuclide initially along N = Z line but then moving steadily to the neutron rich side because of the effect of the Coulomb force. Current knowledge of atomic nuclei suggests around 6000-7000 distinct nuclear species should live long enough to be produced and studied. There are two main ways to study nuclear properties: in nuclear reactions and in a radioactive decay. Respectively, one studies prompt radiation from reactions or delayed radiation from decays.

Varying the projectile/target nucleus or the bombarding energy allows emphasis on some aspects of the nuclear properties to be explored. On the other hand, quite often many reaction channels are open which reduces the sensitivity for measurements of prompt radiation. A compound nucleus, as an example, produced in a fusion-evaporation reaction, is ,,hot" (its excitation energy is not zero) and tends to emit particles (within 10^{-19}s) till its temperature becomes less than the energy separation of the particles.

However, the system is still excited and de-excites by a long γ-ray cascade emission to the ground state (10^{-15}-10^{-19}s). The ground state β decays with a much longer time-scale (μs - years). Generally, this allows one to separate the particular nuclei of interest, which results in enhancement of selectivity. The disadvantage is that decay is essentially random and almost cannot be altered. Thus radioactive decay is a limited tool to study nuclear properties. However, once the existence of a certain nucleus is proven, even a rough measurement of the half-live and Q_β value can provide a key clue to its properties. Even though many processes can occur before the formation of a β-decaying state, the measurements are insensitive to them due to physical/chemical separation. Finally, if separated from other species, it could be studied with only a few atoms [1].

In the case of large Q_β values a β-decay daughter can be left in excited states whose energy is above the neutron separation energy S_n. The probability for this to occur is increasing in the regions above closed neutron shells where the neutron binding energy is extremely low or in the region of nuclei with large neutron excess. The nucleus further de-excites either by γ emission to lower states or by neutron emission. In the latter case, the neutron emitting state is populated by decay from the parent while the neutron emission is instant. Therefore the neutrons are delayed showing the half-life of the precursors. Thus, β-delayed neutron emission (βd neutron emission) is a basically multi step process consisting of a β decay of the precursor (A, Z) which results in feeding the excited states of the emitter nucleus (A, Z+1) followed by the γ de-excitation or neutron emission to an excited state or to the ground state of the final nucleus (A-1,Z+1), Figure 1.1.

In the case of delayed neutron emission, the (β-, 2n)-process occurs when $Q_\beta > S_{2n}$ (S_{2n} two-neutron separation energy). Originally this process was observed at CERN on ^{11}Li [2, 3] and then on ^{30,32,31}Na [4]. Up to now, only a few β-delayed multi-neutron emitters have been measured experimentally in the region of light nuclei. For the fission fragments, due to difficulties of such studies, the (β-, 2n) process was experimentally observed only for the two Rb nuclei: ^{98}Rb ($T_{1/2}$ = 110 ms) and ^{100}Rb ($T_{1/2}$ = 51 ms) [5, 6] and the most recently for ^{86}Ga [7]. However there are theoretical predictions for β-delayed two-neutron emission for a series of isotopes in the range of medium and heavy masses [8, 9]. Failure to detect multi-neutron emission can lead to wrong experimental P_{1n} values which results in errors for the life-times determined from the decay by delayed-neutron radioactivity. Additionally, the study of correlations between neutrons emitted can give information about neutron clusters since neutrons are not distributed by the Coulomb force. The importance of β decay nuclear properties, with emphasis on delayed neutron emission cannot be underestimated. Information of properties on β-delayed emitters is needed for astrophysical r-process scenarios, understanding of nuclear

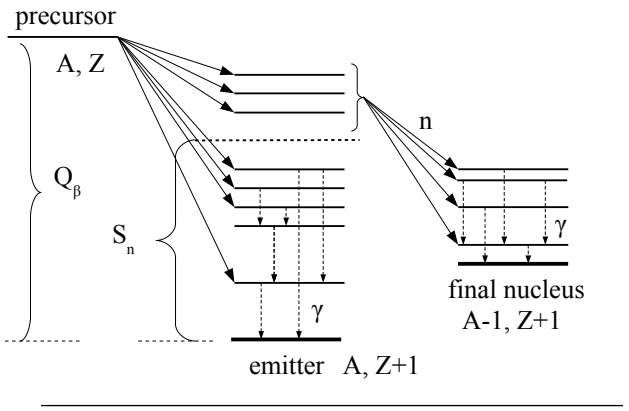

FIGURE 1.1: Schematic representation of β-decay.

structure and calculation of absolute branching ratios. Moreover, β-delayed neutrons play a key role in reactor physics.

1.2 Beta-decay in astrophysics applications. r-process.

In astrophysical environments, under certain explosive conditions, a large number of free protons or neutrons are available. These free neutrons can lead to synthesis of nuclei far from stability via either the rp-process (rapid proton capture followed by β^+-decay) in nova or r-process (rapid neutron capture followed by β^--decay) in Type II super nova [8].

The r-process in nucleosynthesis is a process in which, according to predictions, elements heavier than iron are formed. It consists of a series of rapid neutron captures followed by β-decays and passes through a net of nuclei with large Q values far from stability. The exact position of this net depends on the properties of neutron rich isotopes far away from the valley of stability along with the conditions in the astrophysical environment. Figure 1.2, taken from [10] schematically illustrates what the r-process for a very hot and neutron-dense environment. In the course of the transformation of a given seed into more neutron-rich isotopes by a series of (n, γ) reactions, (γ, n) photo-disintegrations have the increasing rates with the neutron excess or, equivalently, with the associated decrease of the neutron separation-energy S_n. At some moment, the nuclear flow may proceed to the higher Z elements via β-decay. However, the flow takes a special character in neutron closed shell regions. Due to the low S_n nuclei just past a neutron magic number prevents the process from passing to more neutron rich species, and β-decay drives the process back to stability following a path with increasing Z but constant N. As a consequence, elements are accumulated at nuclei with a magic neutron number. Once the process gets close enough to the stability line, S_n becomes sufficiently large to

allow (n, γ) reactions to be more rapid than β-decay and the process proceeds further without being counteracted by (γ, n) photo disintegration. The flow resumes normally until a new neutron magic number is reached [10].

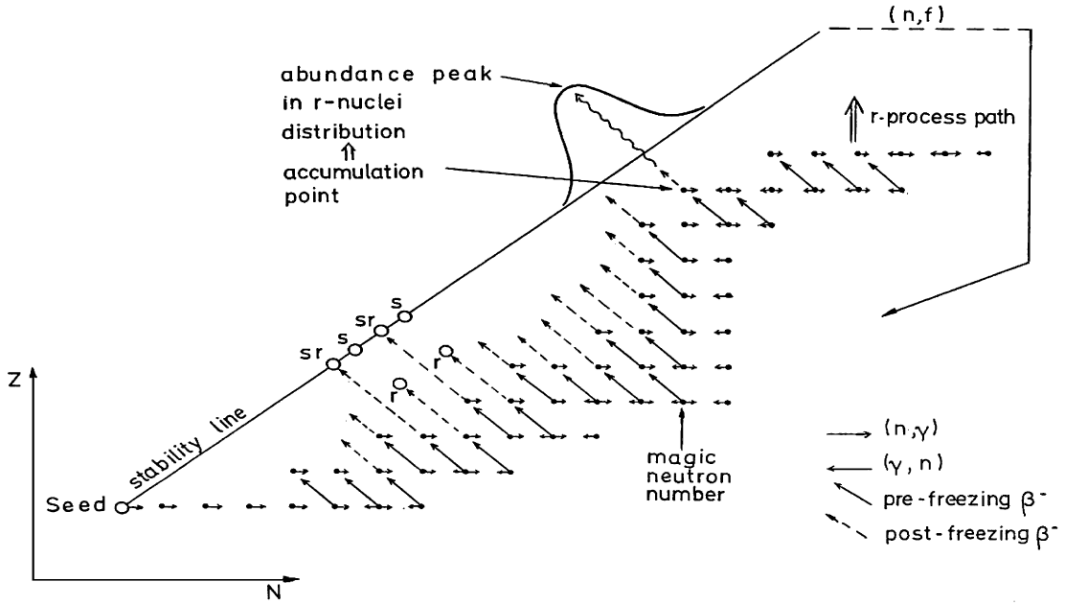

FIGURE 1.2: Schematic representation of the r-process in (N,Z) plane from [10]

The knowledge of weak interaction rates of nuclei is one of the most important factors for resolving astrophysical problems. Most nuclei of interest in astrophysics are the ones which are far from stability, and their β-decay properties have to be estimated theoretically since the areas are not easily accessible experimentally. Therefore, to perform reliable r-process calculations, the key parameters, such as neutron separation energy S_n, Q_β values, β-decay $T_{1/2}$ and probability of β-delayed neutron emission P_n are derived from theoretical models. As it has been shown recently in [11], $T_{1/2}$ of nuclei in N$\sim$50 region can influence the r-process abundances not only in the 75<A<90 region, but also for heavier masses, Figure 1.3.

To justify the impact of P_n on the r-process we collaborated with the Institute of Astronomy and Astrophysics (IAA) at the University of Brussels. In fact β-d neutrons can influence r-abundance distributions in a bit different way than $T_{1/2}$. This impact is illustrated in Figure 1.4 by calculation of the r-abundance after decompression of neutron matter at the coalescence of two neutron stars of 1.35M$\odot$ currently running at IAA. A ,,standard" case is compared to the case where P_n are all forced to zero. Interestingly, the effect of P_n is not at all smooth, the inclusion of β-d neutrons in the process shifts the abundance distribution towards more heavier masses. It happens due to the fact that neutron density increases enabling new neutron captures, especially by the most abundant elements, i.e. for nuclei around N = 126 peak (A = 195). Therefore, the

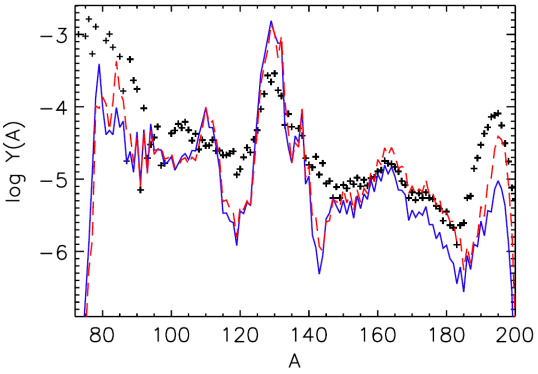

FIGURE 1.3: Calculated r-process abundances (solid line) at FRDM [12] (solid blue line) and at DF3a+CQRPA [11] (dashed red line) in comparison the solar abundances (black crosses).

reliable determination of P_n is necessary for understanding of the r-process, especially in abundance peaks.

As it has been seen lately, most of the theories such as FRDM, QRPA, gross theory and their modifications (see § 2.4) have failed in their predictions for newly measured half-lives of nuclei close to shell closure [11, 13, 14]. Nowadays we all witness the competition of new RIB facilities in different countries to study unknown regions of nuclei. With new data coming there will be further developments in theories. However, it should be noticed that the characteristics of β-decay have been scrutinized in the framework of microscopic models to the largest possible extent. Whereas the information used in models of the r-process depend also on the astrophysical conditions under which the nucleosynthesis is considered to take place, and these conditions are still very poorly identified.

1.3 Nuclear shell gaps near ^{78}Ni and ^{132}Sn

In contrast to the nuclear shell structure along the β-stability line which has been studied theoretically and experimentally quite well, the yet unknown shell structure in drip-line nuclei is currently of great interest [16]. The question is whether the shell effects near the drip lines are still as strong or does quenching take place. The doubly closed ^{78}Ni lies between the region of light nuclei, where the experimental evidences for changing magic number far from stability is well established [17]; and the heavy one, where no quenching of the known spin-orbit shells has been observed so far [18].Therefore, the nuclear region in the vicinity of ^{78}Ni is being extensively investigated nowadays [19]. As can be seen from Figure 1.5 which shows the evolution of experimental energies of 2_1^+ excited states and the ratio of energies of 4_1^+ to 2_1^+ states for Z = 30 - 38 (N = 46 - 54),

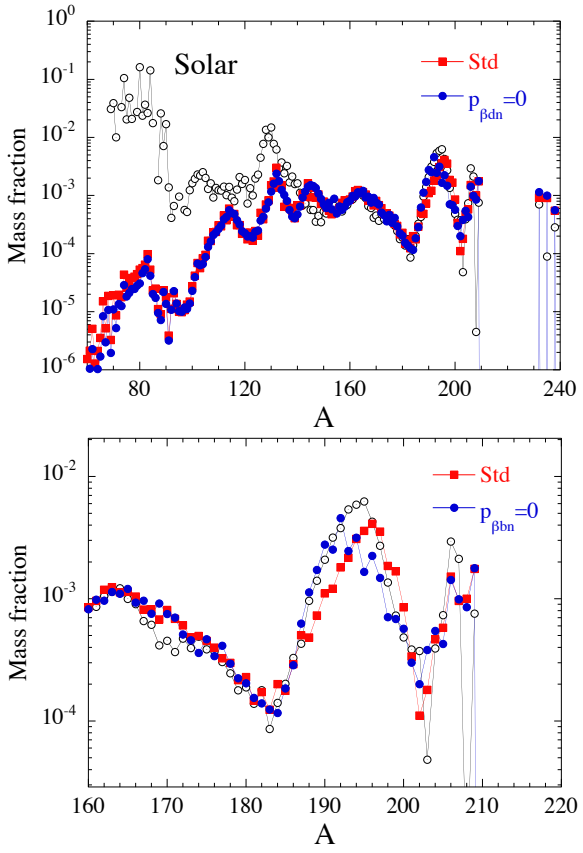

FIGURE 1.4: Top: Example of influence of P_n on astrophysical calculations. The solar abundances (dark dots) in comparison to calculated abundances by the astrophysical model (see text for details) including β-d neutron emission with currently available P_n (red dots) and prohibiting β-d neutron emission (all P_n are forced to 0) (blue dots) [15]. Bottom: the zoom near N = 126.

shell closure has definitely strong influence. However, there is the constant decrease of 2_1^+ energy (E_{2+}) for N = 50 as the nuclei become more proton deficient [1]. What remains from this influence at double shell closure (Z = 28, N = 50) is still an open question [20, 21].

Spectroscopic studies of nuclei near doubly magic nuclei such as ^{78}Ni provide important benchmarks for the shell structure of their neighbors. The simplified structure of these nuclei is a key ingredient for shell model calculations [22]. Moreover, the half live of ^{78}Ni becomes a direct input in certain r-process models [23, 24] and together with the other already known waiting points (^{79}Cu, ^{80}Zn) sets the r-process time scale through the N=50 bottleneck towards heavier elements and also determines the formation and shape of the A = 80 abundance peak [22]. Therefore a massive amount of experimental effort to investigate these nuclei has been concentrated recently.

Two of the most important experiments carried out in this region at PARRNe were studies of decays of ${}^{83}_{31}Ga_{52} \rightarrow {}^{83}_{32}Ge_{51}$ [25] and ${}^{81}_{30}Zn_{51} \rightarrow {}^{81}_{31}Ga_{50}$ [26]. Performed in

[1] though, this dependency is disturbed from Z=32 to Z=30 (Zn)

2001 and 2002 respectively, these experiments were extended later. The level scheme of $^{83}_{32}Ge_{51}$ was complemented by study of the β-n decay of $^{84}_{31}Ga_{53}$ at HRIBF/ORNL [27, 28] and again at PARNNe [29, 30]. The level scheme of $^{81}_{31}Ga_{50}$ was obtained by β-decay of $^{81}_{30}Zn_{51}$ at HRIBF/ORNL. Today, $^{83}_{32}Ge_{51}$ and $^{81}_{31}Ga_{50}$ remain the closest to $^{78}_{28}Ni_{50}$ nuclei whose structure was studied. The Z = 50 shell closure has to be also analyzed in a larger range, between the two doubly magic nuclei at N = 50 and at N = 82.

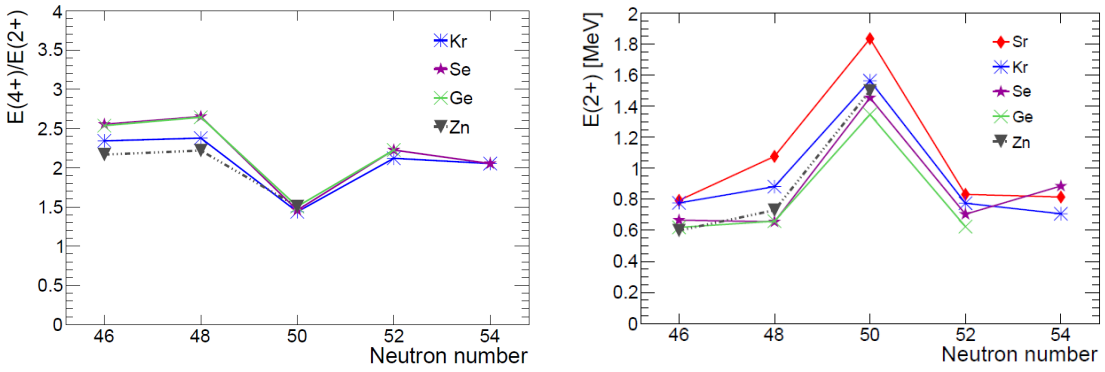

(A) The ratios of E($_4$+)/E($_2$+ energies for Z = 30 - 38 and N = 46 - 54 [29].

(B) Systematics of the experimentally observed $E2_1^+$ in the stable and neutron-rich nuclei near the N = 50 shell closure [29].

FIGURE 1.5: Nuclear shell gap N = 50

The shell closure N = 82 is formed between the $h_{11/2}$ and the $f_{7/2}$ orbits and is so strong that seven N = 82 isotopes with 54≤Z≤62 are stable. The N = 82 chain contains one known doubly-magic nucleus, $^{132}_{50}$Sn. For the heavy N = 82 isotopes, the Z = 64 proton gap is large enough to provide a doubly-closed character to $^{146}_{64}$Gd. The lighter N = 82 isotopes are less studied. The persistence of the N = 82 closure below Z = 50 is an open question which is particularly essential for calculations of r-process scenarios. Approaching the neutron drip-line a quenching of the N = 82 gap is predicted in self-consistent mean-field calculations which treat continuum states [16]. The present situation in mass theory predictions at the shell closure is illustrated in Figure 1.6a by a comparison of the experimental shell gap as a function of Z with theoretical models (for details see [31] and references therein). From this figure it is evident that none of these models can reproduced the overall experimental set and in particular the reduction of the shell gap on both sides of the doubly magic ^{132}Sn. The region N≃82 is important for astrophysical calculations of the A≃130 r-process abundance peak. Following full spectroscopic study of ^{130}Cd beta decay [33], some models of r-process nuclearsynthesis consider ^{130}Cd as the most important neutron magic ,,waiting-point" isotope. It determines to a large extent the bottle neck behavior of the r-process matter flow through the A≃130 r-process abundance peak [31] (Figure 1.3). As it can be seen in Figure 1.6b E_{2+} and E_{4+}/E_{2+} for

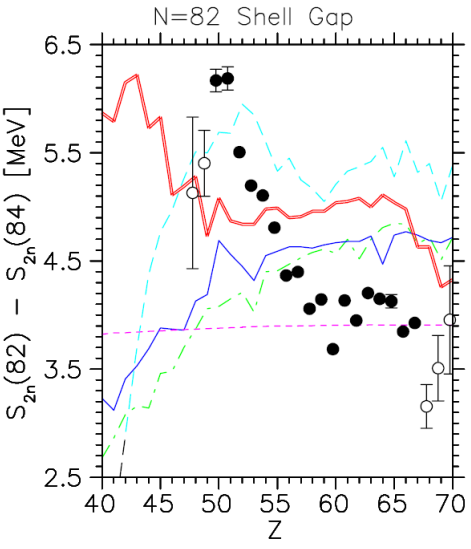

(A) Two neutron gap δ_{2n} for the N = 82 isotopic chain as a function of Z. Theoretical mass predictions: von Groot, magenta dashed line; FRDM, red thick solid line; ETFSI-Q, cyan long-dashed line, HFB-2, green dash-dotted line; HFB-8, blue thin solid line are compared to experimental data (empty and filled circus). See [31] and references therein

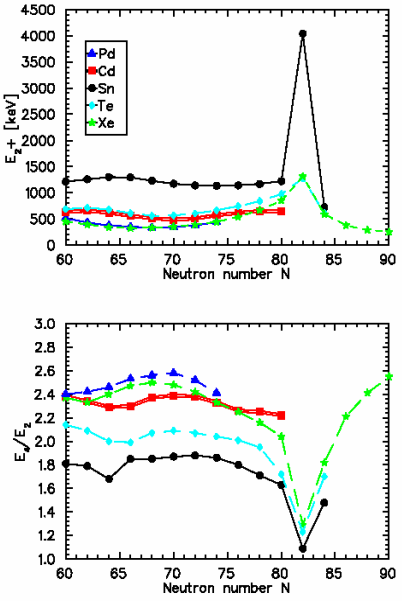

(B) Systematics of the first 2+ levels in neutron-rich $_{48}$Cd to $_{52}$Te isotopes (top); and E(4+)/E(2+) ratios (bottom) [32].

FIGURE 1.6: Nuclear shell gap N = 82

neutron-rich Cd isotopes are different in comparison to their neighborhoods [32]. The weakening of the N = 82 shell closure has been intensively discussed [34]. Moreover, according to prediction, the well-known spherical N = 82 (and N = 126) shell gap near beta-stability will be reduced far from stability and may eventually disappear completely at the drip-line [16].

1.4 Gamow-Teller and first-forbidden decays near doubly magic ^{78}Ni and ^{132}Sn

The QRPA[2] calculations of β- decay properties such as P_n and $T_{1/2}$ based on the FDRM model[3] are more or less in good agreement with experimental data sets for neutron rich nuclei where allowed transitions dominate. However, QRPA acts only in allowed approximations and doesn't take into account forbidden decays. Whereas consideration

[2]Quasi-particle random-phase approximation, §2.4
[3]Finite range droplet model (FRDM) for nuclear masses §2.4

of first forbidden (FF) decays is essential for a reliable β-decay description for nuclei with large Q_β values where these decays start to play a significant role. A significant decrease in the delayed neutron emission probability and $T_{1/2}$ is found in nuclei with the neutron excess bigger than one major shell. The effect originates from the high-energy first-forbidden transitions to the states outside the (Q_β–S_n)-window in the daughter nuclei [13].

According to available experimental and predicted decay schemes, the nuclei in the vicinity of the Z∼28, N∼50 shell closures undergo GT decays which are built on the shell-model configurations $\nu 1f_{7/2,5/2} \rightarrow \pi f_{7/2,5/2}$ and $\nu 1g_{9/2} \rightarrow \pi 1g_{9/2}$ and FF decays due to $\nu 1g_{9/2} \rightarrow \pi 1f_{5/2}$; and $\nu 1d_{5/2} \rightarrow \pi 1f_{5/2}$, Figure 1.7.

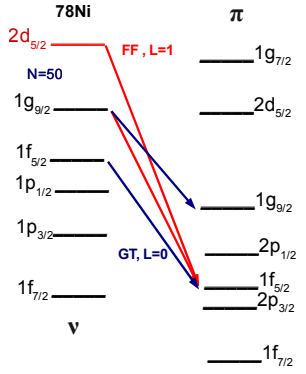

FIGURE 1.7: Gamow-Teller (GT) and Fist Forbidden decays(FF) in the region of ^{78}Ni

Comparison of different calculations for isotopes in the vicinity of N∼50 with experimental data [11, 14, 35, 36] found FF to be of little or no effect for the nuclei close to Z = 28 N<50. However, with filling of the $2f_{7/2}$, $2p_{3/2}$ proton orbitals, contribution of FF to the total half-life gradually increases. As an example, Figures 1.8 and 1.9 illustrate comparison of predicted P_n and $T_{1/2}$ for gallium isotopes [37] to known experimental data. Crossing the N=50 shell inclusion of FF decays has more significant influence on the $T_{1/2}$ and predicts a suppression of P_n as compared to the allowed approximation. It should be noticed, that the discrepancy of experimental data, as in case of ^{83}Ga, is high.

Yet another example of a shell configuration effect is in the vicinity of ^{132}Sn. Calculations including the FF transitions show a dominance of GT for the nuclei Z<50. As in the case of N = 50 shell, the agreement between theoretical models is disturbed crossing the N = 82 shell, Figures 1.10, 1.11.

A simultaneous analysis of the β-decay observables in order to reconstruct the β-strength function is needed. Going beyond the allowed β-decay approximation in order to figure

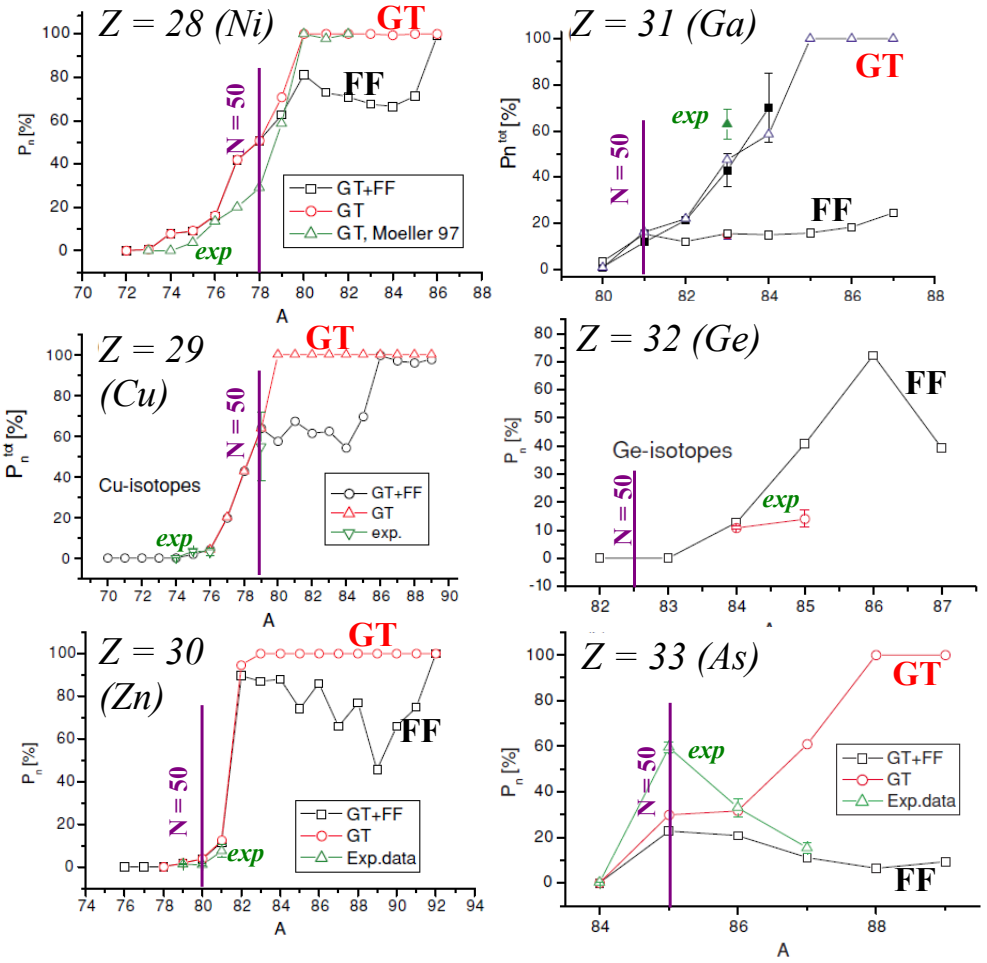

FIGURE 1.8: Experimental P_n for isotopes near N≈50 in comparison to different models from [36](Borzov): GT - calculations in the allowed Gamow-Teller approximations; FF - calculations taking into account both GT and First forbidden decays.

out the relative contribution of the Gamma-Teller and First Forbidden decays is an exciting experimental task.

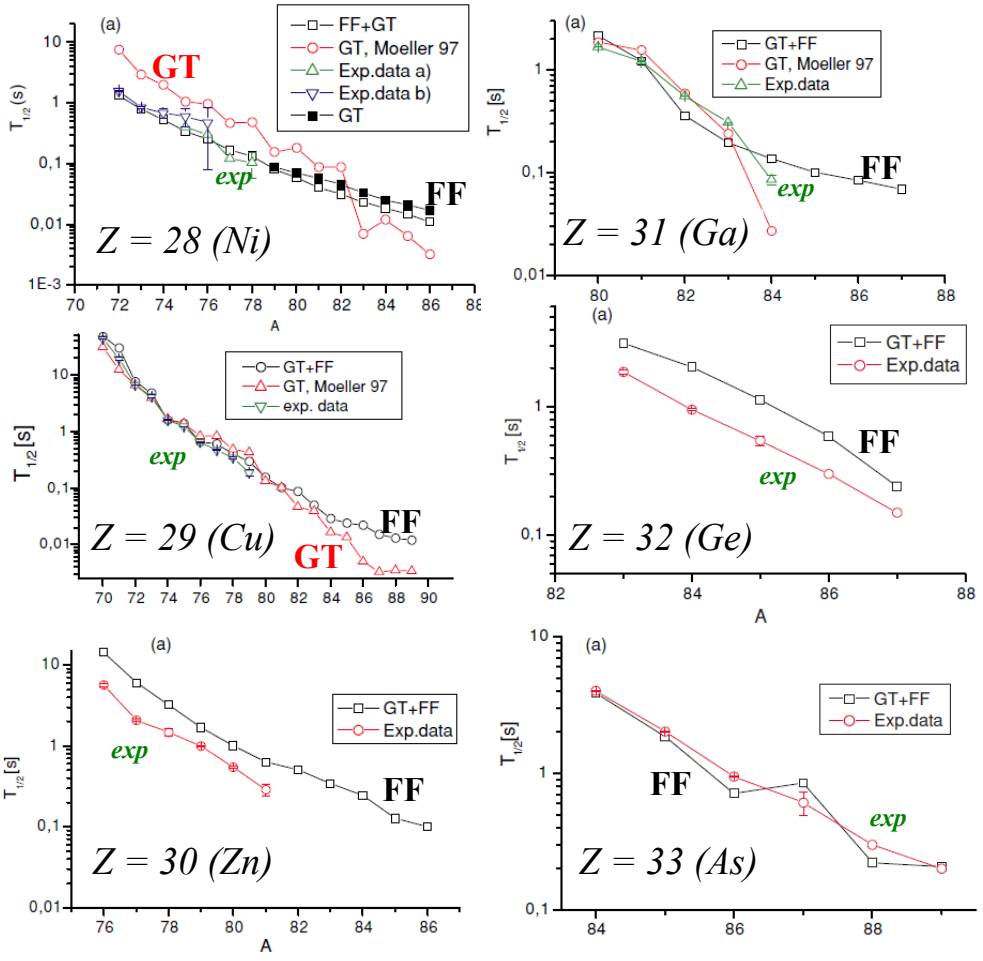

FIGURE 1.9: Experimental $T_{1/2}$ for isotopes near N≈50 in comparison to different models from [36](Borzov): GT - calculations in the allowed Gamow-Teller approximations; FF - calculations taking into account both GT and First forbidden decays.

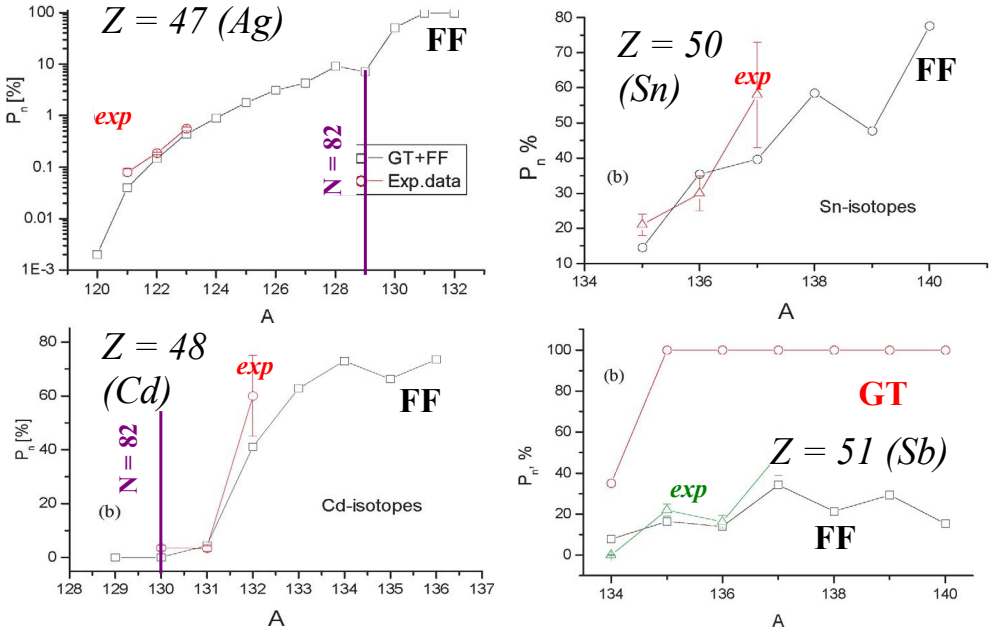

FIGURE 1.10: Experimental P_n for isotopes near N≈50 in comparison to different models from [13](Borzov): GT - calculations in the allowed Gamow-Teller approximations; FF - calculations taking into account both GT and First forbidden decays.

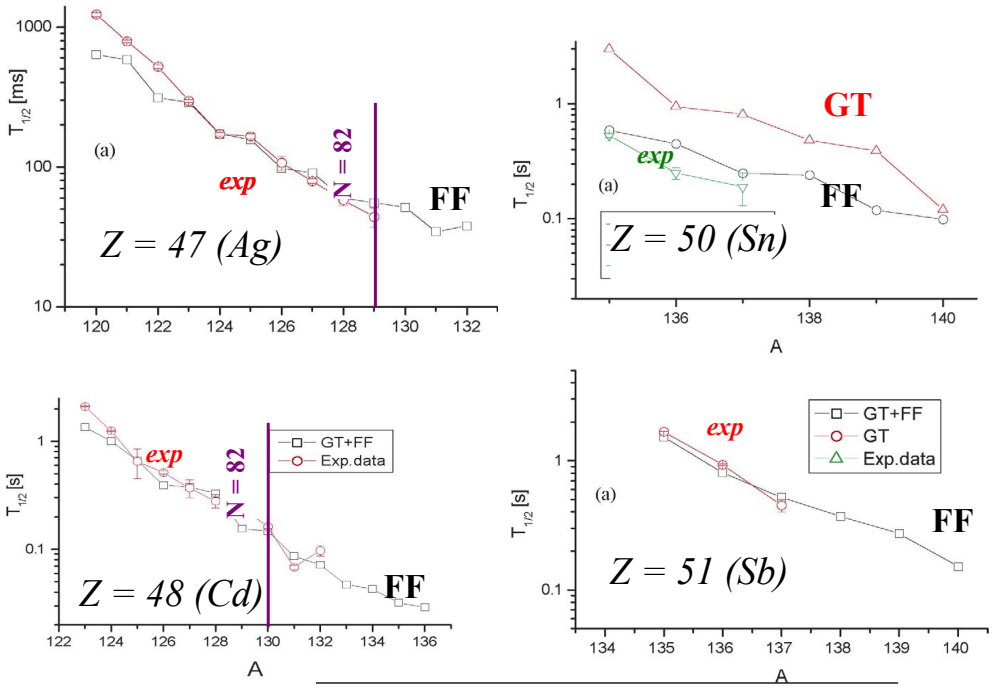

FIGURE 1.11: Experimental $T_{1/2}$ for isotopes near N≈50 in comparison to different models from [13](Borzov): GT - calculations in the allowed Gamow-Teller approximations; FF - calculations taking into account both GT and First forbidden decays.

1.5 Reactor Physics

In a nuclear reactor together with prompt fission neutrons, delayed neutrons from fission fragments are also present. Although, its fraction seems to be only about 1% of all the neutrons, due to much longer time scale of β-delayed neutron precursors (the average is about 13s in comparison to 0.001s for one generation of prompt neutrons) they significantly kick up the average life time to 0.1s [4] [38]. Therefore, delayed neutrons play a crucial role when positive reactivity is added in order to increase the reactor power. The power increase occurs because the rate of production of prompt neutrons changes abruptly as the reactivity is added. This is called a *prompt jump*. After the *prompt jump*, see Figure 1.12, the reactor power continues to increase. However, the increase rate cannot be faster than allowed by the delayed neutron precursor.As a result, the rise of power is controllable, and a reactor can be operated in secure mode[38].

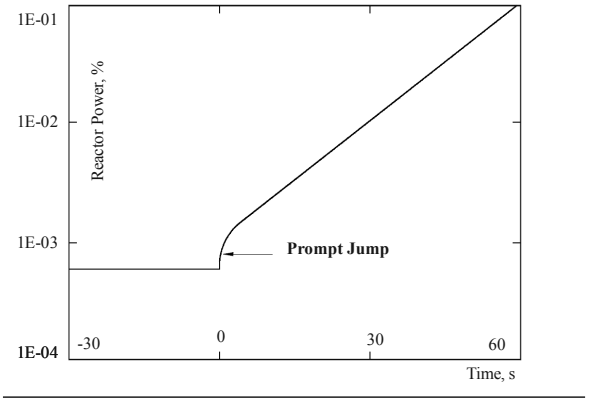

FIGURE 1.12: Reactor power response to positive reactivity addition [38].

Additionally, because delayed neutrons are not as energetic (0.5MeV) as prompt ones (2MeV), they can cause less fast fission, but since they travel a shorter distance they are not lucky enough to escape from the core and have large probability to be absorbed [38]. The cooling system in a nuclear reactor has to remove the residual heat from radioactive isotopes produced, the most part of which is β-delayed neutron precursors. It is exactly the β strength function which can determine how much of the released energy appears as neutrinos and in other forms of radiation which will be absorbed in a reactor. Interestingly, this situation is parallel to that in an exploding supernova [39].

Therefore the parameters of β-delayed neutron emission, such as half life of the precursor, production yield, and the spectrum of neutrons emitted are important for reactor kinetics. All these parameters depend on β strength function and P_n values in a β decay chain of the decaying fission products.

[4] the delayed neutron fraction depends on a given type of fuel

1.6 Beta Decayed studies at Orsay Program.

As was highlighted just above, nuclear structure in the vicinity of doubly-magic ^{132}Sn and ^{78}Ni is not yet fully understood. The measurements of delayed-neutron branching ratios in neutron-rich regions is important for understanding of nuclear structure with an impact on modeling of the r-process. For reactor physics an accurate knowledge of β-decay properties of nuclei with large neutron excess is also required.

The experiments in these regions tend to be more and more feasible. Therefore these measurements provide us with the first constrains on nuclear models and the first clues on nuclear properties for nuclei far from stability. In more exotic nuclei the $(Q_\beta - S_n)$-window becomes considerably wider. Thus, neutron emission becomes a strong if not a dominating channel. Consequently, a gamma spectroscopy only experiment is not sufficient to explore nuclear properties in this region, and neutron measurements are called on to help. In spectroscopy studies, neutrons, if in coincidence with γ and β, can significantly clear a γ spectrum indicating transitions in the β-n decay branch. Neutron-rich nuclei can have long-lived isomers which are also de-excited by β-decay and possible neutron emission. Therefore, as it will be shown below, a neutron detector is an extremely powerful tool for exploring the change of structure with increasing neutron number. It is a well-known fact that a ,,fast" (scintillator) neutron detector can be easily coupled with a germanium detector which leads to nice γ-neutron coincidence spectra. Unfortunately, due to low efficiency registration and quite a high sensitivity to γ-rays, application of scintillators might be limited in an experiment. Consequently, the ^{3}He filled detectors seem to be more preferable for these studies.

On one hand, an extra neutron detection channel can be used for measurements of absolute branching ratios. P_n value probes β-decay strength at excitation energy above the neutron separation energy and therefore can provide complementary information on β-decay. On the other, a neutron coincidence gate provides an additional degree of selectivity at low beam intensities where γ-spectroscopy is difficult. As it will be demonstrated further, ^{3}He detectors are extremely useful for both.

To study β decay properties the BEDO Program was introduced at ALTO. This program consists of two detector setups to be used on the same beam line, Figure 1.13. The first setup, consists of 5 germanium detectors each equipped with a specially designed BGO shield and a Veto plastic detector, $4\pi\beta$ detector and is aimed at nuclear structure studies - γ-*BEDO* branch. The second detection system is done in collaboration with JINR (Dubna) and represents the TETRA neutron detector (90 ^{3}He filled counters) with one germanium detector and a $4\pi\beta$ detector arranged so that the efficiency of neutron registration is the maximum - *n-BEDO* branch. It has an objective to measure the

absolute branching ratio. Sometimes the second part, *n-BEDO* branch, is simply called TETRA. During my thesis I was responsible for construction of this neutron part of the BEDO project, a commissioning experiment and the first real physical experiment. Upon my arrival in Orsay in the beginning of 2011, I practically started from 3.2m^2 a floor space in the ALTO experimental hall. Within 17 months we completed and commissioned a new beam line, a new tape station as well as γ-*BEDO* and *n-BEDO* (TETRA) detection systems. Before going into discussion of our work I am incredibly pleased to present in Figure 1.13 the photos of these detectors. In today's era where high-technology experimental techniques are expensive and complicated, which require patient years and years of development, and typically exceed an average ,,life-time" for a PhD student, I consider that I had an outstanding opportunity to guide the project from its inception until the interpretation of the results and comparison to existing theoretical models .

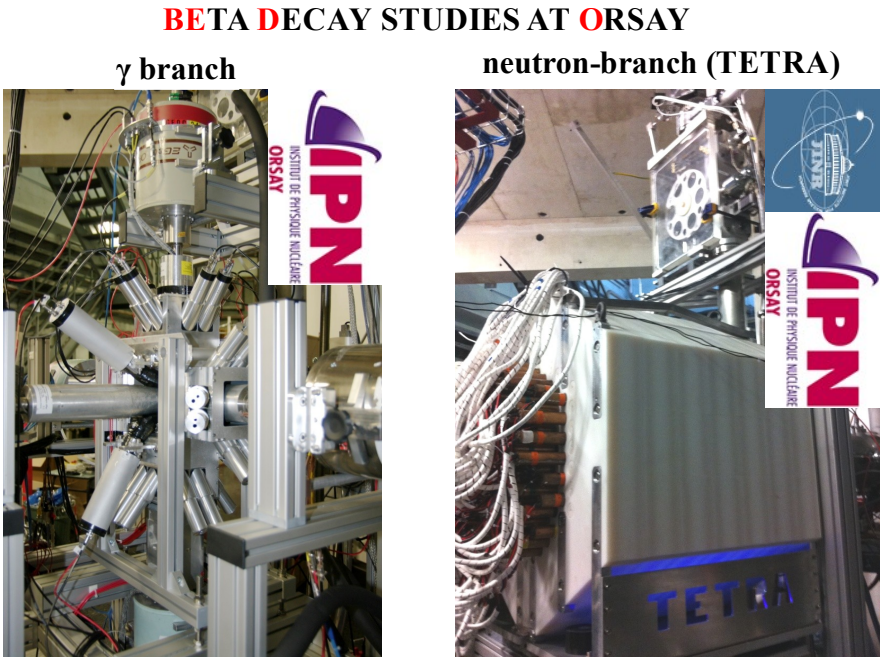

FIGURE 1.13: BEta Decayed studies at Orsay Program.

In Chapter 2 is given a brief introduction to the theoretical approaches to describe β-decay. Since one of the major parts of my thesis was the construction of a totally new experimental setup including the neutron detector TETRA, for the BEDO program at ALTO, Chapter 3 gives a detailed description on the development performed. This chapter has extensions in Appendices: Appendix A considers a general observation of neutron detection techniques. Appendix C contains complementary technical information on TETRA. In Chapter 4 ways for RIB production are considered with special

emphasis on the ISOL method and the ISOL-type facility ALTO. The final experimental setup is described in Chapter 5. The analyzing procedure and the results obtained are presented in Chapter 6. Finally, the physical significance of the results is put in the discussion in Chapter 7. In Chapter 8 I present the outlook and the perspectives of the research performed in the thesis.

Chapter 2

Outlook on beta-decay theory

"Quantum theory provides us with a striking illustration of the fact that we can fully understand a connection though we can only speak of it in images and parables."

W. Heisenberg

Contents

2.1 Weak interactions. Fermi Theory.

There are three types of beta decay: β^+ (for neutron deficient nuclei), β^- (neutron rich) and electron capture (EC). β^- decay dominates for neutron rich nuclei:

$$ {}^{A}_{Z}X_N \rightarrow {}^{A}_{Z+1}Y_{N-1} + e^- + \bar{\nu}_e \tag{2.1} $$

The Q_β value, the energy available in the decay, is defined as the difference between the initial and final nuclear mass energies:

$$ Q_{\beta-} = (M(A,Z) - M(A,Z+1))c^2 \tag{2.2} $$

Thus, the β^- process is possible (exothermic, $Q_{\beta-} > 0$) with emission of an electron and anti-neutrino whenever M(A,Z)>M(A,Z+1). In contrast to the electromagnetic

interaction where a photon is exchanged between the charged particles with zero rest mass and an infinite interaction range, in β^- decay the process appears to be short range and is described by exchange of the intermediate bosons $W^{\pm}$ and Z_0. The weak interactions, in the analogy to strong electromagnetic interactions, were introduced by Fermi in 1934.

Fermi considers β-decay as a result of nucleon interaction with an electron-neutrino field: one nucleon passes to another ($n \leftrightarrows P$) with formation of an e^- (e^+) and anti-neutrino (neutrino). Due to the weakness of the interaction, perturbation theory methods can be applied. Therefore, the probability of a transition from a initial ψ_i to the final ψ_f state is described by Fermi's Golden Rule:

$$\lambda = \frac{2\pi}{\hbar} \mid \int \psi_f^* H \psi_i d\tau \mid^2 \frac{dn}{dE} \tag{2.3}$$

where dn/dE, H, dτ are density of final states, operator, volume respectively. Fermi assumed the form of the operator H from well-known electromagnetic interactions. He found five operators vector (V), axial vector (A), scalar (S), pseudoscolar (P), tensor (T), but used only V or S. A and T forms were introduced later by Gamow and Teller. It was also proven that parity and charge conjugation are not conserved in beta decay.

Assume that the neutrino and electron are described by one-component wave functions ψ_ν and ψ_e, where V represents the spherical volume in the momentum space, and the perturbation operator is a constant (H = g). This is equivalent to the assumption that the neutrino and electron carry away zero angular momentum (L=0, Fermi's original assumption).

$$\psi_e(\overrightarrow{r}) = \frac{1}{\sqrt{V}} e^{\frac{i}{\hbar}\overrightarrow{r},\overrightarrow{p}} \psi_\nu(\overrightarrow{r}) = \frac{1}{\sqrt{V}} e^{\frac{i}{\hbar}\overrightarrow{r},\overrightarrow{q}} \tag{2.4}$$

In the first approach, since $\frac{1}{\hbar}\overrightarrow{r}, \overrightarrow{p}$<0.04 (for an electron kinetic energy 1MeV, p = 1.4 MeV/c) it is possible to approximate:

$$\psi_e(\overrightarrow{r}) = \frac{1}{\sqrt{V}} \tag{2.5}$$

Then

$$\int \psi_f^* H \psi_i d\tau = \frac{g}{V} \int \psi_f^* \psi_i d\tau = \frac{g}{V} M \tag{2.6}$$

where g - is a constant which characterize the intensity of the β interaction (like the charge e) characterizes the intensity of the Coulomb interaction), M - nuclear matrix element defined by the wave functions of the initial and final state of a nucleon. M is 1 when ψ_i and ψ_f are identical. The more they are differ, the more M is smaller [40].

If dn/dE gives the number of states for ψ_i and ψ_f within $p+dp$, the probability of radiation and consequentially the life time to beta decay (τ) for a transition to a particular state of the daughter nucleus is given by[1]:

$$d\lambda = \frac{2\pi}{\hbar} g^2 \mid M \mid^2 (4\pi) \frac{p_e^2 dp_e p_\nu^2}{h^6} \frac{dp_\nu}{dE} \tag{2.7}$$

To find the total decay rate, we have to integrate 2.7 over all values of the electron momentum p_e. The neutrino momentum can be expressed through Q_β as $p_\nu = \frac{Q_\beta - E_e}{c}$, where E_e is kinetic energy of the electron, and also depends on p_e. Thus, we obtain:

$$\lambda = \frac{g^2 \mid M \mid^2}{2\pi^3 \hbar^7 c^3} \int_0^{p_{emax}} F(Z, p_e) p_e^2 (Q_\beta - E_e)^2 dp_e; \tag{2.8}$$

and

$$f(Z, E_0) = \frac{1}{m_e c^3 (m_e c^2)^2} \int_0^{p_{emax}} F(Z, p_e) p_e^2 (Q_\beta - E_e)^2 dp_e \tag{2.9}$$

is the Fermi function - a non-analytical integral which has been evaluated numerically and tabulated for values of Z and E_0(the maximum electron energy). To a first approximation this function is proportional to the fifth order of the energy difference involved: $f(Z, E_0) \approx const \cdot (Q_\beta - E_e)^5$.

The expression $ft_{1/2}$

$$f(Z, E_0) t_{1/2} = ln2 \frac{2\pi^3 \hbar^7}{g^2 \mid M \mid^2 m_e^5 c^4} \tag{2.10}$$

is called a comparative half-life or *ft* value. It gives a way to compare beta decay in different nuclei since the difference in *ft* values comes due to the matrix element M and thus, from the differences in the wave functions. In practice, *ft* takes a very wide range of values, as a result one has to consider a logarithm *log ft*.

See textbooks [1, 40, 41] for more details.

2.2 Allowed and Forbidden transitions. Selection rules.

Fermi transitions.

For allowed transitions, by definition the only change in the nuclear angular momentum must come from the spins of the particles: $\Delta I = l_e + l_\nu + s_\nu + s_e$, where l_e, l_ν is the orbital angular momentum carried away by electron and neutrino, and $s_{\nu,e} = \pm 1/2$

[1] in the assumption of equal probability of all possible distributions of energy between three particles participating in β decay (e, ν and the nucleus)

is their intrinsic spin. According to Fermi selection rules, in the allowed β transitions both the momentum and parity are unchanged ($\Delta I = 0$, $\pi_d/\pi_f = 1$). In this case S = $s_\nu + s_e = 0$, the electron and neutrino have their spins anti parallel which corresponds to Fremi's original assumption.

$L_f = L_i, \triangle L = 0$

$S_f = S_i \neq 0, \triangle S = 0$, but $S_i = 0 \longrightarrow S_f = 0$ forbidden

$\pi = 0$

Gamow-Teller transitions.

Another possibility when the parity is unchanged ($\pi_d/\pi_f = 1$) but spins of e and ν are parallel to each other, S = 1. In this case change in nuclear orbital momentum can be either 0 or ± 1 - such transitions are Gamow-Teller since they satisfy its selection rules.

$\triangle L = 0, 1$ $L_f = 0 \longrightarrow L_i = 0$ forbidden

$\triangle S = 0$, but $S_i = 0 \longrightarrow S_f = 0$ forbidden

$\pi = 0$

the *ft* values can be rewritten in terms of by square matrix elements for Fermi (F) and Gamow-Teller (GT) transitions (i.e. $|M|^2 = \langle F \rangle^2 + g_a^2 \langle GT \rangle^2$):

$$ft_{1/2} = \frac{const}{\langle F \rangle^2 + g_a^2 \langle GT \rangle^2} \tag{2.11}$$

Fermi transitions are the simplest ones. In an area with large Q_β GT transitions, which are more energetic, dominate. In contrast to the Fermi case, where only one state in the daughter nucleus is populated, in the GT case many final states are possible. As a consequence, the total strength can be fragmented between many individual levels with relatively large *log ft* values.

Forbidden transitions

Transitions where $\triangle L \neq 0$ are forbidden ones. Forbidden transitions are not forbidden in reality but merely suppressed to allowed ones and occur with smaller probability. The probability will be even smaller for transitions with $\triangle L = 2$. Forbidden transitions are therefore classified by their degree of ,,forbiddenness", $\triangle L = 1$ - first forbidden (FF), $\triangle L$ =2 second forbidden, etc. Since the parity an electron plus a neutrino function is given by $\pi_p = \pi_d(-1)^L$, FF must assume a change in parity of the nuclear states involved. Looking at Table 2.1, one can see that most FF justify both - Fermi and GT selection rules, and can be a mixture of both kinds of transitions with the exceptions

for $\Delta I = \pm 2$ when only GT are possible - *unique first forbidden transitions*. In other words, in a decay, where allowed transitions are possible, they will dominate, therefore, forbidden ones will be too weak and consequently, invisible in the experiment. However, when one moves away from the line of stability, the Q_β increases with the consequent increase in the average energy of the electron emitted in β-decay. This is where forbidden transitions start to become important.

TABLE 2.1: Classification of forbidden transitions

Decay type	**△L**	**△ S**	**△π**	**log ft**
Superallowed	0+⟶0+	0	no	3.1 – 3.6
Allowed	0, 1	0, 1	no	2.9 ÷ 10
First forbidden	0, 1, 2	0, 1	yes	5 – 19
Second forbidden	1, 2, 3	0, 1	no	10 – 18
Third Forbidden	2, 3, 4	0, 1	yes	17 – 22
Fourth Forbidden	3, 4, 5	0, 1	no	22 – 24

Spin Assignment

Based on the comparative β-decay or *log ft* values, spin and parity assignment for nuclear energy levels can be done. One of the first compilations was done by *Raman and Gove* in 1973 for 169 experimental *log ft* values from eight forbiddenness categories and established a lower limit for each particular forbiddenness category [42]. Since 1973 a considerable amount of new data was accumulated and in 1994 experimental *log ft* has been classified according to degree of forbiddenness for 2859 transitions between A = 11 -100 nuclei [43]. Later, in 1998 another compilation covering 3900 β-decay transitions was introduced [44]. As an example, Figure 2.1 illustrates the summary drawing of *log ft* values from [44].

2.3 Beta strength function

The distribution of β-decay intensity I_β and the fraction proceeding through neutron emission is characterized by the β-strength function S_β. Key β-decay properties including neutron separation energy S_n, Q_β values, $T_{1/2}$ and probability of beta delayed neutron emission P_n, depend on details of beta strength function. S_β which measures the transition probability from the parent to excited states of the daughter nuclei. S_β describes the spectral distributions of the matrix $|M|^2$ for GT and FF transitions to the final nucleus. The partial decay rates to a given final state is determined by the allowed phase-space for the emitted fermions and the Coulomb interaction for the β as well as

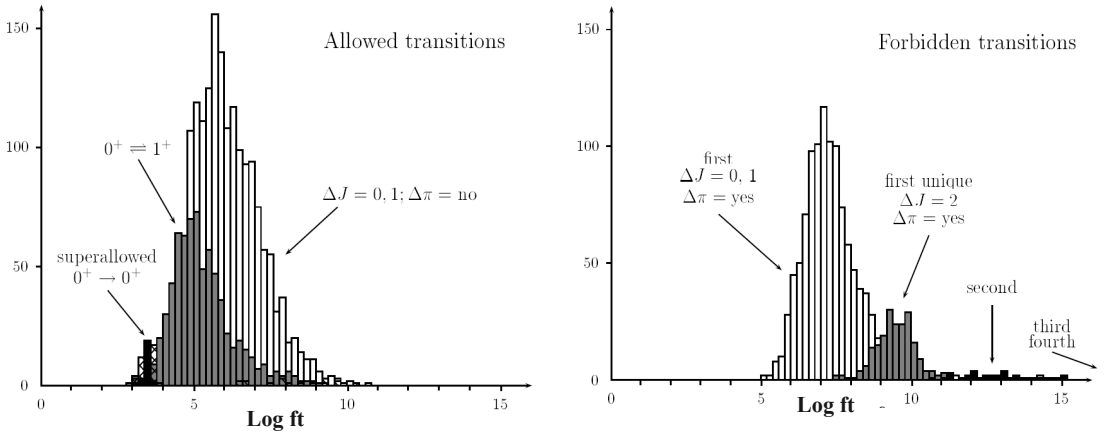

FIGURE 2.1: s summary drawing of *log ft* values from [44].

the amount of overlap between the initial β-decaying state in the parent nucleus and the populated state in the daughter nucleus. The overlap expresses the effect of the nuclear structure of β decay [39]. Theoretically, $T_{1/2}$ are related to S_β by the formula [45]:

$$1/T_{1/2} = \sum_{0 \leq Ei \leq Q_\beta} S_\beta(E_i) \times f(Z, Q_\beta - E_i) \tag{2.12}$$

which actually can provide information about average β feeding of a nucleus. Due to the phase-space factor of β-decay, $((Q_\beta – E_i)^5)$, the largest contribution to $T_{1/2}$ comes from low-lying daughter states (GT, FF transitions).

The probability to populate a state (E_i) above the ground state in the daughter nuclei depends on the energy available ($Q_\beta - E_i$). If we assume that ρ(E) gives the level density, the probability to reach a state within the energy interval (E+dE) is:

$$W(E)dE = const \cdot \mid M \mid^2 \cdot f(Z, Q_\beta - E_i) \cdot \rho(E)dE \tag{2.13}$$

The subsequent de-excitation of the state by a γ-ray or by neutron emission depends on the partial widths Γ_n and $\Gamma\gamma$ and their energy dependence. Therefore, the probability of neutron emission is given by $P_n = \dfrac{\Gamma_n}{\Gamma_n + \Gamma_\gamma}$ which, after multiplying by (2.13) can be represented schematically as the ratio of the integral of β-intensity to states above the neutron separation energy (S_n) to the integral for feeding all states:

$$P_n = \frac{\frac{\Gamma_n}{\Gamma_n + \Gamma_\gamma} \int_{S_n}^{Q_\beta} S_\beta(E_i) \times f(Z, Q_\beta - E_i)}{\int_0^{Q_\beta} S_\beta(E_i) \times f(Z, Q_\beta - E_i)} \tag{2.14}$$

Due to $(Q_\beta – E_i)^5$ dependence of the Fermi function, the physical significance of (2.14) is limited. It simply shows the importance of β feeding to the energy region beyond S_n.

However, if considered together, $T_{1/2}$ and P_n can give some clue on the nuclear structure determining β-decay. However, there are a few theories which can treat independently $T_{1/2}$ and P_n to make predictions in a certain restricted area of nuclei.

Measurements of parameters of beta decay experimentally

The *ft* value and the strength function (S_β) are related to the experimental observables by expressions:

$$\frac{1}{ft} = \frac{I_\beta(E_f)}{f(Q_\beta - E_f)T_{1/2}} \tag{2.15}$$

$$S_\beta(E_x) = \sum_{E_f \in \triangle E} \frac{1}{\triangle\, E} \frac{I_\beta(E_f)}{f(Q_\beta - E_f)T_{1/2}} \tag{2.16}$$

where I_β is the direct β feeding to a state of energy E_f in the energy interval $E_x + \triangle\, E$.

At first sight it seems that I_β can be measured straightforward by measurements of β decay to each individual state. But β-spectra are continuous and in complex decay schemes are difficult to disentangle. The most popular solution up to now is to use the intensities of beta delayed γ rays with high-resolution germanium detectors. Based on the information already known previously, such as transitions in the daughter nuclei, it is possible to establish a decay scheme from the coincidence relationships between the γ rays assigned to the decay. Once the scheme is established, one can determine the balance of intensity feeding each level. If everything is done correctly, the difference in intensity for a given level comes from direct beta-feeding.

2.4 Approaches to calculations of beta-decay properties.

Today in calculations of β-decay properties numerous theoretical approaches are used. In general, all approaches fall between two extreme kinds: macroscopic statistical models (empirical) and (large scale) fully microscopic shell models.

Statistical models: Gross Theory Calculations, Kratz-Herrmann formula

In statistical models, such as gross β decay theory [46] or the Kratz-Herrmann formula [47], no wave functions are obtained and empirical approaches are used to assume the shape of S_β (either constant or proportional to the level density). The number of parameters to determine is usually limited to one or two describing the average properties [48]. In the *gross theory* of β decay, developed in order to treat the gross features, summations over final states are replaced by integration, and the average of the squared absolute value of the matrix element times the final level density is investigated instead of individual matrix elements. This statistical model describes the average properties of

beta strength function and the shell structure of nuclei are not fully included [46, 49]. Later the semi-statistical gross theory including shell effect was introduced and can describe certain nuclei. In general it still has deviations with experimental data to be tackled [46, 50].

Model space

The most reliable predictions of β decay properties may be obtained by a full diagonalisation of an effective Hamiltonian in some model space. The solution of the Schrödinger equation provides nuclear wave function which allows a variety of nuclear properties to be calculated at the same time (e.g. ground state, level energies, spins, parities, $T_{1/2}$, P_{xn}, etc). The ,,model space" indicates the orbitals and the truncation assumed for a given calculation. Generally, the most complete results are obtained in cases when a model space as large as possible is used. However, sometimes an effective Hamiltonian can be defined more precisely in a smaller space [51, 52]. So-called semi-microscopic approaches stand for various nucleon-nucleon interactions and adopt a random phase approximation (RPA) which provides description of excited levels and allows approximation of the ground state: (quasi) QRPA, (continuum) CPRA, (projected) PQRPA, (second) SRPA, (extended) ERPA, (extended second) ESPRA, etc.

sd-shell model space

In the full sd-shell model space wave functions obtained were successfully applied to calculate GT β decay observables [53, 54]. Unfortunately, such a sophisticated approach cannot be applied for the heavier fp-shell nuclei which play an important role in nuclear processes in massive stars [51].

Finite range droplet model (FRDM) for nuclear masses

A key element of some global, unified, microscopic nuclear structure models for the nuclear mass and β decay based on microscopic Schrödinger equations is their reliability outside the region where the model parameters were determined. Thus, the models are valid also for the regions of neutron-rich nuclei beyond the experimentally known area near β stability [12]. Most influential was the *Moller-Nix* model [55], which is currently based on a finite droplet model with a folded-Yukawa single particle potential [56] with predictions ranging from ^{16}O to ^{339}136.

Quasi-particle random-phase approximation (QRPA)

The FRDM model was adjusted for a long range of nuclear masses. Therefore, due to good model reliability for new mass regions of nuclei, the model was completed with calculations of additional nuclear ground-state properties based on the same value of model constant for the same set of nuclei considered in its mass calculations [8]. However,

it treats Pn and $T_{1/2}$ only in allowed approximations and doesn't take into account the competition between GT and FF of beta strength function for nuclei with big neutron excess. Sometimes these large scale calculations are simply named FRDM+QRPA. Also there is a more recent version of this model [12].

pn quasi-particle random-phase approximation (pnQRPA)

This microscopic model is based on a proton-neutron quasi-particle random space approximation [57]. The original model employs a spherical single-particle model and particle hole terms of the separable GT force. The extended pnQRPA is able to calculate the $T_{1/2}$ but failed to reproduce the systematics of $T_{1/2}$. It can be related to the fact, that the calculated GT β decay rates used only the ph force (particle-hole), whereas for GT transitions the pp force (particle-particle) has to be included as well [51].

continuum quasi-particle random-phase approximation (cQRPA)

Continuum particle random-phase approximations based on a self-consistent ground state description within the local energy-density functional theory (DF) [36]. The key ingredients are a self-consistent mean-field potential (for the ground state properties) and universal effective NN interaction (for description of excited states) with both originated from DF. Through approximation of DF, the DF+QRPA approach develops a model in which the effective NN (nucleon-nucleon) interactions in ph and pp channels are introduced independently in comparison to standard QRPA, where these channels are interconnected [36]. Additionally, the cQRPA considers the FF transitions [37].

Extended Thomas-Fermi plus Strutinsky integral approach (ETFSI) for nuclear masses

The ETFSI model to calculate nuclear masses is entirely based on microscopic forces. Although, it gives basically the same results (error rms is about 0.7 MeV) in comparison to the liquid drop model calculations (e.g. FRDM), it is remarkable that ETFSI operates with only 8 parameters. This is presumably related to the much more microscopic basis of the ETFSI method: the FRDM (which has 19 parameters), lacking the unifying link of the force, has to parametrize its macroscopic and shell-model parts separately [58]. For large scale calculations, the ETFSI+cQRPA approach was introduced in [59]. Calculated r-process abundances by FRDM and ETFSI is given in Figure 2.2

Which theory to choose?

In nuclear physics there is no ,,correct" model since all of them are based on compromise between approximations to make equations possible to be solved on one hand, and the physical ,,allowance" of such approximations on the other. Some models emphasis global applicability, others - seek self consistency or the comprehensive inclusion of nuclear correlations. None of these models contains all important aspects in a consistent way. Even recently developed microscopic models are strongly restricted either to GT-transitions, or to a spherical shape and/or to even-even nuclei, to small model space.

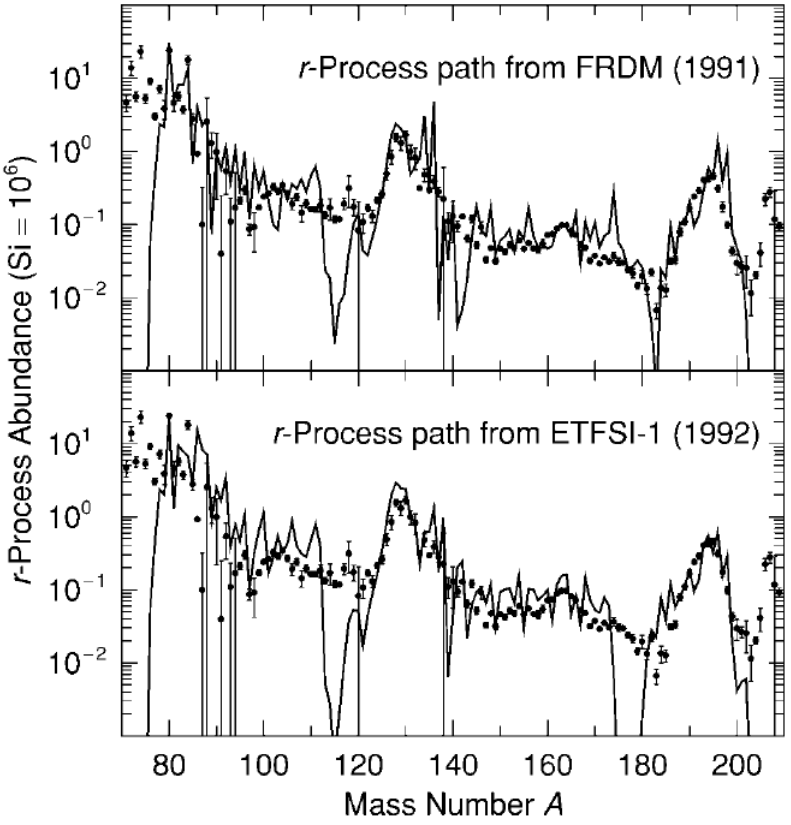

FIGURE 2.2: Calculated r-process abundances (solid line) compared to measured (solid circles). In both parts (top, bottom) half-life and P_n were calculated in a QRPA model. In the top part the r-process part was determined from FRDM [60], and in the bottom part from ETFSI [58]. Comparison is taken from [8].

Consequently, so far, there are no models suitable as a basis for global dynamical r-process calculations [31]. Some of key regions of nuclei have been reached recently thanks to new factories of radioactive beams and advances in selective methods technologies (e.g. ionization laser source). Today about 35 r-process isotopes have been identified via at least β-decay measurements. This leads to the fact that different theories can be tested and adjusted to new data sets.

Chapter 3

Neutron detector TETRA

,,Zero" can be also measured when the detector is off..."

G. Flerov

Contents

3.1 Neutron detection

Neutron detection methods are based on detection secondary charged particles produced as a consequence of neutron interaction with a material in the detector. Various media can be be used resulting in many possible options for a neutron detector. First of all, choice of detector depends on the ,,nature" of neutrons (e.g a type of the process neutrons originated from and consequently - their energy) - fast (E_n >10 MeV) or slow (E_n <1 MeV) neutrons; neutron multiplicity etc. Second, on the experimental challenge - whether one is interested in simply counting the rate and/or is neutron energy important. Finally, background conditions (in intense γ environment, as an example) can significantly modify the choice of a neutron detector. As a result, there is not a ,,uniform" detector which can perform well for every single application and the choice of one or another type of detector is always a compromise based on the precise experimental needs.

I have put in Appendix A a brief review on neutron detectors and their main properties and characteristics.

3.1.1 Detectors with ^{3}He filled counters

Gas-filled thermal neutron detectors can register a neutron due to products of the nuclear reactions caused in the gas:

$$^3He + n \rightarrow ^3 H + ^1 H + 765keV \tag{3.1}$$

$$^{10}B + n \rightarrow ^7 Li^* + ^4 He + 2310keV \tag{3.2}$$

$$^7Li^* \rightarrow ^7 Li + 480keV. \tag{3.3}$$

These reactions are exothermic and release energetic charged particles into the gas. Ionization produced by these particles initiates a process of detection. Typically, two types of gas are used: either ^{3}He or BF_3 (enriched in ^{10}B). ^{3}He is only about 1 ppm of natural helium [61] and is usually obtained by separation from tritium produced in reactors, which makes it really expensive A.3.6 [1].

In the present work ^{3}He proportional gas counters were used. A neutron is registered due to secondary particles produced in Reaction 3.1. As it can be seen from Figure 3.1, the cross section is much larger for thermal neutrons (∼0.0253 eV) rather than for faster neutrons (1 MeV). Thus, to maximize the efficiency, neutrons have to be slowed down to thermal energies. Neutron moderation can be achieved via elastic scattering collisions with hydrogenous material. For this reason, ^{3}He tubes are often embedded in high-density polyethylene (C_6H_{12}) see Fugure 3.2. Cross sections of the Reaction 3.1 strongly depend on the incident neutron energy E as $E^{-1/2}$ [61]. A brief comparison of properties of ^{3}He and ^{10}B gases is given in A.3.1. In practice, ^{3}He filled detectors are used in a multi detector arrangement as shown in the Figure 3.3 and consists of several tens of neutron counters placed in a moderator and arranged around a neutron source. The moderation process certainly gives constrains on the neutron energy. Usually, the total efficiency is uniformly high (up to 50-70 %) for the 0.15 - 2 MeV neutron energy range and depends on: gas admixtures (§A.3.4) and gas pressure (§3.7); kind and density of moderator (§3.7); geometry (number of counters used, their relative position to each other and to a source).

3.1.2 History of TETRA

A neutron detector, which later would be part of TETRA, was one of the first ^{3}He-filled detectors built at JINR (Dubna) in 1981 [63] originally aimed at measurements of spontaneous fission neutrons. The method of neutron detection was considered as a

[1] Some aspects of production of ^{3}He as well as none-fundamental physics applications are listed in the A.3.6

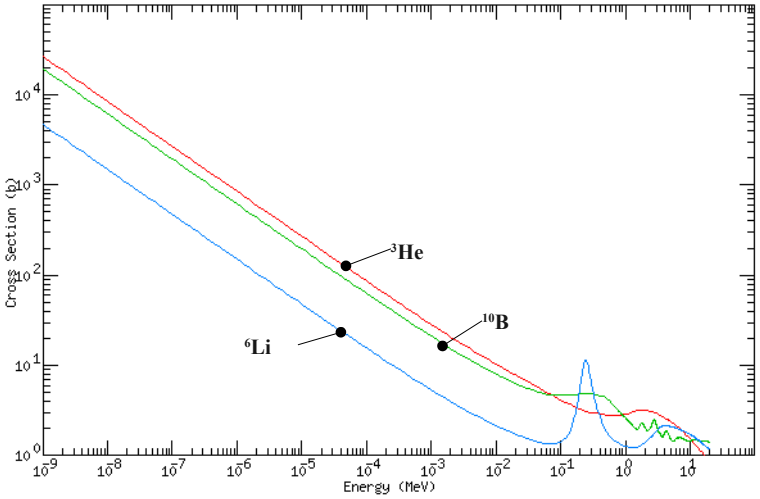

FIGURE 3.1: ^{3}He (n,p) - red, ^{10}B(n,α) - green, ^{6}Li(n,α) - blues cross sections as a function of incident neutron energy [62]

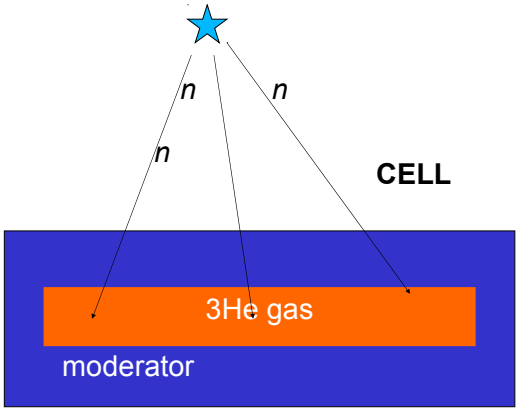

FIGURE 3.2: The mechanism of neutron registration by a ^{3}He counter. Neutrons are slowed down before entering the active material (^{3}He-gas)

tool in studies of the properties of new heavy and super heavy elements synthesized at JINR, studies of spontaneous fission, and the search for super heavy elements in nature.

Such types of neutron multidetectors have been designed and produced at JINR to be adaptable for various experiments. Among these, one may quote the experiment at VASSILISSA (FLNR) [64–66] which allowed the measurements of properties for neutron emissions from heavy and superheavy nuclei: the multiplicity of neutrons emitted, $T_{1/2}$ values of these nuclei in the domain N (140-184) and A (160-270). Experience from these experiments helped to guide construction of another detector of this type to search for the best candidate for a superheavy element in nature, element with Z=108. This experiment (SHIN) [67] is going on successfully in the underground Laboratory (LSM, France). Yet another neutron detector was devoted to the study of rare modes of spontaneous fission at the FOBOS spectrometer [68] and later at miniFOBOS (see comparison Table 3.5).

Initially, the detector had 56 counters 500 mm length and 32 mm in diameter filled by ^{3}He at a pressure of 7 atm with an addition of 1 % such as CO_2. The admix of electronegative gases of CO_2 or methane (usually, in quantity $< 10\%$) ceases the discharge[2]. Each counter with preamplifier and high-voltage circuit represented a separate module placed in a moderator. To exclude interference a high voltage of +1800 V was applied to each counter via an RC-filter from the same power supply. In oder to eliminate the probability of spark discharge the bushing of each counter was armed with a guard ring.

In 2005, in the framework of the IN2P3-JINR collaboration, part of the detector for measuring neutron multiplicities and angular correlations which consisted of more that 300 counters [69], was transported to IPN Orsay to be used in experiments to investigate β-delayed properties of neutron rich nuclei. At that time the detector was named TETRA with respect to its 4π geometry and possibility to study correlation in multi neutron emission.

Upon its arrival TETRA consisted of 90 ^{3}He counters arranged in 5 layers in a hexagon as it shown in Figure 3.3 with the central hole about 5 cm. Each tube was placed in its individual hexagon brick of moderator and had a built-in preamplifier. The distance between centers of tubes was 5 cm. No shielding from background neutrons was applied. Efficiency measured for a spontaneous fission source placed at the center of the detector was ∼70%. The description of the detector of that period is given in [67].

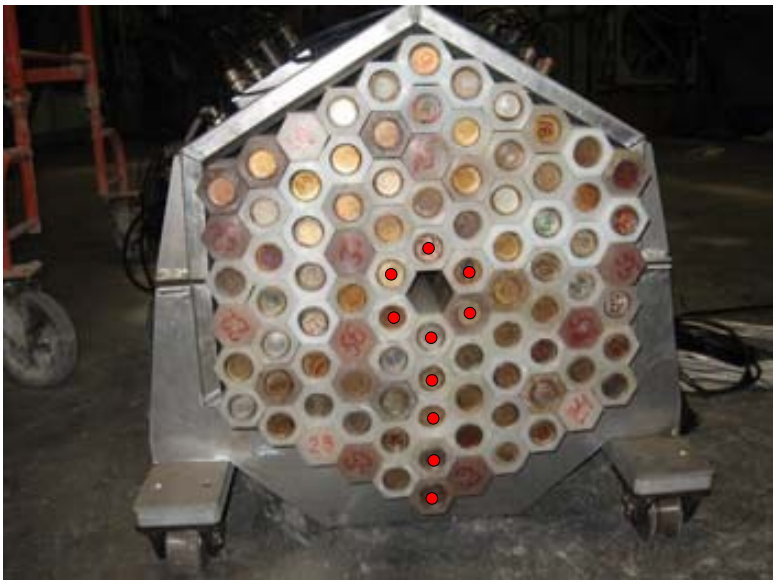

FIGURE 3.3: Overall view of TETRA before the upgrade. Red marks means the modifications in the configuration discussed in § 3.1.5

[2]see Appendix A.3.4 for more details

The idea to use individual cells of moderator rather than a big piece with holes for counters was introduced at Flerov Lab and was successfully employed in different experiments. By spitting into independent cells (counter + moderator) the neutron detector can be easily re-installed at setups where its application as a single item is difficult. However, only the close (,,barrel" geometry can provide the highest efficiency. The ,,barrel" or ,,honey-cell" design is the closest to the cylindrical one which minimizes effects at borders of the detector.

3.1.3 Our choice of the detector

TETRA came to France specifically for experiments seeking neutrons emitted after beta decay of nuclei with large neutron excess, which were supposed to be produced at ALTO. TETRA was selected for this mission because of its high efficiency - the most important parameter to study isotopes with low production rates. The uniformness of efficiency up to 1 MeV neutron energy was achieved owing to the geometrical configuration. A neutron ^{3}He filled detector must have at least 4 rows to insure the constant dependency of neutron detection efficiency as a function of neutron energy till 1 MeV, as it was shown by Dubna scientists in [70]. It is generally assumed that the energy of neutrons emitted after β-decay is relatively low and doesn't exceed 1 MeV. There were evidences of that in delayed neutron energy spectra experimentally measured in [71–75] for delayed neutron precursors. In our experiments it was also observed some evidences in favor of low (<0.5MeV) neutron energy (see §6.4).

TETRA:

- is relatively insensitive to γ-rays (see A.3.3);
- has no cross-talk [3] since a thermal neutron is consumed (in the Reaction 3.1) during the registration;
- has no threshold for neutron energy;
- allows studying of angular correlations [69][4];
- ^{3}He gas is not toxic (as with BF_3);
- can operate a long time with stable parameters;

[3] Cross-talk - a typical effect in multi detectors systems manifested in the fact that a detected particle can be seen by more than one detector as a consequence of incomplete energy deposited in the active volume of the first detector touched, leading to registration of false events by the electronics, for more see §A.5.

[4] with the angular resolution ∼20

- is simple in transportation and exploitation (compare to liquid scintillators).

But efficiency of TETRA is not its only advantage - the comparison of the most important characteristics of neutron detectors are given in Appendix A.

The major drawback one can notice is that ^{3}He-filled detectors are ,,slow" (see §3.5.3 for more details). Nevertheless, an attempt to observe γ-neutron coincidences was successfully made in 1999 at GANIL with a ^{3}He-filled detector built at JINR [76]. In spite of the ,,slowness" of TETRA, as will be shown in the following sections, we obtained nice γ–β–n coincidence spectra (see results in Chapter 6). Obviously, the energy information provided with such a neutron detector is very poor. However, as it was proposed by Reeder in [74], by mapping the counter fired it is possible to restore the initial neutron energy: the less energetic neutrons will be registered in the first layer of the detector; whereas more energetic ones require a longer path in the detector to become thermal thus touching the outer counters. Even though it exists, this technique is not precise. Therefore, for measurements where a neutron energy is required another type of neutron detector should be used. In the present research, we were able to indirectly estimate the neutron energy through neutron efficiency measured via γ–β–n and MCNP calculations (Chapter 6).

3.1.4 TETRA/ALTO commissioning experiment in 2009. Conclusions.

The first commissioning experiment with the detector was performed in 2009 together with one of the first technical tests of the ALTO facility and reported in [77]. A radioactive source accumulated by beam at a collection point was transported by the tape system to the detection system located 2 m away. The main difficulty came from long transportation time - from the collection point to the detection system, and the fact that TETRA had to work in conjunction with $4\pi - \beta$ and γ detectors which had to be put inside TETRA. Based upon the results obtained, the concept of the future installation for β decay neutron studies was essentially born on the fact that the beam should be accumulated inside the detection system. Also, it turned out, that the current TETRA-DAQ system didn't provide sufficient information to monitor the parameters of the detector on-line and, if coupled with an external data acquisition system, provided only limited information on neutron events. The following list of upgrades was considered.

$\star$ Development of proper support to have TETRA installed right on a beam line in the most appropriate orientation for the highest efficiency configuration. Moreover, there should be three, easily re-produced, geometry configurations possible: from an option for maximum neutron efficiency (ε_n^{max}) and minimum efficiency of gamma registration

(ε_γ^{min}) - to measure absolute branching ratios; to the opposite one - with ε_γ^{max} at reasonable cut in ε_n^{min} (§ 3.1.5) - for spectroscopy of fission fragments.

⋆ Design and production of a proper shield from background neutrons (§ 3.7, § 3.1.5);

⋆ Development of new devoted electronics and software to allow multiplicity counting and coupling with any external DAQ (§ 3.2).

During the first stage of my thesis I successfully fulfill each of the points mentioned above. At the second stage I performed series of physical measurements and proved workability of the final system created by results obtained.

3.1.5 Optimization of the TETRA setup for on-line measurements at ALTO

Basic requirements

There are three types of detectors to be used in the installation: the neutron detector TETRA (measurements of neutron activity curves), a Ge detector for γ detection (isotope identification, estimation of production rate) and a plastic beta counter (measurements of beta activity curves). To keep the neutron efficiency high the barrel geometry is the optimum as discussed above. From this viewpoint, the configuration presented in Figure 3.3 is, actually, the best one. However, to house a beam line and a $4\pi\beta$ detector, the central cavity was extended by removing the inner 6 counters. The necessity to collect and guide the light from the plastic scintillator forced us to remove another four counters as it is shown in the Picture 3.3 (marked by red). The geometry was preserved by using a single peace of moderator in place of the detector modules.

Three configurations were envisaged as a trade off between neutron and γ-ray efficiencies (Figure 3.4). Neutron efficiency for each configuration was carefully calculated with MCNP (§3.7) [78].

3.1.6 New on-line configuration for TETRA

Mechanical support

Based on the previous TETRA design and a model of the detector done in MCNP (§ 3.7), a new mechanical design for support and shielding from background neutrons was introduced [79]. The overview of the setup is presented in Figure 3.5. The support represents two identical parts which can move on rails to reassure easy access to a beam line located at the *center cavity* and a beta detector. 90 counters are placed

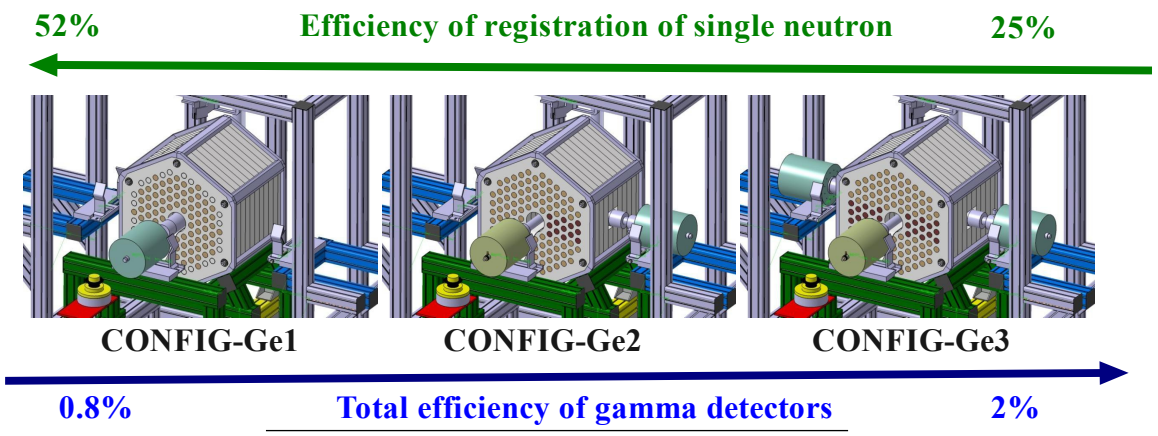

FIGURE 3.4: Three configuration of the installation assumed. The ε_γ is for 1 MeV γ ray, $\varepsilon_{neutron}$ for 1 MeV neutron

inside the single piece (density 0.93 g/cm^3) of *polyethylene moderator* and wrapped all round by a 15 cm thick layer of borated polyethylene used as shielding from background neutrons. The 15-cm thick borated polyethylene slice ensures almost total suppression of the background (simulation details in § 3.7). There are 4 rows to accommodate all neutron counters around the central cavity of only 13 cm diameter for maximum neutron efficiency. At the center of the detector there is another cavity for a light guide to evacuate the light from β scintillator. The fifth layer, temporally filled by polyethylene rods, will be used to accommodate an extra 20 neutron counters when higher efficiency of germanium detection is required (configurations **Ge2, Ge3**, Figure 3.4). Also there are 8 aluminum rods to reinforce the installation mechanically.

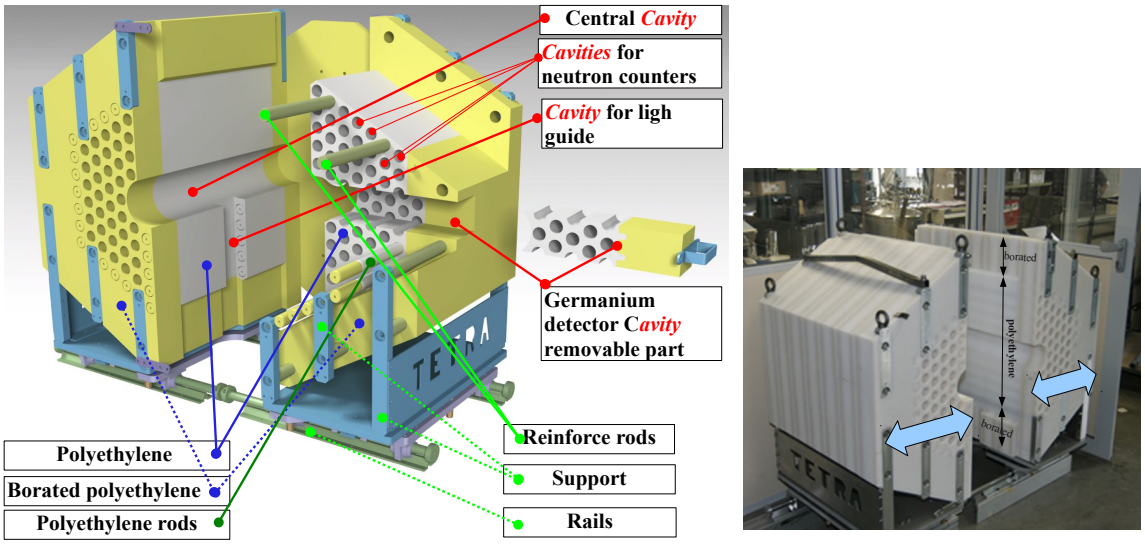

(A) Drawings of new mechanics for TETRA. Side view.

(B) Produced mechanics for TETRA.

FIGURE 3.5: TETRA design

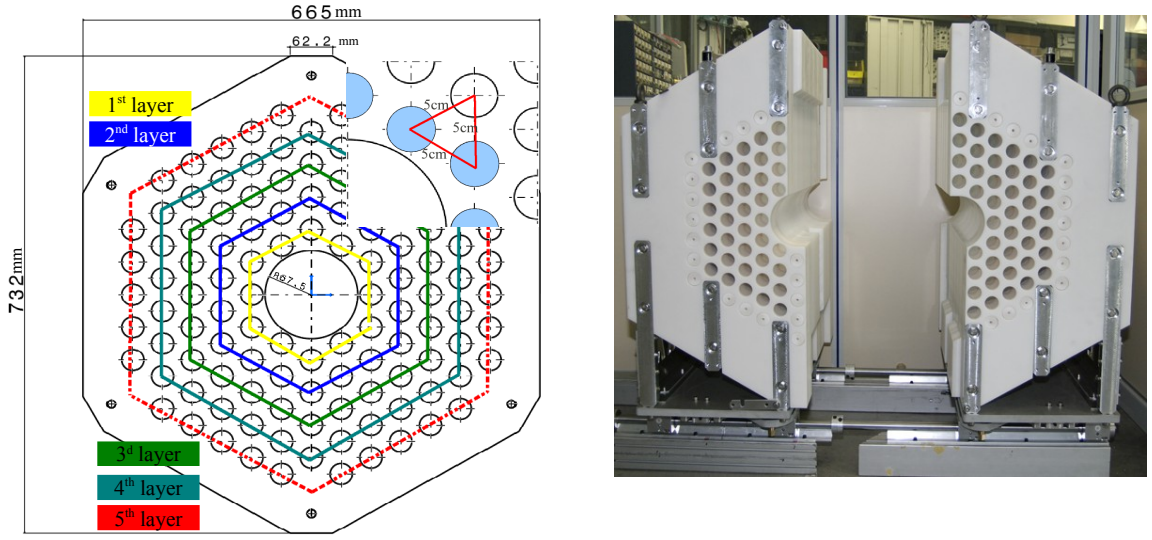

(A) Drawings of new mechanics for TETRA. Front view.

(B) Produced mechanics for TETRA.

FIGURE 3.6: TETRA design

3.2 Electronic system for TETRA

The 96 channel TETRA electronic system consists of two parts - the Control (to set channels parameters); and the data acquisition part (T-DAQ). Commercially available alternatives of Control part are too expensive due to exclusiveness. Whereas, data collection part can be fulfilled by currently available to physicists DAQs with sufficient number of channels.

I contributed to design of the electronic system produced at JINR Dubna, tested on the demonstrator and then delivered to Orsay, where I verified and adjusted it to TETRA.

Appearance of the counter

A single ^{3}He proportional counter is shown in Figure 3.7 (top). It is a 500mm length, 32mm in diameter steel cylinder with a tungsten wire at the center. At the end of each counter there is a preamplifier installed on plexiglass. In order to prevent a spark discharge there is a small guard ring. The typical electronic scheme for gas filled detectors is shown in Figure 3.7 (bottom).

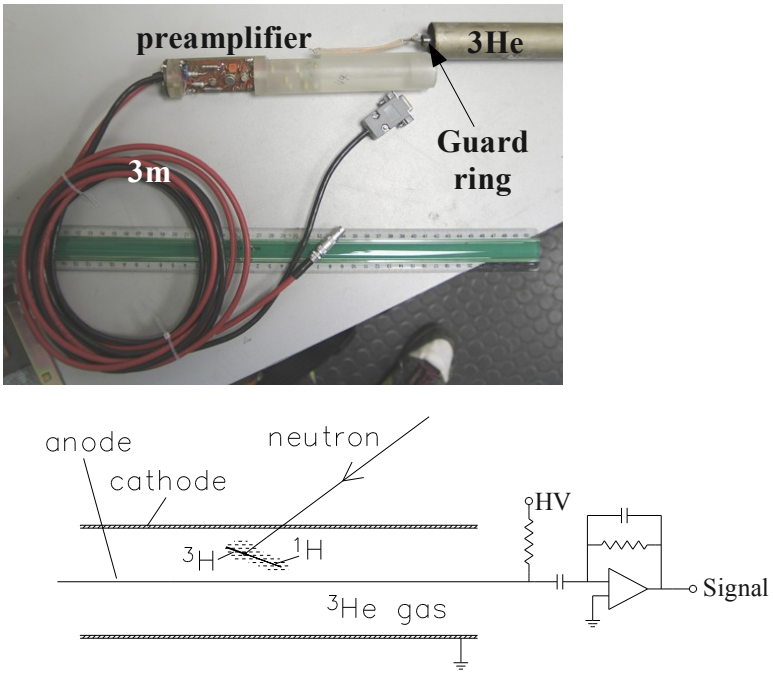

FIGURE 3.7: Single counter with its pleamplifier (top). Gas detector setup (bottom).

3.2.1 How it works? Internal T-DAQ.

A ∼0.1V signal from the preamplifier, rise time 1.5μs and fall time 5μs, enters one of 96 input amplifications channels (Figure 3.8) with individually set coefficients of amplification (K_i, i=0..96) through unique channel ID number (N_i, i=0..96[5]). To separate a neutron signal (from gamma, noise, ...) two discriminators are used: all the events below the *low* discriminator are rejected, whereas the special mark (§3.2.3) is added to the data buffer if the *high* discriminator is reached. The values for the discriminators are the same for all channels. The amplitude after amplifiers can be monitored by sockets IDC-40M. If the signal is not rejected by the discriminator, the channel ID is encoded and ,,is held" till it's requested by the multiplexer.

For the multiplexer it takes 50 ns to interrogate an ,,empty" discriminator [6] and for 850 ns the discriminator holds an event. In the beginning the first 16 channels (1 - 16) are interrogated, on the 17th act the multiplexer verifies if there is a channel touched among higher channels (17 - 96). If not, the search comes back to the first channel. In case there is a higher channel fired the next channels (16 - 32) are interrogated. If the responded channel is still not found the multiplexer requests the next sixteen channels (36 - 48) and etc. till the touched channel is found.

The number of this channel (it is number 19 = 16 + 3 as in the example) is transmitted by the Converter into a serial code and is sent through TTL-NIM converter and further by bus *Data* simultaneously with the *Clock* and the rim signal *Frame* [7]. The widths of serial transmission of the number (address of the counter touched) is 850 ns. If there are no more channels fired, the channels of interrogation from 17 to 32 and 1 ÷ 16 are sequentially reset and the search restarts from the beginning. This peculiarity reasonably insists on putting counters with expected higher counting rate to the lower channels of electronics since they are interrogated first.

Signals from the Data, Clock and Frame bus join the shift register of the USB interface, where they are recorded in a 16x32 buffer together with information about the time of arrival of the *Frame* signal. The time is defined by a 20-byte timer counter with a 20-byte capture register. On the input of this timer counter special signals each with $\tau_{step} = 2\mu$s are sent to be able to restore time of events after the beginning of a run. The 32-byte word is formed and sent via the USB interface to a computer. Each ∼2 second time interval the time counter produces an overflow mark which creates a word corresponded to number 0, time 0 and 1 in the higher rank (the format of output file is described in §3.2.3).

[5] external signal (synchronization) has an index 255
[6] therefore, the time needed to request an empty detector is 5μs
[7] the transmission of the *Data* is wrapped by the *Frame* signal

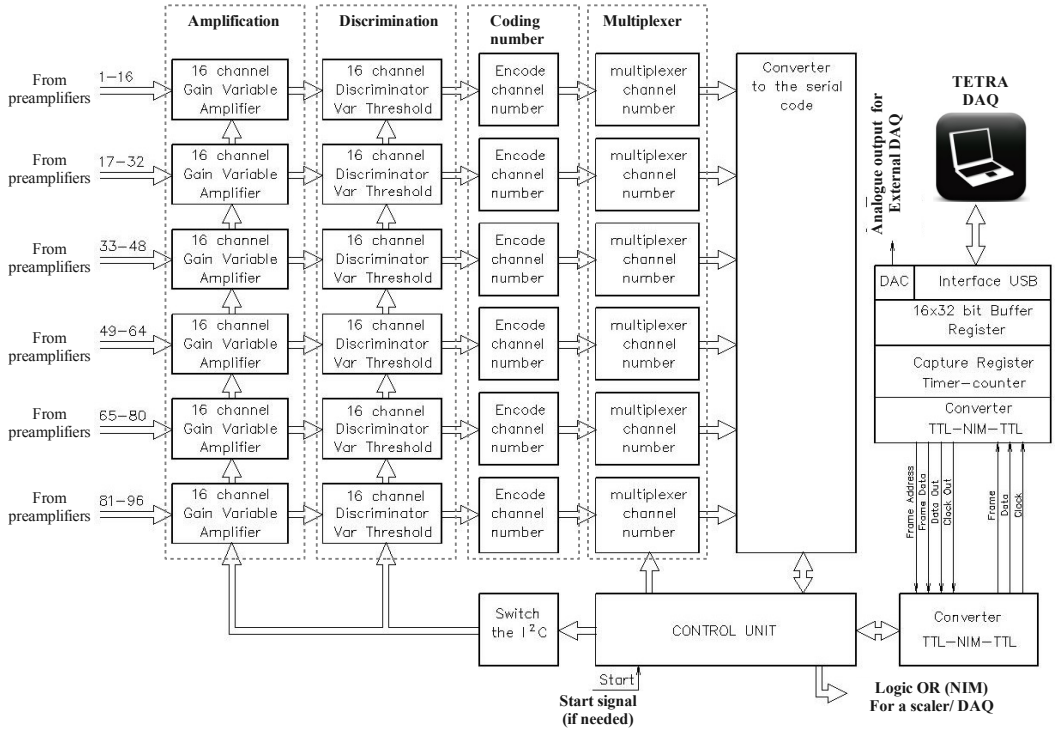

FIGURE 3.8: Scheme of TETRA electronic system

Since for higher neutron channels (>32) the process of interrogation takes a longer time, as it was explained in this chapter, we applied a time correction coefficient which depends on the channel number touched. Correction for channels 1-32 is 2μs; 33-64 is 4μs; 65-96 is 6μs. Although it can slightly influence the neutron distribution in time, due to long moderation and diffusion time it does't influence much the data analysis.

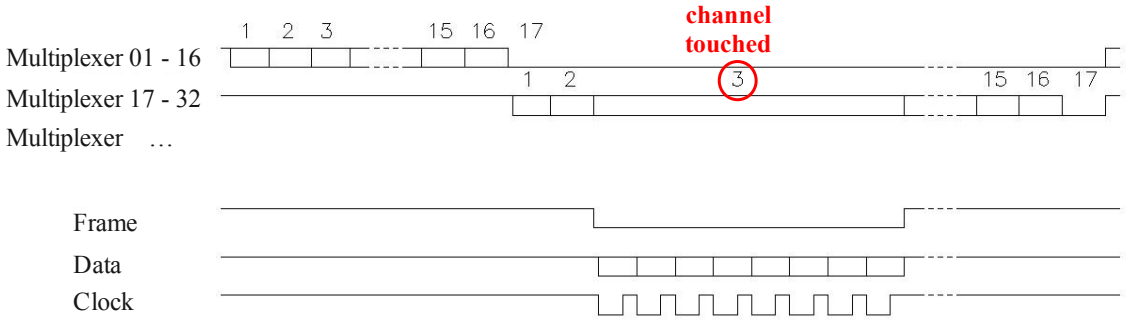

FIGURE 3.9: How does the Multiplexer work

Appearance of the electronics system

The appearance of the electronics system is given in the Appendix C, Figure C.1. There are two modules (*Input Unit 1*, *Input Unit 2*) with 48 input channels each connected by the ribbon cable located next to the detector. Each input socket has 9 pins - pins 3,5 (-12V, +12V) alimentation of preamplifier; pin 2 is a preamplifier signal; 1,6 - the

ground (the other pins are not used). Furthermore, the input channels are grouped by 8. Each eight has a logical output OR (*OR1-8*, *OR9-16*, etc). Also there is a logical output *Global OR* for all 96 channels[8]. Amplitudes after amplifiers can be controlled by the sockets *Analog OUT 1-16*, *Analog OUT 17-32*.

The *USB module*, on one hand, is connected to the *Input Unit 1* by seven 50-Ω cables and can be installed far away from the detector (in the Physics Room, for an example, as in our experiments). The data from the detector is transferred by the cables named *Frame, Data, Clock*. The coefficients of amplifications (K_i) and thresholds are set by the cables *Frame address, From Data, Data Out, Clockout*. On the other hand, the *USB module* is linked to a computer to allow for control of the detector and to record collected data.

The high voltage is the same for all the counters and is applied from a high voltage power supply via the *high-voltage distribution* unit.

3.2.2 Dead time of internal DAQ.

The time needed to interrogate the empty detector is about 4.8μs (50ns × 96 channels) and 0.85μs to record an event. Therefore, the maximum dead time possible (τ_{max} = 5.65μs) is in the case when the last channel is touched. This means that the electronics can deal properly with an event flux up to 10^5/s. However, the DAQ is designed specifically to deal with neutron flashes of high multiplicity. As an example, in spontaneous and in multi neutron emission after β- decay, all the neutrons are emitted right after the fission/decay within a short time interval Figure 3.10. Consequently, the dead time τ_{max} may cause significant loss of true events. The influence of dead time on multiplicity distribution is shown experimentally in §3.5 and §5.4.

If not to eliminate, but at least to considerably decrease the effect of dead time, our system is made to hold in a buffer up to 16 channels, even if they all have been fired exactly at the same time, until they are interrogated by the multiplexor. Obviously, once the limit of 16 events is achieved, no more events can be stored within τ_{max} needed for the first event to be recorded. Since an event with multiplicity 16 is considered as almost impossible, there is always room for an event to be held and to be written later. To events held in the buffer the time of interrogation is attributed. Additionally, as was explained in the previous chapter, τ_{step} = 2μs is the minimum possible time difference between two consecutive events. Both events are registered, but with a shift τ_{step} in time. In summary, the negligible low dead time is reached due to offset in the time distribution. From my viewpoint it is strongly beneficial for the ^{3}He filled neutron

[8] *OR1-8*, etc and *Global OR* are NIM with length 200ns.

detectors, which are considered as ,,slow ones" owing to moderation time which in one way or other, corrupts the time. Moderation and diffusion time is discussed in 3.5.3.

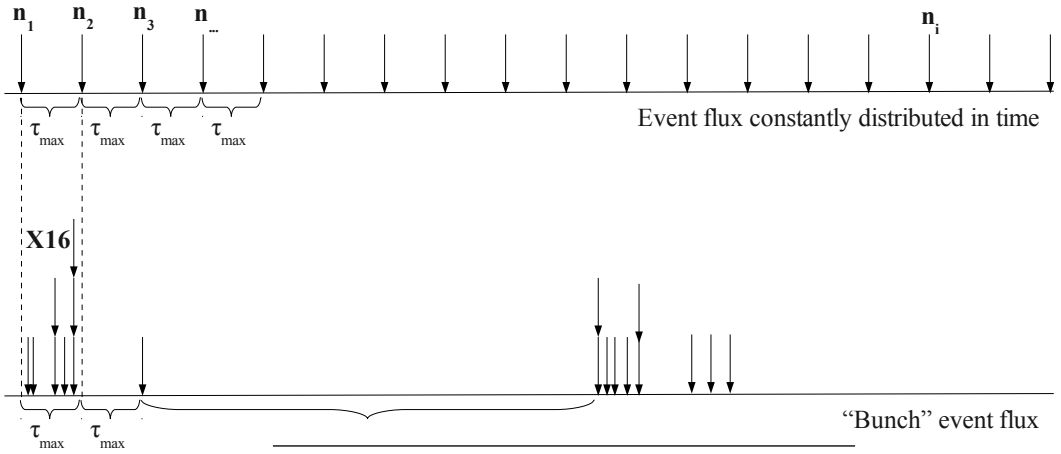

FIGURE 3.10: Flux of events differently distributed in time

3.2.3 Format of output data.

A buffer transferred to a computer contains a channel number (number of counter fired), time when the event was registered and a mark if the high threshold is achieved. In a buffer there are 4 words of 8 bites each (see Figure 3.11). The last bite of the first 3 words is always 0 whereas it is always 1 for the 4^{th} word. The buffer is not considered as a true one unless the control bite sequence is 0-0-0-1.

The software provided with DAQ works under *Windows XP* and *Windows 8* and simply allows one to collect and to store data, by USB-port, on a hard disk in the format just described. In order to reconstruct a neutron event and to represent them in a more comprehensive way, I developed a C++ application.

3.2.4 Different outputs. External DAQ.

The electronics allows storage of the neutron data in 3 ways. First, the internal storage (T-DAQ) is the fastest and provides the most full information on neutrons detected, e.g the number of counter fired, the time and information on whether the amplitude of the signal was higher than the upper threshold. In parallel, an independent analog signal, to be sent to an external DAQ, is formed by the Digital to Analog Converter. The amplitude of this signal is proportional to the number of the counter touched. Since it demands time to form a signal of certain amplitude, this channel is the slowest one.

Bit №	7	6	5	4	3	2	1	0
Word 1	0							
Word 2	0	0/1						
Word 3	0							
Word 4	1							

	Control sequences	4 bites
	Number of channel (counter) fired	7 bites
	High threshold	1 bite
	Time of Frame Signal Data (neutron time)	20 bites
	Total:	32 bites

FIGURE 3.11: Data format of internal DAQ

Finally, there is a fast NIM signal *OR* from all the counters to be alternatively sent to an external DAQ. In this case, the dead time is determined by an external DAQ (and is about 10μs for COMET - see § 5.4). The comparison of these three outputs is highlighted in the Table 3.1. The reliable multiplicity counting can be done only with the T-DAQ due to absence of the dead time. In contrast, the dead time of the external DAQs can significantly corrupt the multiplicity distribution (see §5.4).

During tests and tunes of TETRA the internal acquisition only was involved. Whereas in physical measurements, due to low neutron counting rate, the External DAQ NIM(2) was used to facilitate the analysis procedure.

TABLE 3.1: Comparison of different outputs of TETRA electronics

	TETRA DAQ(1)	External DAQ NIM(2)	External DAQ COMET(3)
Dead time	no	10 μs	25 μs
Multiplicity	yes	-	-
Information of the neutron channel fired	yes	-	yes
Information on the upper threshold	yes	-	yes

3.3 Cabling

Originally, the tubes of TETRA had 0.5m HV, LV/signal cables, which put limits on geometrical configurations, and had old USSR sockets, which were extremely reliable

but incompatible with current standards in the world today. That is why it was decided to exchange all together - cables and sockets. The current view is shown in Figure 3.7, on page 38. The HV cable is a shielded one which can operate at 5kV maximum with a lemo high voltage socket at the end (*FFB.0S.250.CTAC*) and a (*ERA.0S.250.CTL*) socket on the high voltage module. The signal/low voltage cable uses a simple 9-pin socket. Pins 1 and 6 are grounded; pin 2 is a signal; pin 3 and 5, respectively, provide with +12V, -12V (red/blue cable, Figure 3.7) needed for the preamplifier. The 3-m cable length is long enough to be flexible in any TETRA installation.

3.4 Performance of the new electronics system

3.4.1 High voltage and count rate

A common high voltage was applied to all counters via the High Voltage Distribution Unit through an RC-filter. Figure 3.12 illustrates the counting characteristic of TETRA. Saturation is achieved at about +1800V. However, the signal from each counter has its own unique amplitude which needed to be adjusted to the same level, for all tubes, before being sent to the discriminator. The coefficient of amplification for each channel was chosen individually by pulse height spectra obtained for all 90 counters.

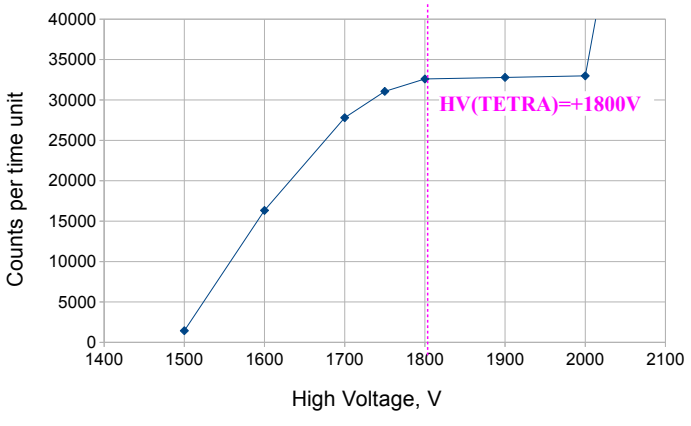

FIGURE 3.12: Counting characteristic of detector of TETRA

3.4.2 Pulse Height Spectra.Fine tune of TETRA.

The shape of the spectra depends on the kinematics of the Reaction 3.1, page 30, choice of amplification parameter, high voltage applied to the tube, gas properties, γ flux. The

full energy peak represents the 765 keV from collection of the kinetic energy of both particles produced in the reaction (proton and triton). If one of the particles enters a wall of the counter before to have given up all its kinetic energy, less energy is collected in the gas which results in a low-energy tail. Since two charged particles are emitted back-to-back one of them is certain to be detected. Thus, there is a minimum collection energy with a wide valley below. The low-energy increase results from noise and piled-up gamma-ray events. Finally, there are a few events of high amplitude, which probably corresponds to α-particles from spontaneous fission of uranium which naturally occurs in the steel from which the tubes are made.

The wall-effect can be eliminated or at leas minimized by increasing gas stopping powers. Obviously, this could be done either by a larger tube size or by higher pressure of ^{3}He. In practice, a gas mixture with heavier gases, such as Argon, is used. The presence of an argon fraction increases the relative size of the full-energy peak because the reaction products have shorter ranges to deposit their energy. On the other hand, an argon gas admix is a very poor performer in a γ-ray field. TETRA has a 1 % of CO_2 admixture which makes the counter a bit slower but more resistant to γ-rays (see Appendix A.3.4 for more details)[9]. The choice of amplifier time constant determines the

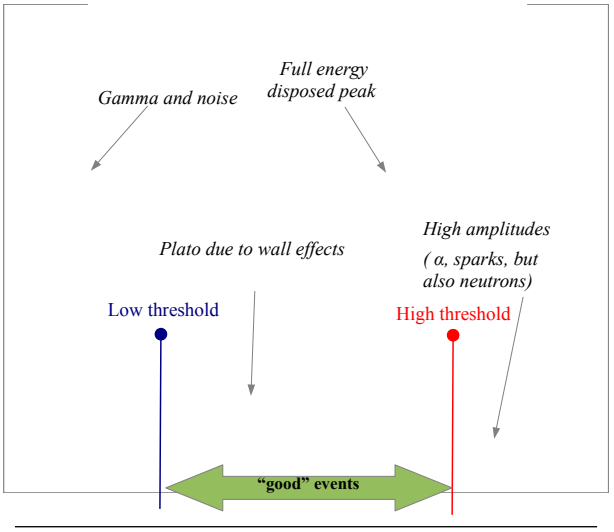

FIGURE 3.13: Typical Measured Pulse Height Spectra (for a ^{252}Cf source) from a ^{3}He counter with new electronics

degree of charge collection from the tube. Time constants of 2 μs or greater result in nearly complete charge collection and yield spectra such as the spectrum shown in 3.13, with 5 to 15% resolution (FWHM) of the full-energy peak. Time constants of 0.1μs to 0.5μs cause complete loss of the peak shape but allow for counting at higher rates with

[9] A neutron detector for the SHIN experiment [67], the one I worked on before this thesis, has 7 atm pressure of ^{3}He with 2 atm admixture of argon. Even being much smaller in size (60 counters) it has higher, up to 70 %efficiency but worse neutron-γ separation. Therefore, it is a precise physical task to determine the type of neutron detector to be employed

less noise pickup and gamma-ray interference. A 0.5μs time constant is a commonly used compromise between good resolution and high-count-rate capability. Pulse height spectra measured for each counter of TETRA are given in Appendix C.3[10].

When ^{3}He tubes are used in multiple detector arrays, like TETRA, it is important to achieve a good resolution (on the order of 5% FWHM) and to a uniform gas mixture so that the position and width of the full-energy peak will be the same for all tubes. This uniformity is provided by newly developed electronic system created.

A typical signal from a counter after amplification (the one which can be seen using *Analog OUT* sockets, §3.2.1) is shown in Figure 3.14. Coefficient K_i for each channel was set so that the amplitude the amplifier output was 3V. In the fine tune, with use of an intense *AmBe* source, the K_i was tuned so that the full energy peak drops at the same channel [11]. Please note that if K_i is set to be 0 it simply means that the signal from this channels is not amplified, but its amplitude is not zero.

Once all the signals were aligned, they are sent to the discriminator, common for all the channels. To see the full list of pulse height spectra for each counter refer to Appendix C.3. The value of thresholds ranged over 0.04V<U_{low} <1.39V and 0.06V<U_{high} <3.78V, and are set in a decimal numeral system (§C.4). All the events, with corresponding amplitude below U_{low} are completely rejected, whereas if U_{high} is achieved, the event is recorded with a special mark in the data (the output format § 3.2.3) and can be separated in the analysis.

3.4.3 New benefits

In the previous version of the electronics system, 90 outputs from counters were organized in six groups (16 counters each) according to their amplitudes from the preamplifiers. Since all counters in the same group had the similar amplitude, only one discriminator per group was used. Although the electronics provided an on-line diagram displaying number of counts in each counter, no proper internal DAQ was present. To carry out an experiment an OR signal (NIM) from all the 90 counters was delivered to a single channel of COMET - an external DAQ. The dead time of COMET (10 μs) made it impossible to measure neutron multiplicity (see §5.4). The new electronics produced is free of all these drawbacks (see part **Electronics** in comparison Table 3.4). Moreover, the implemented fast T-DAQ with an external start signal (from β of fission fragments) brings a certain degree of independence in technical tests and long-run background measurements.

[10] time constant is 0.5μs

[11] the pulse height spectra, definitely, does not conserve exact information concerning initial neutron energy

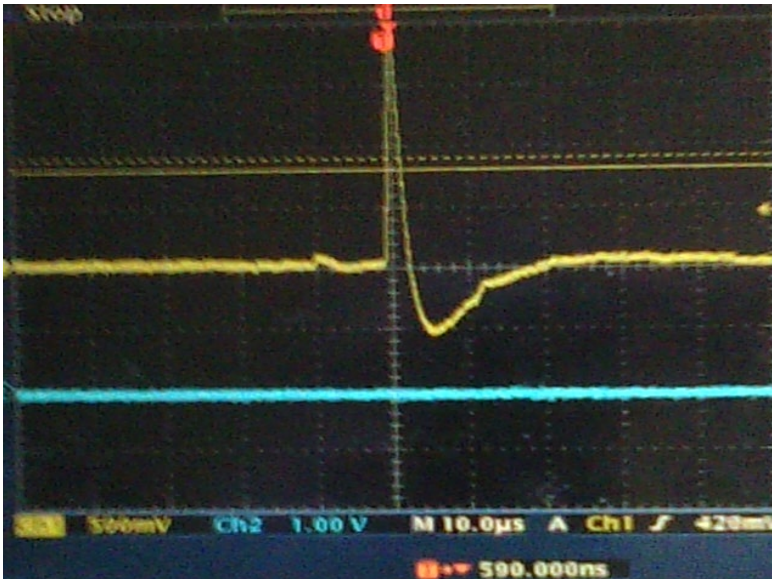

FIGURE 3.14: Typical signal after amplifier

3.5 TETRA efficiency calibration

A ^{252}Cf source was used in our efficiency calibration. Since ^{252}Cf emits on average 3.75 neutron/fission [80], within small time window after the moment of fission, only the internal DAQ with minimum dead time could be used for correct measurements (see Table 3.1). Here and further on the manuscript if only the efficiency of single neutron registration is considered.

3.5.1 Direct calibration

An efficiency of a detector is generally given by a ratio of registered particles to a number of particles emitted. Once the activity of the ^{252}Cf source was known (1450±50 neutrons s^{-1} in 4π on the 28/12/2011) we were able to measure $\epsilon_0(n) = 53\pm4\%$. Although, the value is exact enough and can be used in analysis of experimental data, it depends on precision of initial measurements provided in the calibration documentation, errors in the half-live of ^{252}Cf, determination of time intervals and subtraction of background. In order to free a calibration from of all the factors mentioned, the method, which benefits from multiplicity distribution of neutrons of ^{252}Cf, originally proposed long ago in [81] was employed.

3.5.2 „Smart"calibration by neutron multiplicity

To perform a precise efficiency calibration the method proposed in [81] was applied. Multi neutron emission is described by the average of neutrons per decay and by multi neutron emission probabilities P_l, l=0,1,2..l $_{max}$. In our case the prompt spontaneous fission neutrons are emitted by excited fission fragments from ^{252}Cf. For a detection efficiency (ε) lower than 100 % the observed multiplicity distribution is different from the real one. In the assumption that neutrons are registered independently the probability to register n neutrons (F_n) is a sum of the partial probabilities of detection for the emission of ν=n, n+1, ..., ν_{max}:

$$\sum_{\nu=n}^{\nu_{max}} K_{n\nu} P_\nu = F_n, \quad n = 1, 2, ..., n_{max} \tag{3.4}$$

$$K_{n\nu} = \frac{\nu!}{n!(\nu-n)!} \varepsilon^n (1-\varepsilon)^{\nu-n} \tag{3.5}$$

where P_ν are the components of the true neutron distribution (the emission probability of ν neutrons) and ν_{max} is the maximum possible number of neutrons per spontaneous fission. $K_{n\nu}$ is the matrix of the transmission coefficients between real and measured components. The exact solution of Equation 3.4 is given in [81].

Knowing the exact components of the real neutron distribution (P_ν) for the ^{252}Cf, [82] (see Table 3.2), it is possible to calculate the unknown components F_n as a function of the detector efficiency.

In Figure 3.15 is shown the calculated probability to detect 0 neutrons per fission (F0), 1 neutron per fission (F1), 2 neutrons per fission (F2) etc. as a function of neutron efficiency in the range 0.01 - 1. To perform the calculations I developed an C++ application. The full table of calculated ratios F1/F2, F1/F3, F2/F3 ... is given in Figure C.10, Appendix C. Assume that N_{dec} is the number of decays and N_i is the number of events with i neutrons emitted, then, taking into account equations 3.4, 3.5:

$$N_i = N_{dec} * F_i = N_{dec} \sum_{\nu=n}^{\nu_{max}} \frac{\nu!}{n!(\nu-n)!} \varepsilon^n (1-\varepsilon)^{\nu-n} P_\nu \tag{3.6}$$

If N_j is the number of events with $j \neq i$ neutrons emitted, and N_j with j neutrons registered, in the same number of decays N_{dec}:

$$\frac{N_i}{N_j} = \frac{F_i}{F_j} = f(\varepsilon) \tag{3.7}$$

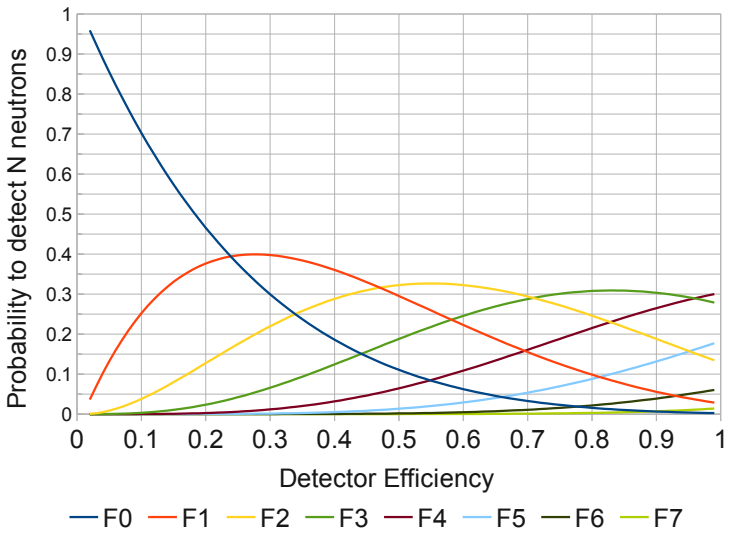

FIGURE 3.15: Detection Probability of N neutron as a function of efficiency of detector

In other words for a given efficiency ε the ratio of probabilities to register i and j is a constant.

Number of neutron emitted, ν	0	1	2	3	4	5	6	7	8	9
Emission Probability, Pν	.0175	.1121	.2996	.3387	.1768	.0473	.0072	.0007	.0001	<.0001

TABLE 3.2: Prompt neutron emission probability for fission fragments in spontaneous fission ^{252}Cf [82].

During the calibration, the first registered neutron was considered as a start to open a 128μs gate. Within the gate the number of events of multiplicity 1,2,3,4 was found to establish ratios N_2/N_3; N_2/N_4; N_3/N_4 (Table 3.3). As it can be seen from comparison to calculated values, the efficiency ϵ_0(n) is somewhere between 51 and 55% which is well in agreement with the direct measurements §3.5.1. Normally, low 1 neutron events are considered as background and rejected in the analysis[12]. The method is extremely beneficial since it doesn't depend on properties of a particular source and can be applied successfully in different background conditions. Beside, the multiplicity distribution measured

[12] one can also use single events but should consider the background rate as well as the rate of β-delayed neutron from fission fragments [83]

TABLE 3.3: Determination of efficiency via multiplicity distribution of ^{252}Cf. See text for details.

Eff	**N2/N3**	**N2/N4**	**N3/N4**
exp.	1.58(1)	4.10(3)	2.59(2)
0.51	1.62	4.49	2.77
0.52	1.58	4.26	2.69
0.53	1.54	4.04	2.63
0.54	1.50	3.83	2.56
0.55	1.46	3.64	2.5

with any detector and any DAQ *must* satisfy a calculated one for a certain efficiency. Otherwise, it is a strong witness of systematic problems either in the electronics system or in the data analysis procedure. That is why we consider a calibration with a spontaneous fission source such as ^{252}Cf or ^{248}Cm or any others, but with known multiplicity distribution for emitted neutrons, as a strong self-check of the detector. The limit is imposed by random coincidences. To minimize their contribution a source should be as weak as possible, typically not more, than a few hundred neutrons per second in 4π. In principle, one can proceed to higher multiplicity ratios (F5, F6, F7, ...) but it demands a much longer exposure time.

3.5.3 Neutron Life Time in the detector

Neutron life time consists of a moderation and diffusion time, and can be estimated via the time distribution of neutron detection relative to the start. In Figure 3.16 is shown the time between registration of two subsequent neutrons (1^{st} neutron opens an 128μ gate, 2^{nd} closes the gate). The fit function is (exp(-t/τ) + const) where τ is considered as a time in which half of the neutrons are detected and is called ,,moderation" time. For present TETRA configuration τ = 27 μs. Large χ^2 comes because of the peak at 2 μs - the time bin of TETRA acquisition. It is seen that almost all neutrons are registered within 128μ. That is why $\tau_{gate} = 128\mu s$ was chosen.

3.5.4 Efficiency of TETRA as a function of Q_β

The efficiency of single neutron registration measured with ^{252}Cf source $\epsilon_0 = 52\pm2\%$ (3.5) in comparison to 49±6% calculated by MCNP (§ 3.7). However, the average energy of fission neutrons from ^{252}Cf is accepted to be about 2.1 MeV. A prompt neutron energy spectra can be found, as an example, in [84]. Thus, ϵ_0 is a good reference point, but can be used in analysis only under assumption that energy of neutron of interest is close

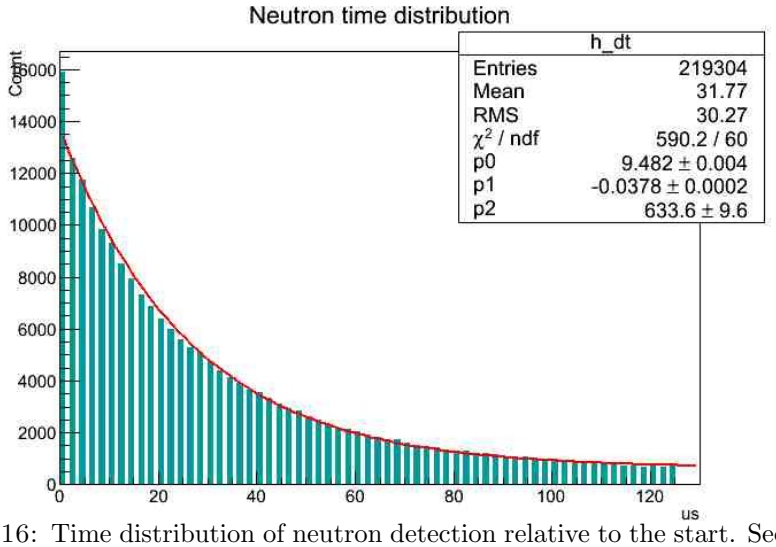

FIGURE 3.16: Time distribution of neutron detection relative to the start. See text for details.

to one from spontaneous fission of ^{252}Cf. The efficiency of TETRA to be used in the analysis was determined by comparison of γ-β to γ-β-n gated spectra in § 6.4.

3.6 TETRA before and today. TETRA vs other setups.

Table 3.4 explicitly outlines the modifications of TETRA I performed during my thesis. During verification of each counter 10 of them were recognized as being bad, mostly because of bad amplitude spectra which is a manifestation of the bad quality of the gas. The overall efficiency of single neutron registration (ε_0) was decreased, but is still at high 52 % and is almost constant for $E_n < 0.8MeV$. The central cavity is of the right size (13.5mm diameter) to include β and γ detectors. New electronics works smoothly and has many options leading to low dead time and the possibility to measure neutron multiplicity. Thus, TETRA is ready to perform breathtaking discoveries at the neutron rich side of stability!

Nowadays there are two other similar active[13] ^{3}He filled detectors: BELEN [85] and NERO [86] employed in β-decay studies. They have roughly the same efficiency as TETRA 40-50 % which doesn't depend much on neutron energy up 1 MeV and similar geometrical configurations. The comparison of these detectors is given in the Table 3.5. It is interesting to mention that NERO employs two types of gas counters ^3He and BF_3. The ^3He counters are mounted in the inner ring which detects the most neutrons. BELEN is an example of a detector which uses high pressure (20 atm) ^{3}He counters. At the same time, at JINR, Dubna there are at least three another ,,active" neutron detectors employed mostly to study spontaneous fission, Table 3.5.

[13] active - in terms of recent publications

Table 3.4: Comparison of TETRA before and after my thesis

	TETRA <2011	**TETRA> 2012**
General		
Number of counters	90	80
Efficiency, %	70	52
Central cavity, r, cm	5	13
Shielding	no	15 cm boron
Electronics		
Internal DAQ	-	yes
External DAQ nim	yes	yes
External DAQ Comet	-	yes
Sync. With Ex. DAQ	-	yes
Multiplicity Counting	?	yes
Remote Control	-	yes
Caballing		
Length HV cable, m	0.5	3
HV sockets	USSR	lemo
Length LV, signal cable, m	0.5	3
LV, signal sockets	USSR	HV9
Conjunction		
Beta detector	yes	yes
Gamma detectors	yes	yes

From my viewpoint, the low-energy neutron detector scintillator system VANDALE [87] recently built at Oak Ridge, which is able to measure β-delayed neutron spectra, might be practically useful in certain β-decay experiments. We hope to see new results obtained at VANDALE very soon.

TABLE 3.5: Comparison of different ^{3}He filled multi neutron detectors

	TETRA	**BELEN**	**NERO**
Efficiency (252Cf), %	52	42	45
Gas/Pressure (atm)/N counters	^{3}He/7/80	^{3}He/20/20 ^{3}He10/10	^{3}He/10/11 ^{3}He/4/5 BF_3/1.2/44
Shielding	Borated polyethylene	polyethylene	Cd, water
Home institution	JINR	UPC	MSU
Current facility	ALTO	GSI	MSU

	VASSILISSA	**SHIN**	**miniFOBOS**
Efficiency (252Cf), %	25	70	12
Gas/Pressure (atm)/N counters	^{3}He/7/72	(^{3}He/7+Ar/2)/60	^{3}He/7/28
Shielding	different	Borated polyethylene	different
Home institution	JINR	JINR	JINR
Current facility	JINR	LSM	JINR

3.7 Simulations for the neutron detector TETRA with MCNP

To perform the designed modifications a validated computer model of TETRA was highly needed. This model was created using MCNP code [88] (Monte Carlo N Particle transport). The MCNP is a traditional powerful tool for neutron-transport calculations initially aimed at reactor calculations. In comparison to Geant4, MCNP originally has all the necessary cross-sections for neutron interactions in the thermal-energy range of neutrons for a wide range of temperature. Geant4, being initially developed for high energy physics, only recently included modules for the propagation of thermal neutrons. There are still verified discrepancies between Geant4 and MCNP for the thermal neutron capture [89], that is why the neutron cross sections and physical models implemented in Geant4 are constantly updated by the Geant collaboration. On the other hand, neutron transport in MCNP is widely used for any neutron energy range and has been constantly compared with experimental data showing a good agreement.

Though the manual given in [88] is full and comprehensive, illustrated by many useful examples, from my view point it is challenging for new users to differentiate between information needed to learn how to use the code and information specified for more complicated cases. I found the tutorial in Reference [90] covered better practical problems which beginners can face. The manual gives many of the technical details of code mostly needed for MCNP experts. Some of the notation used in the MCNP documentation uses historical terminology. Thus, the term *card*, historically a punched card, should be interpreted as a line of the input file. Briefly, to prepare an input file one should define the *Geometry* of the setup (§3.7.1), list of *Materials* and corresponding cross section tables (§3.7.2), specify the *Source* (§3.7.3), indicate the physical process to be studied (Reaction 3.1 in our case) and the *Results* required (tally) (§3.7.4). An example of an input MCNP file is found in Appendix B.

3.7.1 Geometry specification

In MCNP a *cell* is a volume bounded by set of *surfaces*. However, to create too many objects specifying each time a new volume can be very tedious that is why MCNP offers *universes* and *lattices*, which are able to repeat elements simplifying the users work. A *universe* is composed of all *cells* that are specified in it. A universe is either a lattice or an arbitrary collection of cells. *Lattices* - repeated structures, basically, are equivalent to lattices in a reactor and can be rectangular or the hexagonal.

TETRA has the shape of a hexagonal prism to minimize the corner effects. Naturally, the hexagonal repeated structure was used in building of the model. The main virtual

neutron ,,bin" in the simulation is an hexagonal prism defined by the *universe* 52 (u=052) which includes a steel *tube*, inner *gas* volume filled with ^{3}He and 1% of admixture of CO_2, and an hexagonal piece of *moderator* so that the distance between parallel sides is 5 cm. The same bin but filled differently by other materials represents complimentary bins listed in the Figure 3.17.

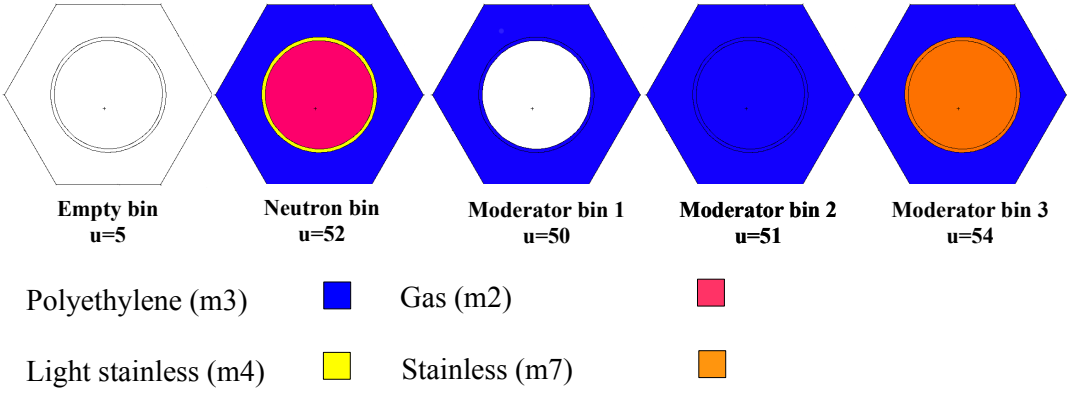

FIGURE 3.17: Main bin filled by different materials

In the model it is logical to group neutron bins in four rows and operate during calculations only by these four rows instead of 90 independent bins (see Figure 3.6a), which significantly shortens the computing time. The central cavity is simply described by the empty cell 500 (see Figure 3.18). The first group (525) is a lattice-2 defined geometrically by its surfaces filled with virtual neutron bins to match exactly to the first row of counters of TETRA. Analogously, the cells 535, 545, 555 map respectively the 2^{nd}, 3^d and 4^{th} layers of the detector. The cell 565 is made in the same way but contains only complementary (moderator) bins and corresponds exactly to the additional layer of moderator. The shielding all around is simply defined by cell 570 filled by borated polyethylene. During the experiments the neutron detector is put on a stainless table (cell 703) in an experimental hall with concrete walls (cell 705). Finally, cell 902 defines everything else. As it was shown in the stimulation the table and the walls gave no noticeable effect on results. The preamplifier part was specified similarly (refer to universe 62).

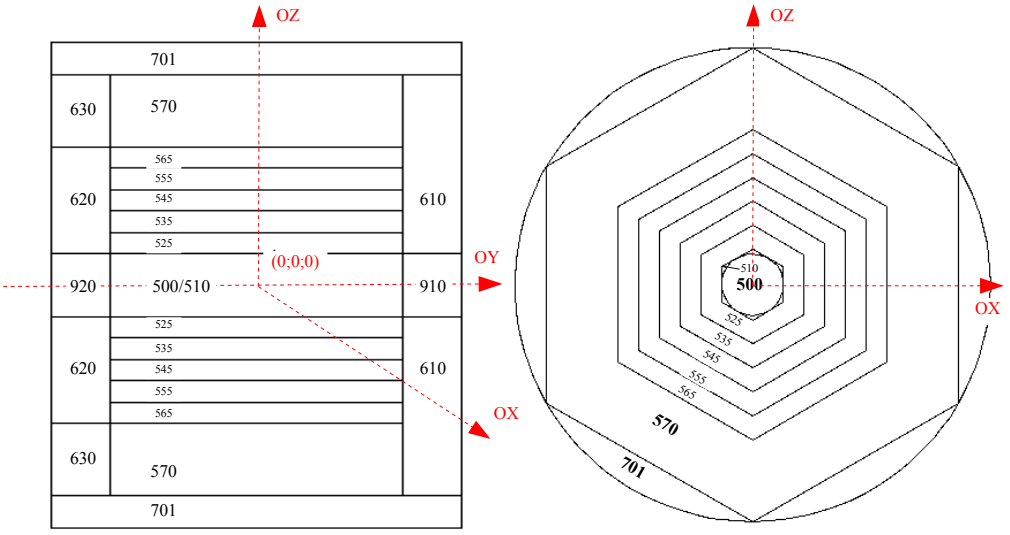

FIGURE 3.18: Geometry cell specification

3.7.2 Material specification

To specify materials filling the various cells in an MCNP calculation involves: (a) defining a unique material number, (b) the elemental (or isotopic) composition, and (c) the cross section compilations to be used. The density is specified on the cell definition card. This permits one material to appear at different densities in different cells.

Table 3.6 gives a list of materials used in the simulations. The isotopic composition for most of them was found in the literature [91]. The contributions of other materials were considered as negligible and were not taken into consideration. Finally, the geometry cells presented in the Figure 3.18 are filled bins as it is shown in Figure 3.19.

TABLE 3.6: The list of main materials used in the simulation. The isotopic composition can be found on cells *m2-m9*; for (*) was taken from [91]

card	**material**	**Density, g/cm^3**
m2	^{3}He	0,00086
m3	polyethylene	0,93*
m4	Light steel	7,93*
m6	Borated polyethylene, 5%,	1005
m7	Stainless steel	7,93*
m8	Concrete LA	2,25*
m9	Plexiglas	1,18*

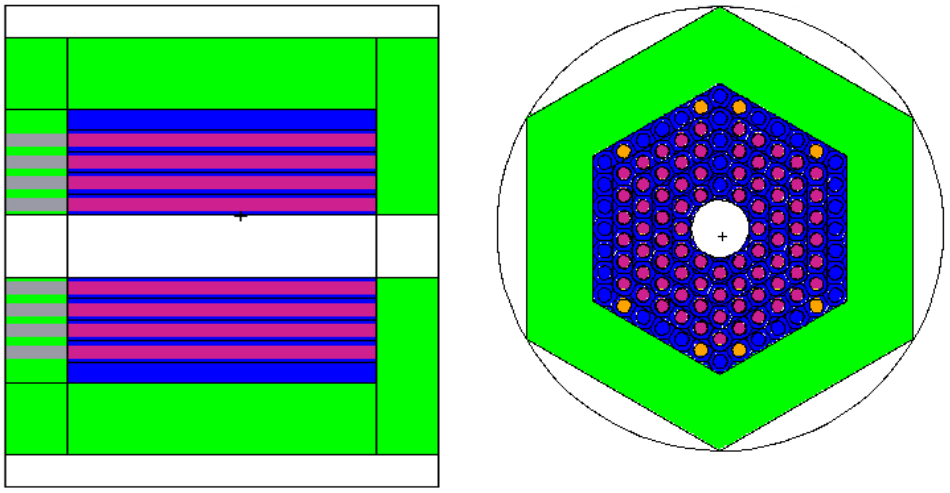

FIGURE 3.19: The same geometry as in Figure 3.18 but filled with materials

3.7.3 Source specification

The source and type of radiation particles for an MCNP problem are specified by the SDEF card which has numerous variables and parameters to define all the characteristics of all sources in the problem. Only one SDEF card is allowed in an input file.

The point isotopic source used in the problem is defined on the SDEF card. The energies (E_n) of the neutrons emitted by spontaneous fission of ^{252}Cf (average neutron energy is 2.1 MeV) are typically described by a Maxwell-Boltzmann distribution function with an effective temperature of kT=1.42 MeV.

3.7.4 Tally specification

„Tally" in MCNP is a means to specify the output results required. At least one tally card is required. The first entry on the card begins with F*id:TP*, *id* is the tally id number (the last digit of which determines the type of tally), and *TP* stands for N (neutron tally), P (photon tally), N,P for joint neutron and photon tallies, and E for electron tallies.

The tally F4 (neutron fluency through a cell in n/cm^2)) used with the FM option is considered as the most appropriate to reconstruct the efficiency: F4:N cell number (Cn); FM4: C (constant) M (material) R (reaction). MCNP multiplies the neutron fluency from the F4$_n$ tally (in n/cm^2) by the reaction cross section defined by M and R (in barns) and finally, the result is then multiplied by C. The most common use of C is to provide

the atomic density of the material. If it is given in atoms/barn/cm the result of the tally is reaction per source particle in 1cm^3. With the volume of the Cn, also calculated by MCNP, the neutron flux through Cn is determined. The tally F4 is by default already normalized to the number of particles emitted by a source. There are five tallies in the solution: f524, f534, f544, f554 to calculate a neutron flux through the 1^{std}, 2^{nd}, 3^{nd} and 4^{th} layer, respectively, and f54 determines a flux through the entire detector. We checked that the overall efficiency of TETRA is exactly the sum of efficiencies of each layer. All the tallies calculated passed all 10 statistical checks. Also the particle loss check was performed to avoid errors in geometry specification.

3.7.5 Validation of the model. Reliability.

The statistical error in MCNP is defined by the number of tracks (histories) used and can be as low as 0.1% (with 10^6 histories). However, the decisive role is played by systematic error arising from uncertainties of the model. To estimate the systematic error, the model of TETRA was validated using a spontaneous fission source ^{252}Cf. In Figure 3.20 is presented the efficiency of TETRA as a function of the distance of the ^{252}Cf source, placed on the beam axis, from the center of the detector with zero coordinates in comparison to experimental data. The maximum efficiency is, obviously, at the center. Within the next 1-2 cm the efficiency is almost flat gradually falling down with the increasing distance. As it can be seen, the calculations regularly underestimate the experimental points measured by the method described in §3.5.2 . Such a deviation originates from uncertainties in the modeling such as: neglecting minor materials and the fact that the exact composition of materials as well as exact densities cannot be known with certain accuracy; uncertainties in the geometrical dimension of the real parts of the detector. Nevertheless, the validation process shows that our model can be trustful within 6% of absolute value.

3.7.6 Gas pressure and moderator density.

Pressure of ^{3}He and density of moderator material are the most crucial parameters which influence the efficiency. As it is shown in the Figure 3.21 an increase in gas pressure, i.e. quantity of the gas, doesn't bring any significant positive effect after 10 atm. From our view point the saturation is reached somewhere around 7-8 atm. However, due to shortage of ^{3}He nowadays it might be even more beneficial with the same quantity of the gas to construct more counters with 4 atm pressure of ^{3}He to make a detector bigger in size and, therefore, more sensitive to more energetic neutrons (E_n>1 MeV).

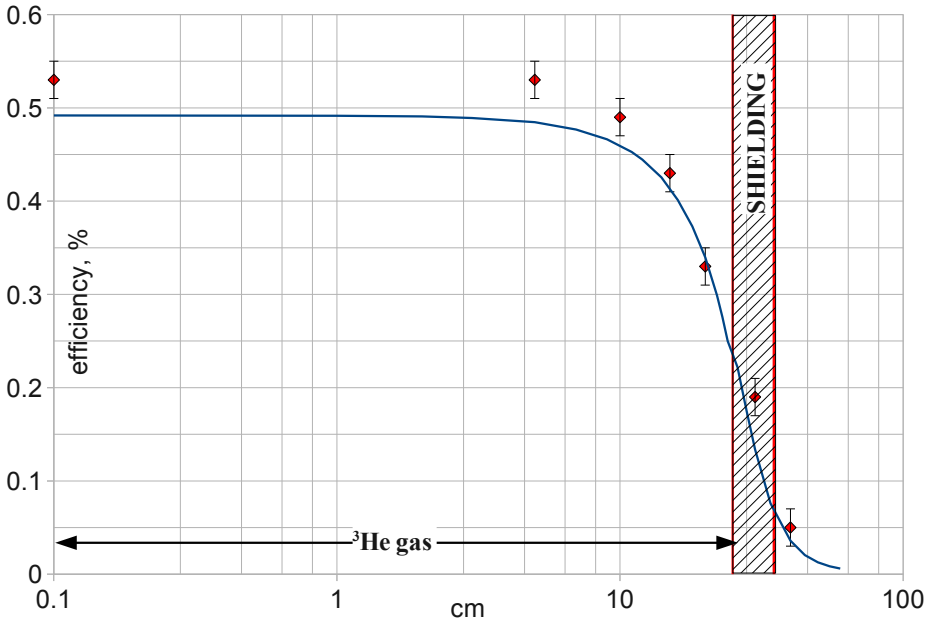

FIGURE 3.20: Validation of the model: calculated (by the method described in §3.5.2) and measured efficiency of TETRA for the ^{252}Cf source as a function of distance of the source from the center of the detector

The high-density polyethylene (HDPE) (0.93 g/cm^3) was used since it was considered as the most appropriate material for neutron moderation. Some other options could be paraffin and plexiglass, but usually their performances are slightly worse. In the calculations we compared the performance of the HDPE (0.93 g/cm^3) with the low-density one (0,465 g/cm^3) for 0.01-10 MeV neutron energy range, Figure 3.21. As seen, the HDPE is a better performer since the efficiency below 1MeV is nearly flat.

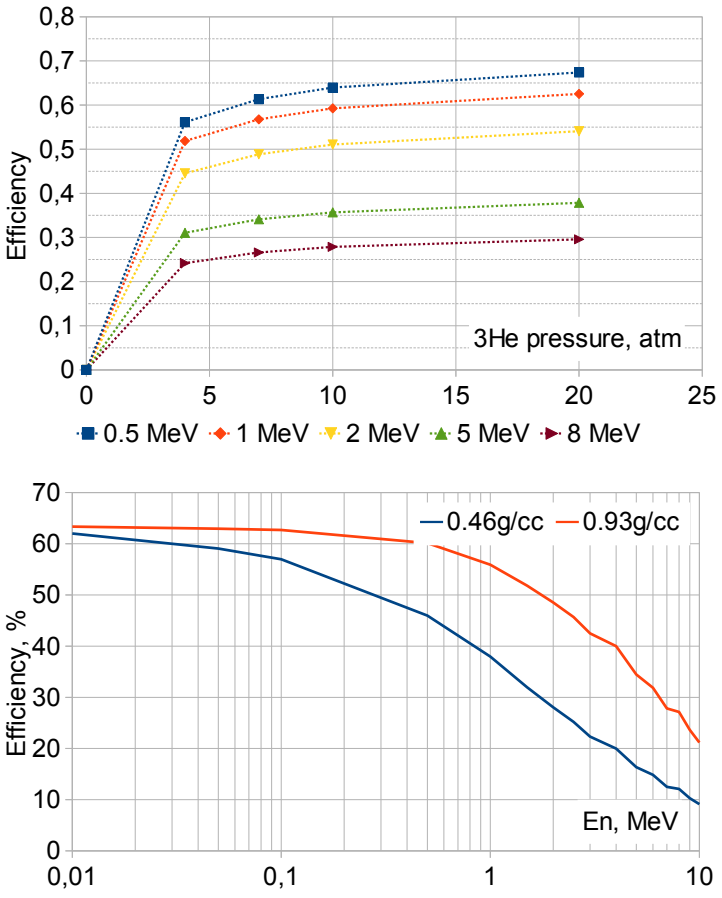

FIGURE 3.21: Efficiency of neutron detector as a function of: gas preassure (top), density of moderator (bottom)

3.7.7 Efficiency as a function of neutron energy.

The efficiency must be constant in the energy range for the neutrons of interest. Since energy of β delayed neutrons is typically below 1 MeV, the ^{3}He filled detectors seem to be the most suitable tool for β delayed studies. The flatness of the efficiency can be reached by bigger number of rows with ^{3}He counters as it was experimentally shown by the Dubna group [70]. Figure 3.22 represents the calculated efficiency of TETRA as a function of neutron energy - the efficiency is flat almost up to 0.8 MeV. The calculations were performed in the range of $0.01<E_n<10$ MeV. Figure 3.22 illustrates the efficiency of each of the four layers. Simulations confirm that the inner layer is more efficient to detect less energetic neutrons. The higher a neutron energy is the longer path in moderator the neutron should pass to become thermalized. In case of $E_n>10$ MeV neutrons can go through the detector without being registered.

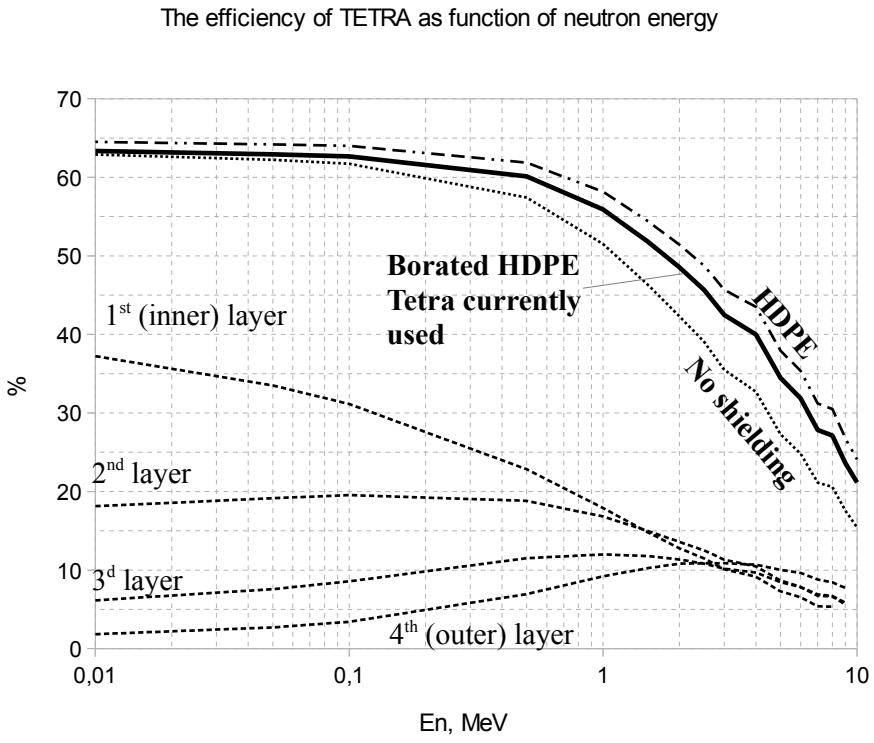

FIGURE 3.22: Calculated efficiency of TETRA as a function of neutron energy for different shielding: solid line - 15cm of borated polyethylene (currently used); dashed line - without shielding; dashed-dotted line - 15cm of polyethylene (HDPE). Dashed lines below are the efficiency of each layer for the currently installed 15cm borated polyethylene shielding.

3.7.8 The background protection qualitative estimation.

Under real experiment conditions, in the experimental room of ALTO, several background sources are present: β delayed neutrons from decay of isotopes accumulated at the separator located 5 m away; neutrons from interaction of cosmic rays with material inside the room and inside the detector. Correctly defining a realistic background neutron environment in MCNP is a very challenging task. Thus it was decided to simplify the problem in order to use one of the standard sources available which allowed us to proceed to qualitative estimation of the shielding to be constructed.

Cosmic rays which interact with materials inside/outside of the detector give an experimentally measured constant count rate as low as 5 n/s without shielding (and later to be measured 1 n/s with shielding installed).

Background source from neutrons from beta decay of fission fragments was approached as a neutron cloud - neutrons without dominated energy or direction. This approximation is valid due to low potential of beam extraction 30 keV, pie shield applied around the separator (polyethylene, cadmium, lead). However, the major source of neutron background during the experiment was expected to come directly through the beam line together with the beam. To minimize the effect, the detection system was located at a beam line which made a 90 degree angle with the separator. Even though this precaution was taken, this source was considered to contribute much stronger in comparison to ,,neutron cloud" or cosmic rays.

Under the assumptions stated above, a point source collimated into a cone direction, injected 60 cm away right on the axis of the detector (OY), so that the cone passed through the edges of the detector, was accepted as a background source approximation. The calculated efficiency of TETRA without any shielding at all was accepted as 1 (Figure 3.23). Results for another configurations of shielding considered during the simulation procedure were normalized to this case.

The shielding did not need to exceed a 15 cm width layer due to the detector geometrical configuration. Although, the application of polyethylene shielding only rejects relatively well the neutron background for E_n<0.5 MeV, it increases the impact of high energetic part due to neutron moderation and consequent increasing probability to interact with ^{3}He (Figure 3.23, dotted line). In its turn the polyethylene shelter of the same widths with a 5% admixture of boron deals more properly with the neutron energy range 0.01<E_n<10 MeV (Figure 3.23, dotted-dashed line). Therefore, based on these results the 15-cm thick borated polyethylene background shielding was adopted.

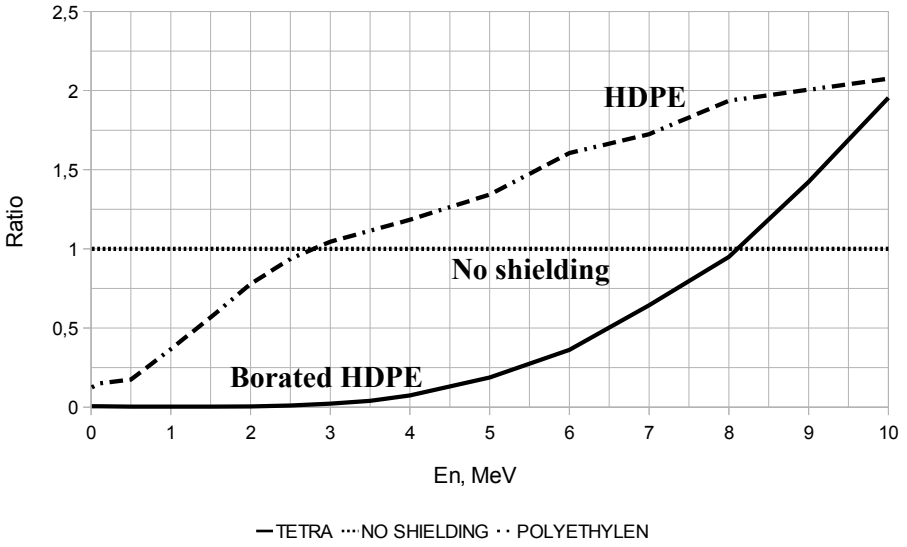

FIGURE 3.23: Background estimation. Top: The relative to none-shielding case efficiency of TETRA as a function of neutron energy for the background source described in the text.

Shielding impact on the detection efficiency

Eventually any background shielding positively impacts the overall neutron detection efficiency of TETRA for neutrons emitted from a source at the center of the detector as is shown in Figure 3.24. This effect is due to the fact that neutrons which already have passed through the detector without interaction with ^{3}He gas can be reflected by the shielding back and, finally, be detected. As seen in Figure 3.24, the application of shielding doesn't disturb much the efficiency of the first layer, whereas it kicks it up for the outer layer.

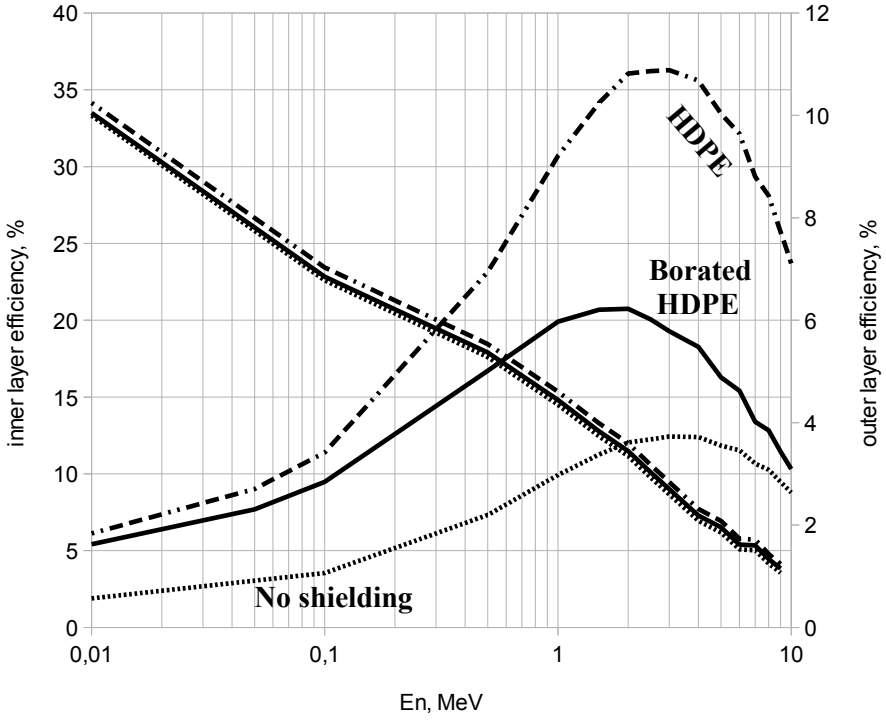

FIGURE 3.24: Effect of the background protection on the efficiency: comparison of efficiency of inner and outer layers as a trend of different shielding, the same as in Figure 3.22

3.7.9 Future configurations.

All three configurations proposed in Figure 3.4, on page 36 were considered in my MCNP calculations. The results are plotted in Figure 3.25.

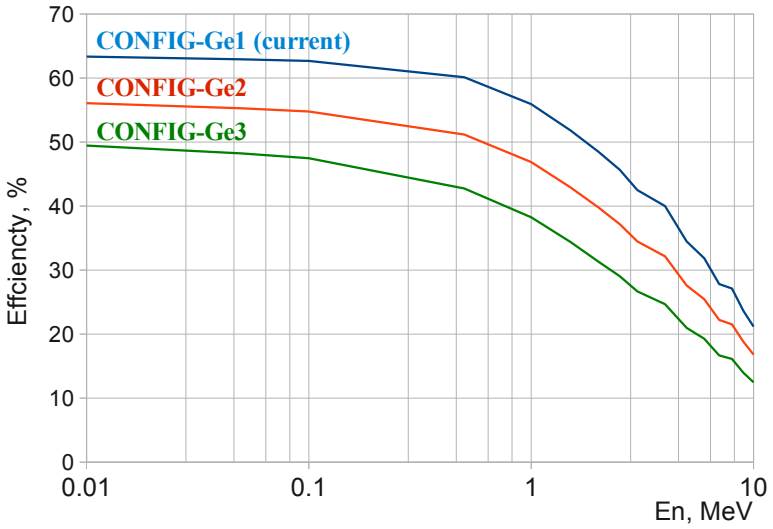

FIGURE 3.25: Calculated efficiency as function of neutron energy for three configuration proposed, Figure 3.4. **CONFIG-Ge1** is the currently exciting configuration.

3.7.10 Conclusion.

The reliable MCNP model of TETRA was created and validated using experimental data. Based on the results obtained, the new mechanical polyethylene support as well as a borated polyethylene shield were developed and constructed. This model is flexible enough to be used in the future to calculate different geometrical configurations needed for spectroscopy studies of neutron rich nuclei.

Chapter 4

Production of Radioactive Ion Beams at ALTO

"Physics is becoming too difficult for the physicists"

D. Hilbert

Contents

4.1 Production methods

There are several ways to produce exotic beams of nuclei with neutron or proton excess by different reactions: multi-nucleon transfer reactions, induced fission, spallation and fragmentation reactions. If one moves away from the valley of stability they must

confront serious difficulties from extremely low production cross sections, production of undesirable species in the target, and the very short half life of nuclei of interest. Commonly there exists two complementary ways to achieve a better quality of exotic beams: the in-flight separation technique and the isotope separation on line (ISOL) technique which can be followed by post-acceleration. In both methods nuclei of interest are transported from the place where they are originally produced to a well-shielded, low background cavity with a detection system.

In-Flight separation

In the In-Flight separation method nuclei are obtained by the fragmentation reaction - a high energy heavy ion beam is sent into a thin target (less that a gram/cm^2, in order to avoid absorption of reaction products and to narrow their energy distribution). Nuclei leave the target highly ionized. Therefore, due to reaction kinematics, combination of magnetic and electrical fields, atomic mass and number, the nuclei of interest can be identified and separated from primary beam and other fragments produced in the same reaction. In this method produced nuclei are available instantly (the time scale is much shorter than for β-decays - μs). It has the advantage, that varying the projectile/target nucleus or the bombarding energy allows one to emphasize aspects of nuclear properties to be studied. At the same time, the products quite often are too energetic for decay studies, with large energy, sometimes angular distributions and low purification. List of the main facilities employing the technique: FRS (GSI, Germany), LISE (GANIL, France), A1900 (NSCL, USA), RIBF (RIKEN, Japan).

Isotope Separation on-line

In the ISOL method a beam of light particles (proton, electron, etc.) hits a thick intermediate- or heavy mass target. Depending on the kind and energy of the projectile various reactions are possible: fusion-evaporation, fission, multi-nucleon transfer reactions up to energy 100MeV/u; and fragmentation and spallation (e.g. a few hundreds of MeV for neutrons and 1 GeV for protons). In some cases a converter is used to transfer a primary beam of protons/electrons into a flux of neutrons and γ-rays respectively. The choice of target is, generally, based on the highest production cross section, the lowest amount of contaminants and the property of material to withstand the highest possible beam currents. The produced fission fragments are stopped, or, as ones say, thermalized, in the target/catcher from which they subsequently escape by diffusion through a transfer line to the ion source where they are ionized. The diffusion becomes possible due the to sufficiently high temperature of the target/catcher. In contrast to the In-Flight Separation method, beams of exotic nuclei obtained by the ISOL method have less energy spread and small angular divergence. Therefore, they can be post-accelerated. Unfortunately, a relative long extraction time makes study of the shortest lived species almost

impossible: a nucleus has to be produced, thermalized and extracted before it decays. Because of the limited choice of target the chemical selectivity is restricted. List of main facilities employing the technique: ISOLDE (CERN, Switzerland), IGISOL (Jyvaskyla, Finland), HRIBF (ORNL, USA), Spiral (GANIL, France), ISAC (TRIUMF, Canada), ALTO (IPN, France).

4.1.1 Production by ISOL method via Fission Reactions

Nuclear fission is a process in which a heavy nucleus breaks into two lighter fragments accompanied by emission of fission neutrons. The reaction is exothermal since the total mass of the daughter nuclei is less than the mass of the mother. The energy of fission can be released as kinetic energy of the fragments due to strong Coulomb forces. Additionally, exited fission fragments can suffer β decay and, if fission energy is high enough, emit neutron(s). The presence of a potential barrier prevents instantaneous spontaneous fission of nuclei. In order to break a nucleus one has to transfer the energy, higher than the potential barrier. The height of the barrier depends on the parameter of divisibility (Z^2/A) and is about 50 MeV for medium and heavy nuclei, whereas for actinides (^{233}U, ^{235}U, ^{239}Pu, ^{241}Pu, ^{241}Am) is of the order of 5 MeV. In the last 50 years fission has led to the production and study of more than 400 new isotopes. Even though no complete model of fission has been developed, there are sufficient amounts of experimental data to describe the mechanism of the reaction.

4.1.2 Neutron induced fission

At IPN Orsay, a 26 MeV deuteron beam produced at the Tandem accelerator is delivered to a converter placed 5 to 110 mm from the center of an uranium target. As a deuteron has a low binding energy it can break up in the converter (up to 0,013 neutrons per deuteron can be produced). The protons from the break-up are absorbed by the converter while the neutrons can escape and travel to the uranium carbide target (at energy 0.4 of the deuteron incident energy). Many efforts have been devoted to optimize the neutron (E_n) and deuteron (E_d) beam energy [92, 93]. Thus, Figure 4.1(left) illustrates the saturation in the production of fission fragments with increasing E_d. The right hand of Figure 4.1(right) shows that the reaction cross sections can increase only up to E_n = 40 MeV. Another important parameter is selectivity of fission fragments. The fission of ^{238}U can be asymmetric (at low energy) and depends on the energy of the deuteron beam. In order to obtain the most neutron-rich species in the vicinity of nickel, the energy of the deuteron beam must not exceed 20 MeV. There were a few experiments carried out using a deuteron beam [25, 26] at ALTO. Even though there is

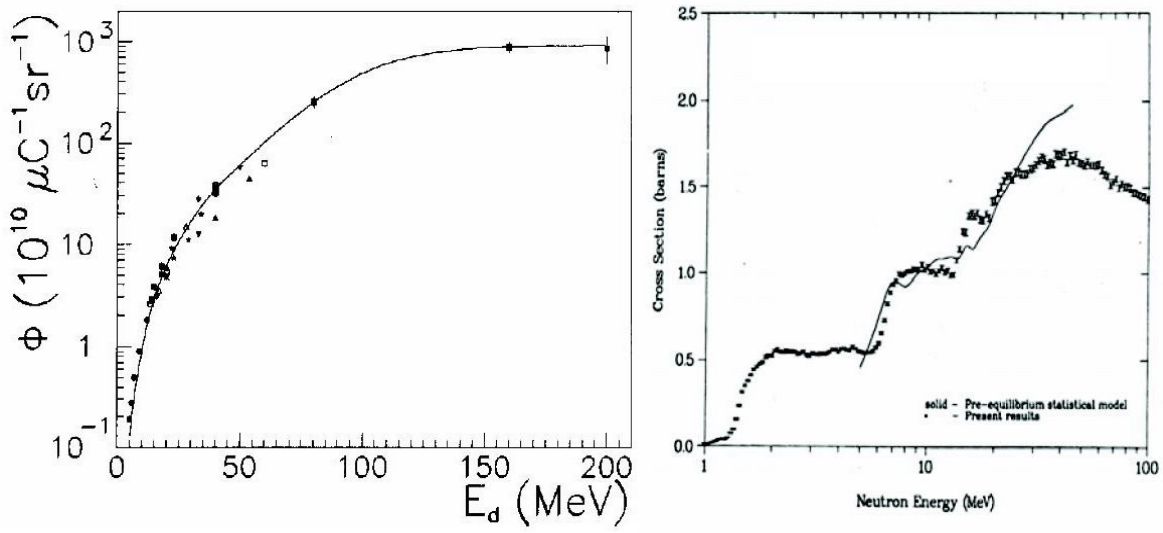

FIGURE 4.1: Left: Neutron production at 0^o as a function of deuteron beam energy [92]. Right: Fission cross section of ^{238}U as a function of neutron energy [93].

still an opportunity to use the deuteron beam at ALTO for RIB production, the electron driver is mostly used, since, simply, production via photo fission at ALTO is higher.

4.1.3 Photo induced fission

In photo fission fast electrons interact with atoms which results in production of a continuous spectra of gamma rays, which triggers the fission process in the target. It was introduced by physicists, such as Diamond [94], to use photo induced fission in an uranium target for radioactive isotope beam production. The calculations of Diamond were validated a few years later in Dubna by Oganessian [95]. In his experiments Oganessian used an uranium target 40 g/cm^2 in thickness and generated an average 1.5×10^{11} fission events per second with an 25 MeV and 20μA (0.5kW) electron beam and a 2.5 mm thick tantalum plate as a converter.

As is commonly known, in the interaction of electrons of energy E_e with a converter material, γ-radiation, with a continuously falling intensity to $E_\gamma^{max} = E_e$ spectrum, is generated. Fission of heavy nuclei induced by γ-rays with different energies is determined by the region of the giant dipole resonance (GDR). The cross section of ^{238}U(γ,f) as a function of σ_f versus E_γ is presented in Figure 4.2. The yield of γ-rays in the GDR region (E_γ = 1017 MeV) depends on the energy of the electrons. Now it is easy to estimate $\sigma_f(E_e)$ Figure 4.2 which shows rapid growth up to E_e = 30 MeV and saturation somewhat about E_e^{sat} = 50 MeV [95]. Therefore, E_e^{sat} seems to be the optimal energy for an electron beam.

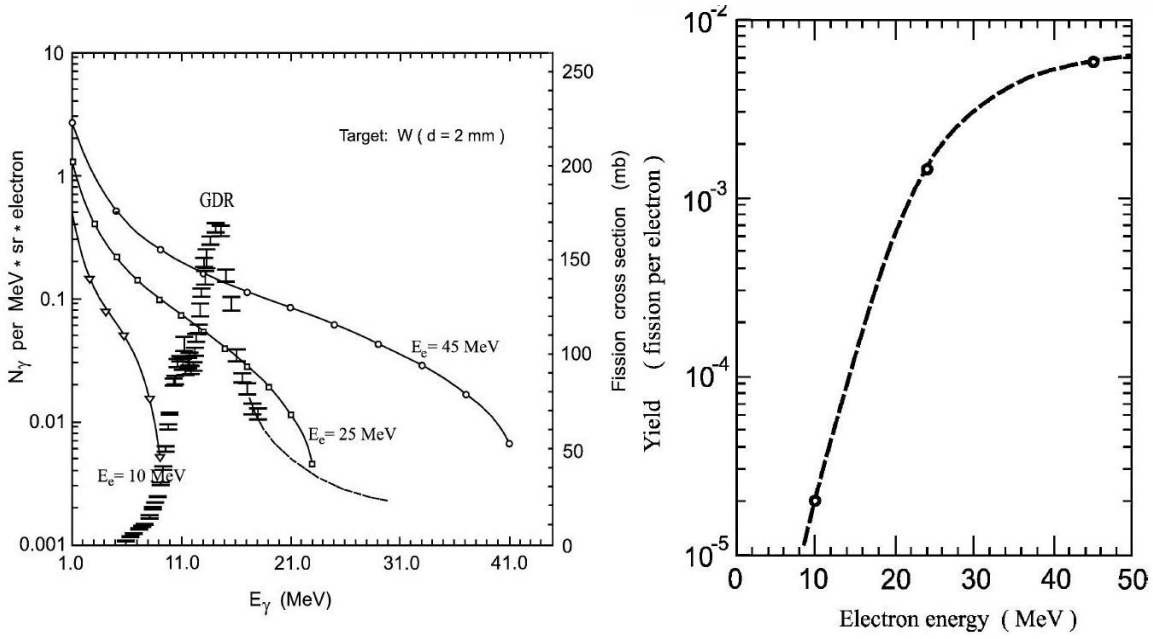

FIGURE 4.2: Left: The solid lines (the left-hand scale) are the γ-quanta spectrum produced by electrons with various energies (indicated in the figure). The experimental points (the right-hand scale) represent the ^{238}U photo-fission cross section. Right: The fission yield per electron for ^{238}U as a function of electron energy [95].

4.2 ALTO - ISOL-type installation

ALTO is an ISOL-type facility located in Orsay, France. After almost a decade of constant interaction with security authority, ALTO was finally give an authorization to run at its calculated parameters in 2012 and inaugurated later in May 2013. During all this time together with necessary security tests, the research program was also performed and resulted in the brilliant works of students: M. Lebois [96], B. Tastet [97], K. Kolos [29].

At ALTO a 50 MeV, 10 μA electron beam is applied to a production UC_x target to obtain low energetic beams of radioactive isotopes. Extracted isotopes can be ionized either in a hot plasma or in a laser beam. After the mass separator PARNNe, separated fission fragments are delivered to physical beam lines (Figure 4.3).

4.2.1 LINAC

The LINAC electron accelerator consists of an injector, an acceleration section and a transport line. The electron gun of the injector delivers a pulsed electron beam of 100Hz and an adjustable pulse width between (0.2 - 2 μs) length. At the exit of the electron gun there are two high frequency cavities (a pre-buncher and a buncher) for pulse acceleration up to 3MeV. Then electrons are injected into a 4.5 m acceleration

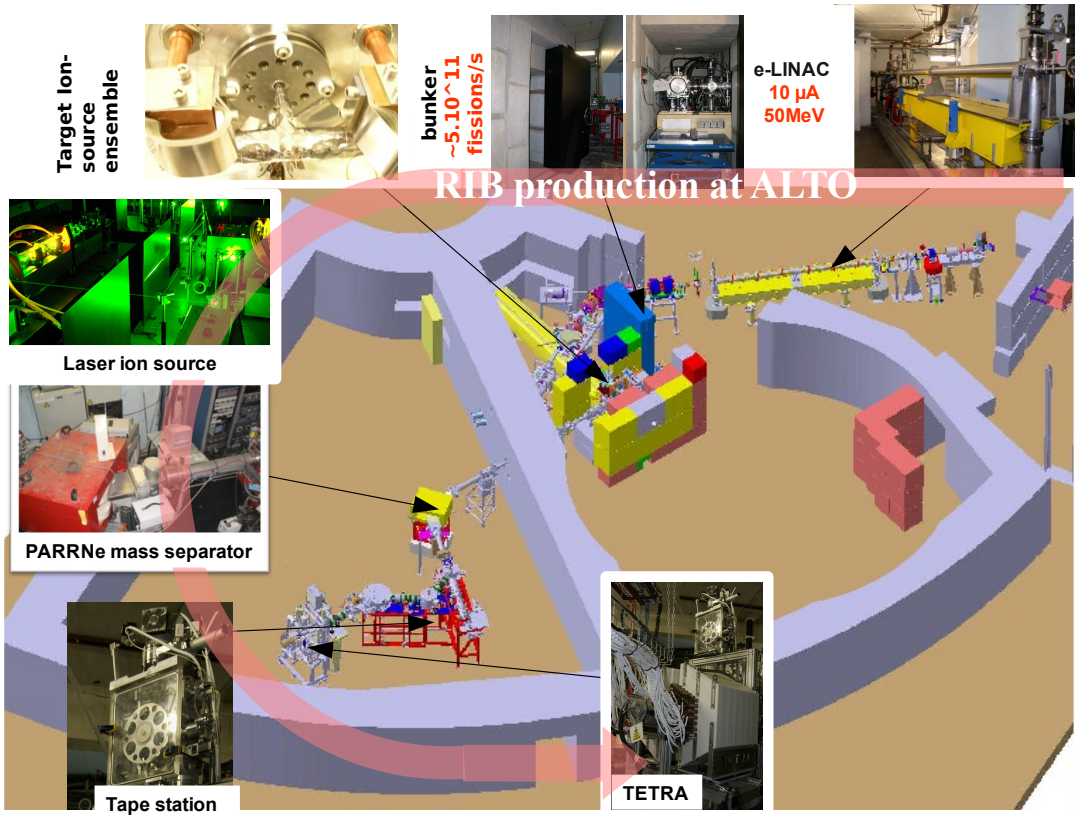

FIGURE 4.3: ALTO facility

section which allows them to reach 50 MeV energy. The acceleration section in fact is a former LEP pre-injector. Once the electron beam is formed it has the average maximum current of 10 μA [1] and a width of 15 ps with a repetition period of 333 ps. After the LINAC the beam is sent through a transmission line to the target. The line is equipped with two magnetic dipoles to deflect the beam at 30^o angle. The transmission line can be used also for a deuteron beam for experiments with fast neutrons.

4.2.2 Uranium carbide target UC_x

After the deflection in the dipoles, the electron beam strikes a uranium carbide target (UC_x). Electrons are converted into photons (Bremsstrahlung) in the first centimeters of the target. The generated cascade initiates the fission process. The ALTO UC_x target consists of 143 pellets, 14 mm in diameter and density of 3.36 g/cm^2 assembled in a cylindrical graphite container. In totally it contains about 70 g of uranium [98]. The cylinder is mounted inside a 20cm long and a few millimeters thick tantalum oven to

[1] technically it is possible to increase the intensity of electron flux. However, ALTO is limited by current safety regulation, taking into account the safety measures at ALTO, not to exceed 10 μA.

heat the target up to 2000^{o}C. At the center of the oven there is a 8 mm diameter hole to which a transfer tube is welded. It permits the effusion of the elements to the ionization source, Figure 4.4.

The release of a given element from the target depends on various physical-chemical parameters. Thus, the most volatile elements (Li, Na, K, Rb, Cs, Fr) and noble gases (He, Ar, Xe,...) have the boiling temperature relatively low. The saturation vapor pressure allows them quickly to diffuse from the target and effuse to the ion source. Whereas for other elements such as metals (Al, Ga, In, Sn, Tl, Pb, Bi) or earth alkaline metals (Be, Ma, Ca, Sr, Ba, Ra) the boiling temperature is high enough to cause, in fact, these elements to possibly remain in a solid form and to be difficult to extract. A special research program at IPNO is aimed at studies of production of neutron rich beams extracted from thick targets [99] of the ALTO design [100]. "Easy" element beams have already been sent to physical beam lines. For elements further away from stability, with short half life and low production cross sections, continued studies are required [101]. Different materials were tested and used in ISOL targets. The release properties of UC_x and molten U thick targets were investigated at PARRNe [102, 103]. Such developments are fundamental for the next generation of ISOL facilities such as SPIRAL-2.

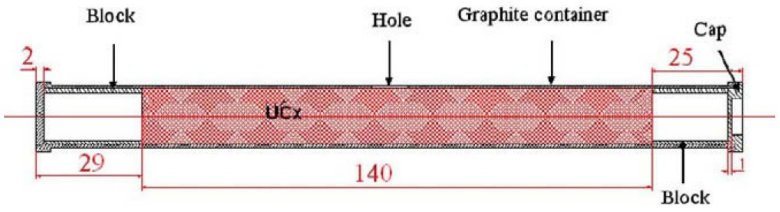

FIGURE 4.4: Structure of the ALTO target.The cap is used to trap the target in the container. By means of two blocks, the 14 cm-long target is put in the middle of a 20 cm tantalum oven so as to have an homogenous heating temperature. The fission fragments can only escape by the central hole [98].

4.2.3 Ion sources

At an ISOL facility, after release from the target, atoms have to be ionized to be delivered to a mass separator and further physical beam lines. Different ionization mechanism are implemented in the ion sources of ISOL facilities. The ionization efficiency is the ratio of the number of an isotope extracted from the ion source to the number of the isotope injected. The type of source to be employed depends on the ionization potential of an element of interest, the required charge state and selectivity. At ALTO the choice

of plasma ionization, surface ionization or laser ionization can be employed depending upon the specific requirements.

The surface ionization ion source

When an atom interacts with a heated surface it can loose or gain an electron before leaving the surface as a positive or negative singly charged ion. This technique can be used efficiently for elements with low ionization potential <7 eV for creation of positive ions (positive surface ionization) and with electron affinity EA>1.5 eV for creation of negative ions (negative surface ionization). Even though the source doesn't allow multi-charged ions its selectivity can be extremely high if the ionization potential of the elements produced is very different. Obviously, the efficiency depends on the temperature of the source and the difference between the work function of the material and on the ionization potential or the electron affinity of the element of interest [104].

The plasma ion source

Plasma high temperature ion sources can ionize atoms with higher ionization potential. Electron impact is used for ionization of atoms present inside the source in the gas phase. An electron flux is created by discharge in a low-pressure environment. One of the most successful and commonly used source is FEBIAD (forced electron beam induced arc discharge). The electrons are extracted from a heated cathode and accelerated into a low pressure plasma [105]. The efficiency can reach 50% for elements above argon [106]. In general, arc-discharge ion sources are not selective because the energy spectrum of the electrons is broad which allows ionization almost of each element. At ALTO, a MK5-ISOLDE [106] source is heated up to 1900 C by an electric current of 300-400A which permits it to also ionize less violate elements. The production rate for certain isotopes has been measured and compared with previous measurements in 2008 [96].

The laser ion source

The principle of a laser ion source is based on the resonant ionization method [107, 108]. The ionization process can consist of two (or three) steps. The first step is always resonant and, consequently, is chemically selective due to the unique level structure of an atom. The first step brings an atom to an intermediate state. During the second step of laser ionization atoms are exited by laser photos to the continuum, to an auto-ionizing state, or to highly excited states (Rydberg state [109, 110]) close to the continuum.

If the auto ionizing states or Rydberg state are not known, the second step is non-resonant ionization directly to the continuum with relatively small cross section $\sigma = 10^{-17} cm^{-2}$ which requires a strong laser - about 5mJ/pulse. However, in the case of resonant reactions (e.g. auto-ionizing states and high lying Rydberg states), due to

higher cross section ($\sigma = 10^{-14} cm^{-2}$), the requirements for the laser power are more relaxed. The auto-ionizing state is a two electron excitation above the atomic ionization potential and decays (with lifetime about 10^{-10}-10^{-15}s) by a radiationless transition into an ion and an electron. While one electron is ejected the other one drops to the ground or to the excited states of the ion. Although all multiple-electron atoms have auto-ionizing states, the knowledge about them is not sufficient yet. To excite an electron from the Rydberg state to the continuum a strong static field ($\sim$ 10kv/cm) is required which makes this method difficult to apply.

4.2.4 Laser Ionization of radioactive gallium isotopes at ALTO

Laser ion source, the first try

The first successful test with the laser ion source at maximum intensity of the electron beam was performed at ALTO in 2011 and was fully described in [29]. A two step non-resonant laser ionization scheme was applied (Figure 4.5a). The first transition produced by a UV beam (λ_1= 287.4 nm), was from the ground state $4s^2 4p^2 P_{1/2}$ to an excited state $4s^2 4d^2 D_{3/2}$; while the second transition due to a green laser (λ_2= 532 nm) was into the continuum. The ^{69}Ga isotope was resonantly ionized with a 287-532 nm scheme and an enhancement factor of 10 compared to surface ionization with a tantalum cavity was observed. Ionization efficiency for radioactive ^{84}Ga was 10% in comparison to 1% efficiency for the surface ion source. However, there was room to increase the efficiency

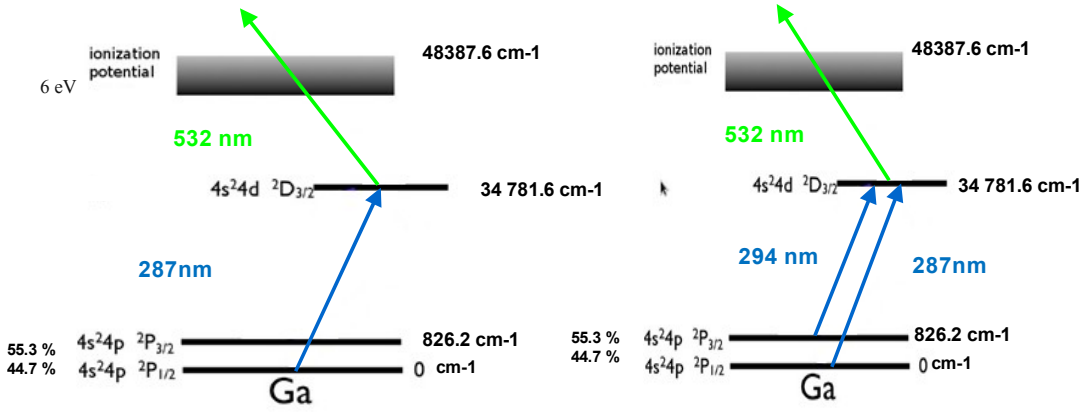

(A) Year 2011 (B) Year 2012

FIGURE 4.5: Laser ionization schemes at ALTO

of laser ionization at least by factor 2 due to the possible ionization from the metastable state $4s^2 4d^2 P_{3/2}$ (Figure 4.5b) which is highly populated as a result of excitation by the high temperature applied to the ionization tube (Figure 4.6). The population of this metastable level was estimated to be as much as in the ground state.

Upgraded Laser ion source

In order to ionize the atoms from the metastable state $4s^2 4d^2 P_{3/2}$, a second UV laser was installed. Today the laser ion source at ALTO, Figure 4.7, consists of a dye laser system at 10 kHz pumped with a 532 nm Nd:Yag laser with a maximum power of 100W (model INNOSLAB IS2011-E). Recently two new commercial grating tuned high repetition dye lasers have been installed. Each dye laser has a laser resonator, a power amplifier and a single-pass doubling unit. The typical power of the lasers, for a pumping power of ∼30 W, is ∼8 W after the amplifier and ∼500 mW after frequency doubling with a conversion efficiency of ∼6%. The pulse width of the lasers is ∼10 ns and the line width is ∼3 GHz [111].

The on-line laser ionization of Ga with the new dye laser system was then repeated in November 2012 with a 287/294-532 nm scheme, Figure 4.5. Inside the Nd:Yag laser, the cavity produces light at a wavelength of 1064 nm. The frequency of this beam is doubled inside the laser with a nonlinear BBO (Barium Borate BaB_2O_4) crystal to obtain at the exit a green laser beam of 532 nm. Since the previous experiment, the power of the Yag laser reduced to the level of 90 % from the original value. This power was split into three beams. The first beam of 532 nm (10W) was guided directly to the ionization tube (see Figures 4.7, 4.6) with transmission of 60%. The rest of the power was equally distributed into two beams pumping the two dye lasers.

To obtain the UV light, a Rhodamine 6G dye was used. A dye laser, basically, has an oscillator part which is responsible for a selection of desirable wave length; and a amplification part to amplify the beam of the right wave length obtained in the oscillator. With the frequency doubling, lasers of 287nm (300mW) and 294nm (150mW) were obtained. As it can be seen from Figure 4.8, the saturation in the first ionization step is achieved already at 120 mW. The transmission for UV laser was estimated to be about 40%.

To monitor the position of the beams in the tube, a partial reflection from a thin quartz plate placed in front of the prism was used as is shown in Figure 4.7. The distance to the ionizer was equal to the distance to the monitor screen. Therefore, any deviation of the beam in the ionization tube definitely led to the same deviations on the screen.

Table 4.1[2] compares the laser source in [29] and the present work. With the same ionization scheme, the ϵ_{laser} measured for the stable isotope was higher in comparison to the previous experimental campaign in 2011. This might be due to different alignment of the laser which allowed it to ionize more atoms in the ionization tubes. Unfortunately, there

[2]The laser power is given before transmission

was a sudden drop in ϵ_{laser} possibly related to violation of laser alignment or synchronization, wrong wavelength, quality of dyes, etc. All these factors were considered, but didn't bring the laser efficiency back. Therefore, in the experiment using a radioactive beam ϵ_{laser} didn't exceed 5%, even though atoms from the metastable state were ionized as well. The successful implementation of laser ionization in further experiment requires more beam diagnostic, for instance installation of MCP in the beam line to check the pulse temporal profile.

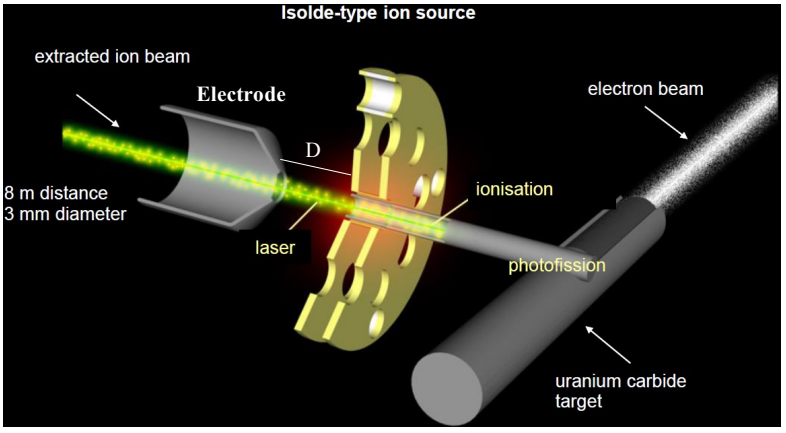

FIGURE 4.6: Isolde-type ion source

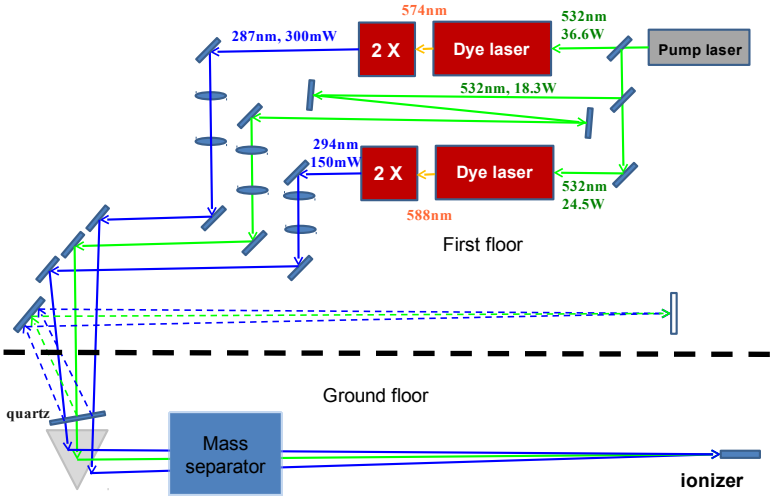

FIGURE 4.7: Laser ion source at ALTO.

Updated information concerning the latest developments in the laser technique for production of radioactive beams can be found in [112].

TABLE 4.1: Comparison of ALTO laser sources in 2011 and 2012

	2011, Fig.4.5a	**2012** Fig. 4.5a	**2012** Fig. 4.5b
Green laser, 532nm	30W	18.3W	18.3W
UV, 287nm	500mW	300mW	250mW
UV, 294nm	-	-	150mW
ϵ_{laser} for ^{69}Ga (stable)	10%	17%	3%
$\epsilon_{surface}$	1%	1%	1%

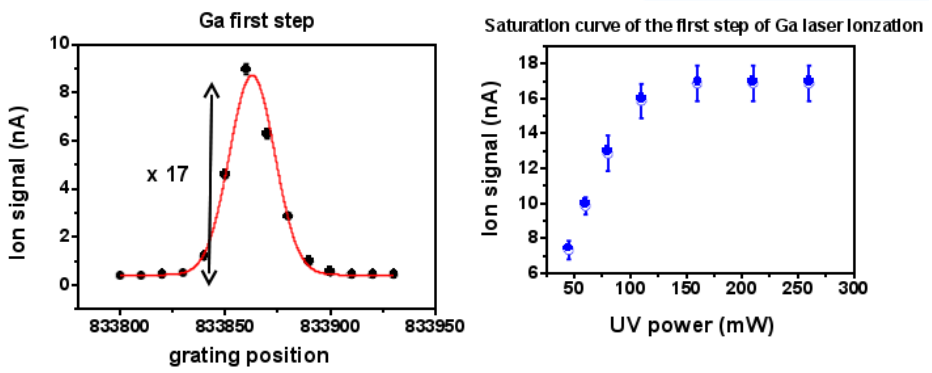

FIGURE 4.8: Left: Ion signal as a function of the wavelength of the first ionization step (2012). Right - saturation curve of the first step [3]

4.2.5 Mass separator PARNNe

Ions, extracted from the ion source at an energy of 30 keV, are delivered to the mass separator PARRNe which is well-shielded from radiations coming from the production target by 1.5 m concrete wall. Since separated fission fragments are stopped in the separator they strongly contribute to the background conditions in the experimental hall due to delayed radiation. In order to make background conditions less severe for both - experiments and personal, the separator is surrounded by concrete wall 15 cm thick and a shield "pie" to protect the environment. Additional "pie", aimed precisely at decreasing the neutron background, consists of a 10cm polyethylene layer to slow neutron downs, a 0.5cm thick a Cd layer to absorb neutrons and, finally, lead bricks to absorb γ-rays born via interactions of neutrons with the cadmium layer.

The beam is smoothly focused for optimized transmission and resolution of the separator. The ions are separated in mass with an H-shaped electromagnetic dipole separator [113] which has a homogeneous adjustable magnetic field B with deflection angle of 65^o and a radius of curvature ρ of 60 cm. The mass selection is proportional to the mass number of the nuclei of interest and inversely proportional to the charge of the ion: $\rho B = \frac{\sqrt{2EM}}{qe}$, where M is the mass of the isotope. Most ions have a charge +1, those are mass separated. The separation between a mass m and m+$\triangle$ m is expressed: $\triangle\, m = D\frac{\triangle\, m}{m}$,

where D = 1370 mm is the dispersion of the magnet. The resolution of the separated masses 100 and 101, as an example, is 13.7 mm [114].

4.2.6 New beam line for TETRA/BEDO. Beam guidance.

A new beam line to house the BEDO/TETRA setups was constructed at ALTO additionally to the one which existed before. To deliver a beam of radioactive isotopes to the detection system, a beam tune was performed using beam of a stable species of mass 85 (Rb) [4]. Rb was chosen because it is located close enough to the area of our interest (82-84 Ga). The first run of a new beam line, such as the one constructed for BEDO/TETRA, demands a few days of beam time and endless patience to complete a beam tune from the source till the collection point of the detection system. Figure 4.9 schematically illustrates the most important elements of the beam line optics. The optimum values found for my experiment are listed in Table 4.2. Below it is given some benchmarks for beam tuning.

The temperature of the source (hot tube, T_{four} ~2000^{o}C) and the extraction potential (around E_{extr} ~30keV) as well as the position of the extraction electrode from the ionization tube (D = 0 to 122 mm) influence directly both the number of photo fission fragments extracted from the source and beam guidance until the end of the line. Extracted fission fragments travel through quadruples Q_1, Q_2 to a Faraday Cup ("Cage de Faraday" - CF1) placed right afterwards. Once the optimum values for T_{four}, E_{extr}, Q_1, Q_2 are found, the current at *CF1* is the maximum, and the beam is led to proceed further to Q_3, Q_4 and to the separator. Q_3 is eliminated from the beam guidance and governed by the DAQ. It allows deflection of the beam. The beam is "ON" when HV(Q_3) = 0 and the beam is "OFF" then HV(Q_3) = 1 kV. Q_4 seems to be quite an important quadruple since it can impact the beam just before the separator. Usually, the high voltage applied to HV(Q_4) = 0.2-0.3 kV is relatively low in comparison to other quadruples. Due to the magnetic field of separator only selected masses can come to *CF2*. Then the beam can continue straight forward to the old ALTO-line be deflected by the deflector (*Deflecteur Plan Focal*) to the BEDO/TETRA line. After Q_9, Q_{10} the beam is again deflected by the deflector *Deflecteur 60 ^{o}*. Then after the *steerer*, which can correct the height of the beam, *the beam profile* detector *BP6* is installed. It can be moved inside the beam line by remote control. Alternatively, CF6 can be used at the same position to control beam current. Usually in this section of the line, fluctuations in a beam profile and transmission between BP6 (CF6) and BP8 (CF8) are controlled. Between them the beam has to move through Q_{11} and then its direction to the *Bender* is set by the *Kicker* which allows it to turn finally to the TETRA/BEDO setup. There

[4] for the surface ionization source. For FEBIAD Xe, Kr are used

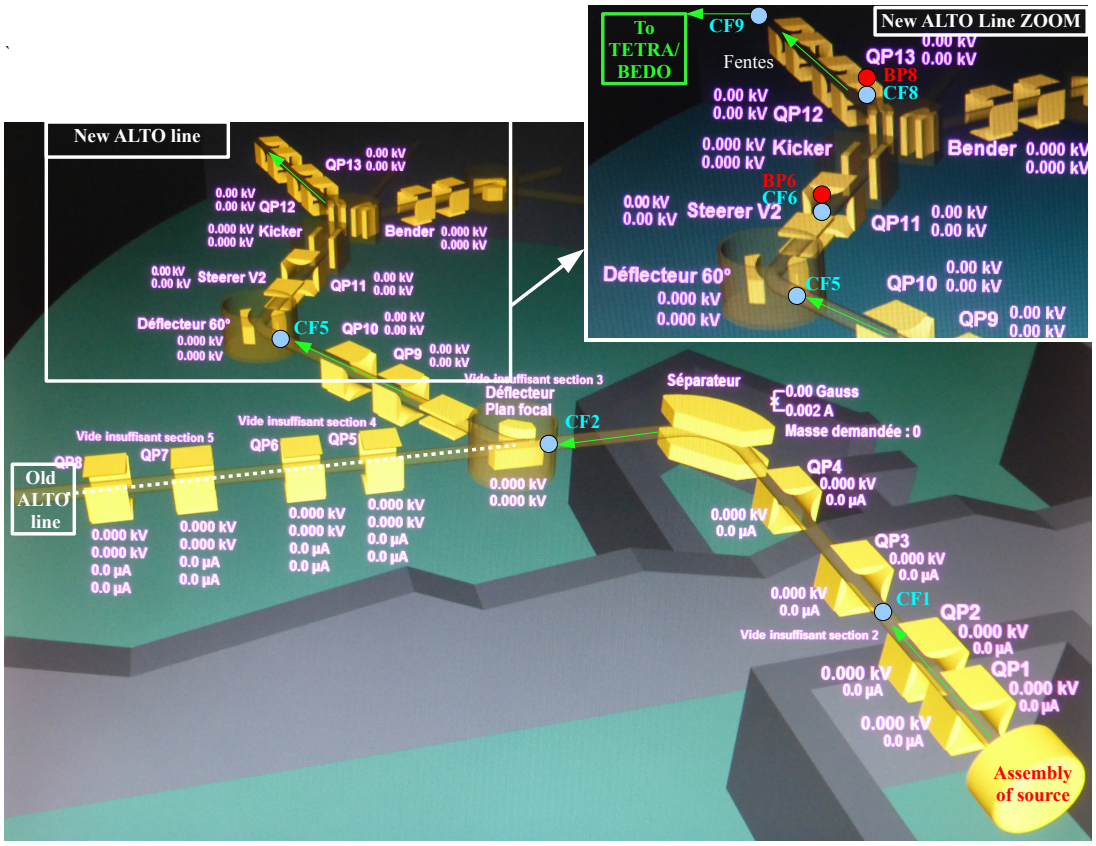

FIGURE 4.9: Beam guidance at BEDO/TETRA beam line of ALTO. Screen shot of control panel. Originally existed ALTO line is labeled by dashed white line; the line constructed for my experiments is zoomed. The beam directions are shown by light green narrows. All the major optic elements are labeled in rose text. Blue circles - Faraday cups; red circles - beam profile detectors.

TABLE 4.2: The values for of voltage applied to optic elements (in kV) to insure the best transmission. For quadruples two values are given for horizontal (h) and vertical (v) shift.

	Q1	**Q2**	**Q3**	**Q4**	**SEP**	**DF**	**Q9**	**Q10**
h	1.406	1.13	0	0.217	3871.89 G	7.124	1.534	2.054
v	1.888	1.317	0	0.229	A=85		1.534	2.054
	DEF60	**ST**	**Q11**	**K**	**B**	**Q12**	**Q13**	**Q10**
h	8.512	0.168	0.703	1.39	1.824	1.372	1.942	
v						1.372		
	D	**Ifour**	**I cathode**					
	121.4mm	750A	350A					
	CF1	**CF2**	**CF5**	**CF6**	**CF8**	**CF9**	**Eff**	
	-	3.5nA	-	-	-	2.5 nA	70.00%	

are two pairs of "fentes" to cut the beam in order to make it exactly the size of the tape (1cm X 1cm at maximum) and at the end *CF9* is the "last" Faraday Cup in the line located just before the detection system. The tune was one gradually, section by section, from the one CF to the next one trying to obtain the best transmission rate. The final transmission rate achieved between *CF2* and *CF9* was 70%.

The beam profile detector consists of 42 wires in both vertical and horizontal directions. The current in each wire is measured which helps to obtain the spacial distribution of beam. As an example, Figure 4.10 illustrates the beam distribution along the X axis (blue area) and Y axis (white) area. The profiles were captured at the same moment at BP6 Figure 4.10a and BP8 4.10b Once the tunning is completed, the magnetic field of

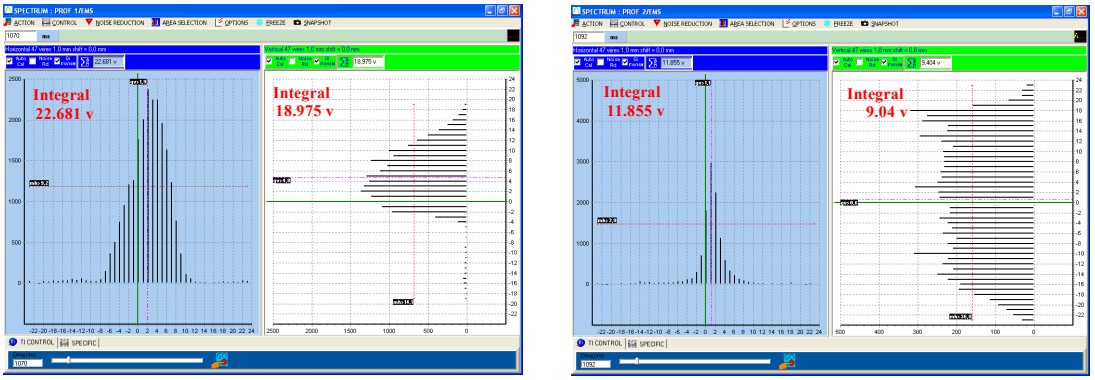

(A) BP6, time 18:51 (B) BP8, time 18:51

FIGURE 4.10: An example of beam profilers

the separator has to be corrected. There is "theoretic" field which is calculated by the formula giving above (in §4.2.5). However, as always happens under real experimental conditions, the field has to be adjusted for each experiment. The adjustment is made using rations of isotopic abundances for two neighboring masses (in my case - A = 85 and A = 87) by current in *CF2*.

Chapter 5

Experimental setup

"A theory is something nobody believes, except the person who made it. An experiment is something everybody believes, except the person who made it."

A. Einsten

Contents

Separated nuclei of interest are finally collected on the mylar tape, at the collection point, Figure 5.1. The collection point (in red) is surrounded by a $4\pi\beta$-detector (in yellow) and by 4 layers of neutron counters placed in a single piece of high-density polyethylene protected from background neutrons by 15-cm thick borated polyethylene slice, and a germanium detector which is put in from the back on the beam axis. The collected nuclei, whose lifetime is relatively short, undergo β decay. In their turn, the daughter nuclei also suffer from β decay. However, since they are closer to stability, they have a longer half-life. In order to evacuate unwanted radioactivity from these nuclei, the tape is moved with a period depending on a particular isotope to be studied.

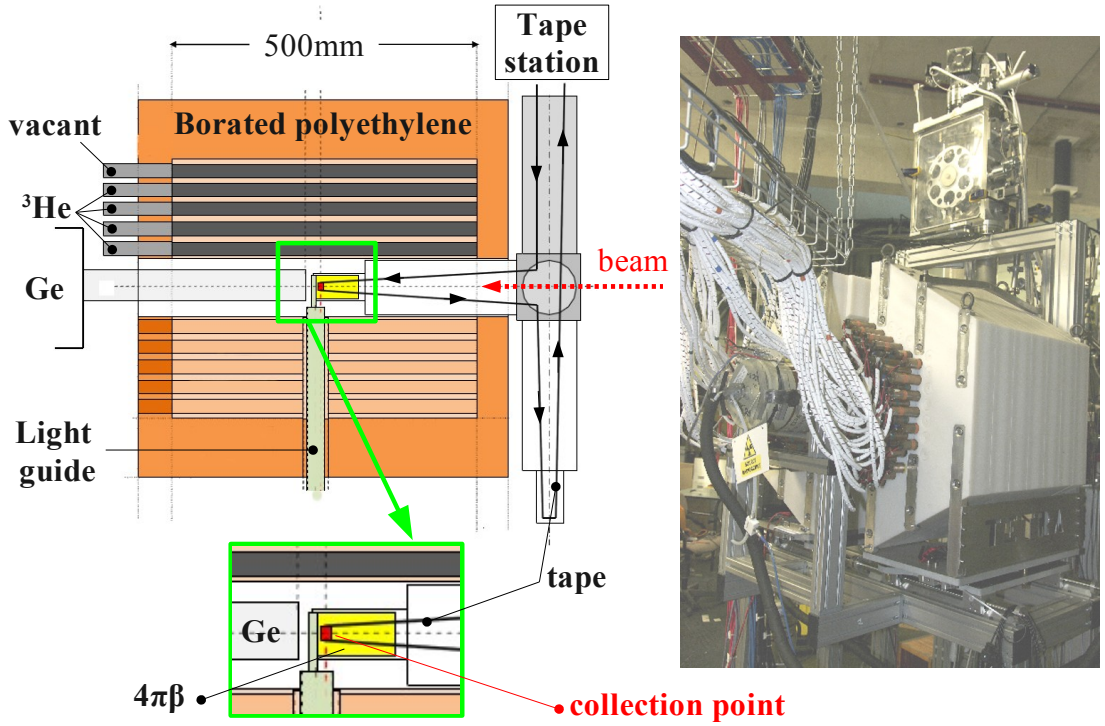

FIGURE 5.1: Overview of the experimental setup

5.1 Moving tape system (MTS)

A single cycle (the time between two consecutive tape movements, Figure 5.2) starts with a background measurement (T_{bg}), and followed by beam time T_{beam} and decay time T_{decay} chosen individually for each isotope. If $T_{beam}>T_{1/2}$ one should expect a saturation in the activity curve as it is shown in Figure 5.2.

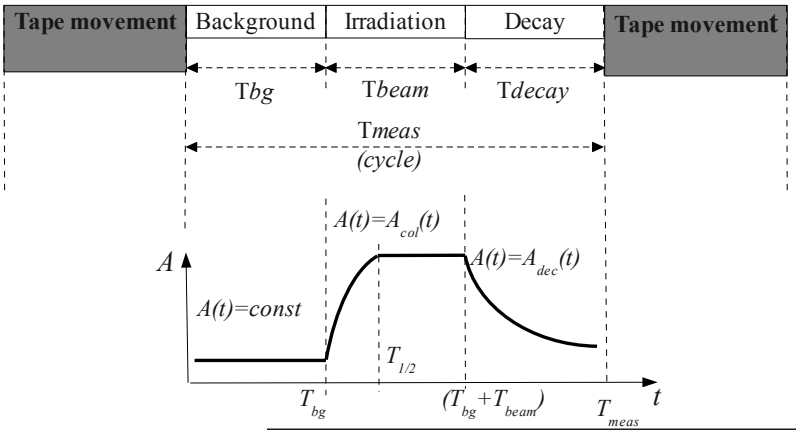

FIGURE 5.2: Cycle: background measurements, collection and decay time.

The tape can be moved with the maximum speed of 1 m in 0.1s with a precision of about ±1 mm. When the end of the tape is reached the tape is automatically reversed. The total time needed for tape rewinding depends on the current position of the tape and the length of the tape to be rewound - about ∼2s for ∼10m of tape. The MTS has a few km of tape and provides a maximum of 2 displacements per second. To prevent the data acquisition system (DAQ) from recording data when the tape is moving the MTS produces the signal ("coding enable") which is used to stop DAQ and to deviate the beam (see details §5.7).

5.2 Gamma Detector

Efficiency calibration

The efficiency of the germanium detector (database reference *GeFoc29*) was measured with a calibrated ^{152}Eu source placed at 5 cm (the distance from the collection point to the detector) in front of the detector. Due to geometrical limitations (elements of the tape support) it was impossible to have the ^{152}Eu source right at the collection point. To verify the measurements, therefore, a ^{60}Co source placed nearly at the collection point was used. The total efficiency and a fit are plotted in Figure 5.3. The efficiency of the detection system was about 0.8% at 1 MeV. As seen, there is a difference between measurements with ^{152}Eu source and ^{60}Co source. Therefore, in the analysis this difference was included as additional error to the gamma efficiency. The problem of a germanium detector efficiency will be solved for the forthcoming experiments by utilization of a new ^{152}Eu small enough to fit the collection point.

Energy calibration. Resolution.

The energy calibration of the germanium detector was performed using a calibrated ^{152}Eu source. The energy calibration of the germanium detector is presented in Figure 5.4. The energy resolution of the detector was 1.7 keV in September 2012 and 2.1 keV in December 2012 for 1 MeV γ is plotted in Figure 5.5 .

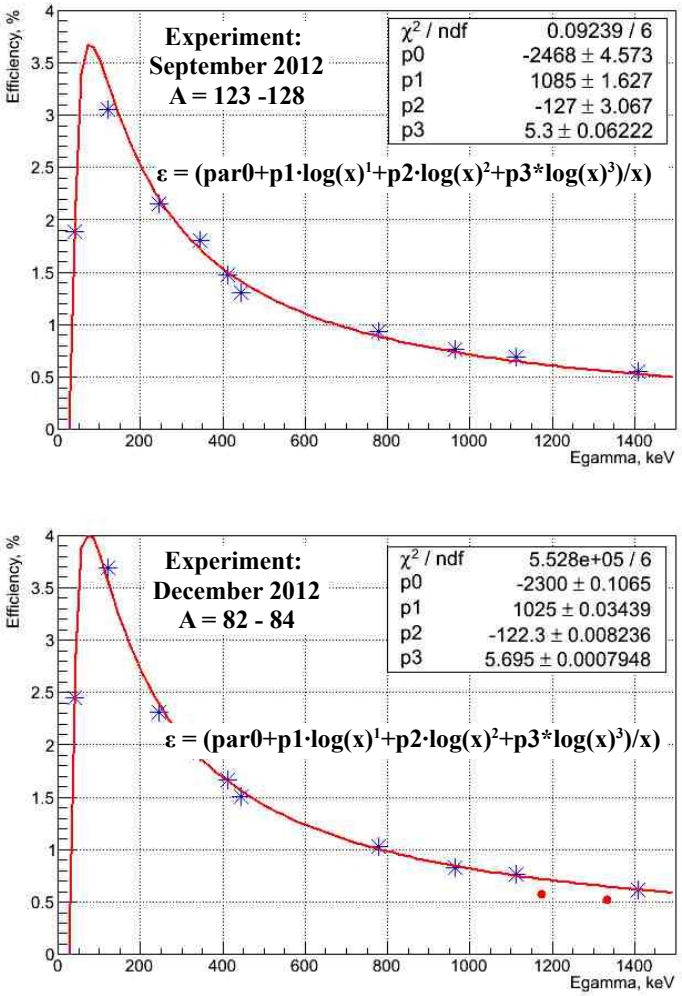

FIGURE 5.3: GeFoc29, efficiency calibration. Blue stars - experimental points obtained with ^{152}Eu fitted by the red line; red dots - experimental points obtained with ^{60}Co.

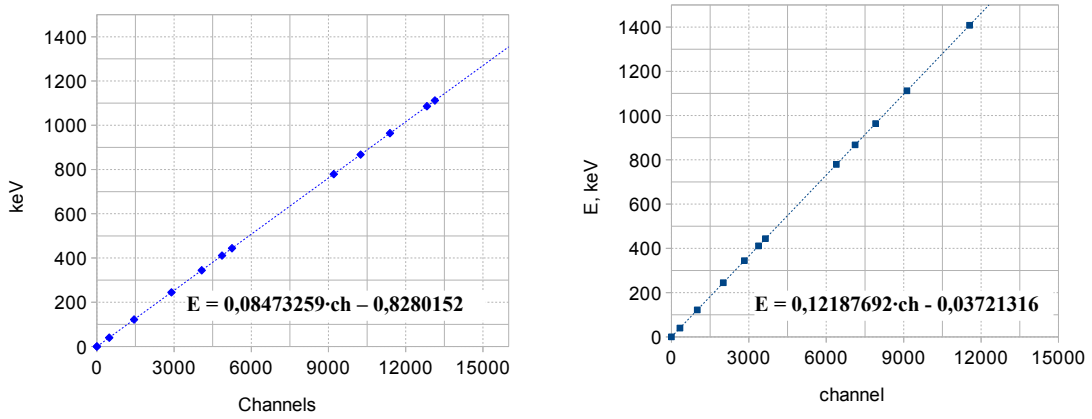

(A) Experiment: September 2012, A = 123 - 128 (B) Experiment: December 2012, A = 82 - 84

FIGURE 5.4: GeFoc29, Energy calibration

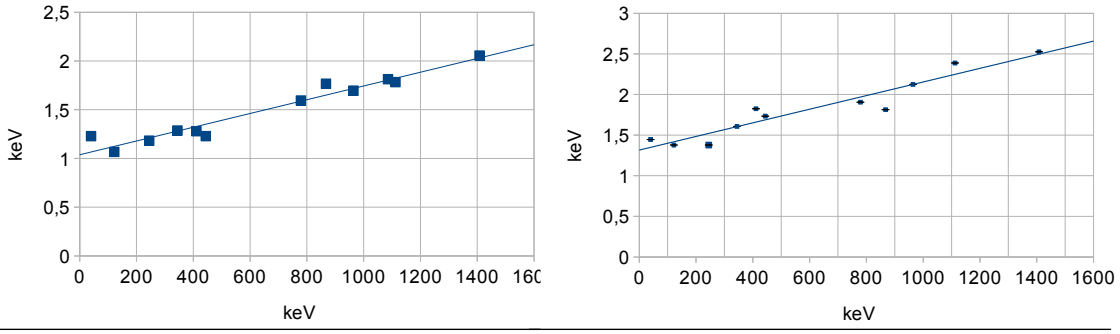

(A) Experiment: September 2012, A = 123 - 128 (B) Experiment: December 2012, A = 82 - 84

FIGURE 5.5: GeFoc29, Resolution

5.3 Beta Detector

The efficiency of the β detector is mostly determined by geometrical factors, calculated from technical drawings, Figure 5.6, to be 92% (coverage of solid angle). Additionally, the unique feature of this setup is a transparent beam line. It helps to monitor visually tape movements as well as facilitate repair of the tape in case of accident. Therefore, the outside of the plastic was covered by thin layer of dark material (a few micron thick) in order to prevent light coming inside.

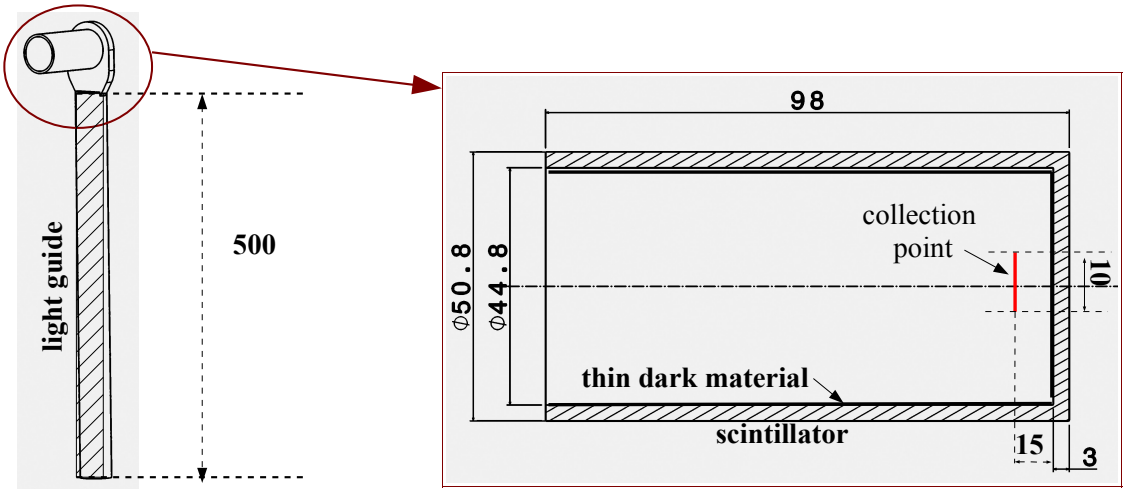

FIGURE 5.6: Schematic view $4\pi\beta$ detector, values are given in mm

A signal from the plastic $4\pi\beta$ was sent to the Constant Fraction Discriminator and then directly into the DAQ. The ^{60}Co source was used to optimize the parameters of the Discriminator.

Beta Detector efficiency calibration with ^{60}Co source

The efficiency of $4\pi\beta$ was found from peak ratios in the direct γ and $\gamma\beta$ gated spectra measured for a ^{60}Co source. The source β decays with a period of 1925 days to exited levels of ^{60}Ni which further de-excite by emission of γ-rays (Figure 5.7). Thus, the two most intense γ rays: $E_{\gamma 1} = 1173$ keV and $E_{\gamma 2} = 1332$ keV have to be in coincidence with a β. The ratio of their peak areas (Equation 5.1) is the β efficiency of the detector.

$$\frac{S_{\gamma i}}{S_{\gamma\beta i}} = \epsilon_\beta \tag{5.1}$$

It was found that $\epsilon_\beta^0(^{60}\text{Co}) = 51\pm3\%$. Such a low efficiency might due to the fact that low-energy β from ^{60}Co (about 300 keV [115]) are moderated by the thick dark material. In consequence, the energy deposited by β in the scintillator is not sufficient

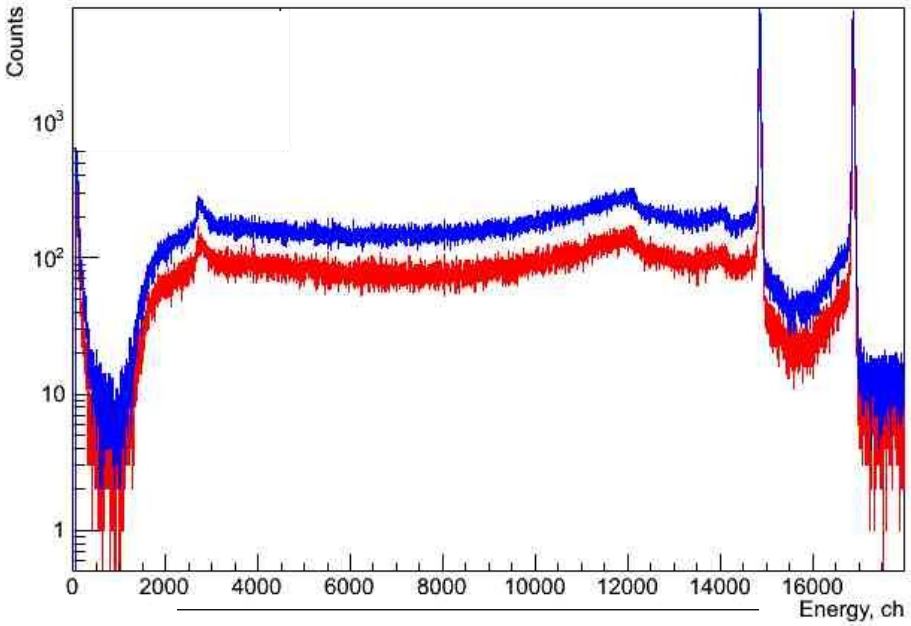

FIGURE 5.7: Measured direct γ (in blue) and γ-β gated (in red) spectra for mass ^{60}Co source

for ionization and/or the light seen by the photomultiplier is too weak and is cut by the discriminator threshold. Due to significant big distance (5cm) between the source and the gamma detector, the effect of coincidence summing is negligible.

With respect to fact ϵ_β was determined individually for each mass studied by direct γ and γ-β gated spectra in §6.4. Since the γ efficiency is canceled out in the ratio, this method is free from the parameters of germanium detector as well as parameters of the source. Moreover, in case of high count rate in the β detector one should make a correction for dead time in the electronic channels §6.5.

5.4 Comet Data Acquisition System. Its limits.

The analog signals from the electronics were transmitted to the acquisition card COMET-6x (Coding Marked Time) where they were converted into numeric format. The card has 6 channels consisting each of three inputs: (fast) time, energy and input. The energy signal is coded in 15 bits, the time 47 bits and the marker is a logic NIM 1-bit signal. The COMET system is a trigger-less system. Each detector (plastic scintillator, germanium detector) is considered as an independent source for which the physical signal associated with an absolute time is coded. The time accuracy is 400 ps. During the experiment the CODEN (Coding Enable) signal was used. It is a special signal sent by the tape station system which inhibits the coding while the tape is moving (24 V coding inhibited (COMET is "closed"), 0 V coding enable (COMET is "open")). Each cycle

the absolute COMET time is reset back to zero. Only radiation measured by detectors from isotopes decaying at the collection point when COMET is "open" is stored. The data can be monitored on-line during the experiment with the computer program cvisu. This program creates the energy spectra of 15 bits and time spectra of 47 bits.

Each channel has quite a big dead time - $\tau_{comet} = 10.3\mu$s. In previous experiments only coincidence between two (or many) channels was studied. Typically, the number of input channels can be increased by using a larger number of COMET cards. There were about 30 channels at ALTO available at the time. Bearing in mind that the TETRA detector has about 90 neutron counters it becomes clear, that the number of COMET channels was merely insufficient. Therefore, the obvious solution was to use an "intermediate" data electronics system which was responsible for interrogation of all neutron channels and served COMET just one signal *OR* from TETRA whichever neutron channel(s) fired. In this case only one COMET channel is needed - see *External DAQ NIM*,Table 3.1, page 43. Consequently, the dead time is determined by time necessary to process an event by COMET - τ_{comet}. This seems reasonable for my experiments since a neutron flux of more than 10^5/s is too unlikely due to the low production rate of neutron rich isotopes. However, as it was explained above (see Figure 3.10, page 42), such a τ_{comet} intervenes drastically in measurements of neutron multiplicity of the neutron source. In Figure 5.8b is plotted neutron-neutron coincidence from a ^{252}Cf neutron source. It is clearly seen that neutrons which are coming with a time shorter than τ_{comet} are totally lost from measurements which causes both the loss of efficiency, and, what is much more important, the distortion of the multiplicity distribution. The latter can lead to a wrong understanding of physical processes. If all neutron channels are split into a few(6) groups with a single *OR* independent from each, it results somehow in a decrease in influence of τ_{comet} on neutron-neutron coincide, Figure 5.8b . The only way to fully get rid of it is internal DAQ of TETRA (T-DAQ) § 3.2.1 to store neutron data, and COMET to record data from other detectors (β, γ). Therefore in an experiment, where a multi neutron emission is expected to be measured in coincidence with beta-, gamma-, both DAQ (TETRA + COMET) must be used.

5.5 Synchronization of COMET and TETRA DAQ

To synchronize TETRA and COMET DAQs one, firstly, should clearly understand what the coding signal, created by the tape system, exactly is. Start/stop of measurements are controlled by tape automatically. To be precise, the coding is not even a signal, but a change of the potential level (U). When tape is moving, electric circuit is connected and $U = +24$V. When measurements are about to start the tape automate disconnects

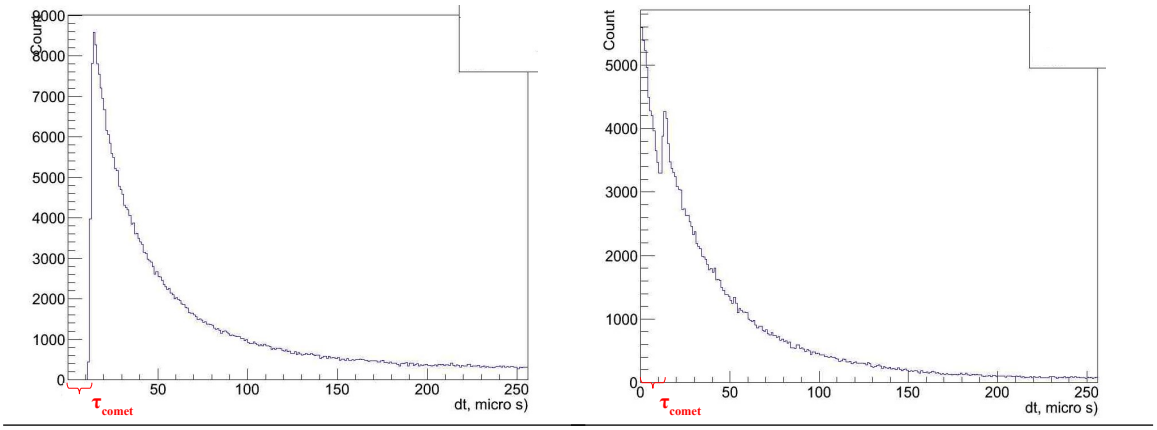

(A) One COMET channel is used. (B) Six COMET channel are used.

FIGURE 5.8: Time distribution of neutrons obtained by textitExternal DAQ NIM. See in comparison to 3.16, page 51

the circuit, so that U=0V, as a result, DAQ is open. The idea was to generate a NIM signal on each change of level U to be sent to TETRA DAQ to the "start" input. This signal would be recorded with its time of arrival. Therefore, in off-line data analysis it would be possible to eliminate events which have come in between of two cycles of measurements.

The tape automatically generates independently two simultaneous outputs Figure 5.9. The top one is directly linked to COMET. Whereas the second one, which has +24V amplitude and 10 ms length, which is generated each time when the level is changed (goes from 0 to 24V and from 24V to 0), is sent, firstly, to a Function Generator which is set to make a 10Hz pulse with an amplitude of +5V. Now, since the amplitude corresponds to TTL standard, the signal is transmitted to TTL-NIM convertor to form a NIM signal at the beginning and at the end of each pulse. These NIMs are sent to the "start" input of TETRA DAQ. Tape station, COMET and TETRA DAQ are synchronized.

5.6 On-line monitor of TETRA at CVISU

CVISU is a software program to govern COMET DAQ. Also it can be used to display some predefined spectra on-line. The output *External DAQ COMET* (Table 3.1 § 3.11, page 43) being slow was only used to monitor TETRA on-line at the CVISU interface. In analogy to a germanium detector, T-DAQ serves COMET with two inputs: a fast timing signal which opens a 16μs gate to register the maximum amplitude on the second, energy, signal. The amplitude of this energy signal is formed by T-DAQ to be unique for each neutron channel in the range 0 - 5 V. Finally, a kind of spectra, similar to a γ-ray spectrum, can be displayed by CVISU. A raw "tetra" spectra is shown in Figure 5.10.

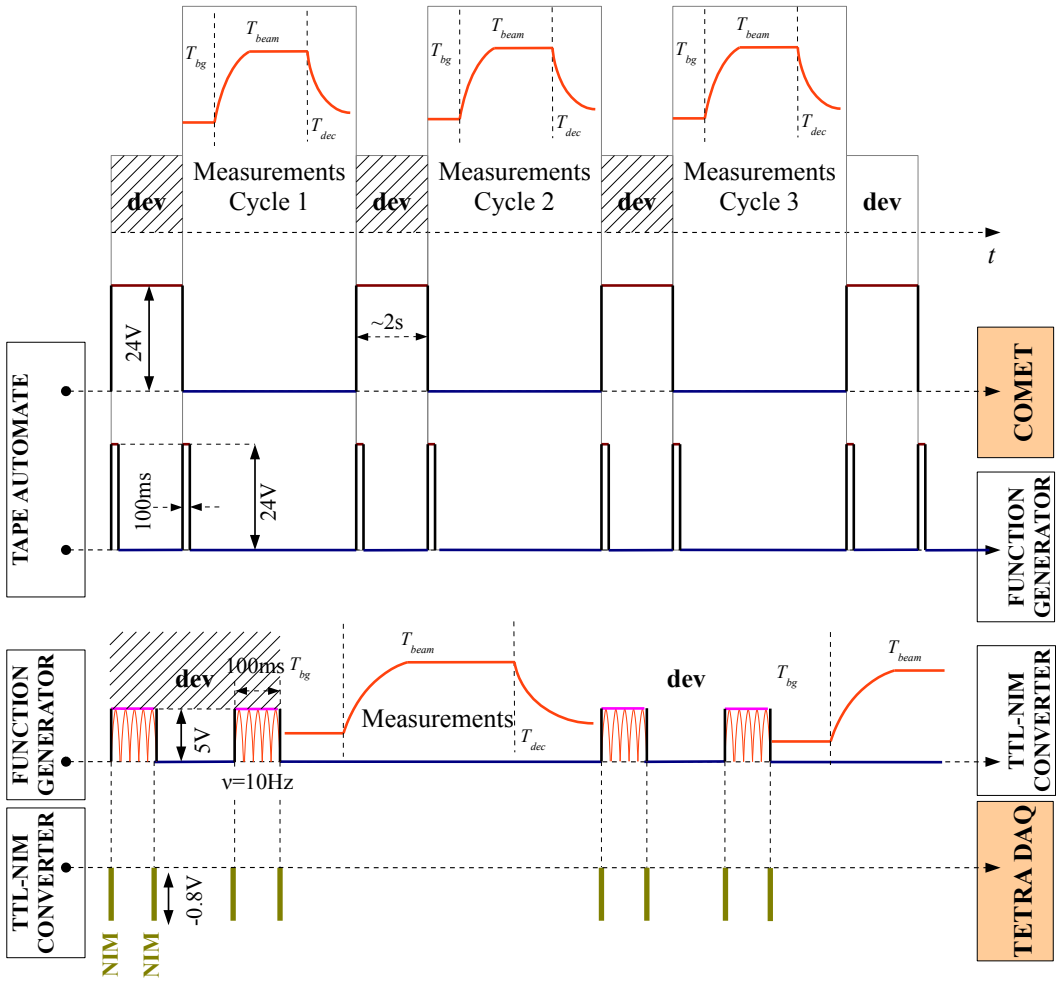

FIGURE 5.9: Synchronization of COMET and TETRA DAQ.

The very first peak is number of overflow of time buffer in T-DAQ. The number of counts in this peak multiplied by ∼2s gives the time from the beginning of the measurements. Then, in my experiments, counters occupied channels from 9 to 96 (with some gaps). Higher channels correspond to firing the high threshold. These events, as it is explained in § 3.2.3, are treated by T-DAQ by adding "1" to the higher rank of the word sent to a computer. For COMET (and CVISU), T-DAQ provides a higher amplitude such that the number of the counter($N_{counter}$) fired is shifted by 128 ($N_{highthr} = N_{counter} + 128$). All the channels are nicely separated. Calibration, similar to energy calibration of germanium, is necessary to link COMET(CVISU) units to real neutron channels Figure 5.11.

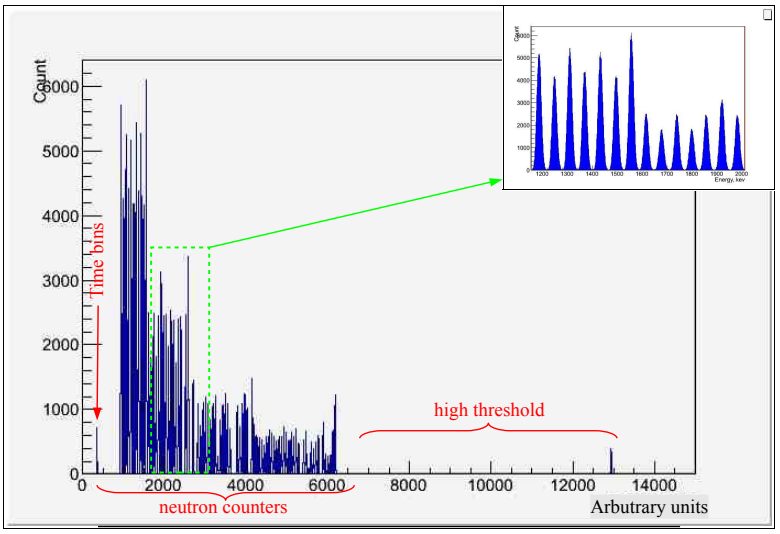

FIGURE 5.10: Count rate in each neutron channel.

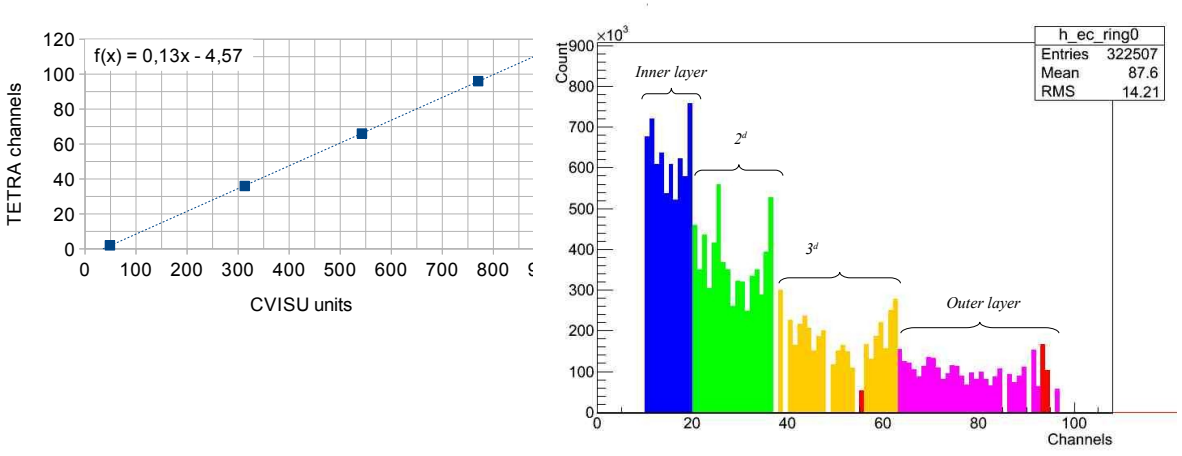

(A) Calibration in CVISU to match TETRA channels (B) "Calibrated" neutron channels in CVISU

FIGURE 5.11: "Calibrated" neutron channels in CVISU

5.7 General review of electronic system

The schematic view of the electronic system is drawn in Figure 5.2.

- Germanium detector (GEFOC29 in Figure 5.12): the signal from the preamplifier (located close to the crystal in order to reduce the thermal noise and achieve an optimum charge collection) is sent to Linear Amplifier which also forms the semi-Gaussian shape of the signal. The decay part of the signal is determined by the feedback circuit of the preamplifier. To avoid so called undershoots (which is the differentiation of exponential tail from the preamplifier), which may cause an amplitude defect cases where the second signal arrives just after the first one, the pole-zero cancellation circuit is used. The second (the same) signal from the preamplifier is sent to the Fast Timing Amplifier (FTA). It provides voltage pulses which amplitudes are proportional to the incident amplitudes. This signal is then changed into a logical signal by Constant Fraction Discriminator (CFD). The rising edge of this logic signal is used to trigger the acquisition of the energy channel. Since the Linear Amplifier process is much slower than the FTA or the CFD, in order to fulfill the condition of coincidence, the signal is delayed before entering to the acquisition card.

- Plastic detector $4\pi\beta$: The signal from the plastic detector $4\pi\beta$ is sent to the Constant Fraction Discriminator and then directly to the acquisition card. This logic signal was used in the analysis process to build the coincidences between the germanium and the neutron detectors.

- Neutron detector TETRA: signals from all the built-in preamplifiers are connected to the TETRA electronics. There are three ways the information from the TETRA can be simultaneously recorded as discussed in §3.2.4.

  1) The NIM output[1] "OR" from all the counters is sent directly to the acquisition card and used further in the analysis.

  2) Since this signal doesn't bring any information on the number of the counter fired. This information is available on the second output: the logical (time) signal is sent directly to the data acquisition simultaneously with the amplitude signal whose amplitude is proportional to a number of a counter fired. This output is similar to one used for a germanium detector, with the exceptions that the signals are already formed inside the TETRA electronic modules.

  3) Finally, the independent (from an external data acquisition system) TETRA-DAQ sends the data via USB-port to be recorded in the hard drive of a computer.

[1] see §3.2.4 describing different outputs

The same USB-port is used to setup the individual coefficients of amplification (see §3.2.1).

- The "coden" signal is sent simultaneously to the COMET DAQ and to the TETRA electronics upon the tape movement in order to provide synchronization between COMET and TETRA DAQ (see §5.5).

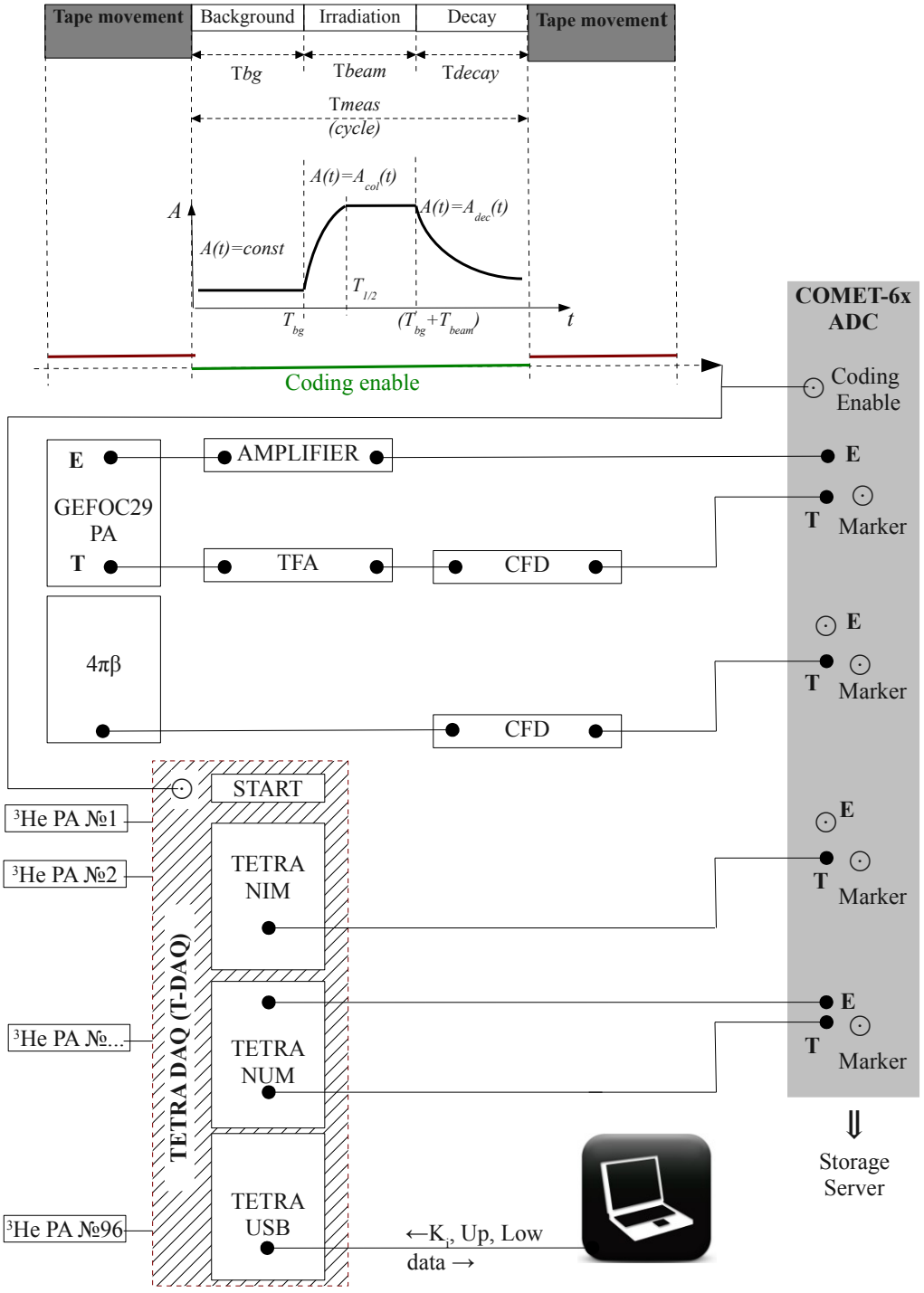

FIGURE 5.12: Schematic view of electronic system.

Chapter 6

Data analysis and Results.

"If your experiment needs statistics, you ought to have done a better experiment"

E. Rutherford

Contents

6.1 Methods of measurements of P_n-values

The P_n value of a neutron precursor (A, Z) is the ratio of the number of decays to the β-delayed neutron daughter (see Figure 1.1 on page 3) to the total number of decays. There are a few general methods to experimentally determine P_n which differ in the way mother/daughter nuclei are measured [8, 116].

- *Ion counting* - the number of mother/daughter nuclei is determined directly by any suitable ion detector. This might be a very effective technique at current experimental facilities where reliable identification and counting techniques can be applied.

- *Neutron-beta coincidence counting(n/β)*, P_n is the ratio of coincidence events ($N_{\beta n}$) to the number of betas N_β, $P_n = \frac{1}{\varepsilon_n} N_{\beta n}/N_\beta$, where ε_n is the absolute neutron efficiency, and doesn't depend on beta efficiency ε_β. Even though, ε_n depends on neutron energy, in practice P_n can be measured under the assumption that neutron efficiency ε_n = *constant* for a certain neutron energy range. The proper knowledge of $T_{1/2}$ is needed to be able to separate betas and neutrons emitted in the decay of the mother nucleus from decays of its daughters.

- *Neutron-beta counting(n/β)* - neutron and betas can be counted not in coincidence, but simultaneously, $P_n = \frac{\varepsilon_\beta}{\varepsilon_n} N_n/N_\beta$. Two absolute efficiencies are needed. The method can be advantageous if the geometry of beta and neutron detectors can cover a solid angle close to 4π.

- $\gamma - n$ *and* $\gamma - \gamma$ - the number of mother decays can be obtained by γ -ray transitions in its direct β-decay daughter or longer lived β-decay grand daughters -

$$P_n = \frac{1}{\varepsilon_n} \frac{N_{neutron}}{N_{mother}(\varepsilon_\gamma, I_{abs})} \tag{6.1}$$

  where I_{abs} is the absolute γ intensity for β-decay and $\varepsilon\gamma$ is the efficiency of the γ detector. Alternatively, sometimes one can rely on the number of β-n daughters also measured by γ-rays:

$$P_n = \frac{N_{neutron}^{daughter}(\varepsilon_\gamma^{daughter}, I_{abs}^{daughter})}{N_{mother}(\varepsilon_\gamma^{mother}, I_{abs}^{mother})} \tag{6.2}$$

  Absolute γ-intensities are required, which means a complete knowledge of the decay scheme including β going to the ground state or eventually competing β-decays from levels above the neutron separation energy. Error bars in determination of P_n can be bigger due to uncertainty of measured peak areas.

- *Efficiency normalization* - the ratio $\varepsilon_\beta / \varepsilon_{neutron}$ is obtained for a precursor with well-known P_n^0:

$$P_n^0 = \frac{\varepsilon_\beta}{\varepsilon_{neutron}} \cdot \frac{N_{neutron}^{known}}{\cdot N_\beta^{known}} \tag{6.3}$$

  This ratio is used to normalize to an unknown isotope X measured in the same experiment:

$$P_n^X = P_n^0 \cdot \frac{N_\beta^{known}}{N_{neutron}^{known}} \cdot \frac{N_{neutron}^X}{\cdot N_\beta^X} \tag{6.4}$$

  It might be more beneficial than individual determination of ε_β and $\varepsilon_{neutron}$ though the method is still based on an assumption that beta and neutron spectra are the same for both isotopes.

In my experiments β and neutron activity curves were measured. Analysis based on solutions of Bateman equations allowed separation of the contributions of different isotopes participating in decay chains to these curves.

6.2 P_n evaluation solving the Bateman system

The decay path of the radioactive source created by accumulation of the beam depends on both the decay constant λ_i and P_{ni} (see an example in Figure 6.1). This chain is characterized by the set of coupled linear differential equations 6.5

$$\begin{cases} \frac{dN_1(t)}{dt} = -\lambda_1 \times N_1(t) + \phi_1, (^{84}Ga) \\ \frac{dN_2(t)}{dt} = -\lambda_2 \times N_2(t) + (1 - P_{n1}) \times \lambda_1 N_1(t), (^{84}Ge) \\ \frac{dN_3(t)}{dt} = -\lambda_3 \times N_3(t) + (1 - P_{n2}) \times \lambda_2 N_2(t), (^{84}As) \\ \frac{dN_4(t)}{dt} = -\lambda_4 \times N_4(t) + P_{n1} \times \lambda_1 N_1(t), (^{83}Ge) \\ \frac{dN_5(t)}{dt} = -\lambda_5 \times N_5(t) + P_{n2} \times \lambda_2 N_2(t) + \lambda_4 N_1(t). (^{83}As) \end{cases} \tag{6.5}$$

where ϕ_1 - production rate of isotope of *i=1*, $P_{n1,n2}$ - probability of β- delayed neutron emission and λ_i - decay constant, (i = 1, .., 5 is the index of corresponding isotopes). A general solution for $N_i^{col}(t)$ (the number of nuclei of *i-th* isotopes accumulated at the moment t during the collection time) can be found with zero conditions $N_i^{col}(0) = 0$. Analogically, for decay of accumulated nuclei, $\phi_1 = 0$, $N_i^{dec}(t)$ (the number of nuclei of *i-th* isotopes at the t moment during the decay) the solution of system (6.5) is obtained with initial conditions $N_i^{dec}(0) = N_i^{col}(T_{beam})$, where $T_{beam}$is the irradiation time. This also assumes a pure beam.

The analytical solution for N_i^{col} and $N_i^{dec}(t)$ is to bulky, but can be easily obtained using any computer application for numerical computations. For an example, we used *Wolfram Mathematica* - there is an example input file in Appendix B.1. The total

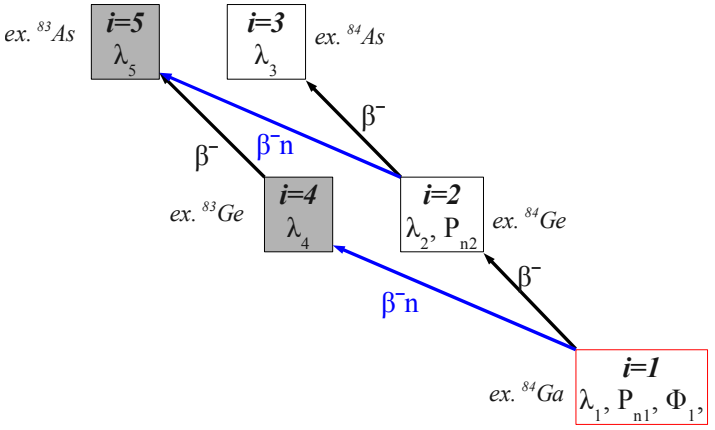

FIGURE 6.1: Illustration of β-, β-n decay chain of isotope 1. i index, λ_i, P_i the decay constant and probability of beta decay neutron emission for i_{th} isotope. The case matches exactly to β decay of ^{84}Ga.

activity (number of decays per time unit) is given by

$$\begin{cases} A_{col}^{tot}(t) = \sum_{i=1}^{5} A_i^{col}(t) = \sum_{i=1}^{5} \lambda_i \times N_i^{col} \\ A_{dec}^{tot}(t) = \sum_{i=1}^{5} A_i^{dec}(t) = \sum_{i=1}^{5} \lambda_i \times N_i^{dec} \end{cases} \tag{6.6}$$

where $A_i^{col}(t)$ and $A_i^{dec}(t)$ are the activity of each isotope during collection and decay respectively. Since all the nuclei in the region are 100% β- decay it is reasonable to assume that the number of decays is equal to the numbers of β emitted: $A^i(t) = A_\beta^i(t)$. Thus the curve shown in Figure 5.2 can be described by the defined function (6.7).

$$A^{tot}(t) = \begin{cases} const, 0 < t < T_{bg}, \\ A_{col}^{tot}(t), T_{bg} < t < (T_{bg} + T_{beam}), \\ A_{dec}^{tot}(t), (T_{bg} + T_{beam}) < t < T_{meas}, \end{cases} \tag{6.7}$$

where $T_{bg}, T_{beam}, T_{meas}$ are varied individually for each nucleus of interest to be studied. During the experiments two activity curves - β and neutron - were recorded as a function of time. If $A_\beta^{tot}(t)$ defined in (6.7) is the β activity as a function of time (in the tape cycle shown in Figure 5.2), the neutron activity, in the case shown in Figure 6.1, is defined by

(6.8):

$$A^{tot}_{neutron} = \sum_{j=1}^{2} A^{j}_{\beta}(t) P_{nj} \tag{6.8}$$

where P_{nj} is the probability of beta delayed neutron emission. Extracting the total number of betas (N^{exp}_{β}) and neutrons ($N^{exp}_{neutron}$) registered in an experiment as a function of time, corrected by efficiencies of the $4\pi\beta$ (ε_{β}) and 4π neutron ($\varepsilon_{neutron}$) detectors and background beta (N^{bg}_{β}) and neutron ($N^{bg}_{neutron}$) events one can directly obtain P_{n1} and ϕ_1 as a solution of the system of equations (6.9) in the condition that P_{n2} is known:

$$\begin{cases} (N^{exp}_{\beta} - N^{bg}_{\beta})\dfrac{1}{\epsilon_{\beta}} = \displaystyle\int_0^{T_{meas}} A^{tot}_{\beta}(t), \\ \\ (N^{exp}_{neutron} - N^{bg}_{neutron})\dfrac{1}{\epsilon_{neutron}} = \displaystyle\int_0^{T_{meas}} A^{tot}_{neutron}(t), \end{cases} \tag{6.9}$$

Since there are only two unknowns (P_{n1} and ϕ_1), the Equations 6.9 have only one solution. Since neutron and beta integrals were found for a given number of cycles, ϕ_1 (per second) is the integrated production rate over all cycles. Thus, to restore the real production rate one should divide the integrated production rate by the number of cycles. The uncertainties in the roots arose from uncertainties in parameters - published values of λ_i, P_{n2} and the errors in determination of number of β and neutrons (taking into account the errors in background measurements and detectors efficiencies). σ for each root P_{n1} and ϕ_1 were found separately as a root square from the sum of sigmas squared for each parameter:

$$\sigma = \sqrt{\sum_{i=1}^{5} \sigma_i^2 + \sigma_n^2 + \sigma_{\beta}^2} \tag{6.10}$$

In practice, the biggest uncertainties came from N_{β} and N_n.

Wolfram Mathematica was also used to solve Equations 6.9 (Appendix B.1). Once P_{n1} and ϕ_1 are found, experimental β and neutron activity curves could be reproduced to verify the solution.

Fitting β and neutron activity curves in ROOT.

To verify the results obtained in *Wolfram Mathematica*, a fit of β and neutron activity curves was performed using the ROOT system [117]. The fit functions were set in an analytical way, $A^{tot}_{\beta}(t)$ and $A^{tot}_{neutron}(t)$, with P_{n1} and ϕ_1 as free parameters with initial values given by the solution of Equations 6.9. The parameter minimization and error analysis were performed with MINUIT packages built in ROOT. The decay parameters

of the daughters are well known in literature, hence they were fixed at the given values. The impact on P_{n1} and ϕ_1 of varying these parameters within the uncertainty quoted in the literature was found.

6.3 Gamma-beta-neutron coincidence technique.

As seen from Figure 6.2 which illustrates typical γ–β and γ–β–n time coincidence spectra, the β–γ coincidence window didn't exceed $\sim$0.5μs, whereas due to long neutron diffusion time (§3.5.3) the γ–β–n coincidence window was much higher - 128μs. The

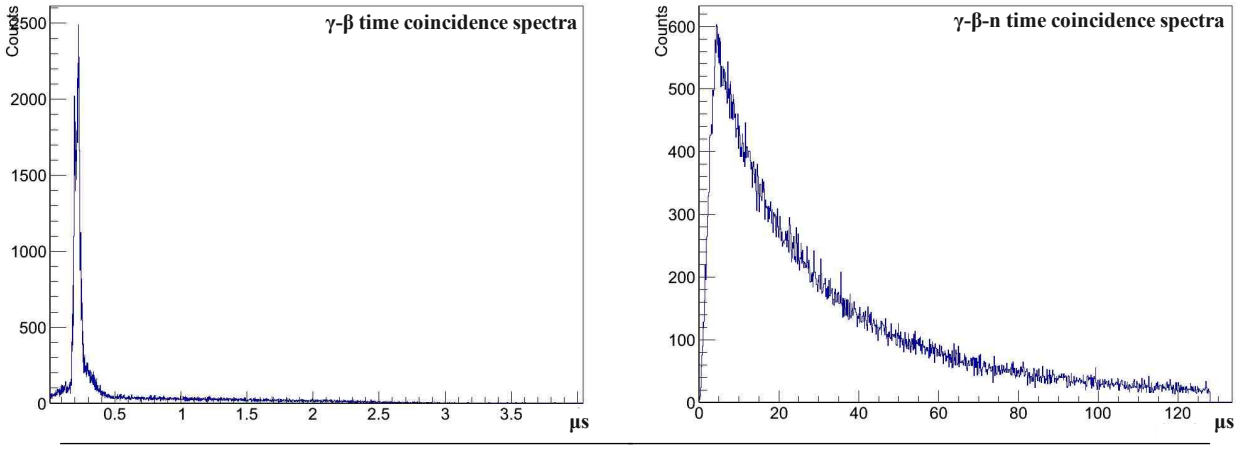

FIGURE 6.2: Typical γ–β (left) and γ–β–n (right) time coincidence spectra.

neutron gate, as it will be shown later, significantly clears up γ-β spectra suppressing γ-transitions irrelevant to the β-n branch. This is a very powerful tool for decay spectroscopy which significantly simplifies data analysis. Even immediately on-line an experimentalist can obtain rich information to correct a running experiment.

Random coincidence.

When calculating peak areas in $\gamma - \beta$ gated spectra random coincidence should be taken into account. They can be basically found by $r_{\gamma-\beta}[s^{-1}] = S_{\beta}^{peak}[s^{-1}] \cdot N_{\beta}[s^{-1}] \cdot T_{window}$[s], where T_{window} is a coincidence window, $r_{\gamma-\beta}$ - coincidence $\gamma - \beta$ counting rate, S_{β}^{peak} gamma-peak counting rate, N_{β} - β counting rate. Summing up for the time of measurements we obtained $R_{\gamma-\beta}$, which was typically as low as 0.1%.

In the same manner one can measure random coincidence in $\gamma - \beta - n$ gated spectra. In contrast to $\gamma - \beta$, due to larger neutron coincidence window (128μs) random coincidence at the level of 3-5% are more significant here.

6.4 Efficiency of beta and neutron detectors as a function of Q_β

Large Q_β values of isotopes of interest result in different energies for emitted betas and neutrons whose efficiency of registration can be different. It was considered therefore to measure efficiencies of beta ϵ_β and neutron ϵ_{TETRA} individually for each mass by γ spectra.

Assuming that a γ ray of a certain energy accompanies a β, the ratio of corresponding peak area in direct γ (S_γ) and $\gamma - \beta$ gated ($S_{\gamma\beta}$) spectra is ϵ_β. Considering dead time of beta D_β and gamma D_γ channels:

$$\epsilon_\beta = \frac{S_{\gamma\beta}(1-D_\gamma)}{S_\gamma(1-D_\gamma)\cdot(1-D_\beta)} = \frac{S_{\gamma\beta}}{S_\gamma\cdot(1-D_\beta)} \tag{6.11}$$

We consider the measured efficiency ϵ_β which is already linked to the dead time (D_β). To extract the real efficiency, ϵ^0_β, one should make a correction: $\epsilon^0_\beta = \epsilon_\beta \cdot (1 - D_\beta)$.

Analogously, if a γ ray accompanies a β and a neutron, the ratio of corresponding peak areas in $\gamma-\beta$ and $\gamma-\beta-n$ gated spectra is an efficiency of the neutron detector, ϵ_{TETRA}. The dead time for the neutron channel was negligible. Interestingly, ϵ_{TETRA} obtained by this method is higher ($\sim$ 62% for gallium isotopes measured) than the efficiency measured with the ^{252}Cf source ($\sim$ 52%), which emits prompt neutrons of average energy 2.1 MeV. The indirect evidence of a different neutron energy range is illustrated in Figure 6.3. It is clearly seen that the response of the inner layer of counters is significantly higher for β delayed neutrons of ^{84}Ga rather than for prompt fission neutrons of ^{252}Cf. Therefore, since β delayed neutrons are less energetic, the ϵ_{TETRA} should be a bit higher; and $\sim$ 62% seems quite reasonable. As follows from our MCNP simulations (see Figure 3.22, page 61) - the $\sim$ 62% efficiency would correspond to $\sim$0.5MeV neutron energy.

The obtained efficiencies of β and neutron registration (ϵ_β, ϵ_{TETRA}) by the γ coincidence spectra technique described above is given in Figures 6.4 for A = 82-83 (laser ion source) and in Figures 6.4 A = 123-128 (plasma ion source). The efficiencies can vary with a given decay depending on the state to which the decay goes. Therefore, for each mass the weighted average was used.

Note that in the second case it was impossible to determine ϵ_{TETRA} due to strong pollution came from β decay of isotopes in the isobaric chain also delivered with the beam. Moreover, ϵ_β is half compared to the laser ionized beam since, again due to isobaric pollution, the dead time of β and γ electronic channels became considerably higher (see §6.5).

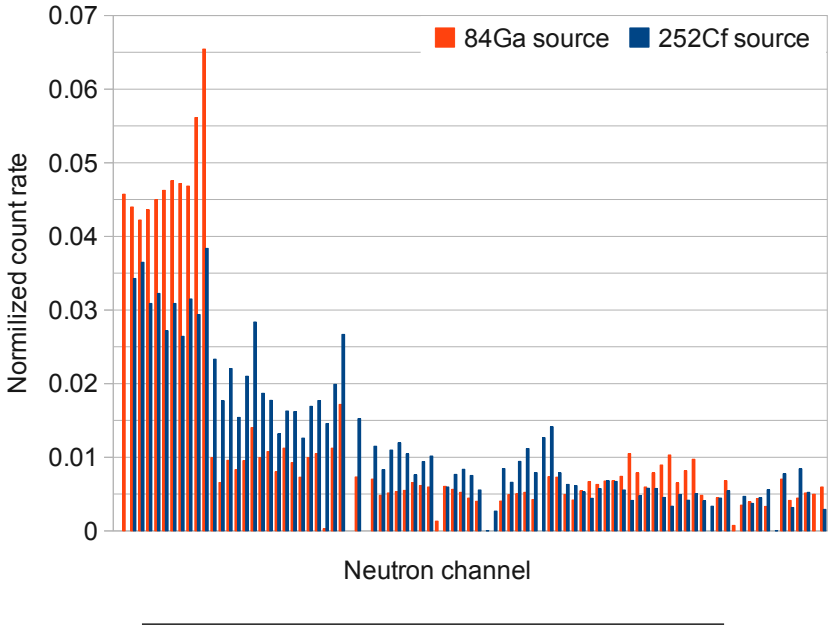

FIGURE 6.3: Normalized count rate in each channel for βd neutrons ^{84}Ga (in red) and prompt fission neutrons of ^{252}Cf (in blue).

6.5 Dead time correction

In the case of high count rate, the dead time of the data acquisition system can significantly influence the data. There is an internal function in the DMA system which allows monitoring the occupation fraction of each channel every 500 ms. A response from the channel means that it is not occupied at the moment. Whereas no-response interrogation happens when the channel is busy. Recorded number and time of no-responding requests represents the real dead time of a channel.

Dead time for plasma ionized beams, A = 123 - 128

Figure 6.5 illustrates, as an example, dead time of β(top) and γ(bottom) channels in experiments on a mass separated beam of A = 124. Due to high production rate of longer lived isobars average D_{β}^{dead}=$\sim$ 38% D_{γ}^{dead}=$\sim$ 30% were observed. At the same time the neutron counting rate was relatively low which resulted in negligible dead time ($<$ 0.01%). The same tendency was observed for each mass A = 123 - 128 studied. Since dead time fluctuates drastically during a cycle, I developed a special C++ code to reconstruct bin-by-bin the real count rate in β/γ channels.

Dead time on laser ionized beams, A = 82 - 84

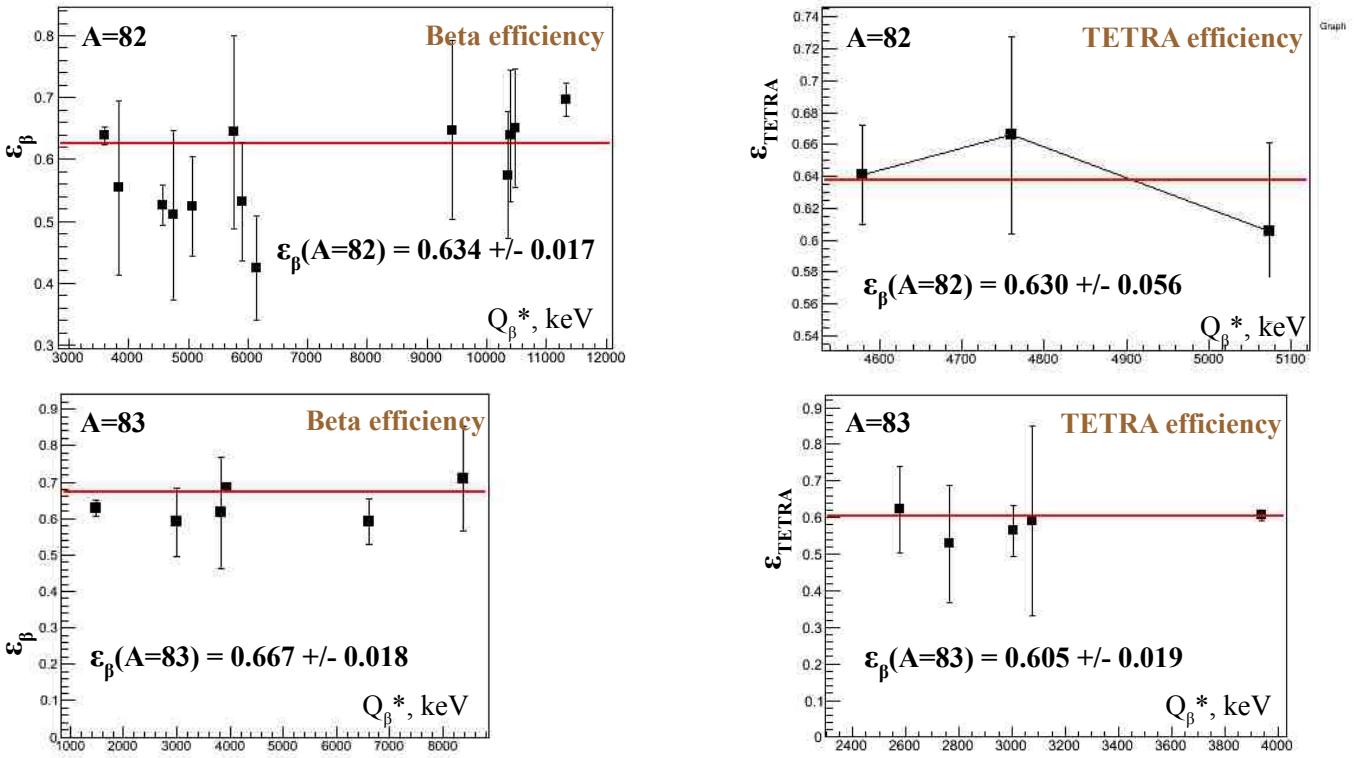

FIGURE 6.4: Efficiency of $4\pi\beta$ and TETRA detectors (for A=82-84) as a function of Q^*_β measured as described in the text Q^*_β is an energy difference to a given state.

In the experiment with laser ionized beams, dead time of the beta and gamma channels was below $< 1\%$ and was included in the final error bars for the results obtained.

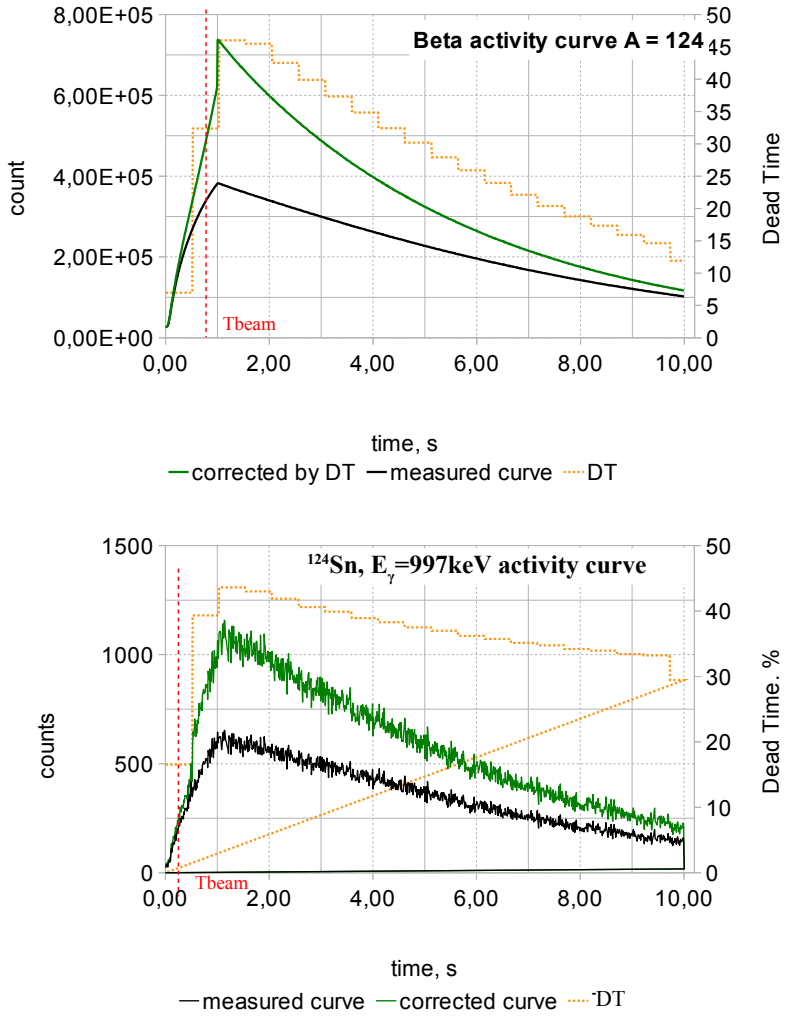

FIGURE 6.5: Dead time of β and γ channels, A = 124 in the grown-in and decay.

6.6 Experimental Results

There were two experiments performed at TETRA. The first one took place the last week of September 2012 with the plasma ion source on mass separated beams of A = 123 - 128 and was aimed at studying the β-decay of neutron rich silver isotopes. The second experiment was performed at the end of November 2012 with the laser ion source and was devoted to study of the β-decay of ^{82,83,84}Ga isotopes.

6.6.1 Results: A = 80

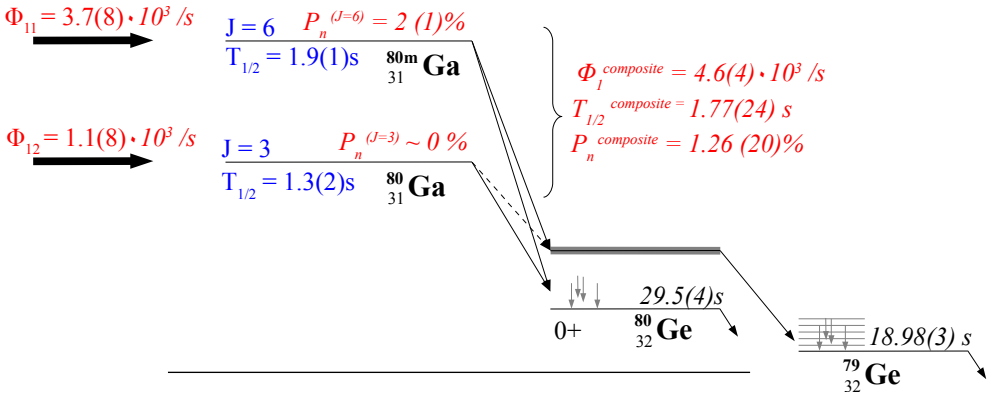

FIGURE 6.6: Decay scheme of ^{80}Ga. Data in black are from [115]. Half live and spin of the two isomers proposed by *Verney et al.* [118] in blue. Presently measured $T_{1/2}$ and P_n are in red.

As it was reported lately by our group, two isomeric states, the shorter lived (J = 3, $T_{1/2}^{J=3}$ = 1.3(2)s) and the longer lived (J = 6, $T_{1/2}^{J=6}$ = 1.9(2)s) in the ^{80}Ga [118] were found.The β decay chain of ^{80}Ga is presented schematically in the Figure 6.6. We collected statistics for ^{80}Ga simply in order to estimate the laser impact on the production rate (as it was shown previously in §4.2.4). β and neutron collection activity curves and γ radiation were measured within 2 seconds of collection time. Nevertheless, the statistics were enough to estimate the composite $P_n(^{80}\text{Ga})$ = 1.26(20)% and the composite production rate with the laser ion source at the level of Φ = 4600(400)/s. The solution of the system of Bateman equations (Equation 6.5) specified for the β-decay of ^{80}Ga with known half-lives from NNDC data (see Figure6.6) is displayed in the Figure 6.7. The red experimental points are reproduced by the calculated blue line with measured P_n and Φ. The contributions to the β-activity curve were due to the background (measured within 0.1s prior to ion collection) as well as β decay of ^{80}Ga (green curve) with the minor part from β-decay of its daughters (^{80}Ge, ^{80}As). Whereas all the neutron activity was assigned either to the background or to the β-n decay of ^{80}Ga. Figure 6.8 demonstrates verification of the results obtained by a ROOT fit analysis as explained in §6.2. In spite of the presence of two isomers the analysis to find P_n

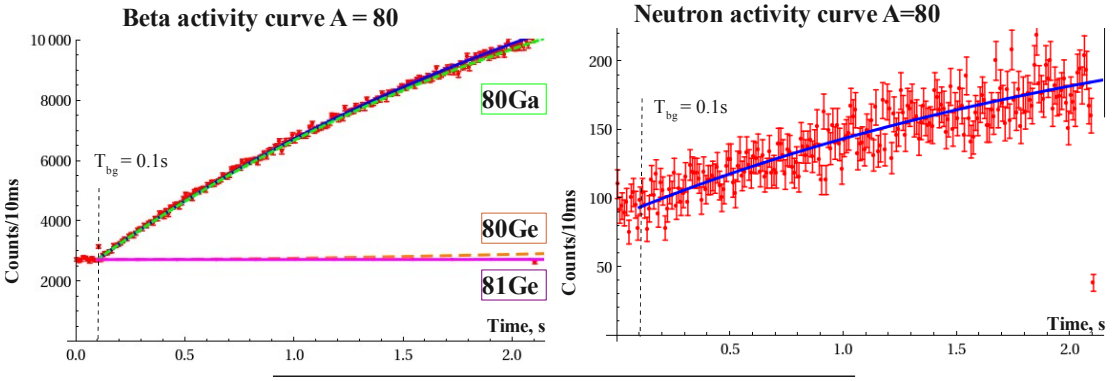

FIGURE 6.7: Beta (left) and neutron(right) activity curves, A = 80

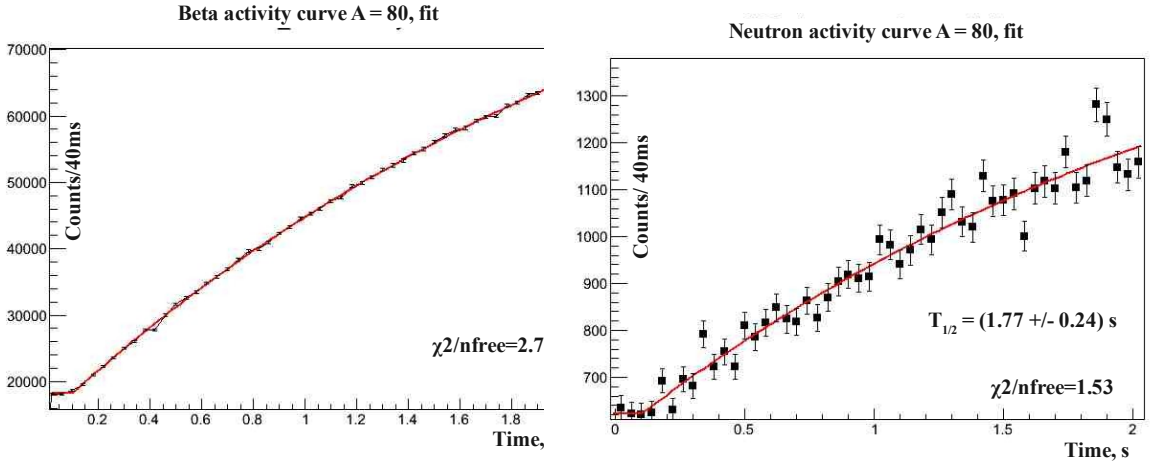

FIGURE 6.8: Beta (left) and neutron(right) activity curves, A = 80

was performed under the assumption that there is only one β-decaying state in ^{80}Ga with the $T_{1/2}^{neutron} = 1.77(24)$s directly estimated from the neutron activity curve (Figure 6.8). The fact that the measured $T_{1/2}^{neutron}$ is in between of half lives of both isomeric states makes us assume that both isomers are also β-decaying with neutron emission. However, it seems that the state J = 6 is a stronger neutron emitter since $T_{1/2}^{neutron}$ is closer to $T_{1/2}^{J=6}$ Figure 6.9. Determination of $T_{1/2}^{\beta} = 1.62(13)$s by β activity depends on precision of the measurements of P_n as well as half lives of other nuclei participating in the β-chain. Such $T_{1/2}^{\beta}$, which coincide with the one from NNDC, shows the mix between betas emitted by the two isomeric states. Therefore, the P_n and Φ measured are the average between the J = 3 and J = 6 states.

In order to estimate independent production rates ($\Phi^{J=3}$, $\Phi^{J=6}$) and independent probability of βd neutron emission ($P_n^{J=3}$, $P_n^{J=6}$) for the states J = 3 and J = 6, where half lifes were adopted from *Verney et al.* [118], we modified appropriately the Bateman system (Equation 6.5). Then we solved the Equation 6.9 under the condition:

$$\Phi = \Phi^{J=3} + \Phi^{J=6}$$

$$P_n = P_n^{J=3} + P_n^{J=6},$$

where Φ=4600(400)/s and P_n=1.26(2)% are the composite production rate and neutron emission probability found previously. It came out that the J=3 state ($\Phi^{J=3}$=1100(800)/s) is less produced at ALTO in comparison to the J=6 state ($\Phi^{J=6}$=3600(800)/s) which corresponds to original assumptions of *Verney et al.*. At the same time the independent $P_n^{J=3}$ ≈0 and $P_n^{J=6}$=2(1)% were determined. Therefore, we considered that these measurements give a strong experimental suggestion that there was only one βd neutron emitting isomer in ^{80}Ga. Furthermore, $P_n^{composite}$ obtained presently, which overestimates other measurements, Figure 6.10, can be explained that in previous works (such as *Hoff and Fogelberg* [119]) the J = 3 isomer had a higher production rate which resulted in a lower P_n value. Unfortunately, low statistics didn't allow us to propose branching ratios for the β-decay. Obviously, the I_β known previously [115, 119] are not valid anym---

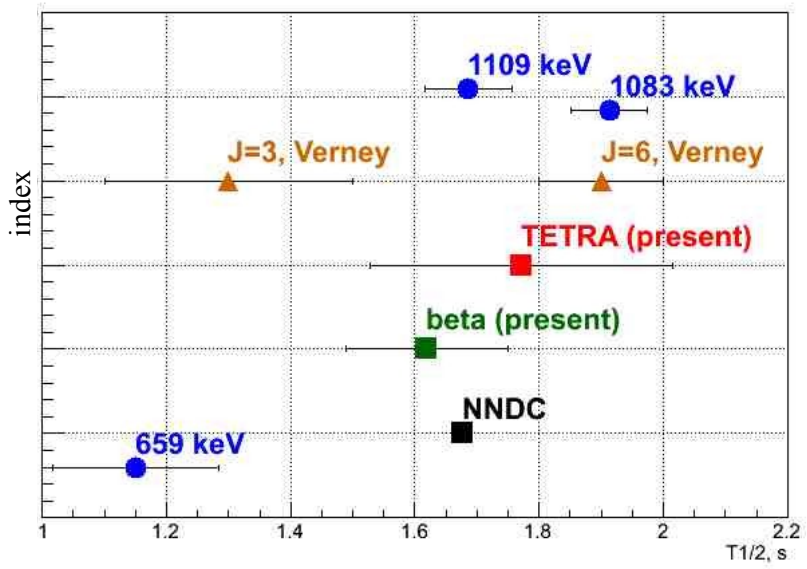

FIGURE 6.9: $T_{1/2}$ for ^{80}Ga. Measured presently: blue points by γ transitions, (Figure 6.11), green by β activity curve and red - by neutron activity. Yellow - two isomeric states proposed by *Verney et al.* [118]. In black the currently adopted value by NNDC [115].

In Figure 6.12 is presented a γ spectrum gated by β for the mass A=80. Most of the peaks were attributed to activity of ^{80,80m}Ga, ^{80}Ge, ^{80}As. The most strongly fed γ transitions in the decay of ^{80,80m}Ga connect the two decays schemes [118]. A comparison of I_γ measured in the present work to *Hoff and Fogelberg* [119] and to *Verney et al.* [118], Table 6.1, confirmed the different isomeric ratio in our experiments at ALTO (via photofission of ^{238}U) and the one of *Hoff and Fogelberg* [119] (thermal neutron induced fission of ^{235}U). The difference in the fission process explains the fluctuation in the

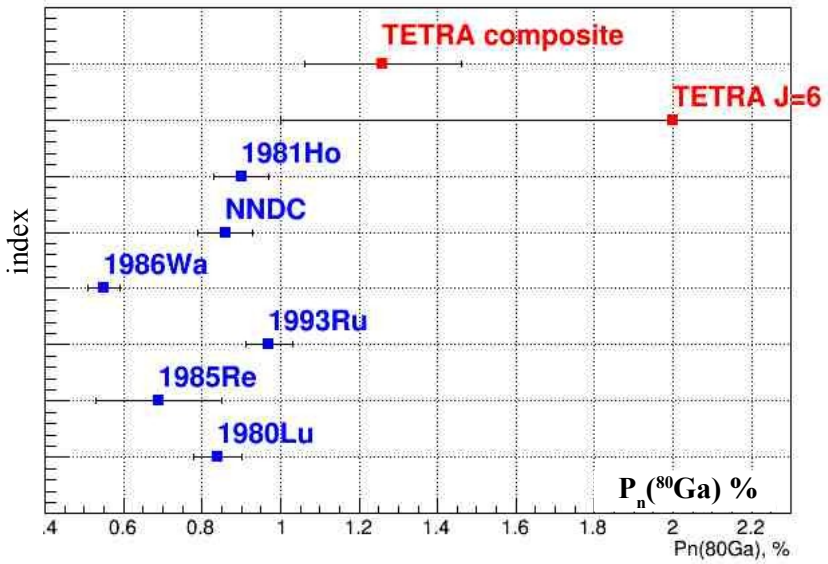

FIGURE 6.10: P_n of ^{80}Ga, Measured presently: *TETRA composite* - attributing neutron activity to the state J=3 and J-6, T*ETRA J=6* to the state J=6 only; blue points by γ transitions (Figure 6.28), green by β activity curve and red - by neutron activity; *1993Ru* - [120]; *1985Re* - [121]; *1986Wa* - [122]; *1980Lu* - [123]; *1981Ho* - [75]; NNDC - NNDC weighted average [115].

isomeric ratio. The only reported γ-transition [124] (E_γ = 204 keV) corresponding to β-n decay was not observed owing, probably, to weak statistics.

TABLE 6.1: ^{80}Ge relative intensities

Eγ	*present*		*Verney et al.* [118]		*Hoff et al.* [119]	
keV	Iγ	dI$^{abs}\gamma$	Iγ	dIγ^{abs}	Iγ	dIγ^{abs}
523.451	13.07	4.01	12.9	0.4	11.7	0.2
659.34	100	31.5	100	3	100	100
1083.519	70.35	27.20	62	2	67.40	0.1
1109.421	30.1	12.3	23.8	0.8	28.1	0.5
1573.25	3.72	0.92	4.4	0.2	4.2	0.2

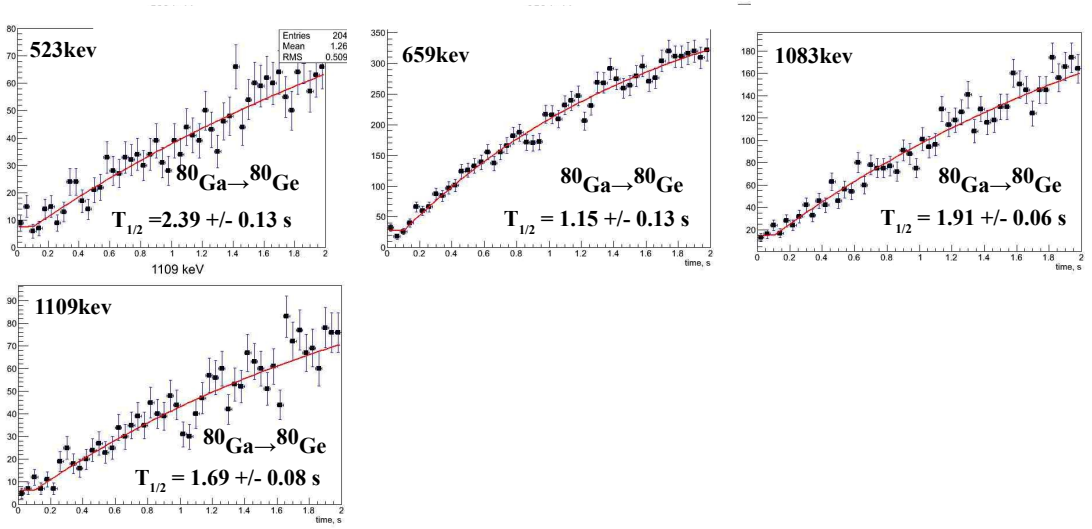

FIGURE 6.11: Half live of isotopes for ^{80}Ga decay chain.

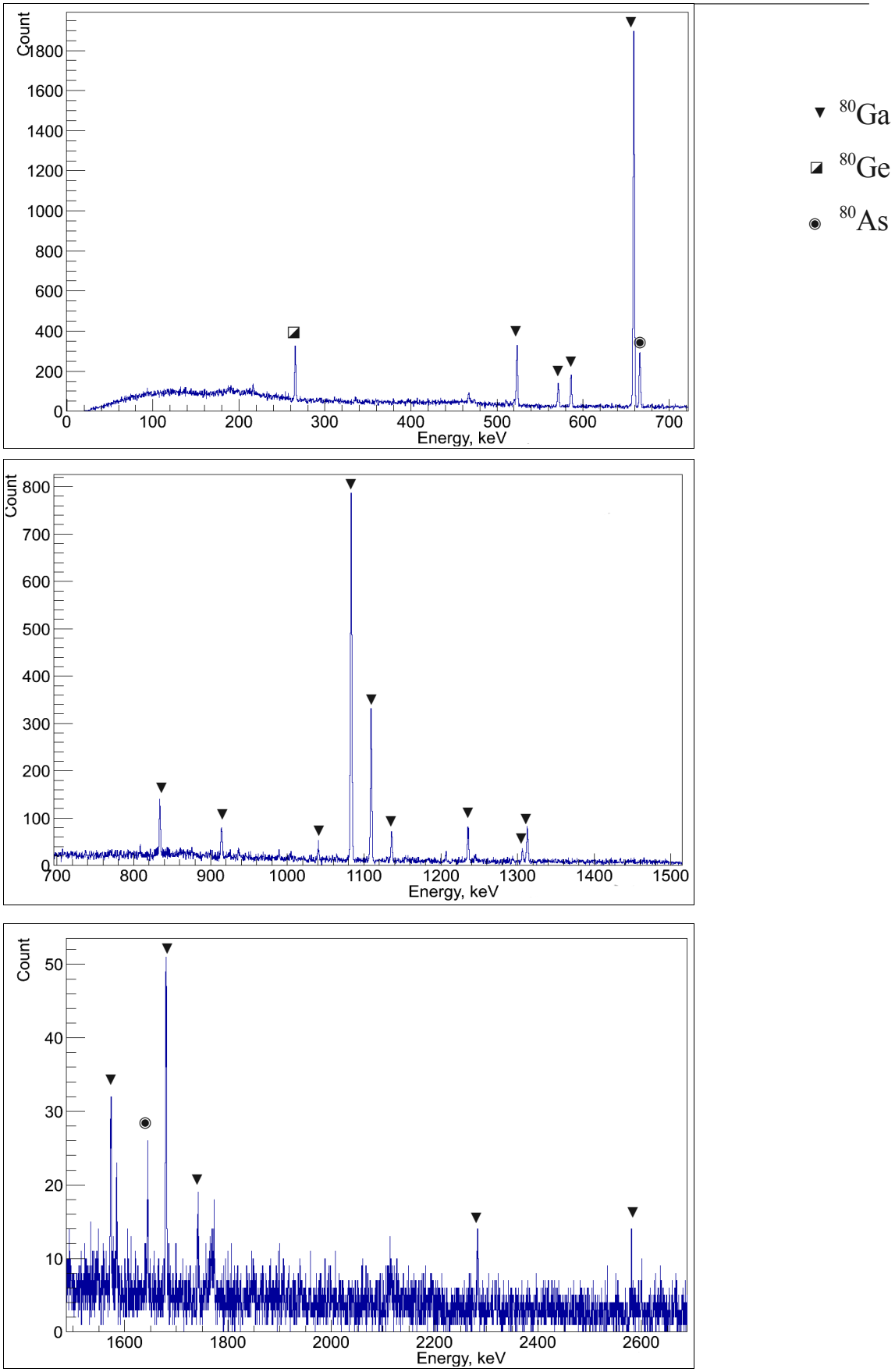

FIGURE 6.12: Measured γ-β (in blue) spectra for mass A=80.

6.6.2 Results: A = 82

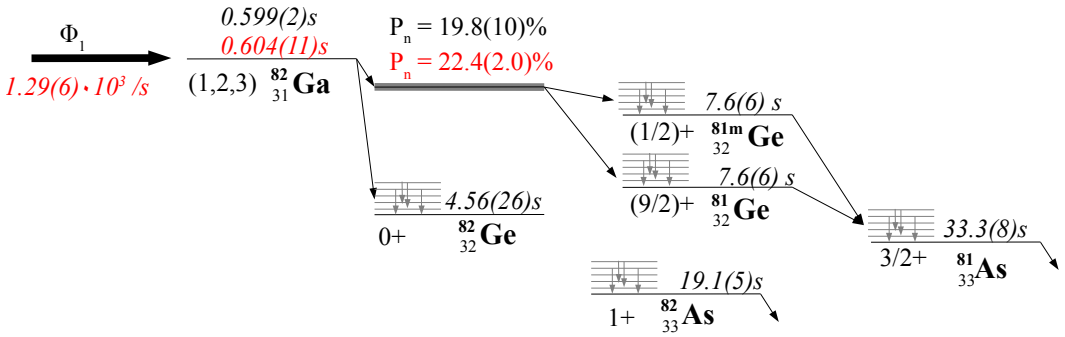

FIGURE 6.13: Decay scheme of ^{82}Ga. Data in black were taken from [115]. In red: measured in the present experiment ($T_{1/2}$ with neutron activity curve).

The β decay chain of ^{82}Ga is presented schematically in the Figure 6.13. As for the previous mass, we collected statistics for ^{82}Ga to verify the efficiency of the laser source. However, the collected data were enough to determine $P_n(^{82}\text{Ga})$=(22.4(2.0)% and $\Phi(^{82}\text{Ga})$=(1290±60)/s. The solution of the system of Bateman equations (Equation 6.5) specified for the β-decay of ^{82}Ga is displayed in the Figure 6.14. The red experimental points are reproduced by the calculated blue line with the measured P_n and Φ. The contributions to the β-activity curve were due to the background (measured within 0.1s each cycle) as well as β decay of ^{82}Ga (green curve) and β-decay of its daughters (^{82}Ge, ^{82}As, ^{81}Ge). Whereas all the neutron activity was assigned either to the background or to the β-n decay of ^{82}Ga. Figure 6.15, demonstrates verification of the results obtained by a ROOT fit analysis as explained in §6.2. Measured $P_n(^{82}\text{Ga})$ is in good agreement with the previously known, Figure 6.16.

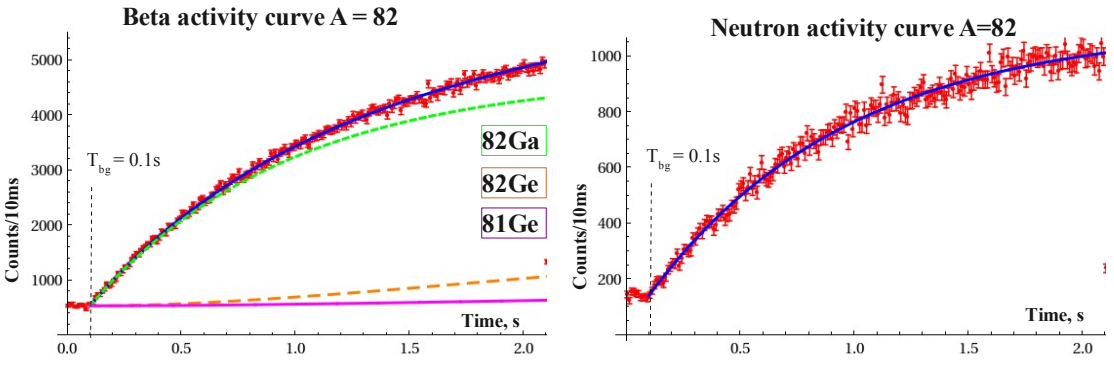

FIGURE 6.14: Beta (left) and neutron(right) activity curves, A = 82

In the Figure 6.17 is presented a γ-ray spectrum gated by β and a γ-ray spectrum gated by β and by neutrons for mass A=82. Most of the peaks were attributed to activity of

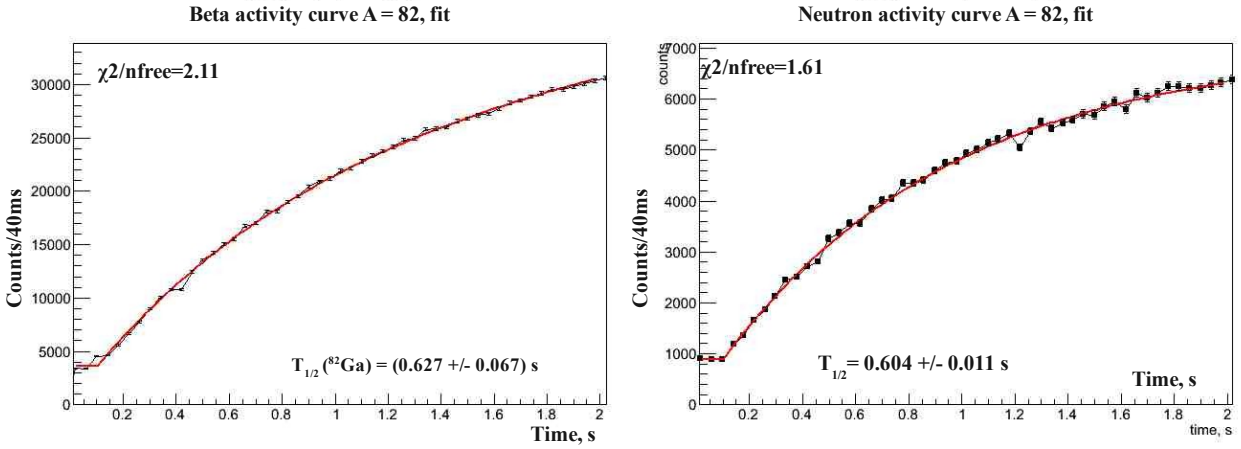

FIGURE 6.15: Beta (left) and neutron(right) activity curves, A = 82

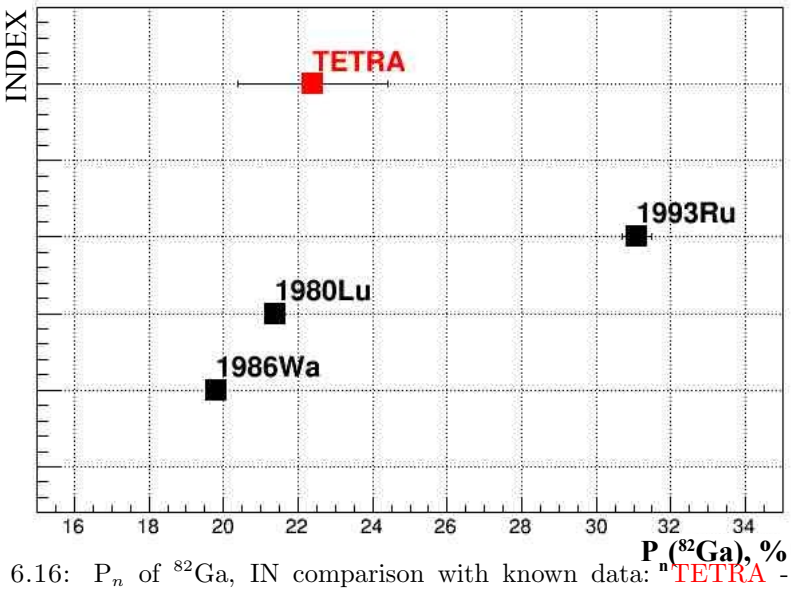

FIGURE 6.16: P_n of ^{82}Ga, IN comparison with known data: TETRA - presently measured; *1993Ru* - [120]; *1986Wa* - [122]; *1980Lu* - [123].

^{82}Ga, ^{82}Ge, ^{82}As and ^{82}Se. Only γ-rays corresponding to transitions in ^{81}Ge are visible in the β–n gated spectrum.

Determination of $T_{1/2}$.

$T_{1/2}^{neutron}(^{82}\text{Ga}) = 0.604(11)$s was determined directly from the neutron activity curve, Figure 6.15,and from from the β activity curve $T_{1/2}^{\beta}(^{82}\text{Ga}) = 0.63(7)$s.

In Figure 6.18 is shown the results of determination of the half life of ^{82}Ga by γ-ray transitions in ^{82}Ge, ^{81}Ge and by neutron/beta activity curves. All the neutrons registered were attributed to ^{82}Ga since in its isobaric chain it is the only neutron emitter. $T_{1/2}^{neutron}$ is the most precise in comparing to the value measured from the β curve and

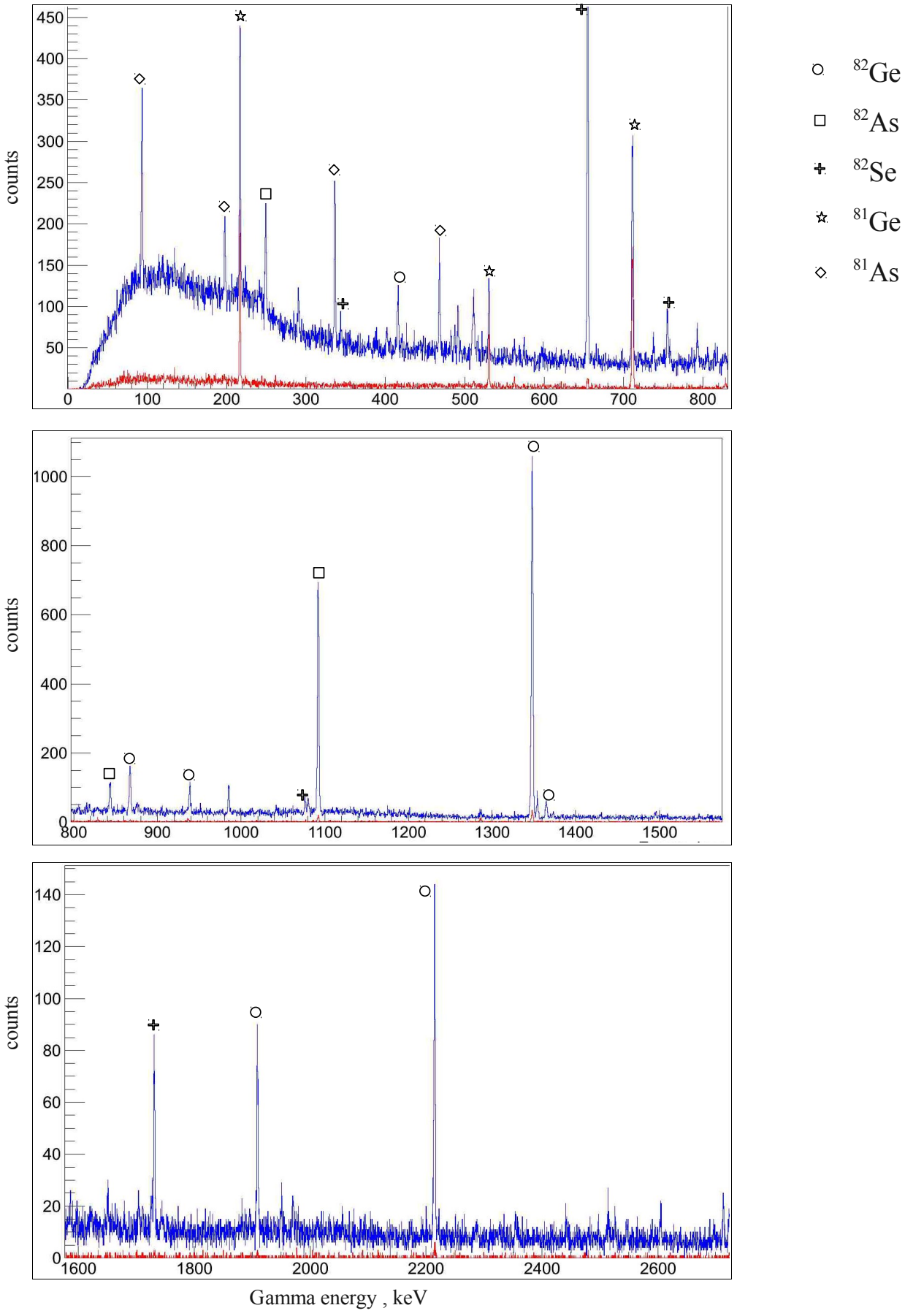

FIGURE 6.17: Measured γ-β gated (in blue) and γ-β-n gated (in red) spectra for mass A=82. The marked lines belong to transitions in the daughter nuclei.

even to the most intense γ-ray transition, 1348keV. It coincides well with the currently adopted by the NNDC evaluator value of 0.599(2)s measured by *K.L. Kratz et al.* by the same method with ^{3}He counters [125]. The smaller error bars might be explained by better statistics.

The compatible $T_{1/2}$ and P_n to the accepted values proved the workability of the detection system and the method of analysis. Then we could proceed further to investigation of more neutron rich nuclei.

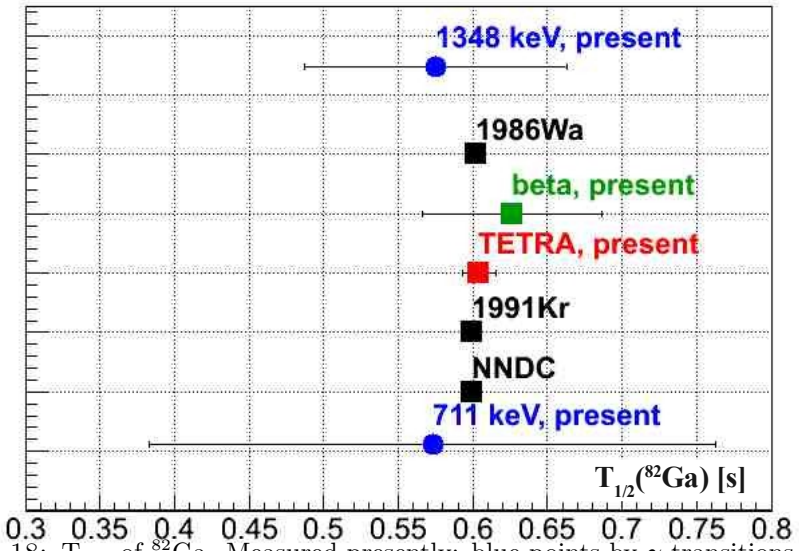

FIGURE 6.18: $T_{1/2}$ of ^{82}Ga. Measured presently: blue points by γ transitions (Figure 6.19), green by β activity curve and TETRA - by neutron activity. In black the currently adopted value by NNDC [115] and from other works: *1986Wa* - [122]; *1991Kr* - [125].

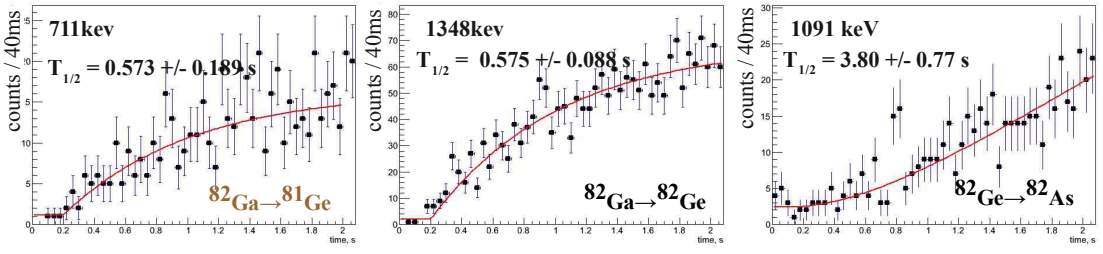

FIGURE 6.19: Half live of isotopes for ^{82}Ga decay chain.

Decay of ^{82}Ga and level scheme of ^{82}Ge.

In the most recent studies of the level scheme of ^{82}Ge performed at ALTO in the thesis of *Tastet* [97] via β-decay of ^{82}Ga the level scheme proposed by *Hoff and Fogelberg* [119] was confirmed. In addition, he extended the level scheme by levels at 2726keV and 2779keV. He also confirmed two transitions at 1348keV and 1365keV observed by *Winger et al.* [27]. In contrast, *Tastet* didn't confirm the 1176keV γ-ray in coincidence with the most intense 1348keV proposed [27]. Eventually, *Tastet* couldn't observe 728keV and 596keV which were absent in his γ spectra gated by β.

In my experiments I was lucky enough to study the level scheme of ^{82}Ge by both β decay of ^{82}Ga, as *Tastet*, and by β-n decay of ^{83}Ga, as done by *Winger et al.*. Even though I was not able to observe γ–γ coincidences I was the first who obtained γ–β-n coincides which gave direct evidence for γ-transitions corresponding to the β-n channel.

The observed γ-transitions with relative (to 1348 keV) intensities measured are presented in the level scheme taken from [115] in Figure 6.20. Neither 564keV, 596keV, 727keV, 1378 keV proposed by *Tastet* and *Winger et al.* were observed. This might be due to relatively low statistics. However, I was able to evaluate the ^{82}Ge ground state direct feeding and to propose the branching ratio of for β decay (I_β, *logft*).

Decay of ^{82}Ga and level scheme of ^{81}Ge.

There are two isomers in ^{81}Ge with similar half-lives (about ~7.6s) and a large difference in spin (Figure 6.20) [119]. Since the lowest states in ^{81}As are (1/2-) and (3/2-), they are fed directly by allowed β-decay transitions from the low spin isomer of the mother nucleus ^{81}Ge. It is possible, that higher lying states are fed from the decay of the (9/2+) level of ^{81}Ge [126]. In [119] *P.Hoff and Fogelberg* identified three gamma rays corresponding to the $\beta - n$ decay of ^{82}Ga: 216keV, 530keV and 711keV. Later, in the thesis by *B.Tastet* at ALTO [97] in a $\gamma - \gamma$ experiment, another four lines were observed (marked by „*" in Figure 6.20).

Implementation of the neutron coincidence technique in my experiments and clear observation of $\gamma - \beta - n-$ coincidence spectra not only confirmed all the γ-rays proposed before, but revealed one possible level and two γ-transitions observed before only in $^{81}Ga \xrightarrow{\beta-} {}^{81}Ge$ decay [127], Table 6.2. Unfortunately, due to low statistics, I was not able to measure population for the $(1/2^+)$ and $(9/2^+)$ states individually. Otherwise it could be possible to estimate their relative population from their β-decay and γ transitions in ^{81}As. The total absolute I_β going to both was found to be about 7.5%.

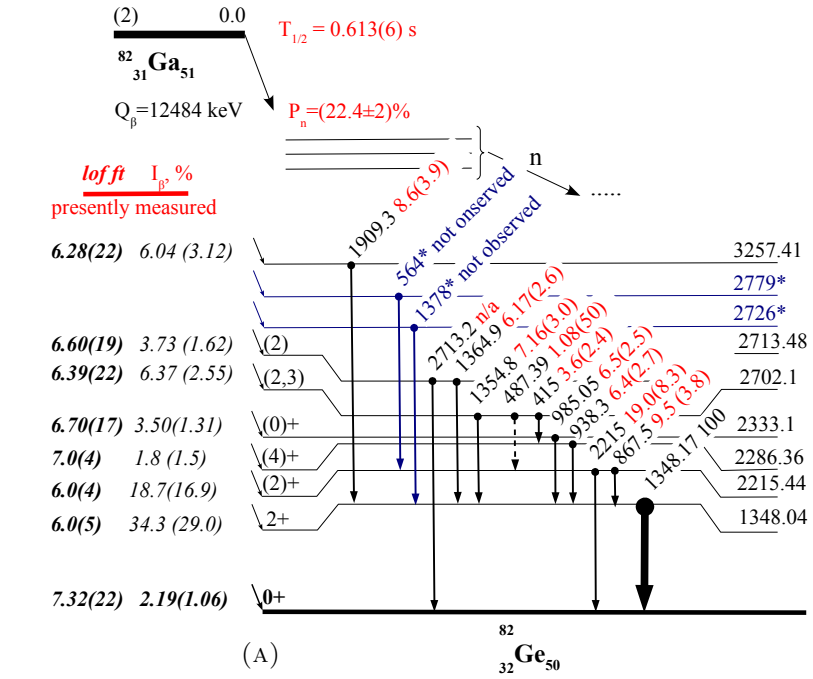

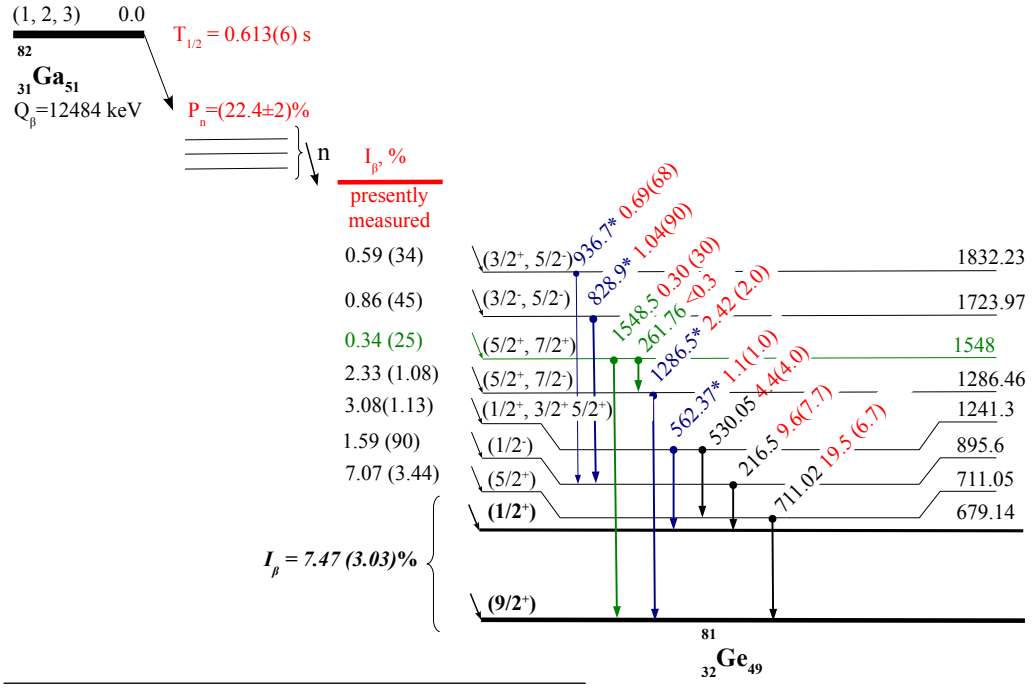

FIGURE 6.20: Top: ^{82}Ga beta decay level scheme. Lines (black) are from [119], the blues lines also marked by ,,*" are from [97]. I_γ and I_β are from the present measurements. Bottom: ^{81}Ga β decay level scheme. Three original lines (black) are from [119], the blues lines also marked by ,,*" are from [97]. In green are the γ-transitions and the level proposed in the current experiment. I_γ and I_β were also measured.

		Hoff and Fogelberg [119]	*Tastet*(**) [97]	**This work**
E_γ keV	E_level keV	**82Ga b-n** I_γ	**82Ga b-n** I_γ	**82Ga b-n** I_γ
711	711	16	100	19.5(6.7)
216	895	6.50	48(3)	9.6(7.7)
530	1241	2.30	27(2)	4.4(4.0)
562	1241	-	6(1)	1.1(1)
1286	1286	-	yes	2.42(2.0)
828	1723	-	yes	1.04(0.9)
936	1832	-	yes	0.69(68)
261*	1548	-	-	<0.3
1548*	1548	-	-	0.3

TABLE 6.2: Summary of γ-ray lines observed in decay of ^{81}Ge studied by ^{82}Ga$\rightarrow^{81}$Ge in the present work in comparison to previous experiments, (*) - newly observed; (**) - not normalized

Decay of ^{82}Ge and level scheme of ^{82}As.

Even after being investigated a few times [119, 128, 129], the level scheme of ^{82}As is still missing some important data. There are two isomeric states (2^-) and (5^-) for which the relative position is not well determined. Only the (2^-) state is presumably populated in β-decay of ^{82}Ge.

In the β-decay study of ^{82}Ge two states (843 and 1092keV) were proposed firmly with indications of a third state at 952 keV [119]. However, *B. Tastet* [97] indicated that the 952 kev transition should be situated above the 1092keV level (Figure 6.21). Additionally he didn't confirm the 139 keV transitions reported by *Hoff and Fogelberg* and observed evidence for another transition of 1198 keV depopulating along with the 952keV transition from a level at 2043keV. The proposed level scheme by *B. Tastet* scheme is shown in Figure 6.21.

We studied ^{82}Ge$\rightarrow^{82}$As in two experiments obtaining ^{82}Ge as a β-decay daughter of ^{82}Ga and a β-n decay daughter of ^{83}Ga. In both experiments three transition (249 keV, 843keV, 1092keV) reported previously were observed with relative intensities measured coinciding well with the earlier data shown in Figure 6.21.

The absolute intensity of the β decay was measured by *Hoff and Fogelberg* who proposed assigning spin 1^+ to the levels at 843keV and 1092keV; and spin 2^- to the ground state. Thus, since the ground state ^{82}Ge is 0^+ *Hoff et al.* assumed no direct ground state transition to ^{82}As [119]. The absolute branching ratio measured by *Hoff and Fogelberg* under this assumption is illustrated in the Figure 6.21. However, the NNDC didn't adopt his value since *Kratz et al.* studying the decay of ^{82}Se attributed spin 1^+ to the ^{82}As ground state [128]. Whereas in more recent experiments to investigate properties of ^{82}As, *Gausemel et al.* proposed spin 2^- to the ^{82}As ground state confirming therefore the original assumption of *Hoff and Fogelberg* of no direct ground state feeding [129]. In both our experiments we clearly observed significant population to the level at 1092keV with completely suppressed direct transitions to the ground state. As a result we tend to confirm the spin 2^- to ^{82}As ground state.

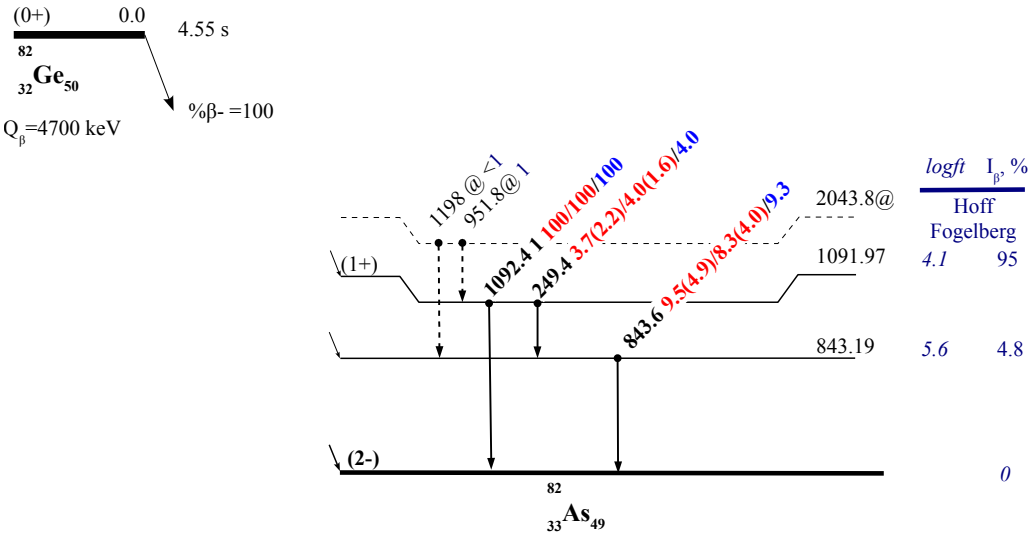

FIGURE 6.21: ^{82}Ge beta decay level scheme. Two levels and three gamma rays established firmly in [97, 119] are in solid lines. The presumable assumptions of position of the third excited state with corresponded transitions are in dashed line, „@" from [97]. I_γ, I_β and *logft* measured in [119] assuming no ground state β branch are in blue; I_γ measured presently in red: first experiment (with ^{82}Ga beam)/second experiment (with ^{83}Ga beam) - see text for details

6.6.3 Results: A = 83

The structure ^{83}Ge has been intensively studied recently at HRIBF via the reaction ^{2}H(^{82}Ge,p)^{83}Ge [130, 131] and recently by β-decay of ^{83,84}Ga produced in proton induced fission of ^{238}U [27]; and at ALTO by neutron induced fission [25] and later by photo induced fission of ^{238}U [29, 97, 132]. This allowed us to establish and scrutinize the decay scheme as well as to extend the level systematics for the N=51 isotones.

In spite of these efforts, the P_n-value obtained in different experiments is still quite contradictory and ranged from ∼15% [120] to ∼60% [133]. In some works a neutron ^{3}He-filled detector was employed (for example [120, 122, 123]), in others ion-tagged γ-ray spectra were used [27, 133]. However, in the latter, due to lack of measurements of absolute branching ratios (in A=83 decay chain), the authors admitted that P_n obtained depended on their estimations of I_β which had to be verified independently. From the theory side, the predicted P_n(^{83}Ga) is also varied a lot: from almost 100% in *Moller, Nix and Kratz* [8] to 15% with first forbidden transitions taken into account by *Borzov* [8].

The β decay chain of ^{83}Ga is presented schematically in the Figure 6.22. We measured neutron and beta activity simultaneously within 3s of beam time and 2s of decay. P_n(^{82}Ga)=84.8(3.6)% and Φ(^{82}Ga)=(370±10)/s were determined as a solution of the system of Bateman equations (Equation 6.5) specified for the β-decay of ^{83}Ga and displayed in the Figure 6.23. The red experimental points are reproduced by the calculated blue line with the measured P_n and Φ. The contributions to the β-activity curve were due to the background (measured within 0.1s each cycle) as well as β decay of ^{83}Ga (green curve) and β-decay of its daughters (^{83}Ge, ^{83}As, ^{82}Ge). Whereas all the neutron activity was assigned either to the background or to the β-n decay of ^{83}Ga. Figure 6.24 demonstrates verification of the results obtained by a ROOT fit analysis as explained in §6.2.

The fact is that the reproduced β-activity curve (in blue, in Figure 6.23) slightly underestimates the experimental points during the beam time and overestimate during the decay suggest at least one of the periods (^{83}Ge, ^{82}Ge) was wrong or an unrecognized shorter lived β-source was accumulated with the beam, which, though, doesn't manifest itself somehow in the measured γ-spectra (Figure 6.25). We tried to solve the Bateman equations within time intervals (0.1 - 0.5)s and (3.1 - 3.5)s where the experimental data are reproduced well. The obtained production rate and P_n were the same as the ones obtained above in solution of the Bateman equations for the complete interval (0.1-5.1)s. Therefore, we came to the conclusion that even if there is an unknown source or incorrect $T_{1/2}$ it didn't influence considerably the final results. The adopted value

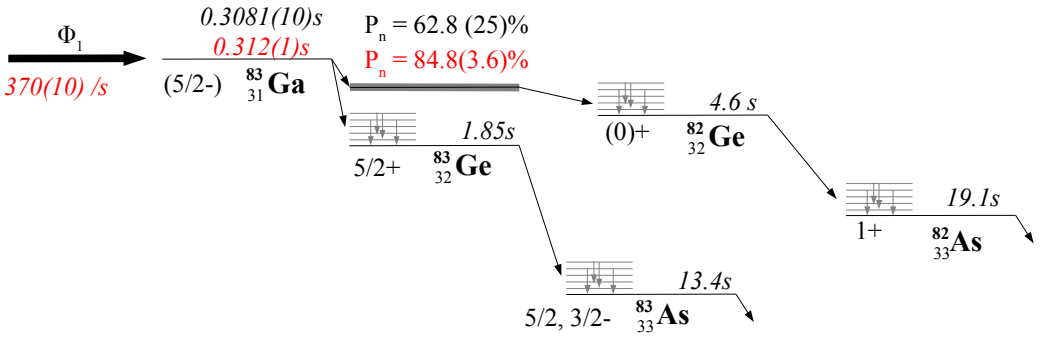

FIGURE 6.22: Decay scheme of ^{83}Ga. Data in black were taken from [115]. In red: measured in the present experiment ($T_{1/2}$ with neutron activity curve).

$P_n(^{82}Ga)$=84.8(3.6)% is different from the ones measured before Figure 6.26. The discrepancy of the experimental data might be due to a presence of an isomeric state whose production rate is different from facility to facility.

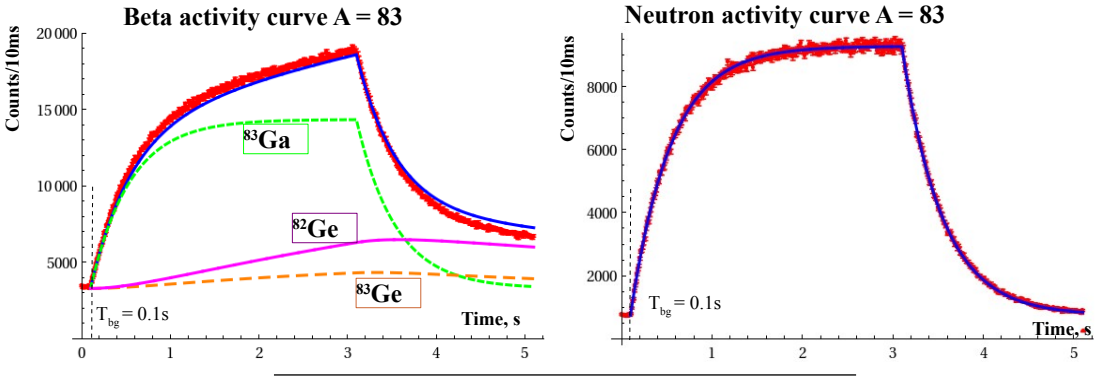

FIGURE 6.23: Reproduced beta (left) and neutron(right) activity curves in comparison to measured ones, A = 83

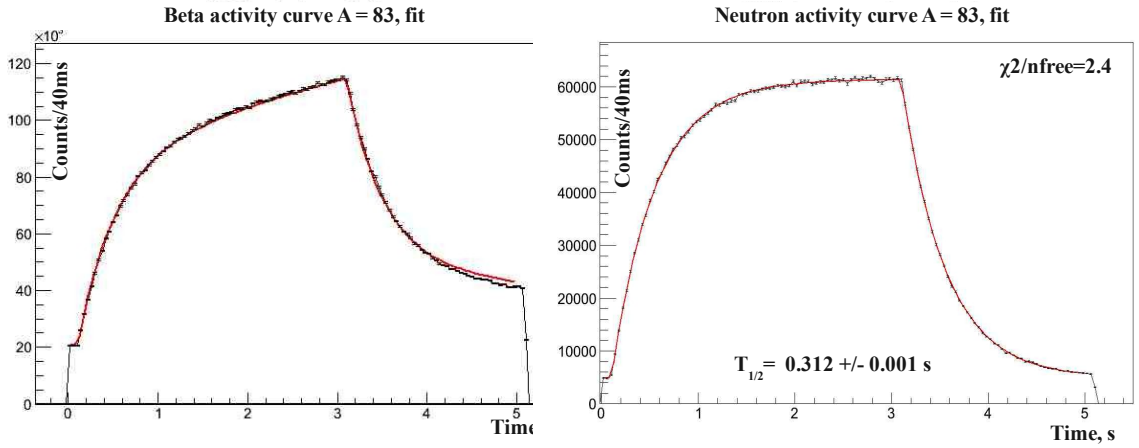

FIGURE 6.24: Fitted beta (left) and neutron(right) activity curves, A = 83

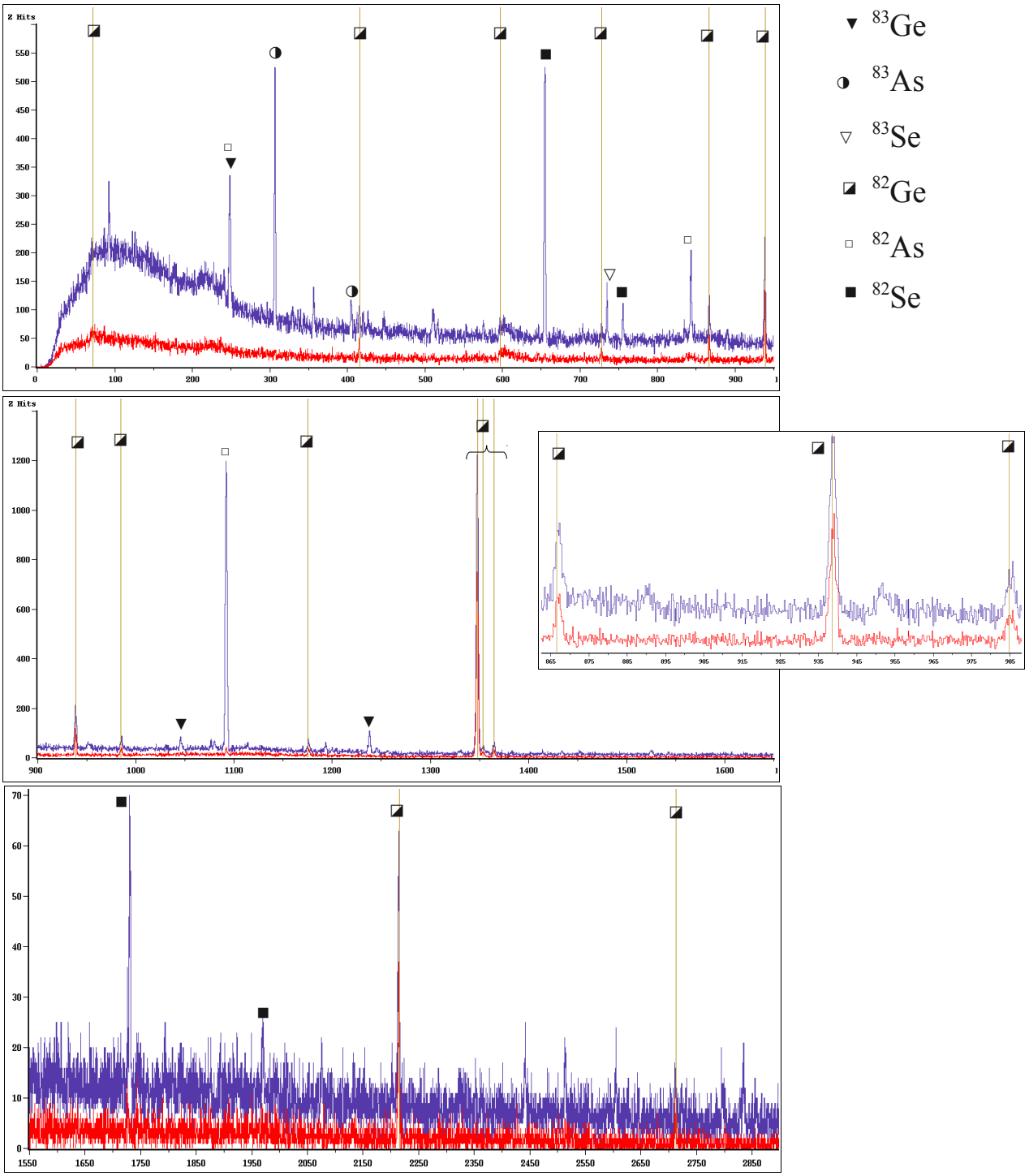

FIGURE 6.25: Measured γ-β,gated (in blue) and γ-β-n gated (in red) spectra for mass A=83. The marked lines belong to transitions in daughter nuclei.

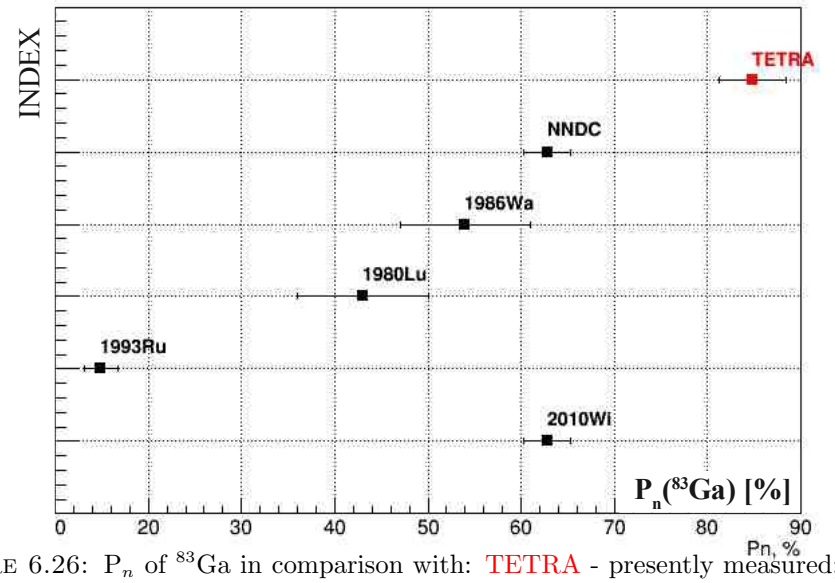

FIGURE 6.26: P_n of ^{83}Ga in comparison with: TETRA - presently measured; NNDC - adopted by NNDC [115]; *2010Wi* - [27]; *1993Ru* - [120]; *1986Wa* - [122]; *1980Lu* - [123]; the weighted average is from NNDC.

Determination of $T_{1/2}$ A = 83

In contrast, the neutron activity curve seems to be described quite well with the P_n and Φ found showing the $T_{1/2}^{neutron}(^{83}Ga)$=312(1)ms. As shown in Figure 6.27, comparing half lives determined by transitions recorded in γ spectra and the β activity curve, the $T_{1/2}^{neutron}$ is the most precise since it doesn't depend either on γ-peak area nor half-lives of daughter β-decaying isotopes. The NNDC evaluator recognize $T_{1/2}^{NNDC}(^{83}Ga)$=308(1)ms measured by delayed neutrons as the most precise. Though, the weighted average from numerous experiments to study beta delayed neutrons is $T_{1/2}^{avr}(^{83}Ga)$=317(17)ms. Therefore, our adopted $T_{1/2}^{neutron}(^{83}Ga)$=311.2(5)ms (measured by the neutron activity) which agrees well with previous measurements and is the most precise. The bigger errors in other experiments might be explained by lower statistic, which in fact could have also originated due to lower efficiency of the neutron detectors used.

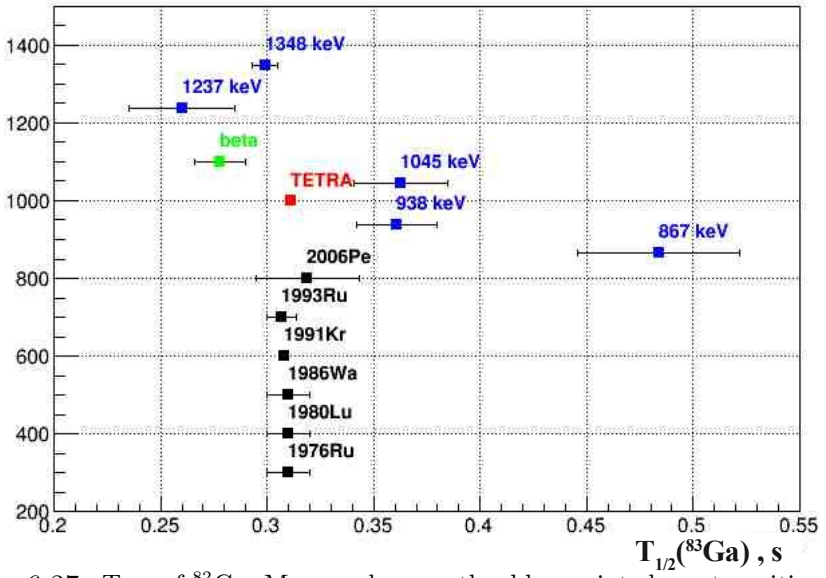

FIGURE 6.27: $T_{1/2}$ of ^{82}Ga, Measured presently: blue points by γ transitions (Figure 6.28), green by β activity curve and TETRA - by neutron activity; *2006Pe* - [25]; *1993Ru* - [120]; *1991Kr* - [125]; *1986Wa* - [122]; *1980Lu* - [123]; *1976Ru* - [134]; the weighted average is from NNDC.

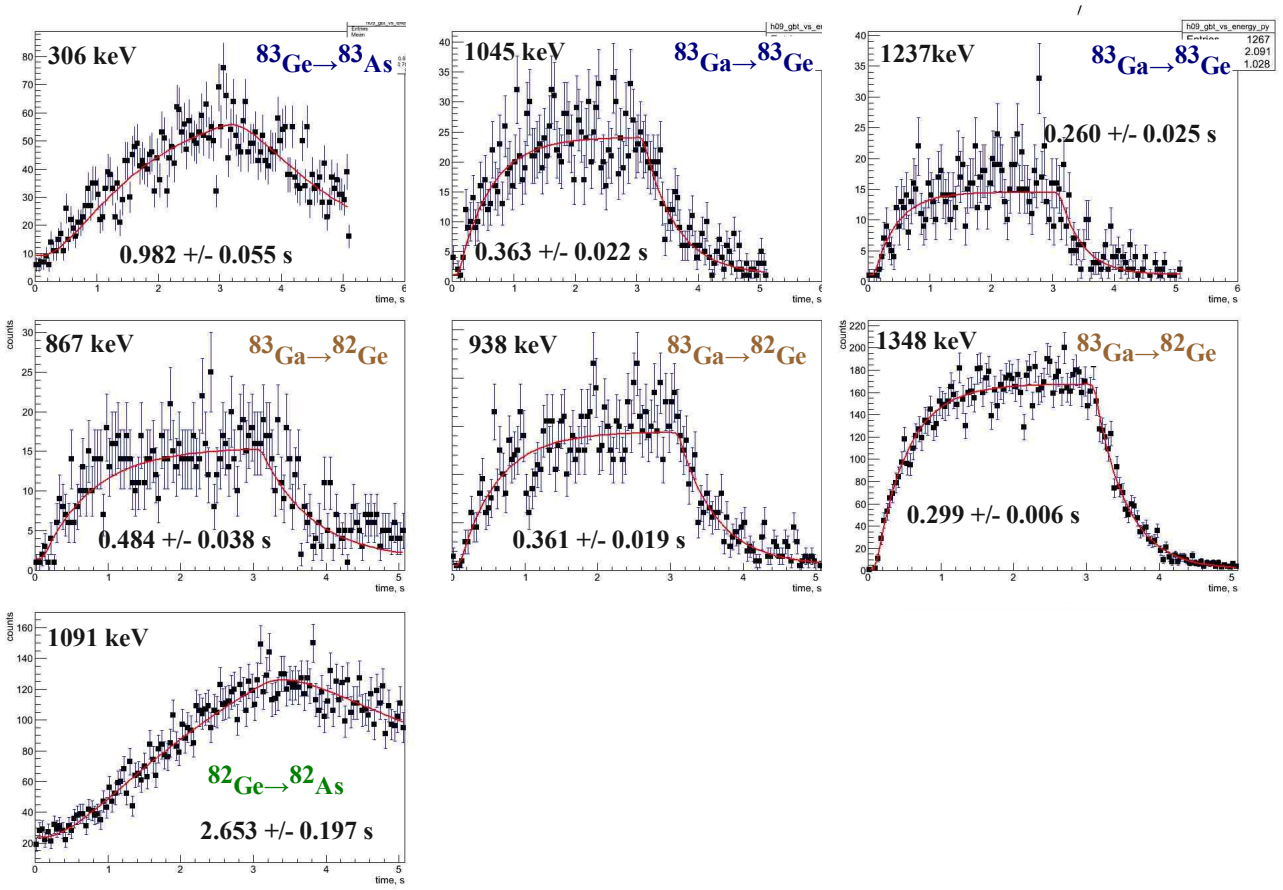

FIGURE 6.28: Half live of isotopes for ^{83}Ga decay chain.

Decay of ^{83}Ga and levels scheme of ^{83}Ge and ^{82}Ge.

The decay scheme ^{83}Ga→^{83}Ge was taken from [27], Figure 6.29. Relative intensities of observed transitions confirmed the ones seen previously [27]. However, due to a larger P_n, the absolute branching ratios were found to be smaller as it is shown in the Figure 6.29. In the same figure is presented the decay scheme of ^{82}Ge in β-n decay of ^{83}Ga. I confirmed the transitions between levels established most recently by *Winger et al.* in [27] with the exception of 596keV γ-ray which was not seen in γ–β–n gated spectra (Figure 6.25). The relative intensities were measured to coincide with their uncertainties with *Winger et al.* - Table 6.3. In addition, we propose new transitions to be placed in the scheme not observed before: 47keV, 71keV, 170keV, 487keV which appeared in coincidence with neutrons but were not listed previously in the literature. Placement in the level scheme is uncertain and based on the levels energy difference. Again, due to larger P_n the absolute branching ratios measured are quite different (Figure 6.29).

Interestingly, the γ-ray observed at 42keV indeed connects the levels at 2333keV → 2287keV, previously attributed to the J^π 0^+ and 4^+ respectively. There is no way such a highly rotated E4 transition could be in competition with an E2 transition connecting the 2333keV with the well established 2^+ state at 1348keV. Other γ–γ–β–n coincidence experiments are needed to confirm placement of these newly observed transitions in the level scheme.

Another fact is also fascinating. Previous ALTO research attributed the 867keV transition to the both level schemes: $^{83}Ga \xrightarrow{\beta} {}^{83}Ge$ and $^{83}Ga \xrightarrow{\beta-n} {}^{82}Ga$ [135]. As it happens it is not the case. Table 6.4 compares the peak areas of transitions in ^{82}Ge measured in γ–βn and $\gamma\beta$ gated spectra (Figure 6.25). The ratio of these peaks is the efficiency of TETRA (as explained above in § 6.4) and is a constant for the γ-rays observed. Should the 867keV be fed also in $^{83}Ga \xrightarrow{\beta} {}^{83}Ge$ we would expect its ratio to be significantly lower as compared to the other transitions. Consequently, we shall recognize that the 867keV is a unique transition in ^{82} Ga.

Therefore, we come to the conclusion that the structure of ^{82}Ge is not fully understood yet. Additional experiments are needed to complement its level scheme. Interestingly, the P_n measured is much bigger than the one obtained by *Winger et al.* - 62.8(25)%. The ,,extra" beta strength mostly results in higher feeding of the ground state of ^{82}Ge. However, I should mention that P_n of ^{83}Ga was measured numerous time (Chapter 8) with different methods but, the discrepancy of the data is high - from 20% to 85% which may manifest, that we obviously don't understand it yet.

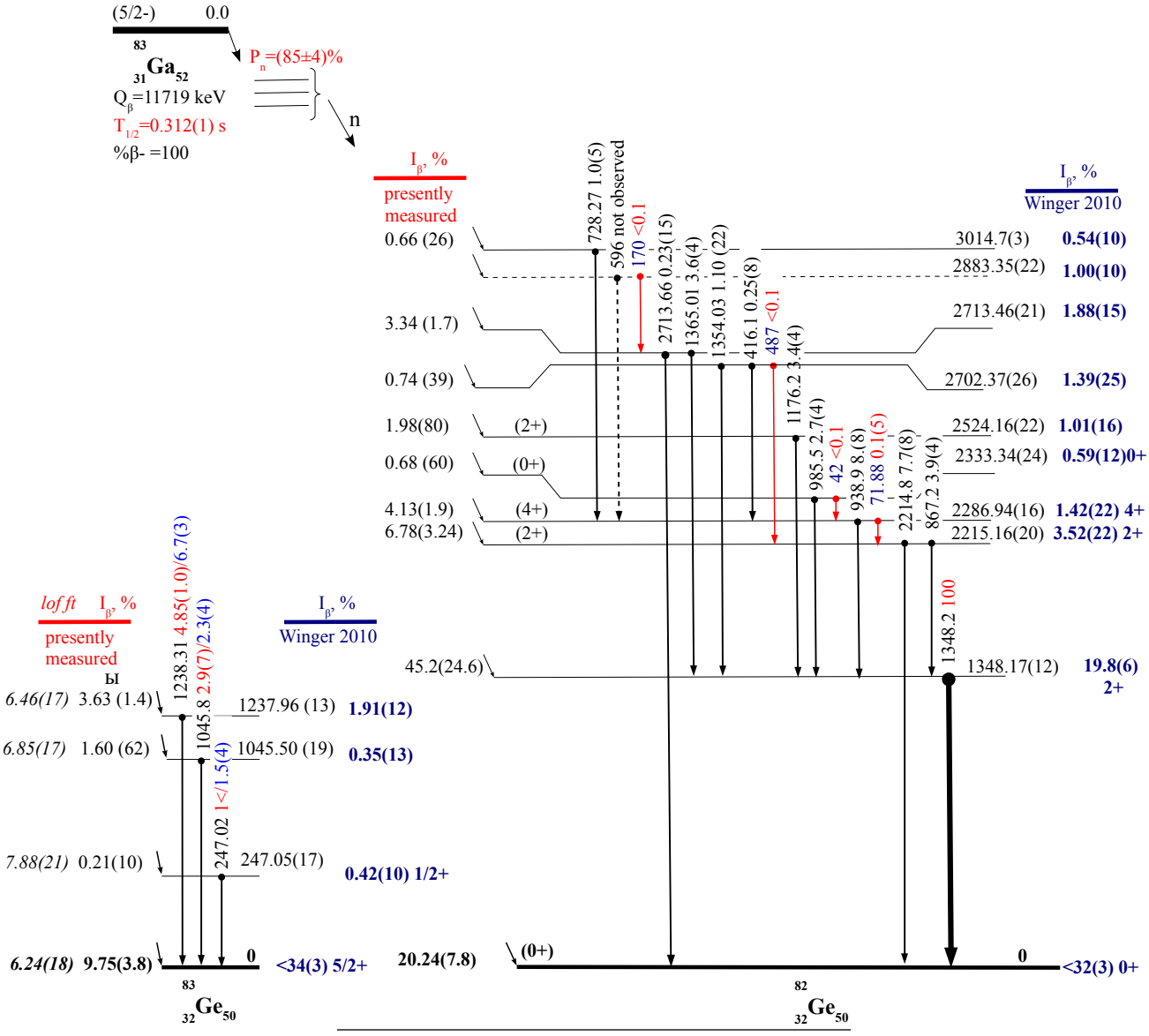

FIGURE 6.29: ^{82}Ge, ^{83}Ge β decay level scheme [27]. The transitions observed are given with I_γ measured; new transitions found in the γ–β–n spectra of A = 83 are attributed to (possible) transitions in ^{82}Ge. The obtained I_β is illustrated with previously known data from *Winger et al.* [27].

TABLE 6.3: Summary of relative intensities of γ transitions attributed to ^{82}Ge studied by ^{82}Ga→^{82}Ge and ^{83}Ga→^{82}Ge in the present work in comparison to previous experiments. (*) γ-rays newly observed

		Benoit, [97]	**Present**	**Winger et al**, [27]	**Present**
E_γ keV	E_{level} keV	^{82}**Ga** β– I_γ	^{82}**Ga** β– I_γ	^{83}**Ga**β–**n** I_γ	^{83}**Ga** β–**n** I_γ
416	2713	2.2(6)	3.6(2.4)	0.8(3)	0.3(2)
564	2779	<1	no	no	no
596	2883	no	n/a	3.5(3)	no
727	3014	no	n/a	1.9(3)	1.4(6)
867	2215	8(2)	9.5(3.8)	7.3(4)	4.6(18)
938	2286	7(2)	6.4(2.7)	11.2(5)	9.7(36)
985	2333	5(1)	6.5(2.5)	2.1(4)	3.0(13)
1176	2524	no	<1	3.6(4)	3.54(14)
1348	1348	100	100	100	100
1354	2702	2.6(9)	7.16(3.0)	4.1(8)	1.0(5)
1365	2713	2.9(9)	6.17(2.6)	4.9(4)	3.6(16)
1378	2726	<1	no	-	no
2713	2713	no	<1	1.7(2)	1.48(70)
47*	2286-2333	-	-	-	<1
72*	2286-2215	-	-	-	0.17(12)
170*	2883-2713	-	-	-	<1
487*	2702-2215	-	-	-	<1

TABLE 6.4: Peak area ratio of certain transitions in $^{83}Ga \xrightarrow{\beta-n} {}^{82}Ga$ in $\gamma\beta$n and $\gamma\beta$ gated spectra. Ratio = $S^{\gamma}_{\gamma\beta}n/S^{\gamma}_{\gamma\beta}$

E_γ, keV	**Ratio**	**abs error**
1365.41	0.62	0.07
1176.1	0.53	0.07
938.83	0.56	0.03
867.2	0.59	0.14
1348	0.60	0.01

6.6.4 Results: A = 84

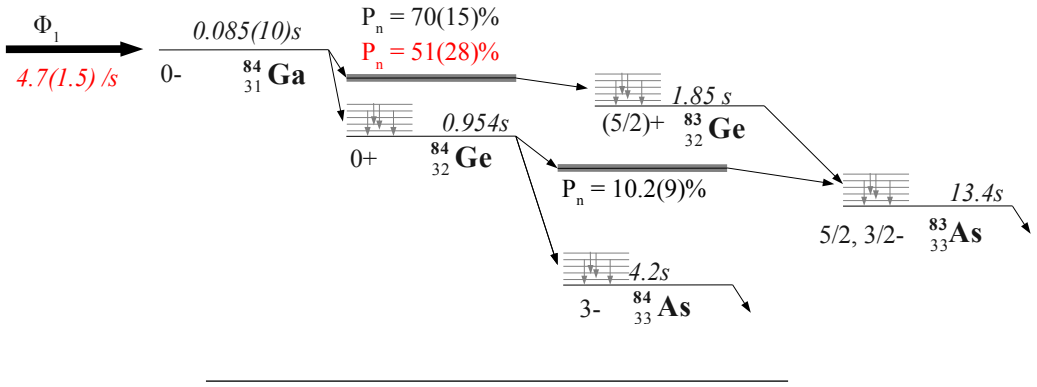

FIGURE 6.30: Decay scheme of ^{84}Ga. Data were taken from [115]. Data in black were taken from [115]. In red: measured in the present experiment.

Attempts to study ^{84}Ga β-decay, whose decay chain is presented schematically in Figure 6.30, have been made at ALTO on several occasions [29, 97, 132]. Even though, the detailed level scheme of ^{84}Ge and ^{83}Ge populated in the $\beta/\beta - n$ decay of ^{84}Ga was proposed recently [30], the P_n was still poorly known (Figure 6.34). In the most recent experiment, *Winger et al.* estimated the P_n by ion-tagged γ-ray spectra [27], but pointed out the lack of measurements of absolute branching ratios. The authors admitted that P_n obtained depended on their estimations of I_β which had to be verified independently.

Therefore, re-measuring the absolute branching ratio in β decay of ^{84}Ga with the neutron detector TETRA was one of the main objectives of my experiment since it could significantly impact the understanding of nuclear structure in the region. Unfortunately, due to (possible) laser misalignment, statistics obtained were considerably lower compared to the previous experiments with the laser ion source reported in [30]. In Figure 6.31 measured γ-β gated and γ-β-n gated spectra for mass A=84 are presented. The strongest transition, 624keV, in ^{84}Ge with relative intensity (59±25%) normalized to 247keV was observed. In the β-n decay daughter, ^{83}Ge, only the strongest γ-rays (247keV, 1045keV) were seen, Table 6.5 and the Figure 6.31.

We measured neutron and β activity simultaneously within 3s of beam time and 0.5s of decay. This lead to $P_n(^{84}\text{Ga})$=51(28)% and $\Phi(^{84}\text{Ga})$=4.7(1.5)/s determined as a solution of the system of Bateman equations (Equation 6.5) specified for the β-decay of ^{84}Ga and displayed in the Figure 6.32. The red experimental points are reproduced by the calculated blue line using the determined P_n and Φ. The contributions to the β-activity curve were due to the background (measured within 0.5s prior to ion collection) as well as β decay of ^{84}Ga (green curve) and β-decay of its daughters (^{83}Ge, ^{83}As, ^{82}Ge). Whereas the neutron activity was assigned either to the background, to the β-n decay

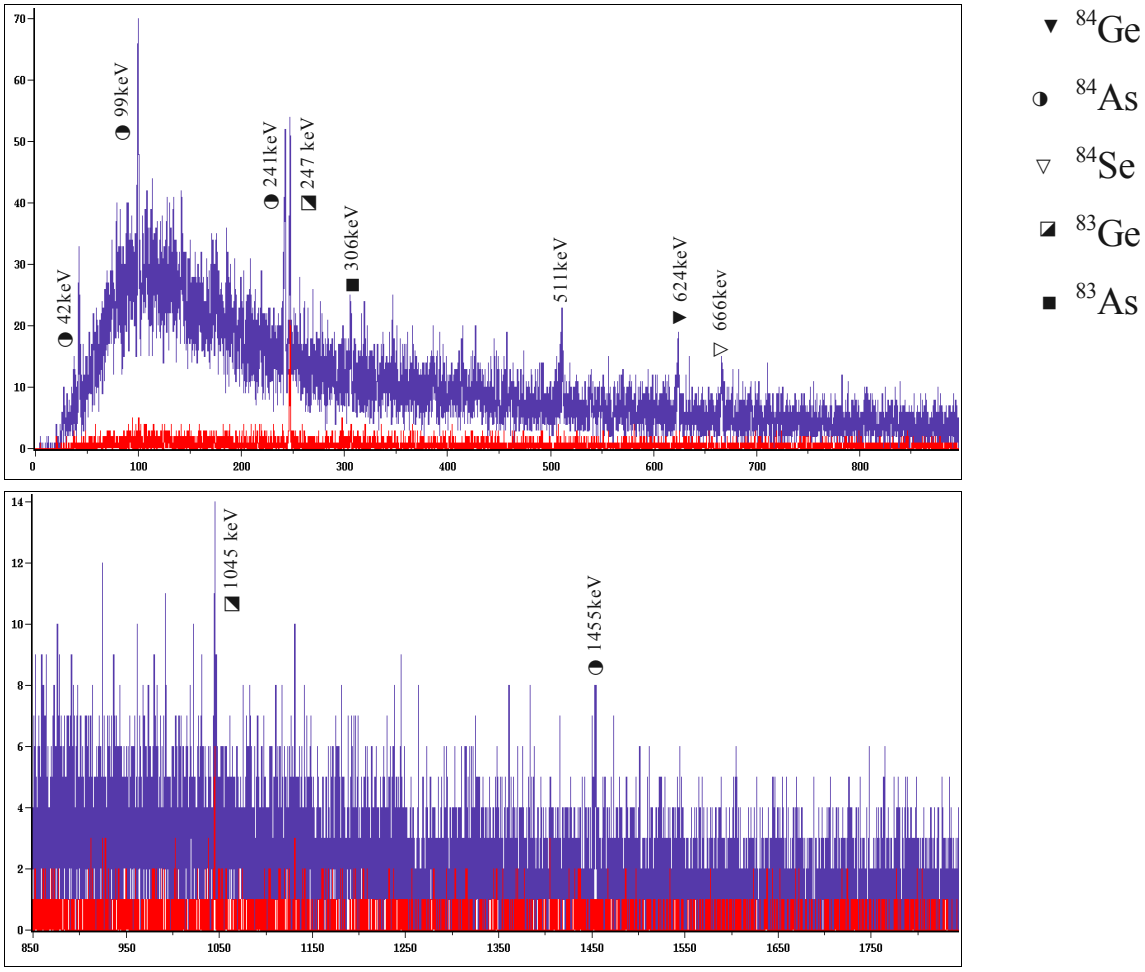

FIGURE 6.31: Measured γ-β,gated (in blue) and γ-β-n gated (in red) spectra for mass A=84. The marked lines belong to transitions in daughter nuclei.

		Winger [27]	**Lebois** [96]	**present**	**Winger** [27]	**Kolos** [29]	**present**
		^{83}Ga β	**^{83}Ga β**	**^{83}Ga β**	**^{84}Ga β-n**	**^{84}Ga β-n**	**^{84}Ga β-n**
E_γ	E_{level}	Iγ	Iγ	Iγ	Iγ	Iγ	Iγ
247	247	1.5(4)	yes	<1	100	100	100
799	1045	no	no	no	8(4)	5(1)	n/a
867	867	no	yes	no	no	no	n/a
1045	1045	2.3(4)	no	3.0(1.2)	48(7)	55(3)	67(23)
1237	1237	6.7(3)	yes	6.3(2.5)	no	9(3)	n/a

TABLE 6.5: Summary of γ lines observed in decay of ^{83}Ge studied by ^{83}Ga$\rightarrow^{83}$Ge and ^{84}Ga$\rightarrow^{83}$Ge from the present work in comparison to previous experiments. *no* - not observed; *yes* - observed but the relative intensity is not provided; *n/a* - not observed due to weak statistic.

of ^{84}Ga or to the β-n decay of ^{84}Ge. Figure 6.33 demonstrates verification of the results obtained by a ROOT fit analysis as explained in §6.2.

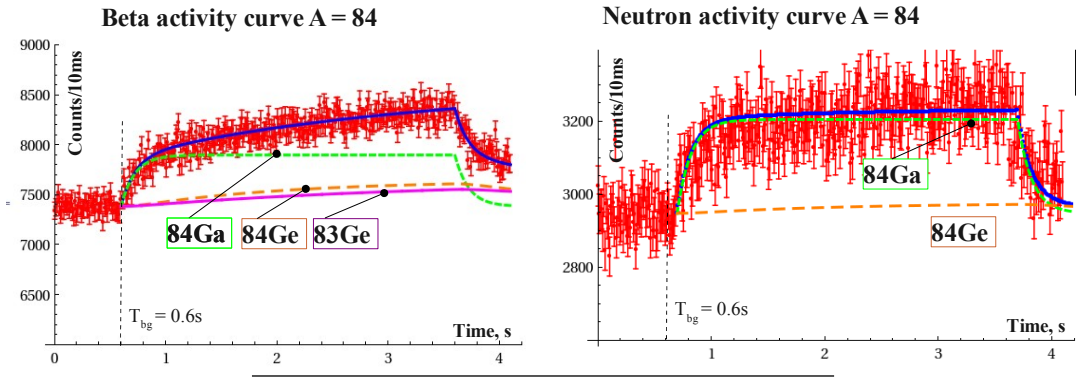

FIGURE 6.32: Reproduced beta (left) and neutron(right) activity curves, A = 84

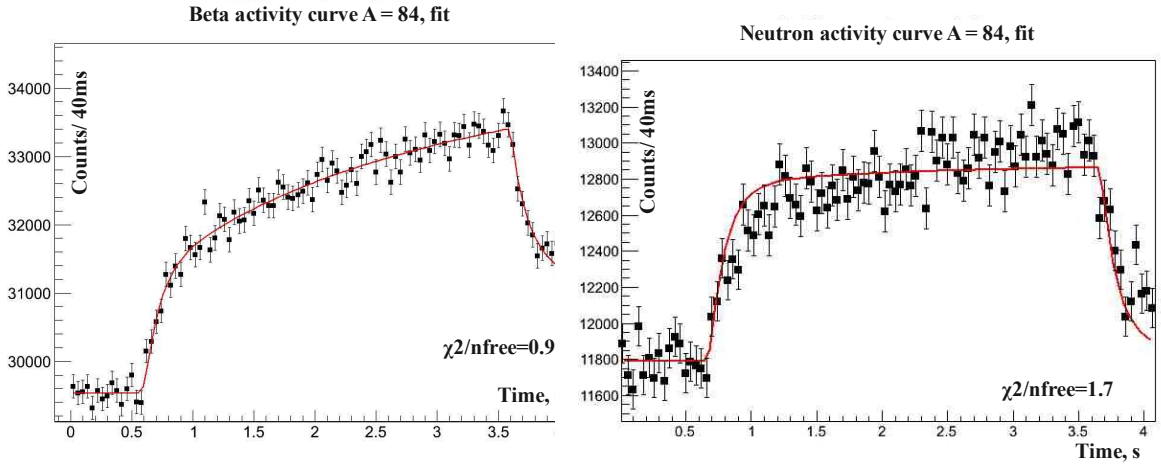

FIGURE 6.33: Fitted beta (left) and neutron(right) activity curves, A = 84

^{84}Ge being the β-decay daughter of ^{84}Ga is a neutron emitter with P_n = 10.9% and $T_{1/2}$ = 0.954s as recommended by NNDC. As it is clearly seen from the neutron fit (Figure 6.33) the increase in the neutron activity in the beginning is relatively fast and caused mostly by β–n decay of ^{84}Ga. Whereas later on the neutron emission from longer-lived ^{84}Ge becomes more significant and further neutron activity increase happens less rapidly. Even though the fit performed based on currently known properties of ^{84}Ge described well the experimental data within error bars, it is seen in the behavior of the experimental curve that it might be governed by a neutron source with a longer half life. To try to explain the curve we came up with a few hypothesis which bring the fit in better agreement to the experimental data, however none of them seemed to us satisfactory. 1)a longer half life for ^{84}Ga (about 180ms) which contradicts the numerous well-established measurements; 2) lower P_n of ^{84}Ga (16%) which is not the case (see Figure 6.34); 3) more significant P_n of ^{84}Ge, though the P_n was found multiple times

by different methods to be about 10%; 4) possible 2n neutron emission due - to large $Q_{\beta-2n}$ window ^{84}Ga tends to emit 2 neutrons to come back to the shell closure (^{82}Ge), but in our previous experiments [30] no γ transitions in ^{82}Ge were observed (but what about direct g.s. feeding by 2n emission channel ?); 5) a presence either in ^{84}Ga or in ^{84}Ge of a longer lived neutron isomer (∼1s) de-excited by β delayed neutrons but for ^{84}Ga a shorter lived isomer was already proposed [132]; for ^{84}Ge it might also but true but still is less probable; 6) ^{84}Ge beam contamination, but since the β activity curve is finely fitted, the contamination, if it took place, was insignificant. Therefore, it seems that for the time being we are not able to explain the shape of the curve. A gamma spectrum with better statistics can help.

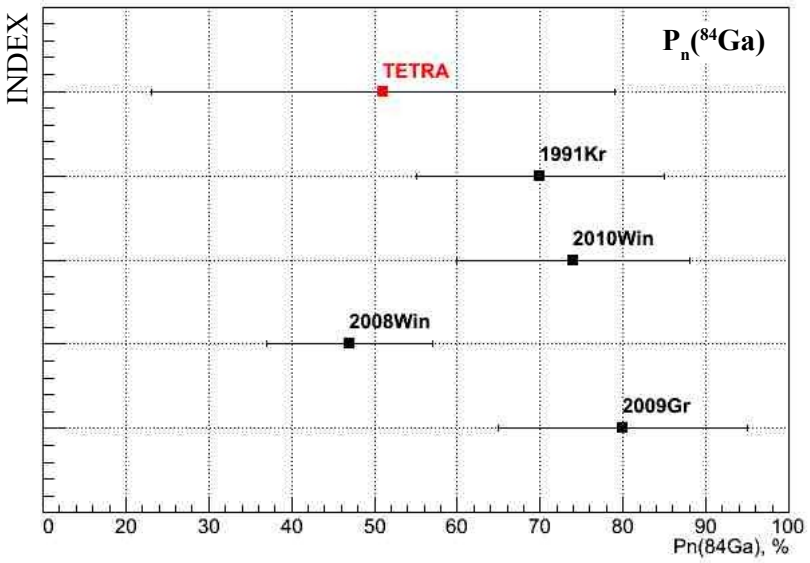

FIGURE 6.34: P_n of ^{84}Ga, comparison with known data: red - presently measured; *2010Wi* - [27], *2009Gr* - [28], *2008Wi* - [136] are from the same measurements; *1991Kr* - [125].

Due to the reasons explained just above, we were not able to measure the half life of ^{84}Ga by the neutron activity curve. The measured P_n assumed the 0.085(10)s period know from literature. Figure 6.35 are shown the half lifes determined by the time behavior of β gated γ spectra. The values determined for the γ lines agree with the already known values within error bars. However, it surprisingly came out, that the time structure of the 241keV transition in ^{84}Ge→^{84}As had a shorter half life as compared to the other transitions. Unfortunately, due to possible laser misalignment and weak statistics we are not able, for a while, to provide any explanation.

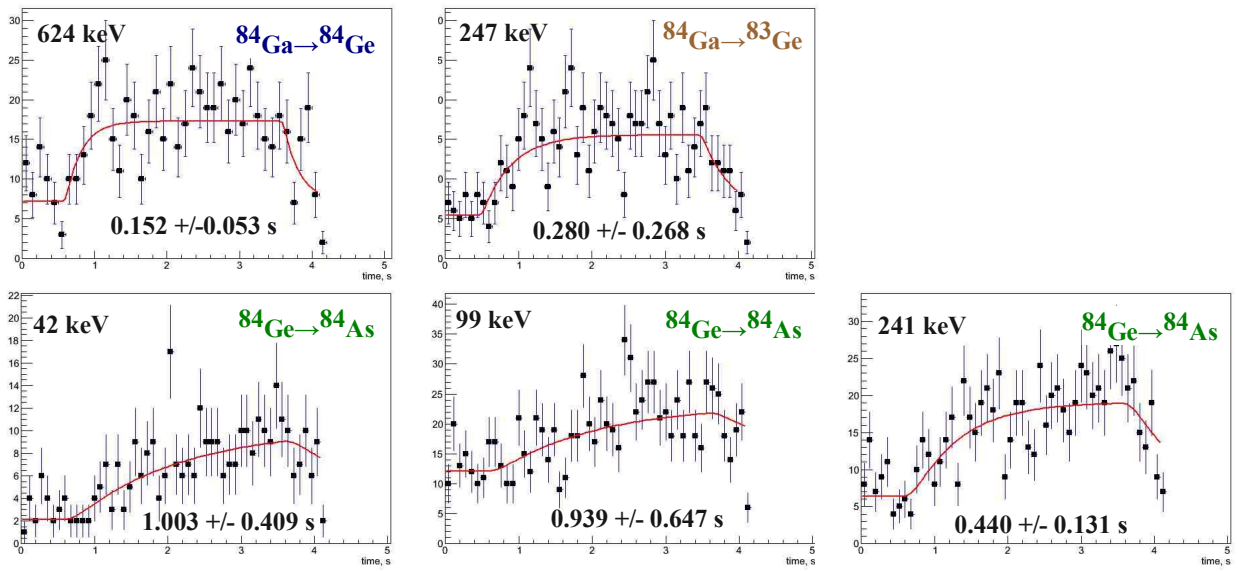

FIGURE 6.35: Half live of isotopes for ^{84}Ga.

6.6.5 Results: A = 123

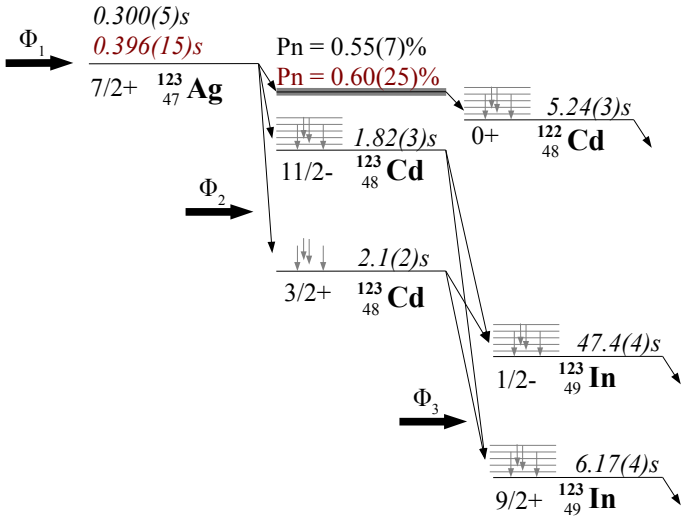

FIGURE 6.36: Decay scheme of ^{123}Ag. Data in black were taken from [115]. In red: measured in the present experiment ($T_{1/2}$ with neutron activity curve).

Absolute branching ratio in β-decay of ^{123}Ag

The P_n for ^{123}Ag is well known from the previous measurements of *Reeder et al.* (Pn=0.55(5)%) [137] and recent studies at NSCL (P_n=1.0(5)%) [138]. Both measurements were performed with a gas filled multi neutron detector - SOLAR [74] and NERO [86], respectively. This was the reason why this nucleus was chosen as a reference point in the region of neutron rich silver isotopes. Similarly to the case of ^{82}Ga, ^{123}Ag is assumed to be the only neutron emitter in its $\beta-/\beta-n$ decay chains. However, ground states of (grand) daughter nuclei were populated not only in $\beta-/\beta-n$ decay of ^{123}Ag but also by the beam as is shown in Figure 6.36, because the universal plasma source was used. This makes application of the method of solving of Bateman equations explained above in § 6.2 impossible - number of parameters (4) $(\Phi_1, \Phi_2, \Phi_3, Pn)$ is bigger that number of equations (2). Thus, to measure P_n of ^{123}Ag another the $\gamma - n$ method was introduced. Due to already known absolute branching ratios for β decay of ^{123}Ag [139] it was possible to obtain the total decayed quantity of ^{123}Ag (N^{tot}) by γ measurements. The P_n value was directly estimated as a ratio of the number of neutrons registered ($N_{neutron}$), corrected by efficiency (ε_n) and background(B):

$$P_n = \frac{N_{neutron} - B}{N^{tot}\varepsilon_n} \tag{6.12}$$

N^{tot} was determined by γ transitions (116keV, 124keV) in ^{123}Cd observed in the direct γ-spectrum. The $\gamma\beta$ gated spectrum, due to considerable (up to 40%) dead time on beta and gamma channels, was not used. The dead time results from β-decay of the

radioactive source accumulated by the beam in which the isobaric chain of isotopes was present. It is possible by the method introduced earlier in § 6.5 to make a correction for the dead time for each channel. However, such a correction for γ–β-gated spectra might be misleading. That is why the direct spectrum was analyzed.

Yet another difficulty was considerably high production rate of isotopes of the isobaric chain with higher Z (Cd, In) whose β decay polluted enormously the γ spectra. Luckily, the half life of ^{123}Ag is significantly shorter (0.3s). It is the reason why only part of gamma spectra measured during collection was analyzed. With this technique (Equation 6.12) we could determine the $P_n(^{123}Ag) = 0.60(25)\%$ in good agreement with previous measurements (Figure 6.37). To estimate the neutron background, the decay time was made to be 40s (Figure 6.38). Under the assumption that ^{123}Ag is a unique neutron precursor on its isobaric chain, the neutron activity curve shows the level of the neutron background from t>10·$T_{1/2}$^{123}Ag. Thus, the neutron integral with background subtraction measured within the collection time, corrected by the efficiency was 4330±360

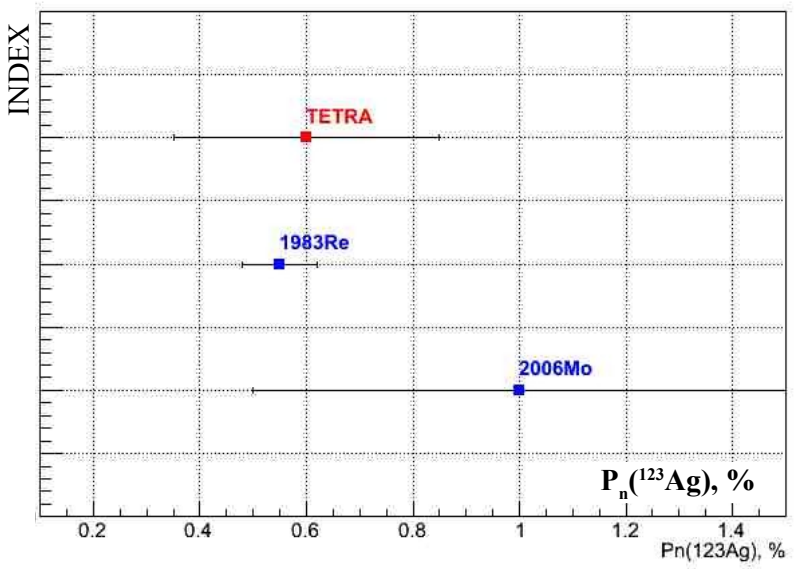

FIGURE 6.37: P_n of ^{123}Ag, comparison with known data: red - presently measured; *2006Mo* - [138]; *1983Re* - [137].

Determination of $T_{1/2}$ (A = 123).

Figure 6.39 shows the half life of the A = 123 isobar. The half life of ^{123}Ag was determined using known γ transitions in ^{123}Cd observed in the direct γ spectra measured with 0.5s of collection time due to the jump in the dead time (see § 6.5) and has significant error bars. At the same time, $T_{1/2}(^{123}Ag)$ measured by the neutron activity curve is much more precise. As is shown in Figures 6.40, thanks to the neutron activity

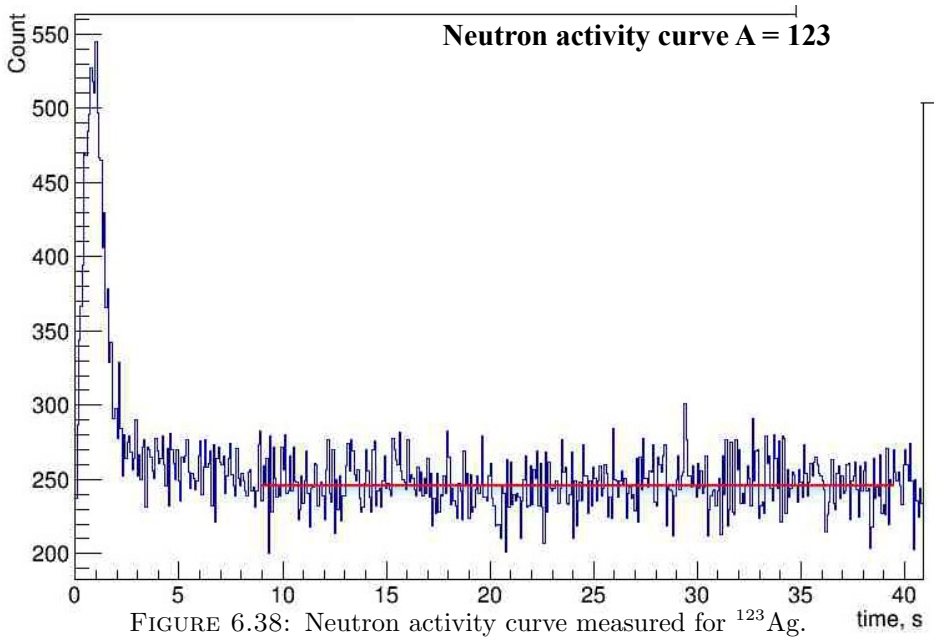

FIGURE 6.38: Neutron activity curve measured for ^{123}Ag.

curve measured in the same experiment with only 3 hours of statistics, with the universal plasma ion source, with significant dead time on β and γ channels (but not the neutron one (!)), the half life obtained under the assumption of the uniqueness of the ^{123}Ag neutron emitter is compatible within error bars with those reported previously.

For other isobars, Cd and In, whose life time is in the range of 1s, the half life was determined only using the decay part. Again, there is an intervention of dead time - it considerably drops after beam is stopped. That is why the fit is done from (T_{beam} + const)s, in the region where dead time is decreasing more gradually.

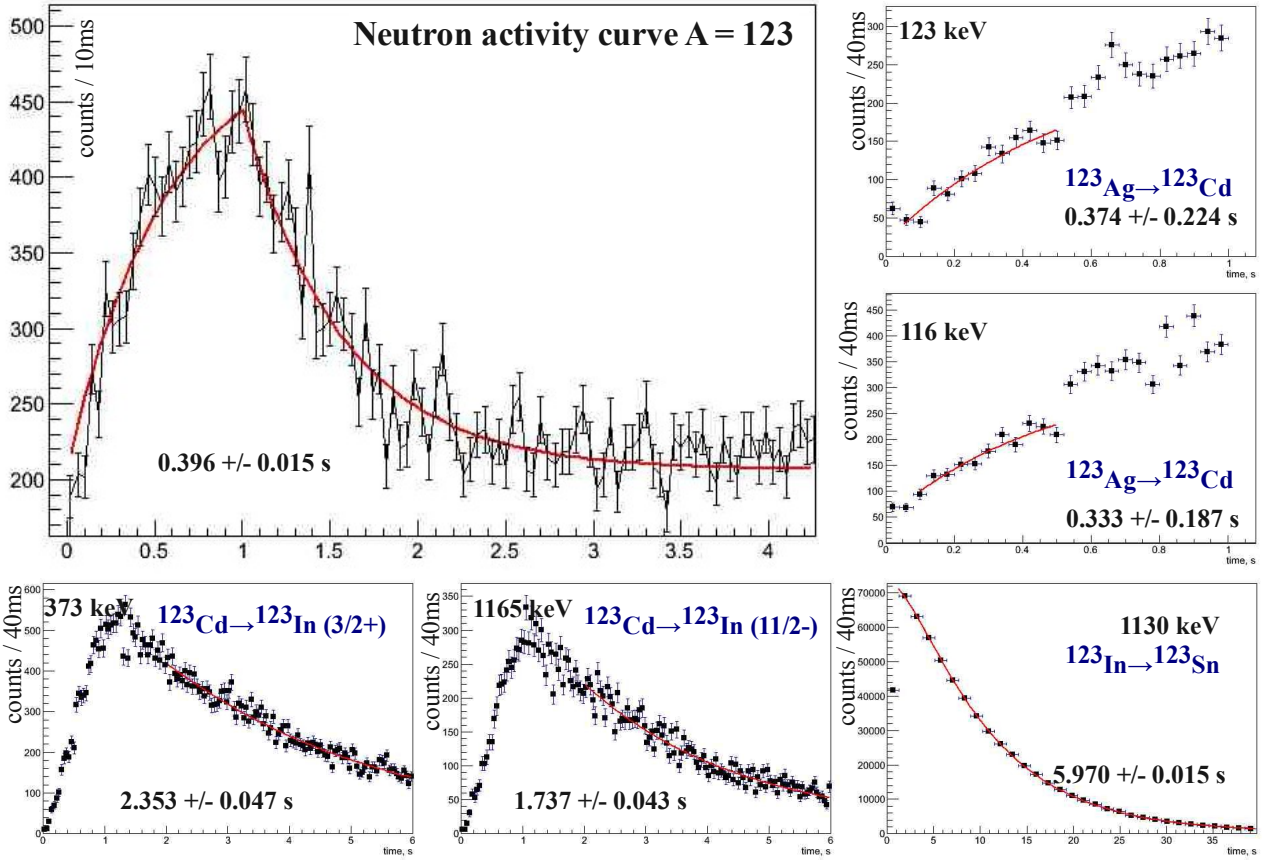

FIGURE 6.39: Half live of isotopes for ^{123}Ag decay chain.

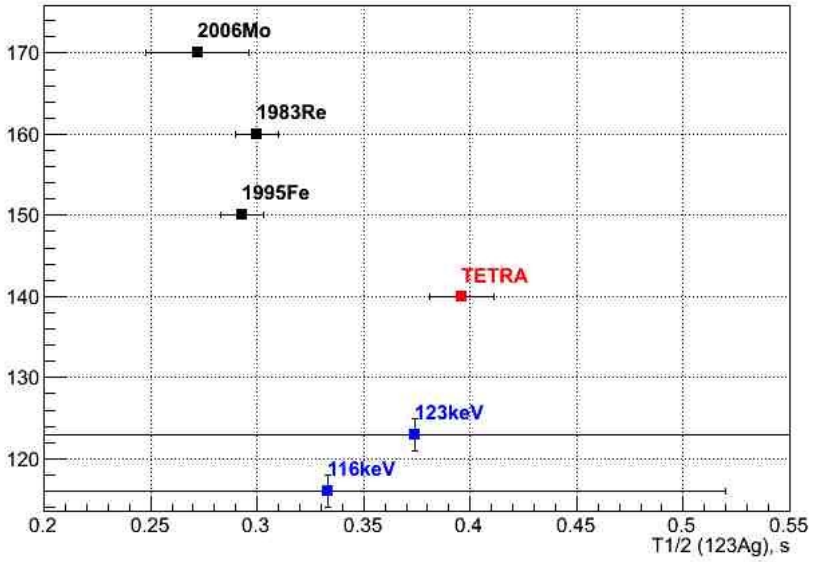

FIGURE 6.40: $T_{1/2}$ of ^{123}Ag, beta delayed neutron data: TETRA - presently measured; *2006Mo* - [138]; *1995Fe* - [140]; *1983Re* - [137]; blue from γ-transitions in ^{124}Cd, Figure 6.39.

6.6.6 Results: A = 124

Even though the A = 124 beam was well delivered and identified by decay of isotopes of In and Sn (Figure 6.41), the production rate for Ag was so low that γ transitions in ^{124}Cd corresponded to β decay of ^{124}Ag were not observed in the γ-ray spectra. However, since ^{124}Ag is the only neutron emitter of the A = 124 isobaric chain, all the neutrons were attributed to β-n decay of ^{124}Ag. The half life obtained by analysis of the neutron method

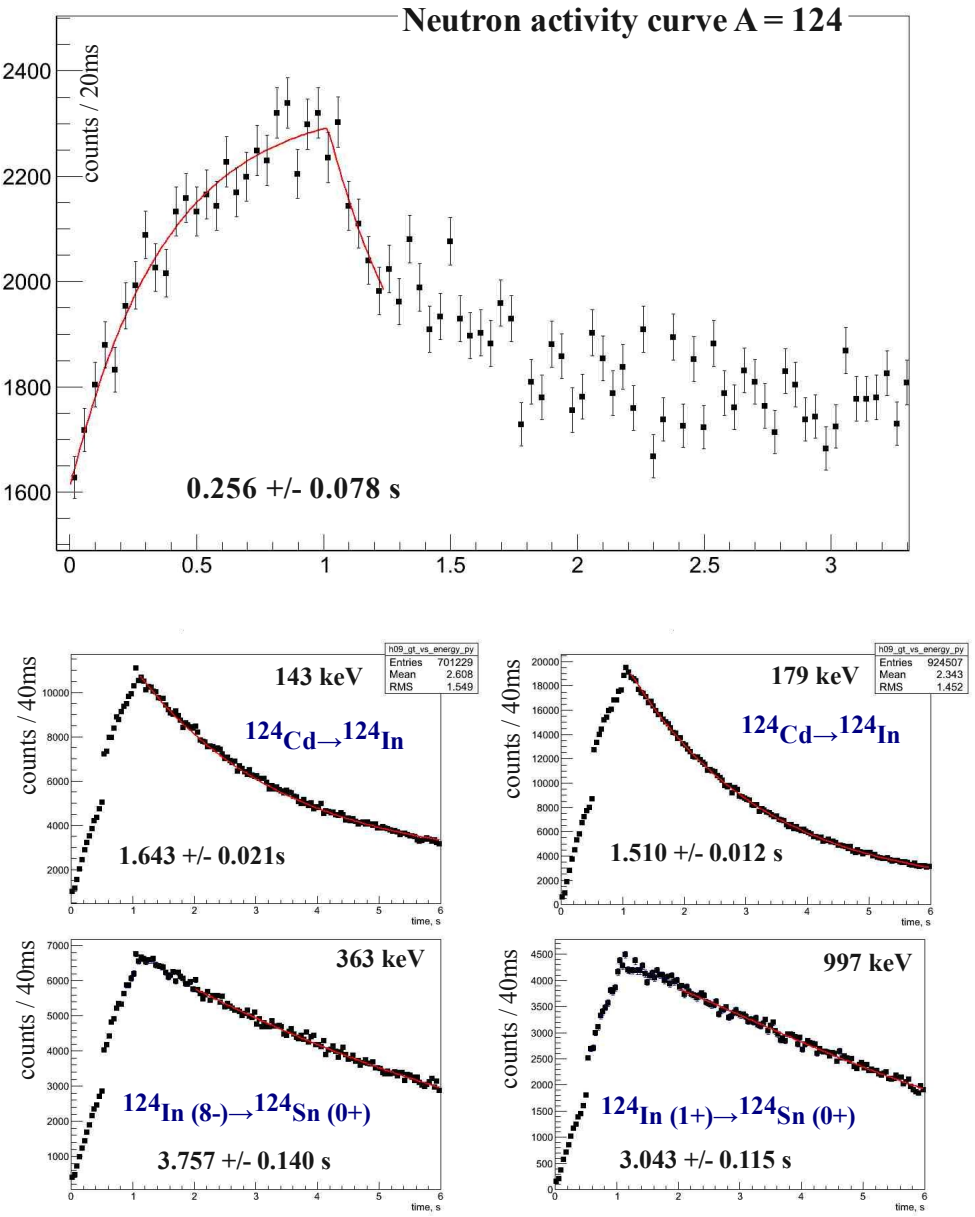

FIGURE 6.41: Half live of isotopes for ^{124}Ag decay chain. Discontinuities are due to the dead time (see §6.5).

nor the γ–n method applied for A = 123 (§6.6.5) worked here, where the isotope of

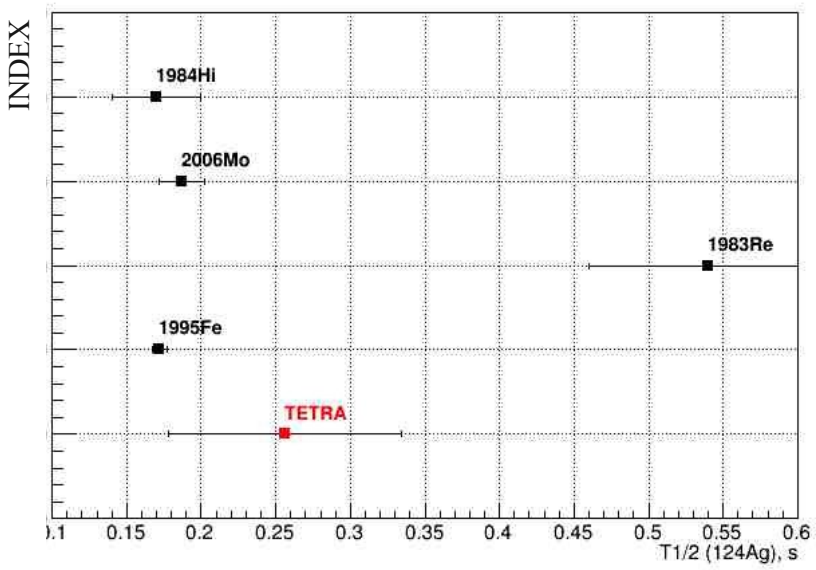

FIGURE 6.42: $T_{1/2}$ of ^{124}Ag, beta delayed neutron data: TETRA - presently measured; *2006Mo* - [138]; *1995Fe* - [140]; *1983Re* - [137]; *1984Hi* - [141].

interest was produced with Plasma Ion Source which is not selective. The production rate of isotope (Ag) of interest is one order of magnitude lower than production of the longer lived Cd and In isobars. Further studies of neutron rich Ag can be performed at ALTO only with laser ionization.

6.6.7 Results: A = 125

The similar situation was observed for the A = 125 isobars: all the neutron activity was attributed to the β-n decay of ^{125}Ag, though due to higher production rate of longer lived isotopes of the A = 125 isobaric chain, no γ-rays corresponding to β-decay of ^{125}Ag were observed (Figure 6.43). The $T_{1/2}(^{125}Ag) = 0.267(10)$s determined by the neutron activity curve overestimates the measurement of *Fedoseev et al.* 0.166(7)s [140]. It is the only experimental data available. Unfortunately, *Fedoseev et al.* don't provide much experimental details in their paper on how this value was obtained. From our side, it seems we are coming to the practical limit of a non-selective plasma ion source. Another experiment with a laser ionization source would be proper here.

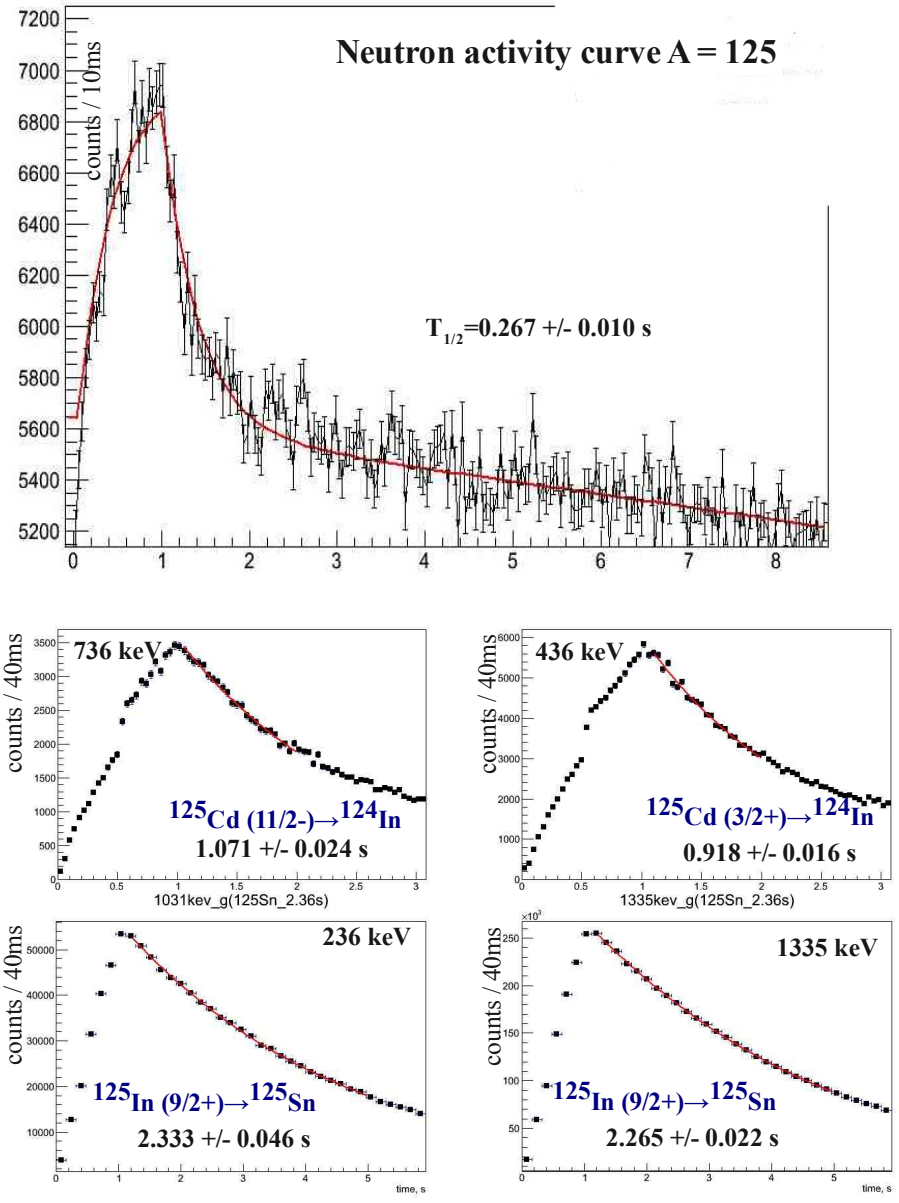

FIGURE 6.43: Half life of isotopes for ^{125}Ag decay chain. The discontinuities are due to the dead time as explained in §6.5

6.6.8 Results: A = 126

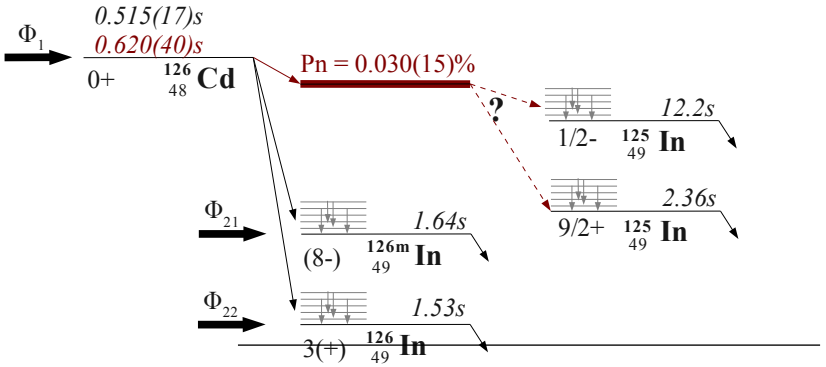

FIGURE 6.44: Decay scheme of ^{126}Ag. Data in black were taken from [115]. In red: measured in the present experiment ($T_{1/2}$ with neutron activity curve).

Even if for the previous mass the production rate of silver was too weak in comparison to other isotopes in the isobaric chains (Figure 6.44) we still were able to observe the decay by the neutron emission. In contrast, the half life measured by neutron activity curve for A = 126, $T_{1/2}$ = (0.620±0.040)s (Figure 6.45), corresponded to ^{126}Cd which confirms that no silver was produced. The period of ^{126}Cd was known before only from γ-activity measurements (Figure 6.46). Our value, measured by the Equation 6.12, is compatible with them within error bars. We also determined P_n (^{126}Cd) = (0.04±0.01)% by the same γ–n method as before (§6.6.5). The 428keV γ-transition in ^{126}In (I_β = 0.66(16) [142, 143]) was utilized to estimate the total number of decays. The neutron integral with the background subtraction, corrected by the the neutron efficiency was (6230±370).

Surprisingly, we observed neutron emission and measured P_n (^{126}Cd) *for the first time*. On the produced A = 126 isobar, neutron emission is energetically favorable only for three isotopes - ^{126}Ag, ^{126}Cd and ^{126}In. ^{126}Ag was studied with the laser ion source at ISOLDE by *Fedoseyev et al.*, who determined the half life for the ground state as ∼107ms [140]. It is possible to assume a longer lived, neutron emission precursor isomer. In a review of production of neutron rich nuclei at ISOLDE [32], it was pointed out that a gross analysis of γ-spectra taken at different laser-frequency settings confirms isomerism also for the heavier Ag isotopes up to (at least) ^{126}Ag. Later *Kautzsch et al.* [144] proposed the most recent decay scheme and noticed that the first 2+ level at 657 keV in ^{126}Cd was populated much more strongly that other levels and concluded that there should be two *short-lived isomers* undergoing β- decay. However, the production rate of Ag in our case was at least one order of magnitude lower in comparison to Cd and In. Moreover, the fact that ^{126}In is not a neutron precursor, as shown experimentally by *Fedoseyev* [140], leads us to conclude that ^{126}Cd was the only possible βd neutron source.

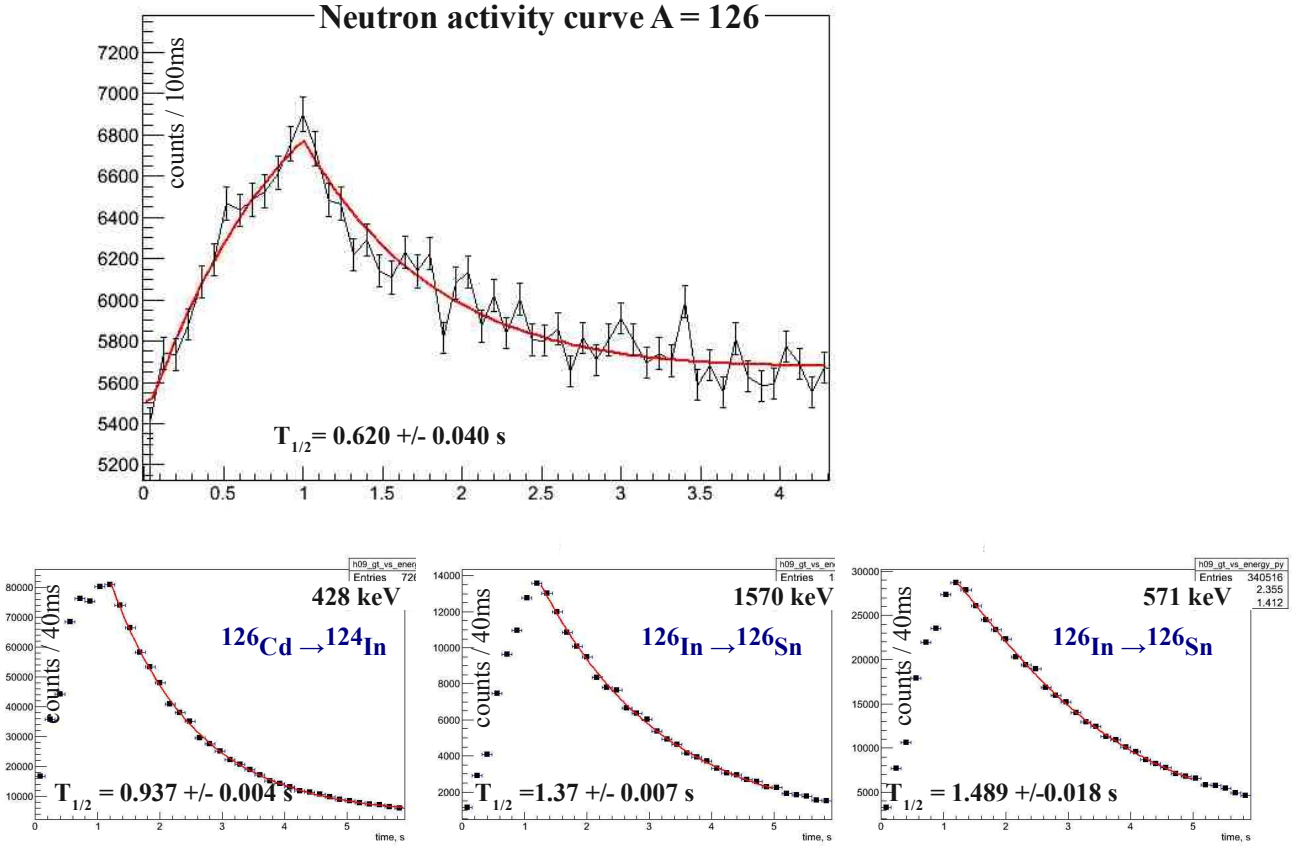

FIGURE 6.45: Half live of isotopes for ^{126}Ag decay chain.

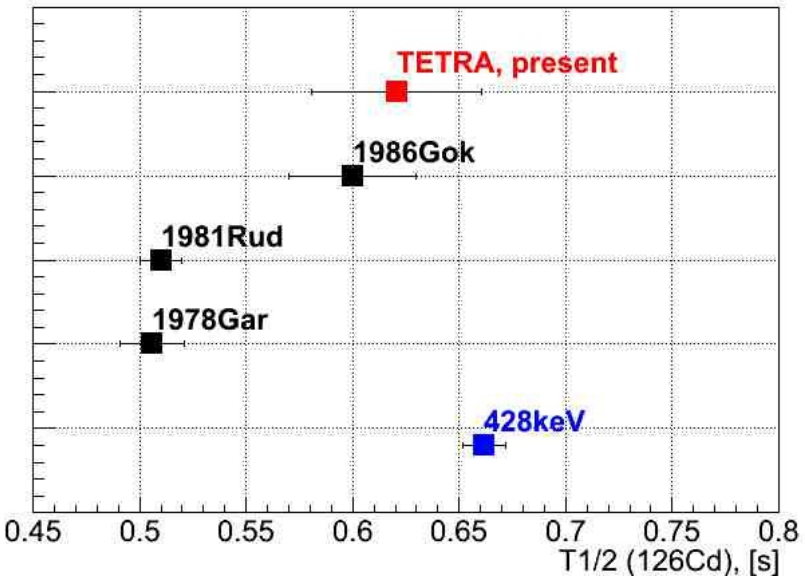

FIGURE 6.46: $T_{1/2}$ of ^{126}Cd: TETRA - presently measured; all data from γ(t): *1978Gar* - [142]; *1981Rud* - [145]; *1986Gok* - [143]; blue from γ-transition in ^{126}In, Figure 6.45.

6.6.9 Results: A = 127

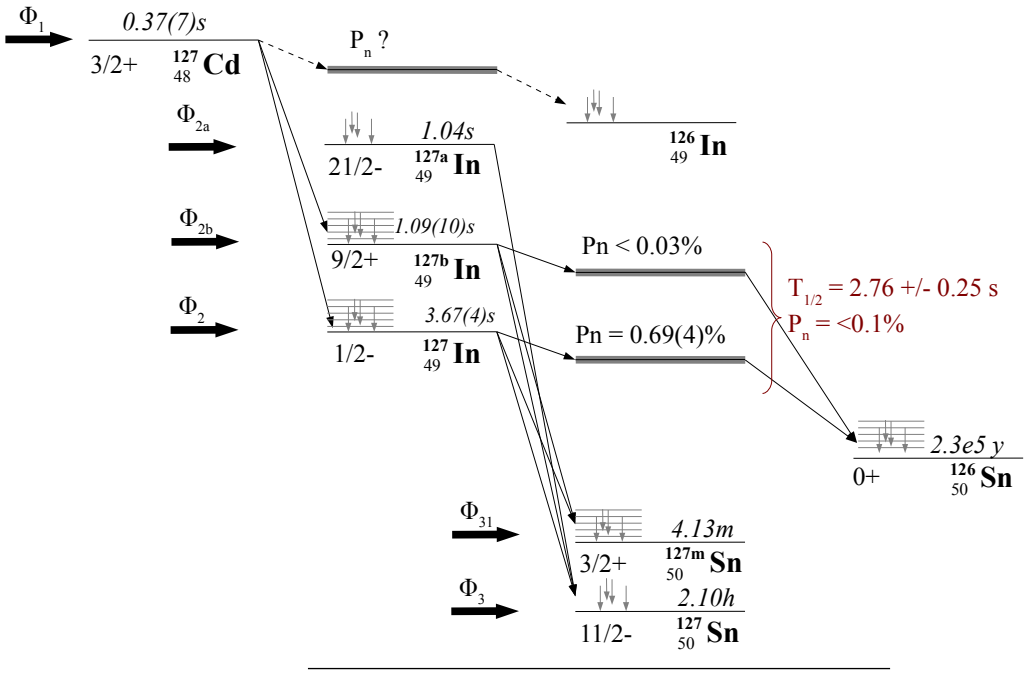

FIGURE 6.47: Decay scheme of ^{127}Ag. Data in black were taken from [115]. In red: measured in the present experiment ($T_{1/2}$ with neutron activity curve).

In ^{127}In there are two β-n decaying isomers with spins (9/2+ and 1/2-)[146] which are produced from one side as primary fission products and from the other their excited levels are populated by β decay of ^{127}Cd (Figure 6.47). Another isomer (21/2-) is not produced at ALTO and was not considered in the analysis. The independent P_n-values ($P_n^{127(1/2-)}$In = 0.68(0.06)%, $P_n^{127(9/2+)}$In < 0.03%) are small as was determined in [123]. Unfortunately, we cannot determine the partial P_n-value for each state since neutron activity cannot be assigned to any specific isomer. The measured composite P_n was at the limit of <0.1%. This low value happens because the (9/2+) isomer, which has the smaller independent P_n, is produced more strongly at ALTO bringing down the composite P_n value. The same γ–n method as before (§6.6.5) was used. Listed in the Table 6.6 are E_γ and I_β for the strongest γ-ray transitions in ^{127}Sn [146] that were utilized to obtain the number of nuclei which decayed. We also assumed the probability of βd neutron emission of ^{127}Cd be to least one order of magnitude lower than P_n of indium. Furthermore, the production rate of Cd is also at least one order of magnitude lower. Therefore, the (possible) contribution of the cadmium neutron precursor to the neutron activity was considered as negligible. The $T_{1/2}$ for A = 127 measured by the neutron activity curve presented in Figure 6.48 is the average between the half-lives of the two β-delayed neutron emitting states. In order to determine the independent P_n-values another production method with a different isomeric yield should be used.

TABLE 6.6: E_γ and I_β in the β-decay of ^{127}In in β-decay of ^{127}In [146]

E_γ, keV	I_β	state
639	2.8(3)	9/2+
646	11.8(5)	9/2+
792	2.4(3)	9/2+
832	2.12(2)	1/2-
956	6.4(6)	9/2+
963	4.9(5)	9/2+
1048	7.6(7)	9/2+
1085	2.64(2)	1/2-
1597	64.0(1)	9/2+

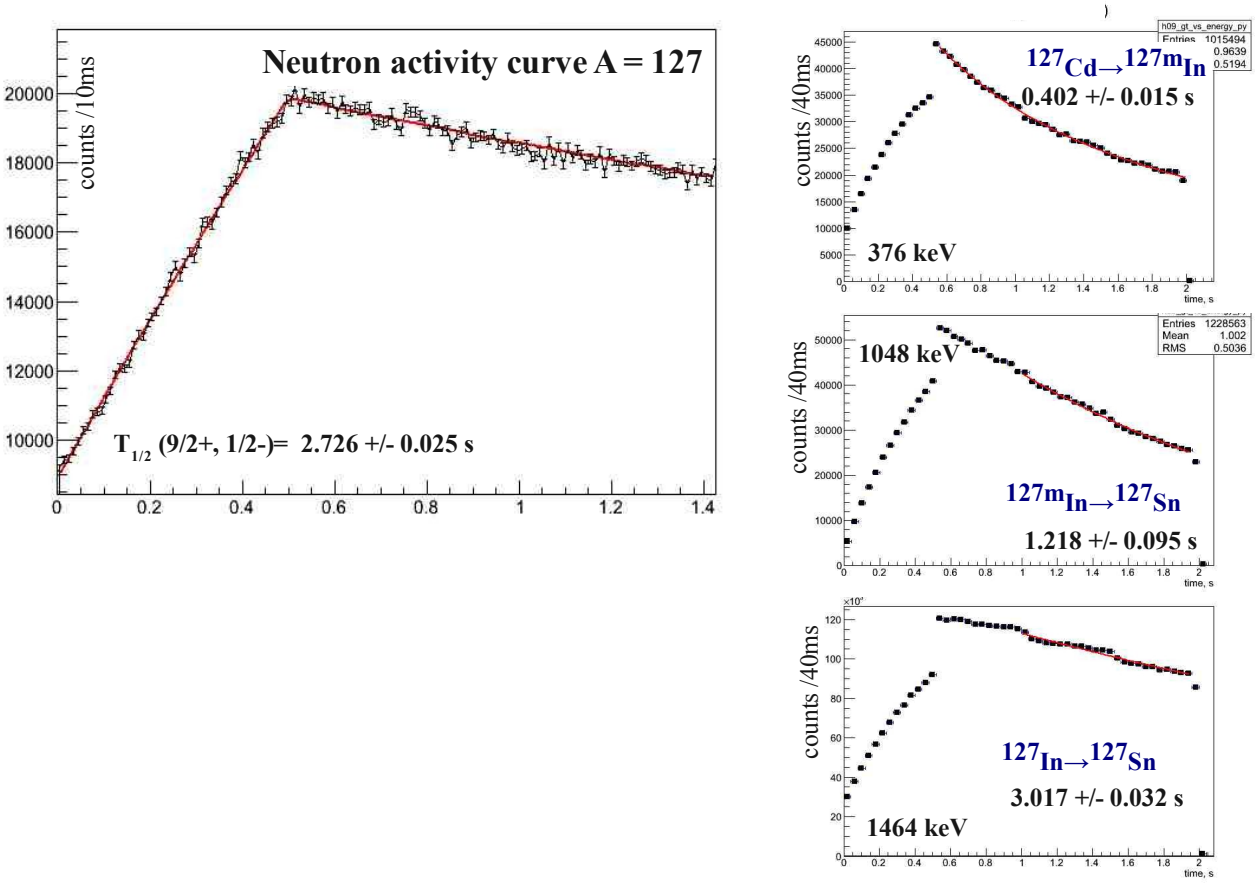

FIGURE 6.48: Half live of isotopes for ^{127}In decay chain

6.6.10 Results: A = 128

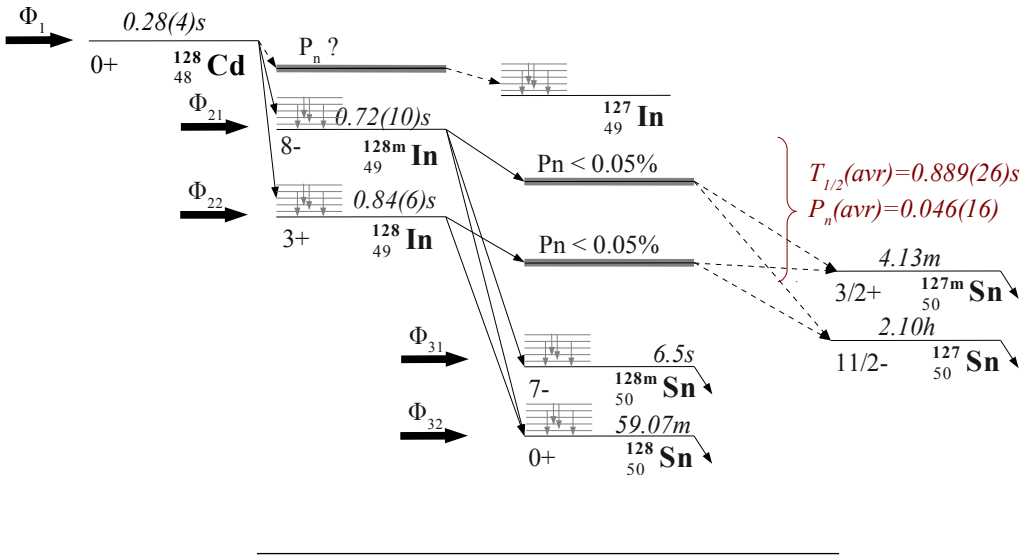

FIGURE 6.49: Decay scheme of ^{128}Ag. Data in black were taken from [115]. In red: measured in the present experiment ($T_{1/2}$ with neutron activity curve).

In ^{128}In there are two β decaying states with similar a half life [147]. Both the isomer and the ground state are produced from one side as primary fission products, and from the other their excited levels are populated by β decay of ^{128}Cd [1] (Figure 6.49). Their $T_{1/2}$ were measured by γ-activity in [143] to be as shown in Figure 6.49. The half-live by the neutron activity was measured for the mixture of the two states. In our experiments, benefiting from the neutron detector we were able to measure $T_{1/2}$ by both γ and neutron activity ($T_{1/2}^{neutron}$) (Figure 6.50). As seen, the $T_{1/2}^{neutron}$ coincides well within errors with the half life of the ground state obtained by γ activity. Therefore, we came to the conclusion that there was only one βd neutron emitter in ^{128}In. We determined the composite P_n-value of the isomer and the g.s. in ^{128}In as well as independent P_n values as it is shown in Table 6.7. However, due to our half live measurements we propose $P_n^{g.s.}$=0.074(10)% to be adopted by the evaluator. To obtain the P_n-values the same γ–n method as before (§6.6.5) was used. Listed in the Table 6.8 are E_γ and I_β for the γ-transitions in ^{127}Sn [147] were utilized to obtain the number of nuclei decayed. The contribution of βd neutrons from ^{127}Cd was considered as negligible due to insignificant production rate.

[1] production of Cd was at least one order of magnitude lower than In and was neglected in the analysis

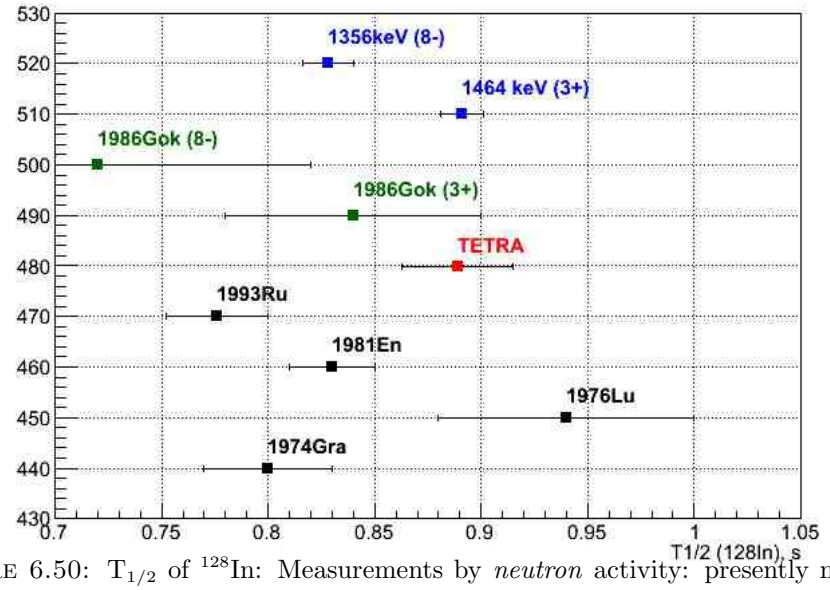

FIGURE 6.50: $T_{1/2}$ of ^{128}In: Measurements by *neutron* activity: presently measured TETRA (Figure 6.51), black - other measurements *1974Gra* - [148]; *1976Lu* - [149]; *1981En* - [150]; *1993Ru* - [120]; by γ activity: presently - blue (Figure 6.51), orange from [143].

	1980 [123]	1993 [120]	1981 [150]	present
^{128}In (g.s.)		0.06(*)		0.074(10)
^{128}In (8-)		0.121(*)		0.12(3)
^{128}In (mixture)	0.059(8)	0.04(3)	<0.2	0.046(16)

TABLE 6.7: P_n of ^{128}In.(*) - adopted by NNDC with a reference to [120] if all neutrons originate from the decay of the g.s. or (8-) state (no error bars are given).

E_γ keV	I_β	state
457	1.6(2)	8-
1089	7.4(5)	3+
1264	1.4(2)	8-
1464	2.5(2)	3+
1473	1.7(1)	3+
1867	32.3(2)	8-
1973	19.5(1)	8-
2104	6.50(4)	3+

TABLE 6.8: E_γ and I_β of ^{128}Sn γ-rays in β-decay of ^{128}In [147]

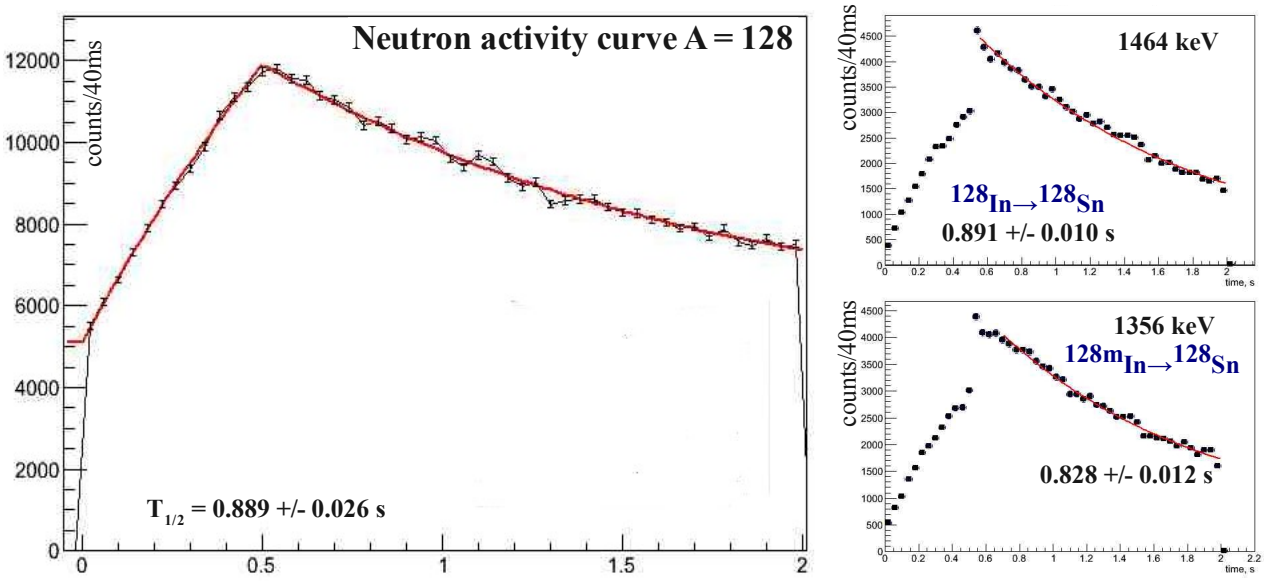

FIGURE 6.51: Half live of isotopes for ^{128}In decay chain

Chapter 7

Discussions

"The interpretation of the experiment - it's a matter of taste."

P. Kapitsa

Contents

7.1 P_n of neutron rich gallium isotopes

The comparison of the present data for the neutron-rich gallium isotopes with results known from other experiments, some of which were carried out over 30-40 years at different facilities, and different theoretical approaches is illustrated in the Figure 7.1. Most of the data presented were obtained with a neutron detector - ^{3}He counters in coincidence and/or separate counting β and neutrons. Whereas in **2008Wi** and **2010Wi** (Figure 7.1) P_n was deduced by γ activity balance.

As seen from Figure 7.1, in general all the theories describe well the experimental data set for N≤50. Crossing the shell at N=50 their predictions differ. The semi-theoretical approach of *Kratz and Herrmann* [48] (*KHF*) predicts correctly $T_{1/2}$ though its P_n calculations regularly underestimate the experimental values. Another semi empirical **gross** β-decay theory [50] fails to reproduce both half lifes and neutron emission probability in the region.

For the *QRPA1*, the FRDM + RPA calculations operated only in the allowed (Gamow-Teller) approximation of *Moller et al* and predict reasonable β decay properties until N = 51. Like the others it predicts a fast jump in P_n from ^{82}Ga to ^{83}Ga as we observed in our experiment. It is important to note, that the *QRPA1* was performed for a wide range of nuclei (∼9000) and the results are published [8]. Therefore, for us the contribution of forbidden decays in half lifes and βd neutron emissions is unimportant at least for N≤52. Although the *DF+CQRPA* (Borzov [36]) takes into account both Gamow-Teller (GT) and First forbidden (FF) transitions it obviously fails to work here. Its latest modifications *DF3a+cQRPA a), b)* [37] tend to make better predictions but still have to be adjusted to the data.

In our opinion, currently there is no uniform theory which describes relatively fair the data crossing the major neutron shell N = 50. This might be explained by limited data on mass measurements in the region. The latest high precision mass measurements at the Penning Trap at IGISOL [151] and ISOLDE [152] were published almost simultaneously in 2008. These data were integrated later to the last evaluation of NUBASE2012 [153] (Figure 7.2). Therefore even rough mass measurements in the region are highly needed to improve the theories. Interestingly, $Q_{\beta-2n}$ for ^{82,83}Ga even being small is not negative. But what is more important, $Q_{\beta-2n}$ for ^{84,85,86}Ga is comparably high ≥5MeV [154] but only for ^{86}Ga has βd2 neutron emission been experimentally observed [7]. It is a very nice question as to why ^{84}Ga never manifested its 2n emission channel in previous experiments [30]. Due to the large $Q_{\beta-2n}$ window it is reasonable to assume that ^{84}Ga tends to emit two neutrons to come to the shell closure. Either its 1 neutron emission strongly dominates over the 2n emission channel or the mass calculations are not precise overestimating the $Q_{\beta-2n}$ window.

According to our data set it looks as if the contribution of FF transitions is not yet significant and allowed, GT transitions, dominate. For gallium isotopes the *QRPA1* can be trusted at least until N = 52 - the limit of the present mass measurements shown in Figure 7.2. However, for validation of different theoretical studies of nuclei with large neutron-proton asymmetry, new experimental data are of paramount importance. With respect to newly the inaugurated ALTO facility, experiments on gallium isotope should be continued.

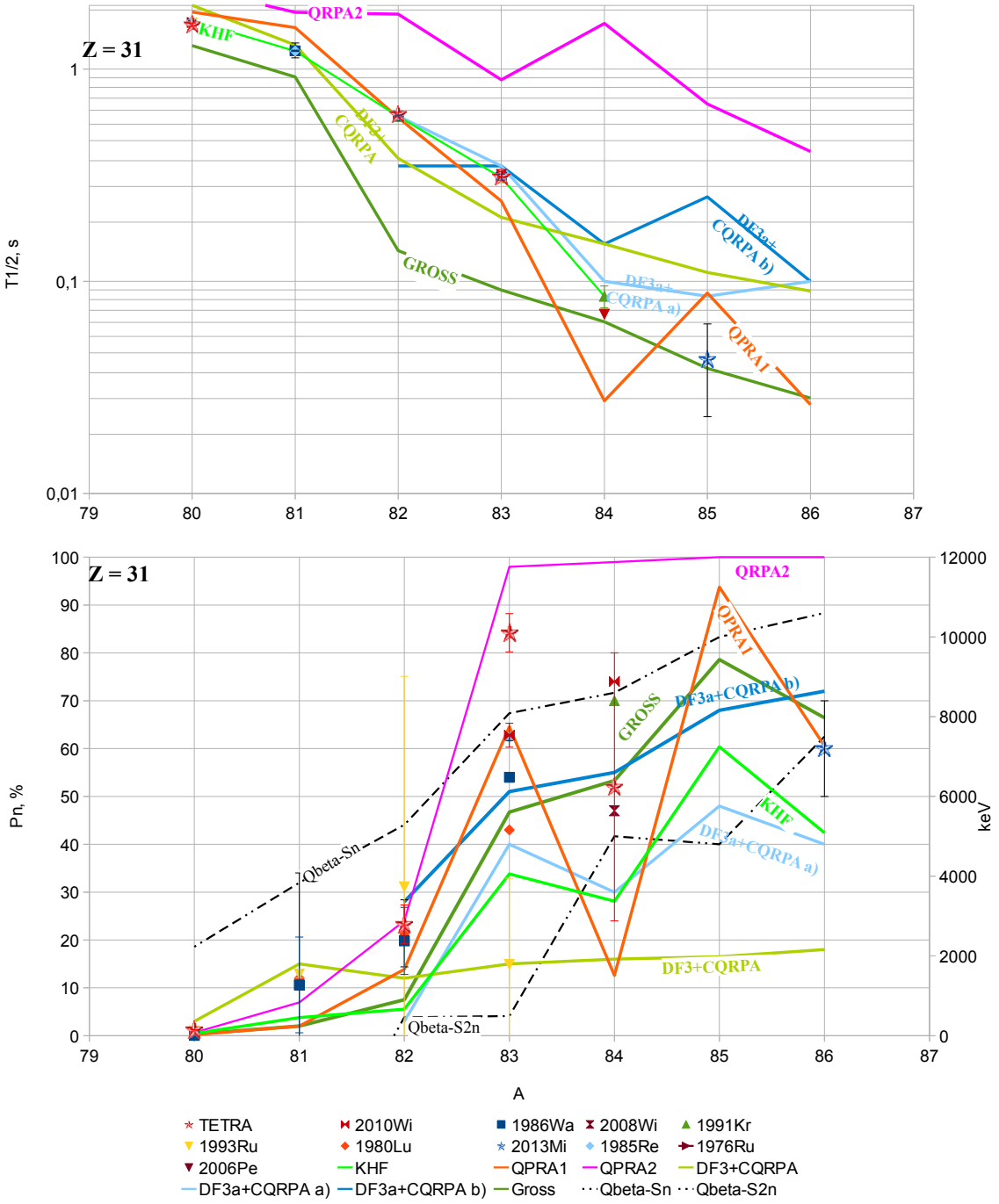

FIGURE 7.1: P_n and $T_{1/2}$ of neutron rich gallium isotopes measured presently (red stars) in comparison to other data and theories: **2010Wi**(γ) [27]; **1986Wa** [122]; **2008Wi**(γ) [136]; **1991Kr** [125]; **1993Ru** [120]; **1980Lu** [123]; **2013Mi** [7]; **1985Re** [120, 121]; **1976Ru** [134]; **2006Pe** [25]; and to theory: *KHF* (Kratz-Herrmann Formula) [48]; *Gross* [50]; QRPA1 [8]; QRPA2 - [48]; *DF3+cQRPA* [36], *DF3a+cQRPA a), b)* [37]; $Q_{\beta-n}$ from [115], $Q_{\beta-2n}$ from [154].

7.2 Half lives of silver isotopes

The half life for neutron rich silver isotopes was first determined by *Fedoseyev et al.* at ISOLDE in [140] (see Figure 7.3). Although in their experiments they used a 4π neutron counter with a thin β detector placed at its center, the paper doesn't provide many details on the experimental technique.

Apart from the data of *Fedoseyev et al.*, curiously, the $T_{1/2}$ measured by the neutron activity curve in [137] and the present work systematically overestimate the values obtained with β activity curve (*Fogelberg* [155] and the most recent [138]). In the "β"-method, such as in [138], Bateman equations are used to find contributions of different β-decay daughter to the measured β activity curve. The $T_{1/2}$ therefore depends on the previous measurements of half lifes of these daughters. In its turn, the "neutron"-method under certain conditions is free from this drawback. The certain condition here is the assumption that all the neutrons are coming only from β-n decay of the nucleus of interest. In the region of $^{123-125}$Ag (Z=47), due to negative $Q_{\beta-n}$-window for all isotopes Z>47, with a big probability the silver isotopes are the unique precursors. Consequently, the neutron activity curve shows directly the $T_{1/2}$ of the precursor. Uncertainties in half lives of β daughters can be caused by the difference between the two methods.

As seen from Figure 7.3 in the vicinity of ^{132}Sn with N$\lesssim$82 in contrast to the ^{78}Ni region (Figure 7.1) the FF transitions dominate bringing the *DF3+cQRPA* calculations into good agreement with the experimental values. In fact, comparing the situation for mass measurements and mass predictions near N≈50 and N≈82, Figure 7.2, we notice that mass estimations are even less precise crossing the major shell at N = 82, but the $T_{1/2}$ of silver isotopes manifests clearly the intervention of the forbidden transitions.

The region of neutron rich silver isotopes is extremely rich in isomers. Going towards N = 82, measuring $T_{1/2}$ and P_n of ground and isomeric states might influence calculations of r-process nucleosynthesis. The measurements of P_n was done up to ^{124}Ag. As it was demonstrated at ALTO, the limit of the plasma ion source has been reached in my experiments. To continue with silver isotopes a selective laser ionization source has to be used.

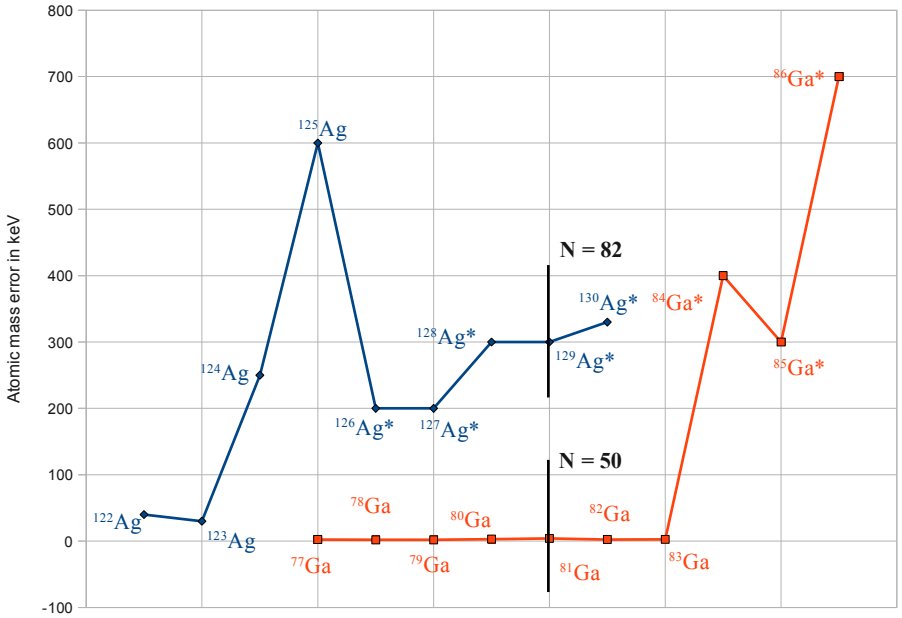

FIGURE 7.2: Comparison of mass deviation error for gallium and silver isotopes crossing the closed neutron shells N = 50 and N = 82 respectively, data from [153]: experiment, if marked by (*) - prediction

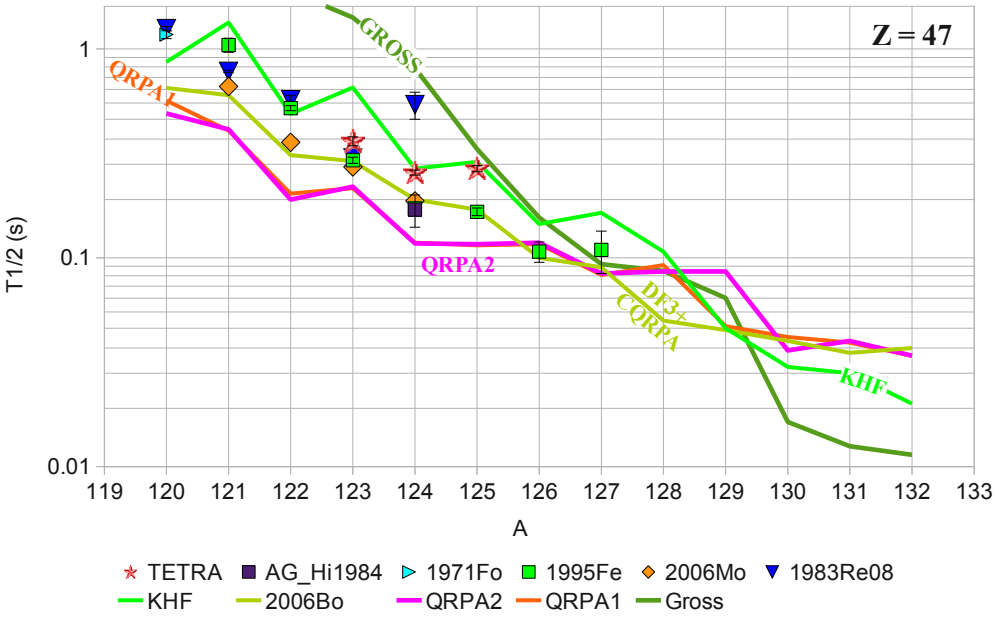

FIGURE 7.3: Half-live of neutron rich silver isotopes measured in present experiment (red stars) in comparison to other data: green squares [140]; blue triangles [137], black rhombus [138], light blue [155]. Where it is not shown, the error bars are inside the dots. Theoretical calculations: KHF - [48]; *Gross* [50]; QRPA1 - *Möller 1997*, [8]; QRPA2 - [48]; GDF3+cQRPA - QRPA calculations including allowed (GT) and forbidden (FF) transitions, *Borzov 2006*, [13].

7.3 First neutron precursor in cadmium isotope chain

Even though for Z = 48 (Cd) $Q_{\beta-n}$ gets positive at A = 126, the theoretical models predict a somewhat noticeable P_n starting at the mass 127. The first cadmium isotope recognized by NNDC [115] as a experimentally measured neutron emitter is the r-process nucleus ^{130}Cd [156, 157]. As the case of neutron-rich gallium isotopes two neutrons more after the N = 82 shell closure there is an abrupt increase in P_n (Figure 7.4). It is seen that statistical theories (*KHF* and *gross β decay theory*) treat well the P_n of ^{131}Cd but are not valid anymore for heavier isotopes. P_n values calculated by *QRPA1, 2* in the allowed (GT) approximation regularly overestimate the experimental data indicating almost 100% already for ^{131}Cd. Inclusion of FF transitions (*DF3+CQRPA*) brings the calculated values at least in a qualitative agreement with the experiment. Remarkably, the only data set for P_n of heavy neutron-rich cadmium isotopes was obtained at CERN/ISOLDE in 2000 [156, 157] by the same group. In summary, taking into account our measurements presented of delayed neutron precursor ^{126}Cd, it is important to investigate all cadmium isotopes starting from A = 126 to obtain the trend in delayed neutron emission probability across the N=82 shell closure.

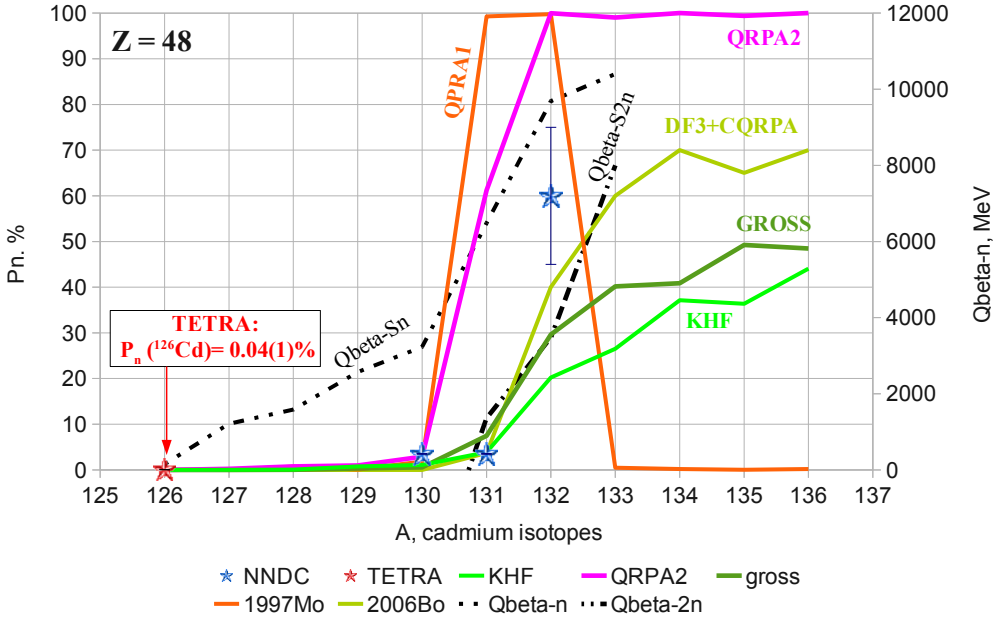

FIGURE 7.4: P_n of neutron rich silver isotopes: TETRA - measured in the present; NNDC - recognized by NNDC data base [115, 156, 157], where it is not shown, the error bars are inside the dots. Theoretical calculations: KHF - [48]; *Gross* [50]; QRPA1 - *Möller 1997*, [8]; QRPA2 - [48]; GT+FF - DF3+cQRPA, *Borzov 2006* including allowed (GT) and forbidden (FF) transitions [13]; $Q_{\beta-n}$ from [115], $Q_{\beta-2n}$ from [154]

7.4 Approaches to systematics of delayed neutron precursors

Charge displacement of delayed neutron emitter

The first estimations for P_n (probability of β-delayed neutron emission) throughout the chart of nuclei leading to systematics of delayed-neutron precursors was given by *Pappas and Keepin* long ago in 1960 and summarized in [158]. They considered the distance of a delayed neutron precursor (Z, N) from stability. For a given precursor (Z,N) it was determined as the distance of the emitter nucleus (Z+1, N-1) from the most stable charge for an isotonic chain of the emitter: $D_{st} = Z_{N-1}–Z$. The charge displacement (D_{st}) of the delayed-neutron precursor in that time gave fair approximations of P_n values and some reasonable correlations with experimental data [159]. However, this approach has not been further developed.

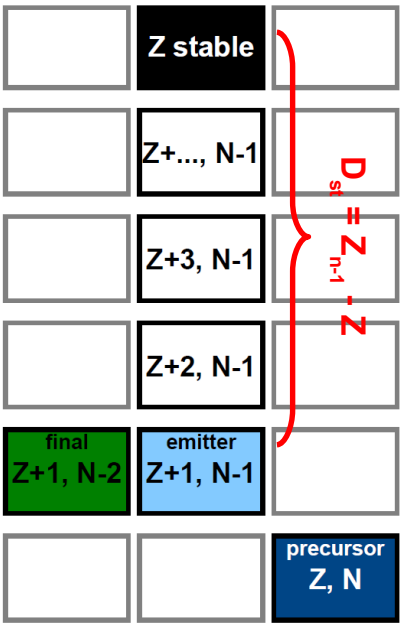

FIGURE 7.5: distance of a delayed neutron precursor (Z, N) from stability

In his further research *Pappas* related neutron emission probability to the available energy "window" ($\triangle E = Q_\beta - S_n$), to the density of available levels ($\omega_j(\triangle E)$) and to the competition between neutron (Γ_n) and γ-ray emission (Γ_γ):

$$P_n = C(\triangle E)^k \omega_j(\triangle E)\Gamma_n/(\Gamma_n + \Gamma_\gamma) \tag{7.1}$$

Based on the mass calculations available in that time [160] he obtained the upper Z limit for isotones that may be delayed-neutron precursors, Figure 7.6. He noticed that the

general trends of delayed-neutron systematics was influenced by neutron shell closures - just above the closed shells the upper limit for delayed neutron emitter is moved towards the stability. This effect increases with higher shell numbers and is roughly 1,2,3,5 charge units at the N=28, 50, 82, 126 neutron shells respectively. The minimum distance of a neutron precursor from β stability (D_{st}) depends mainly on evenness and oddness of Z_β. This is caused by paring energies involved in S_n and Q_β which results in favoring odd Z nucleides over even ones. Thus, odd-Z precursors are two units (in term of $D_{st} = Z_{N-1}-Z_\beta$) closer to stability than even ones. The lower Z limit is governed by the spontaneous emission of neutrons.

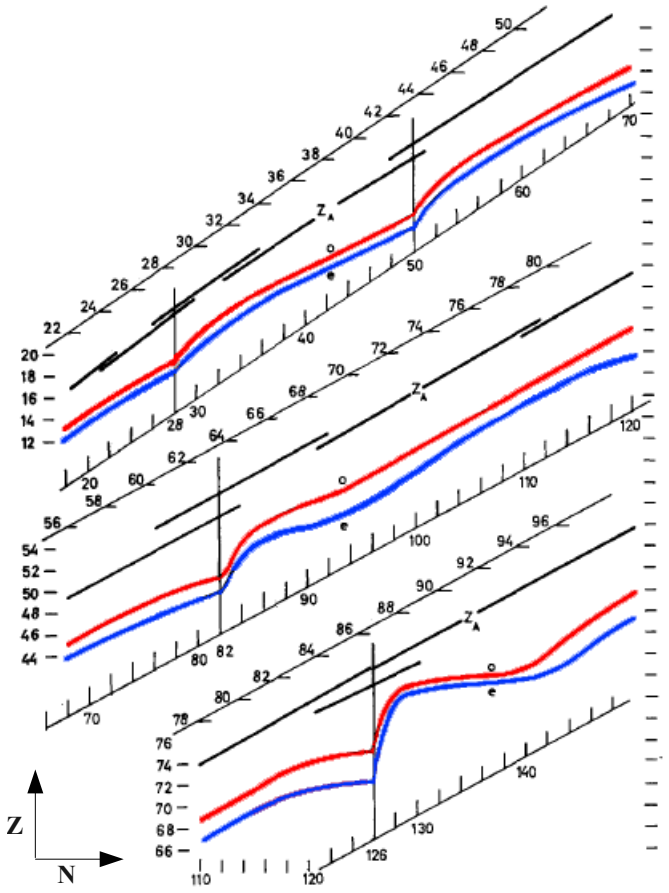

FIGURE 7.6: Systematics of delayed neutron precursors and the influence of closed shells from [158]. Z_a - stability line. Red: upper limit for odd Z nuclides showing characteristics of delayed neutron precursors; blue: same for even Z.

In Figure [115] the Pappas and Rudstam calculations are replotted (in dashed lines) in the region $50 \lesssim N \lesssim 82$ in comparison to the currently available NNDC experimental data [161] (in solid lines). As seen there are there regions where the upper Z limit has not been attained experimentally: below the shell $N \lesssim 50$; $65 \lesssim N < 82$ and $N \gtrsim 90$. The newly discovered neutron precursor ^{126}Cd (Z even) has 4 neutrons less than ^{130}Cd -

the lightest cadmium βd neutron precursor known before [157], and is illustrated by the green star. The green line is plotted assuming neutron decaying states in $^{127-129}$Cd, which is probably true since their $Q_\beta - S_n$ values are one order of magnitude bigger than the one for ^{126}Cd. Therefore, the complemented systematics for the upper-Z limit reveal the general trend similar to one observed in [158]: right after crossing the N=82 closed neutron shells the limit is moved towards stability. Here we observe the stabilizing effect with respect to neutron emission. From the P_n viewpoint there is no visible quenching of the N = 82 shell.

The region N$\lesssim$50 is less well studied which is reflected in significant deviation between the calculated curve with the current experimental data. Therefore, in order to make a conclusion concerning N=50 shell quenching new experiments, particularly for looking for very small P_n values below the shell are needed. Finally, the region N$\approx$100 has to be investigated in the same way. Though to access these nuclei further improvement of ISOL methods are required.

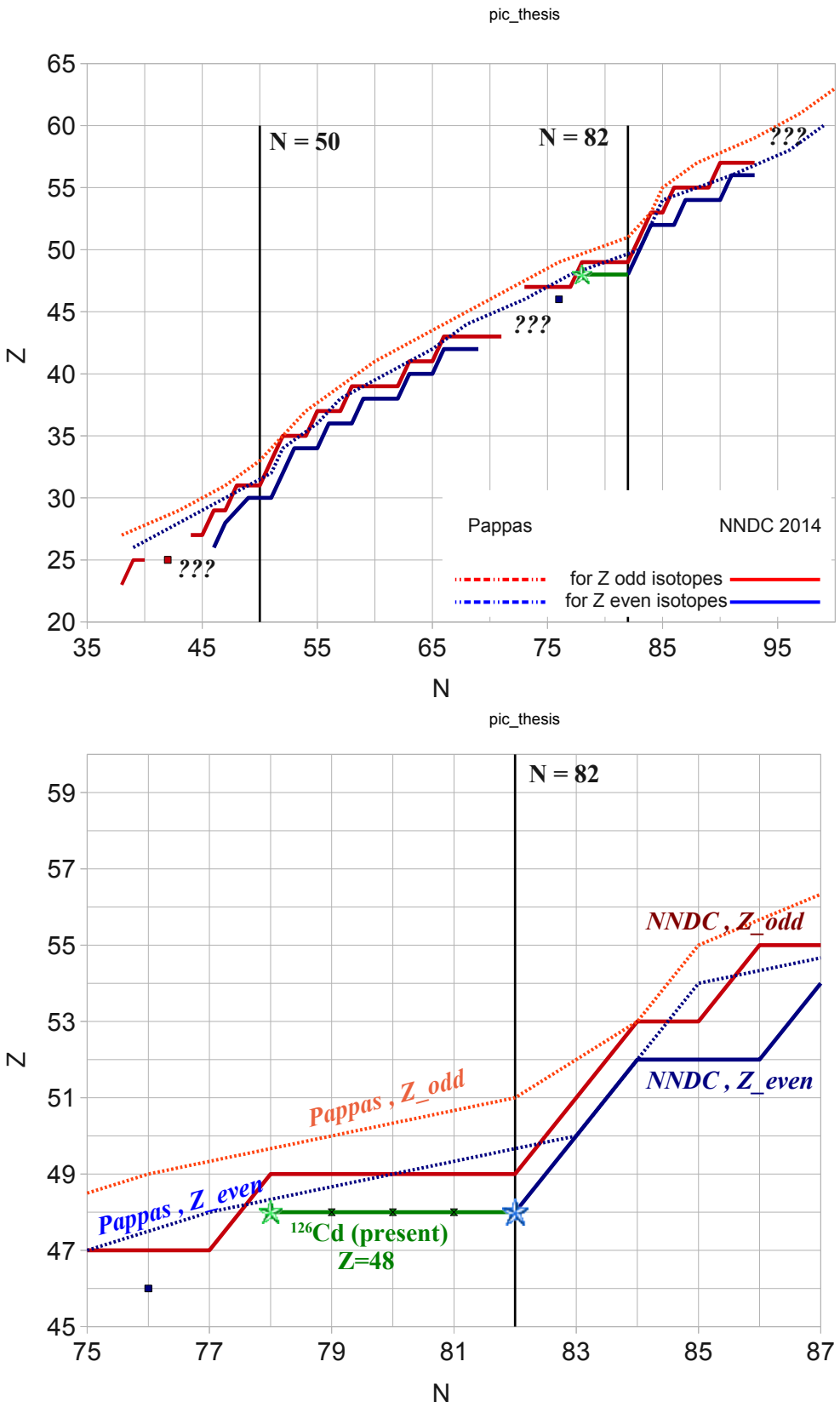

FIGURE 7.7: Systematics of delayed-neutron precursors the similar to in Figure 7.6 (dashed curves) in the region of N = 50, 82 in comparison to presently available NNDC experimental data: [115] (solid curves): in red for odd-Z nuclei; in blue for even Z nuclei; the newly proposed in the present work ^{126}Cd neutron emitter is shown by a green star. The lightest Cd neutron precursor known before ^{130}Cd is in blue star [157]; the green line shows the assumption for $^{127-129}$ to be neutron precursors.

Available energy window

As mentioned above, it is also possible to relate neutron emission probability to the available energy "window", to the density of available levels and to the competition between neutron and γ-ray emission (Equation 7.1). In the assumption that γ-ray competition, due to spin and parity effects, can be ignored, $\Gamma_n/(\Gamma_n + \Gamma_\gamma \approx 1$ (which is probably valid at higher excitation energy); and in the assumption that $\omega_j(\triangle\ E) = (\triangle\ E)^l$ then $P_n = C((\triangle\ E)^{k+l})$. Such a dependence should results in a linear plot of log P_n versus log $(Q_\beta - S_n)$ [162]. There is no distinction observed between the P_n values of "light" and "heavy" mass peaks obtained nor between even and odd masses (contrary to the previous charge displacement approach). Such effects are canceled out, as expected, by difference in the Q_β and S_n values of the corresponding transitions.

In Figure 7.8 are plotted the correlation of experimental P_n values with the $Q_\beta - S_n$ window in the vicinity of ^{78}Ni (top) and ^{132}Sn (bottom). The data obtained presently (in red stars) are compared with the NNDC data base (September, 2013) [115]. As seen the measured in the present work values agree well with the systematics described above.

However, neutron precursors for which $Q_\beta - S_n$<1MeV are excluded from the systematic approach described [162]. For $\triangle$E on the order of 1 MeV or less (250keV in case of ^{126}Cd) the narrowness of the "window" reduces the number of available levels and also the selection rules due to spin and parity effects may be more pronounced, thus P_n is expected to have a lower value (such as in case ^{126}Cd). Therefore the authors admit that the low P_n values are probably not the subject to the present statistical treatment [162].

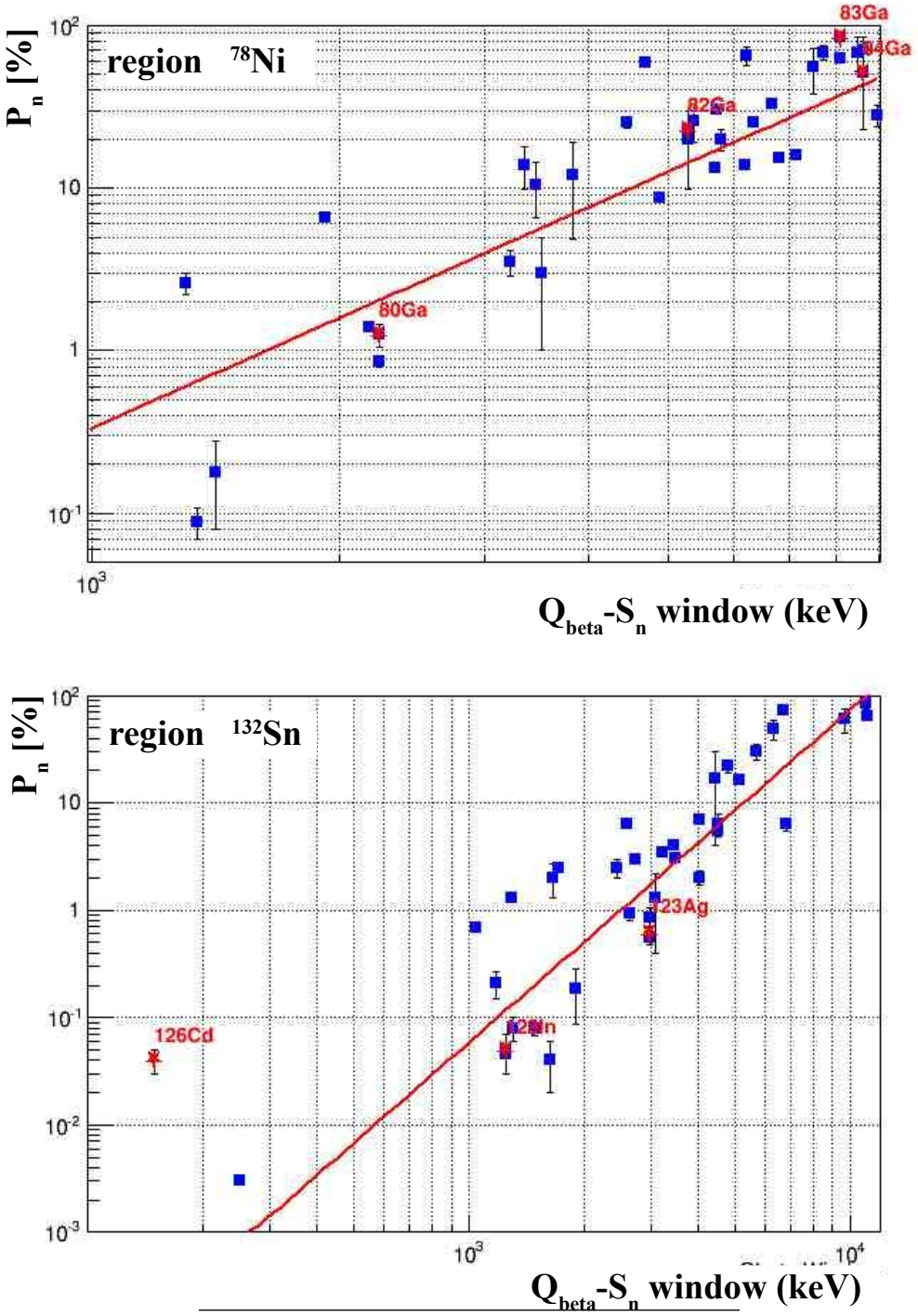

FIGURE 7.8: Correlation of experimental neutron emission probabilities with the parameter (Q_β-S_n) in vicinity of ^{78}Ni (top) and ^{132}Sn (bottom), data are from NNDC (September, 2013) [115]. Data from present work are in red stars

Chapter 8

Conclusions and outlook.

Contents

8.1 Conclusions.

To study properties of β decay of neutron rich nuclei in the frame of my thesis in collaboration with JINR, Dubna a new experimental setup was prepared.

The detection system characteristics

- efficiency for single neutron registration ∼52% measured with ^{252}Cf source (90 tubes ^{3}He);
- efficiency of $4\pi\beta$ ∼60% (plastic scintillator);
- efficiency of γ registration ∼0.8% for a 1-MeV γ-ray (HPGe detector)
- all detectors can work in conjunction;
- moving tape is used to remove unwanted radioactivity from longer lived β-decay daughters.

I took a leading role in its development/construction/commissioning in the following ways:

- MCNP simulation to estimate the best configuration for the TETRA neutron detector/shielding from the neutron background;

- design of unique $4\pi\beta$ detector;
- new support to accommodate all the neutron counters, $4\pi\beta$, HPGe detector, beam line;
- devoted *dead-time-free* electronic system allowing registration of multiple neutron events.

In parallel, at ALTO a new experimental beam line for BEta Decayed studies at Orsay was constructed. We commissioned the beam line in a specially devoted experiment. We also performed a beam guidance passing a beam from the source to the collection point. The optimum values for ion optic elements were found and checked experimentally.

I put much challenge and pressure to speed up the processes and, finally, half-way through my thesis, beginning actually from 3.2m^2 floor space, accomplished this new detection system readily installed on the new beam line. It allowed me to switch to the scientific program and to conduct two experiments - on mass separated beams of neutron rich silver/cadmium/indium isotopes in the vicinity of ^{132}Sn and on laser ionized beams of gallium isotopes in the vicinity of ^{78}Ni. The main results are as follow.

N $\sim$ 50, laser ion source (Table 8.1)

- $P_n/T_{1/2}$ measurements for ^{80,82,83,84}Ga;
- proposition of new transitions in β decay of ^{80,82,83,84}Ga observed mostly due to γ–β–n coincidence spectra;
- confirmation of existing decay schemes of ^{80,82,83,84}Ga;
- absolute branching ratio measurements for ^{81}Ge, ^{82}Ge, ^{83}Ge.

N $\sim$ 82, universal plasma ion source (Table 8.1)

- $T_{1/2}$ measurements for ^{123,124,125}Ag, ^{126}Cd, ^{127,128}In by the neutron activity curve;
- P_n measurements for ^{123}Ag, and ^{127,128}In;
- First observation and first P_n measurement of β-delayed neutron emission from neutron rich ^{126}Cd;

The role of First Forbidden decays (FF) are not so clear in the vicinity of ^{78}Ni. As it was discussed it is the case of so-called "moving theory". Therefore, from our viewpoint,

more theoretical efforts should be done to understand the role of FF transitions in this region. In contrast, in the neighborhood of ^{132}Sn more experimental challenge have to be overcome to go beyond the N=82 shell in order to determine the relative contribution of allowed and forbidden decays.

From the systematics of P_n values considered in the present study, there is no evidence of weakening of the N=82 shell at least up to Z=48. However, the data on neutron emission just below N=50 are highly needed to confirm from the "P_n viewpoint" the possible shell quenching in the vicinity of ^{78}Ni.

Thus TETRA was proved to be a versatile scientific tool for measurements of I_β, $T_{1/2}$ and P_n for neutron-rich nuclei produced with both the laser and the universal plasma ion sources. Also TETRA can play a significant role in the spectroscopic structure studies thanks to γ–β–n coincidence technique. In γ spectra gated by β and by n, transitions irrelevant to the β–n decaying branch transitions are suppressed. Moreover, we found that a neutron activity curve was an extremely useful tool to obtain a first clue (even on-line) on $T_{1/2}$ of a neutron precursor of interest if it is the only neutron emitter on its isobaric chain or if the contribution of other neutron emitters is negligible such as ^{82,83}Ga, $^{123-126}$Ag, ^{127,128}In . The simple fit directly provides the half life of the precursor. The practical limit of nuclei to be studied at TETRA is mostly determined by beam purity. As it was shown, we have reached the limit of the plasma ion source and investigation of more neutron rich nuclei at ALTO can be possible only with the laser ionized beams.

The TETRA neutron detector is accessible now in two configurations - the single moderator support constructed within my thesis, or originally available geometry of "neutron modules" in which each counter is placed in its individual piece of moderator. Essentially, that electronic system developed can be used as a stand-alone module but it is fully compatible with any modern data acquisition system. Therefore, TETRA can also be employed at any existing In-Flight/ISOL RIB facility. It's worthwhile to say that there are two proposals to use TETRA from third parties (outside the collaboration JINR Dubna-IPN Orsay) already approved in 2013: one by ALTO PAC and the second by GANIL PAC.

TABLE 8.1: $T_{1/2}$ and P_n for neutron rich gallium and silver isotopes. NNDC w.a. - weighted average from NNDC data base [115]

	$T_{1/2}$ *(s)*	P_n *(%)*	*method*	*Reference*
A = 80				
^{80}Ga (mixed)	1.77(24)	1.26(20)	n	*present*
^{80}Ga (J=6)	-	2(1)	n	*present*
^{80}Ga (J=3)	-	≈0	n	*present*
	1.66(2)	0.84(6)	n	[123]
	1.69(1)	0.69(16)	n	[121]
	1.65(1)	0.97(6)	n	[120]
	2.85(1)	0.55(4)	n	[122]
	1.66(2)		n	[134]
	1.7(1)		n	[148]
^{80}Ga (6)	1.9(1)		γ	[118]
^{80}Ga (3)	1.3(2)		γ	[118]
A = 82				
^{82}Ga	0.604(11)	22.4(2.0)		*present*
	0.599(2)			[125]
	0.602(6)	19.8(1)		[122]
		21.4(22)		[123]
		31.1(4)		[120]
A = 83				
^{83}Ga	0.308(1)	84.8(3.6)	n	*present*
		62.8(25)	γ	[27]
	0.319(24)		γ	[25]
	0.307(7)	14.9(18)	n	[120]
	0.308(1)		n	[125]
	0.310(10)	57(7)	n	[122]
	0.310(10)	43(7)	n	[123]
	0.310(10)		n	[134]
A = 84				
^{84}Ga	51(28)	-	n	*present*
	74(14)		γ	[27]
	80(15)		γ	[28]
	47(10)			[136]
		0.070(35)	γ	[25]
	70(15)	0.085(10)	n	[125]
A = 123				
^{123}Ag	0.396(15)	0.6(25)	n	*present*
	0.272(24)	1.0(5)	γ, β	[138]
	0.293(1)		n	[140]
	0.35(4)		γ	[139]

Continued on next page

Table 8.1 – continued from previous page

	$T_{1/2}$ *(s)*	P_n *(%)*	*method*	*Reference*
	0.30(3)		γ	[163]
	0.30(1)	0.55(7)	n	[137]
	0.39(3)		n	[149]
A = 124				
^{124}Ag	0.256(7)	-	n	*present*
	0.187(15)	1.3(9)	γ, β	[138]
	0.172(5)		n	[140]
	0.54(8)		n	[137]
	0.187(15)		n	[138]
	0.17(3)		γ	[141]
A = 125				
^{125}Ag	0.267(9)	-	n	*present*
	0.166(7)		n, b	[140]
A = 126				
^{126}Cd	0.514(40)	0.040(1)	n	*present*
	0.506(15)		γ	[142]
	0.51(1)		γ	[145]
	0.60(3)		γ	[143]
A = 127				
^{127}In 9/2+	1.218(95)	-	γ	*present*
		<0.3	n	[123]
		<0.15	γ	[150]
	1.09(1)		γ,n	NNDC w.a.
^{127}In 1/2-	3.017(32)	-	γ	*present*
		0.68(6)		[123]
		0.54(11)		[120]
	3.67(4)		γ, n	NNDC w.a.
^{127}In	2.276(0.025)	<0.1	n	*present*
A = 128				
^{128}In(g.s.)	0.889(26)	0.074(10)	γ, n	*present*
		0.06[1]		[120]
	0.80(3)		γ	[143]
^{128}In(8-)		0.12(3)		*present*
		0.121		[120]
	0.72(10)		γ	[143]
^{128}In mixed	0.889(26)	0.046(16)	n	*present*
	0.776(24)	0.04(3)	n	[120]

Continued on next page

[1] adopted by NNDC with a reference to [120] if all neutrons originate from the decay of the g.s. or (8-) state (no error bars are given)

Table 8.1 – continued from previous page

	$T_{1/2}$ *(s)*	P_n *(%)*	*method*	*Reference*
	0.83(2)	<0.2	n	[150]
		0.059(8)		[123]
	0.80(3)		n	[148]
	0.94(6)		n	[149]

8.2 Perspectives

In the short-term within the framework of the JINR-IPN collaboration, two BEDO detection setups will be extended allowing "parallel" beam installation. TETRA, reinforced by two extra germanium detectors to allow γ–γ–β–n coincidence, will be installed on a special devoted beam-line also equipped with a tape moving station. Therefore, a radioactive source can be accumulated simultaneously at two detection systems (TETRA & γ-BEDO). The collection period at TETRA will correspond exactly to the decay period at γ-BEDO and vice versa (Figure 8.1). Thus, in the same experiment a nucleus can be studied in a more complete way: at the detection system with high neutron efficiency (TETRA) and at the setup with high γ efficiency (γ-BEDO).

This opens tremendous opportunities for our collaboration to access new nuclear structure information in the still unexplored region of heavy neutron rich nuclei far from stability. In the ^{78}Ni region it is already proposed further investigation of gallium (^{85,86}Ga) with possible observation of double neutron emission and measurements of $T_{1/2}$, P_{1n}, P_{2n}. Even if TETRA was originally aimed at measurements of absolute branching ratios in β decay, it came out to be extremely useful in exploring nuclear structure, which is, surprisingly, even for "less neutron rich" gallium isotopes (e.g. $^{80,81,82,83}Ga$) not yet well studied and understood. Whereas, in the vicinity of ^{132}Sn predicted 2n-emission from ^{134}In and ^{136}Sb will be studied. At the same time study of β decay properties of exotic silver isotopes ($^{124-130}$Ag) will be extended with the laser ion source.

In the long-term, TETRA will participate in systematic studies of neutron-rich nuclei, specifically in vicinities of closed neutron shells, until the maximum extent of ALTO production is reached. The enthusiasm of researchers, based on breathtaking results to be obtained, will definitively push them to bring all the experience accumulated to *SPIRAL-2*/*DRIBS-3*-facilities to fall, finally, into even more unexplored regions of the chart of nuclides to solve the mysteries of the Universe...

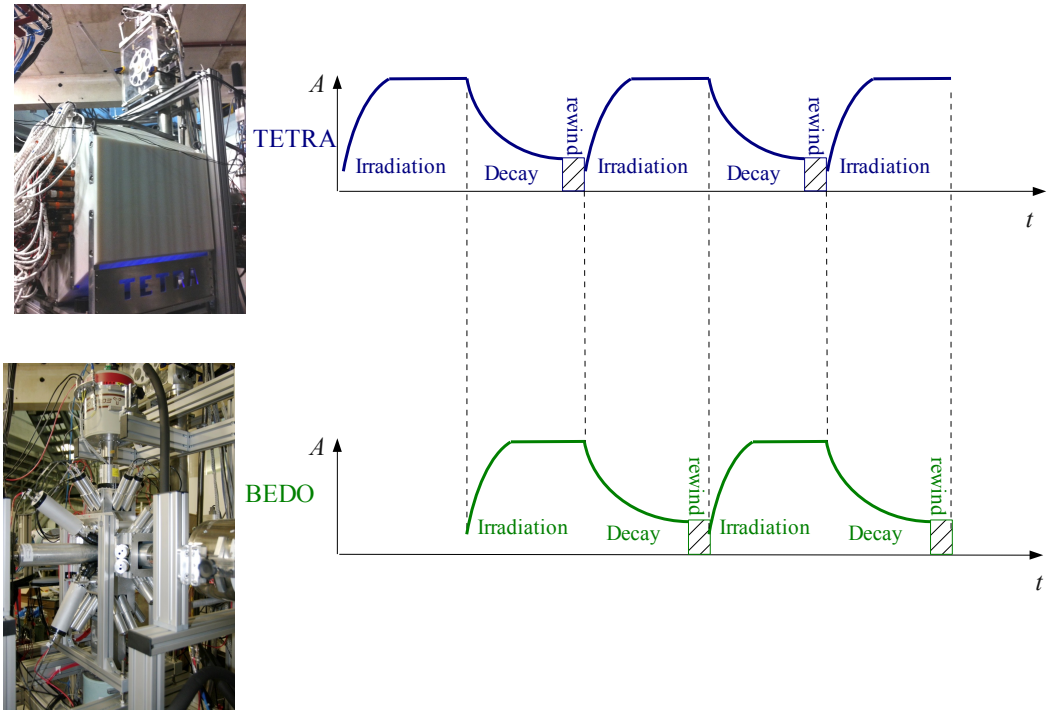

FIGURE 8.1: Project TETRA-BEDO on "parallel" beams

Appendix A

Neutron detectors

Contents

A.1 History

The history of the neutron began on June 1, 1932, when J. Chadwick published his article entitled, ,,The existence of the neutron". In this article he published observations on recoil atoms produced by the neutron radiation. Shortly afterwards, in 1936, a number

of works to systematically describe the absorption and scattering properties of slow neutrons on different materials were carried out [164].

One of the principal difficulties researchers faced in measurement of the total number of neutrons emitted by various sources arose from the fact that the neutrons are usually heterogeneous in energy. Already in 1937 E. Amaldi wrote that detectors available at that time responded differently to neutrons of different energies [165]. The difficulty was avoided by a method proposed by Amaldi and Fermi who observed that all neutrons emitted from a source can ultimately be moderated to thermal energies if the source is put in a large body of water [164]. The efficiency of neutron detection depended on the distance which the neutrons had to go inside a water tank until reaching a detector. The examination of the number of slow neutrons as a function of the distance from the source in such a water bath gave additional information regarding the energy of the neutrons.

A neutron detector which had a uniform efficiency for neutrons of wide energy range has many advantages for certain types of measurements. A huge water bath containing slow-neutron detectors at some point fulfilled this requirement and was particularly useful. However, by 1947 it became clear that for many experiments using a large bath brought erroneous results due to the effect of the degraded neutrons reflected from the bath into the experimental setup. In order to achieve a high efficiency in a detector of reasonable size a boron neutron detector was embedded in paraffin, which acted as a moderator analogous to the to water tank. The first detector constructed consisted of a boron lined ionization chamber 20 cm long, surrounded by a cylinder of paraffin 17 cm in diameter. Preliminary tests on the sensitivity of this counter showed that the sensitivity was very nearly the same for neutron energies of from 0.4 MeV to 2 MeV. These tests encouraged the further development of the similar neutron counters. It is worthwhile to mention that theoretical approaches to describe the detection sensitivity are complicated and were not available that time [166]. Fortunately, with the first accelerators providing a mono energetic neutron flux (Van de Graff) the neutron-proton and neutron-carbon scattering cross sections were measured [167] which helped qualitatively understand the behavior of these counters: neutrons entering the paraffin slowed down primarily by the hydrogen atoms to thermal energies and then, some of them are captured by the central thermal neutron detector, less energetic neutrons need fewer collisions before become thermal whereas high energetic ones thermalised in a bigger width of paraffin.

A.2 Mechanisms for neutron detection

Mechanisms for detecting neutrons in matter are based on indirect methods since neutrons, as their name suggests, are neutral. Also they do not interact directly with the

electrons in matter, as γ rays do. The process of neutron detection begins when neutrons, interacting with various nuclei, initiate the release of one or more charged particles. The electrical signals produced by the charged particles can then be processed by the detection system. Two basic types of neutron interactions with matter are available. In the first one a neutron can be scattered by a nucleus, transferring some of its kinetic energy to the nucleus [61]. If enough energy is transferred, the recoiling nucleus ionizes the material surrounding the point of interaction. This mechanism is only efficient for neutrons interacting with light nuclei. In fact, only hydrogen and helium nuclei are light enough for practical detectors. The second is when a nuclear reaction provoked by the neutron occurs. The products from these reactions, such as protons, alpha particles, γ rays, and fission fragments, initiate the detection process. Although, some reactions require a minimum neutron energy (threshold), most of them take place at thermal energies. Detectors exploiting thermal reactions (reaction with a maximum cross section in the thermal energy range of the neutron) are usually surrounded by moderating material. Detectors employing either the recoil or reaction mechanism can use solid, liquid, or gas-filled detection media. Although the choice of reactions is limited (some reactions are listed in A.3.1), the detecting media can be quite varied, leading to many options [61].

Generally, the energy information obtained in neutron detection systems is poor because of the limitations of the available neutron-induced reactions. Recoil-type counters measure only the first interaction event. The full neutron energy is usually not deposited in the detector, and the only energy information obtained is whether a high- or low-energy neutron initiated the reaction. Reaction-type counters take advantage of the increased reaction probability at low neutron energies by moderating the incoming neutrons. But knowledge of the initial neutron energy before moderation is lost. The energy recorded by the detector is the reaction energy (plus, perhaps, some of the remaining initial neutron energy). Thus, in general, neutron detectors provide information only on the number of neutrons detected and not on their energy. Information on the range of detected neutron energies can usually be inferred from the detector type and the surrounding materials [61]. If information on the neutron energy spectrum is needed, it can sometimes be obtained indirectly, as discussed in Section A.6.

A.3 General aspects of gas-filled detectors

Gas-filled detectors were among the first devices used for radiation detection. After the initial interaction with a neutron, the detection equipment for all types of gas detectors

is similar. However, there might be a difference in high-voltage or amplifier gain settings to compensate for changes in the amplitude of the detected signal.

Usually the exterior appearance of a gas detector is a metal cylinder with an electrical connector. Detector walls are about 0.5 mm thick and are mostly manufactured from either stainless steel or aluminum. Steel is preferred quite often, even though aluminum absorbs much less (0.5 %) of neutrons in comparison to 3% absorption level in steel. But steel requires less careful handling during assembly, the connecting threads are less susceptible to galling, and impurities can be kept lower. In very low count-rate applications, a background of about 1 count/min has been observed and attributed to radium impurity in aluminum [168, 169]. The central wire is typically 0.03-mm-thick gold-plated tungsten. Tungsten provides tensile strength for the thin wire, and the gold plating offers improved electrical conductivity. The wire is held in place by ceramic insulators.

The detection of neutrons requires a part of the full transfer of neutron energy to charged particles. The charged particle ionizes and excites the atoms along its path until its energy is exhausted. With no high voltage applied the ions recombine without producing any output signal. With a positive voltage applied to the central wire (anode), the electrons will move toward it and the positively charged ions will move toward the tube wall (cathode). An electrical output signal is produced whose magnitude depends on the applied voltage, the geometry of the counter, and the gas. These parameters determine whether the detector operates in the ionization region, the proportional region, or the Geiger-Mueller region. These different operating regions are fully described elsewhere [168]. Gas filled *neutron* counters are operated in the proportional region where the electric field strength is large enough for avalanche ionization. Note that in the proportional region the charge collected is linearly proportional to the energy deposited in the gas.

Only a small region around the wire is involved in the multiplication (avalanche) process. In the rest of the volume, the electrons drift toward the anode. Because the amplification process requires a very high electric field, an advantage of the cylindrical detector design is the high electric field near the inner wire. The total amplification is proportional to the electronic field traveled [168].

Because the avalanche is formed near the anode wire, the electrons with a larger drift velocity are collected in an extremely short time interval (within 10^{-8} s); the slower drifting positive ions are collected on the cathode over a much longer time. The pulse reaches maximum amplitude only when the positive ions are fully collected. For a typical counter operated in proportional mode this collection process may take up to 200 μs.

This time dispersion depends on tube voltage, diameter and has been reported [170] as 1.1μs (CH_4); 2.5 μs (^{3}He), and 17μs (^{4}He) for typical gas-filled tubes.

	Detection media	Incident Neutron Energy	Detection efficiency (%) under optimum conditions	Gamma-Ray Sensitivity (R/h)	Interaction probability, Neutron	Interaction probability 1-Mev Gamma Ray	Cross-talk	Time-scale	Range of neutron energy	Operating High Voltage, keV	Price 1)
Plastic scintillator	^{1}H	1 MeV	70	0.01	0.78	0.26	yes	10-100ns	20keV 20 MeV		
Liquid scintillator	^{1}H	1 MeV	70	0.1			yes	10-100ns			
Loaded scintillator	^{6}Li	thermal	50	1							
Hornyak button	^{1}H	1 MeV	1	1							
Methane	^{1}H	1 MeV	1	1							
^{4}He	^{4}He	1 MeV	1	1	0.01	0.001		10-100ns			
^{3}He + Ar	^{3}He	thermal	70	1	0.77	0.0001	no	100 us	<2MeV	1.2-1.8	0.5-1M$
^{3}He + CO_2	**^{3}He**	**thermal**	**70**	**10**	**0.77**	**0.0001**	**no**	**100 us**	**<2MeV**	**1.4-2.8**	**0.5-1M$**
BF_3	^{3}He	thermal	30	10	0.29	0.0006	no	100 us	<2MeV	0.6-0.8	
^{10}Bo-lined chamber	^{10}B	thermal	10	1000							
Fission chamber	^{235}U	thermal	0.5	10^{6}							

TABLE A.1: Comparison of different types of neutron detectors. The line stressed by bold text corresponds to TETRA-type detector

A.3.1 ^{3}He and BF_3 proportional counters

In ^{3}He gas, a neutron causes the breakup of the nucleus into a tritium nucleus (^{3}H) and a proton (^{1}H). The triton and the proton share the 765-keV reaction energy. In the case of ^{10}B, the boron nucleus breaks up into a helium nucleus (α particle) and a lithium nucleus, with 2310 keV shared between them. Ninety-four percent of the time the lithium nucleus is left in an excited state from which it subsequently decays by emitting a 480-keV γ ray. This γ ray is usually lost from the detector, and only 2310 keV is deposited. About 6 % of the time the lithium nucleus is left in the ground state, so that 2790 keV is deposited in the detector. This double reaction mode yields an additional small full-energy peak in the pulse height spectrum of BF_3 tubes.

Figure 3.1 illustrates the cross section for the ^{3}He reaction (3.1) which is 5330 b for thermal neutrons and the cross section for the ^{10}B reaction (3.2) which is about 3840 b for thermal neutrons [62]. Both reaction cross sections strongly depend on the incident neutron energy E as $E^{-1/2}$ [61]. Practically, the nearly optimum efficiency is achieved with tubes at 4 atm of ^{3}He. Increasing the quantity of the gas gives relatively little additional efficiency and are usually not cost-effective (see simulations in §3.7). The detailed study of gas pressure for effects ^{3}He and BF_3 has been performed recently in [171]. Due to the problem of shortage of the ^{3}He gas these days the society has to devote efforts to find a commercial accessible alternatives to it. In this light using low pressure detectors with lower quantity of ^{3}He takes new meaning.

A pulse-height spectrum for a BF_3 proportional counter is in the range of 5 to 30% (FWHM) but usually is not as good as for ^{3}He . To compensate for lower gas pressure, which is typical 0.2-2 atm., the diameter of the tube is bigger (5 cm) and the operating voltage is higher than for ^{3}He (Table A.1). Plateau curves are similar to those of ^{3}He . Being less expensive than ^{3}He inert gas, BF_3 gas, however, is toxic. Ironically, transport regulations classify detectors with more than 2-atm filled pressure in the high-pressure compressed gas category, so that ^{3}He detectors are always more difficult to ship. ^{3}He and BF_3 detectors find many applications in passive and active neutron assay because they are relatively stable, efficient and γ-insensitive.

A.3.2 Fast Gas Filled Neutron Detectors

^{4}He and CH_4 fast-neutron detectors rely on the recoil of light nuclei to ionize the gas in the tube. The interaction is the elastic scattering of the neutron by a light nucleus. If the recoiling nucleus is only a hydrogen nucleus (proton), the maximum possible energy transfer is the total neutron kinetic energy E. For heavier elements the maximum energy

transfer is always less. Therefore, hydrogen is the most obvious choice. It can be used in a gaseous form or, more commonly, in liquid or plastic scintillators. Popular gas detectors usually employ methane (CH_4) with a high hydrogen content or ^{4}He, which has a maximum energy transfer of 0.64 E(n). (^{3}He gas is also a suitable candidate by these criteria but it is usually not used because of the stronger thermal reaction described in A.3.1). The efficiency for detecting a fast neutron by an elastic scattering interaction is about 2 orders of magnitude lower than the efficiency for capture of a thermal neutron (for ^{3}He gas). Thus a single ^{4}He or CH_4 tube has an intrinsic efficiency of about 1 %, Table A.1. Because of the low γ-ray sensitivity, neutron counting can be done in γ-radiation fields of roughly 1 R/h if a moderately high threshold is set to reject low-energy noise and γ-ray events, but low enough to collect many of the medium-and high energy neutron events. Since the threshold must be set on a sharply falling curve, a recoil detector is not as stable as a thermal detector. Despite the apparent disadvantages of recoil-type detectors in terms of lower efficiency and stability, the detection process takes place without prior thermalisation of the incident neutron. Thus the neutron is detected very rapidly and thus are useful for fast coincidence counting with 10- to 100-ns resolving time. Fast-neutron counters can detect neutrons in the energy range of 20 keV to 20 MeV [168].

A.3.3 Gamma ray sensitivity of neutron detectors

The neutron detectors described in this paper are sensitive in some degree to γ rays as well as to neutrons. γ-ray sensitivity of the detector becomes extremely crucial when working in big γ-ray fluxes, precisely for measurements of spent fuel. Basically, in any detector, a γ ray can transfer energy to electrons by Compton scattering, just as neutrons transfer energy to other nuclei by scattering or nuclear reactions. In gas-filled detectors electrons produced by γ-ray interactions evoke small avalanches within the tube volume. As the gamma-ray dose increases, the avalanches begin to pileup and produce pulses that are large enough to exceed the preamplifier energy discriminator threshold for neutron events and are erroneously counted as neutrons [172]. Even if pulses are smaller in amplitude they can pile up within the resolving time of the electronics to yield pulses comparable to neutron pulses [61]. Compton scattering also can take place in the detector walls. Since the wall material is immediately adjacent to the active gas volume yielding high-energy photo electrons which produce a column of ionization as it traverses the detector and consequently pileup.

To understand the origins of γ-ray pileup in ^{3}He tubes, it is useful to examine the construction of a ^{3}He tube: a steel/aluminum cylinder with central wire, filled with

gas. γ-rays can interact in the gas volume itself, in the getter compound[1], and in the tube wall. We ignore the possibility of a γ-ray interacting directly with the anode wire because of its small size. Therefore, these materials should be considered when evaluating the relative magnitudes of the neutron and γ-ray signals. Properties of some materials to absorb neutrons are significantly higher. Table A.1 illustrates an interaction probability for neutrons and γ-rays for thermal and fast neutron detectors. As it can be noticed, thermal neutrons can be absorbed with much higher probability than γ rays. Whereas for fast-neutron detection the neutron and γ-ray probabilities are comparable. Additionally, in some detectors neutrons deposit more energy than γ-rays do. Neutrons may induce a nuclear reaction that releases more energy than the Compton scattering of the γ ray imparts to the electron. Table A.1 also shows that for fast-neutron detection by plastic scintillators the relative neutron and γ-ray energy deposition is comparable.

The charge collection speeds for neutron and γ-ray detection may be different. This effect dependents on the choice of fill gas or scintillator material. In gas detectors, the long range of the electron produced by a γ-ray interaction means that energy will be deposited over a greater distance, and more time will be required to collect it. An amplifier with fast differentiation will then collect relatively less of the charge released by a γ-ray interaction than a neutron interaction. In scintillators, there is less distinction between the two kinds of events. Under some circumstances, however, pulse-shape discrimination between neutrons and γ rays can be achieved (see Section A.4.3).

To achieve good γ-ray discrimination, it is often necessary to use materials or material densities that are not optimum for neutron detection. The result may be a reduced neutron detection efficiency. Ref. [168] gives a sample list of the neutron detection efficiency and approximate γ-ray radiation limit for various neutron detector types.

Finally, installation of a simple shield consisting of a few centimeters of lead can absorb up to 90% of γ rays whereas the neutron flux goes through almost undisturbed (roughly, absorption level for 1 MeV neutrons after 5 cm of lead is around 0.1%) [61]. However, for measurements with low neutron rates, massive lead shielding can produce more neutrons from cosmic-ray spallation than originate from the sample.

Both ^{3}He and BF_3 detectors have high efficiency for thermal neutrons and energy deposited in both gases by the neutron interactions is bigger than by γ-ray interactions, as indicated in the Table A.1. However, at certain γ-ray doses the response function of the detectors is disturbed: for ^{3}He detectors (4 atm) containing argon (2 atm) the practical operating limit is on the order of 1 R/h [173]. Over this limit neutrons and γ-rays cannot be effectively distinguished. One solution to improve the detector performance in high intensity γ-ray fluxes is a gas admixture.

[1] getter compound - see §A.3.4

A.3.4 Different gas mixtures

^{3}He tubes include a gas admixture (quench gas) to affect the operating characteristics of the tube by minimizing the avalanche volume and the time of the charge collection. Although implementation of the typical gas admixtures like argon or methane results in excellent high count rate performance for pure neutron applications, in γ-ray fields this mix is a very poor performer because of its high Z (18) value - which is a primary γ-ray target; and the methane is subject to radiolytic decomposition under prolonged exposure [169].

Replacement of the argon admixture by CO_2 or N_2 mixtures produces a slower tube response, but due to lower interaction cross-section with γ-rays, can be operated in higher γ-ray dose environments. In choosing between N_2 and CO_2 quench gases, the first one is slightly slower, but offers a longer lifetime under prolonged high exposure, because CO_2 is likely to decompose into CO and free oxygen. This chemical change would affect the tube characteristics over time. Disassociated N_2 will recombine without alteration of the tube properties. Therefore, the N_2 quench gas is of interest for permanent installation into high-dose environments [172].

The performance of BF_3 detectors in terms of γ sensitivity is slightly better than ^{3}He because, as it can be seen from Table A.1, the ^{10}B reaction deposits more energy in the gas. The cross section for a gamma-ray interaction depends on the relative amounts of ^{3}He + argon, or BF_3; on the relative tube wall material and thicknesses. Although BF_3 detectors can operate in γ-radiation fields up to 10 R/h, which is better than the performance of ^{3}He + argon, the performance of ^{3}He + CO_2 counters is almost comparable.

A tube behavior in high intense γ environment is crucial when, for an example, measuring freshly discharged spent fuel, and not the subject of the present thesis. Here it is sufficient to mention that ^{3}He neutron proportional counter tubes for use in high γ-ray fields are typically coated on the inner wall with activated carbon. The carbon acts as a getter compound to adsorb gas impurities. The detailed discussions can be found elsewhere [169, 172].

A.3.5 Radiation damage to ^{3}He counters

Operating ^{3}He or BF_3 filled counters in high intense neutron fluxes may cause radiation damage due to the buildup of gaseous poisons (e.g. electronegative gases) inside the tubes. For example, in a BF_3 filled detector three fluorine atoms are released with each neutron capture. The fluorine atoms will combine with electrons released in subsequent

neutron captures [168]. Progressive irradiation of a ^{3}He tube results in effects from reduction of electric pulse amplitude (in a neutron flux of 9x10^{12}n/cm^2 over a period of $\sim$ 700h) to complete deterioration of a tube (2.6x10^{13}n/cm^2 over a period of $\sim$ 700h) [174]. However, a layer of charcoal coated on internal walls absorbs electronegative gases that buildup during the radiation.

The test [174] indicates that it should be possible to get many years of service from ^{3}He tubes when they are used in a pulsed neutron field for the application dedicated precisely to delayed neutron emission from fission products.

A.3.6 ^{3}He gas: production and commercial use. Global shortage.

Supplies of ^{3}He almost entirely come from the decay of tritium used in nuclear weapons in the US and Russia. The sole method currently used to produce the inert gas ^{3}He is simply collecting it as a byproduct from the radioactive decay of tritium [^{3}H($T_{1/2}$= 12.3 y) $\rightarrow$ ^{3}He + β], where it is separated during the tritium cleaning process. Stores of tritium must occasionally be processed to remove the ingrown ^{3}He and maintain the desired tritium concentration. This tritium comes from the refurbishment and dismantlement of the nuclear stockpile. The production of ^{3}He from tritium decay has declined as the nuclear weapons stockpile has been reduced, resulting in a lowered need for tritium to maintain the stockpile. In Reference [175] more information concerning the current capacity for production of ^{3}He gas is given.

Neutron detection is an essential aspect of interdiction of radiological threats for security purposes, since plutonium, a material used for nuclear weapons, is a significant source of fission neutrons. Radiation portal monitoring systems, of which there are thousands deployed for the security and non-proliferation purposes, currently use ^{3}He gas-filled proportional counters for detecting neutrons [175]. There are also uses for ^{3}He in private industry, such as well logging in the oil and gas industry, medical applications, basic research projects in nuclear and condensed matter physics, and as part of the coolant in helium dilution refrigerators [176]. It should be noticed that need for the gas has been astonishingly increased recently, whereas its production has become less. Nowadays commercially offered detectors are incredibly expensive and are hardly affordable to the fundamental science. That is why the ^{3}He detectors which are employed by scientists now are beyond price.

A.3.7 Alternatives to ^{3}He

It is very difficult to meet the performance capability of ^{3}He for neutron detection, and there are no existing alternatives that combine all the capabilities of ^{3}He. When considering neutron detection characteristics, only complete systems of comparable physical size (or smaller) can be included. The required characteristics of any detector system are: neutron detection efficiency, γ-neutron separation, commercial availability, and robustness for deployment. The available alternative technologies to ^{3}He for neutron detection include BF_3 filled proportional counters, Boron-lined proportional counters, Lithium-6 loaded glass fibers, non-scintillating fiber optic coated with scintillator and lithium [177]. Some of their properties, advantages and downsides were listed briefly previously. Also there are technologies mentioned but not yet available or non-viable or not studied enough yet [175].

Possible temporary solutions that could be utilized while a more permanent solution is being identified have been introduced in [171]. The idea is to reduce the ^{3}He pressure in the proportional counters and to use boron trifluoride gas-filled proportional counters. Reducing the mount of ^{3}He would decrease the rate at which ^{3}He is being used. It is definitely not enough to solve the shortage, but perhaps enough to increase the amount of time available to find a working replacement. Boron trifluoride is not appropriate for all situations as these detectors are less sensitive than ^{3}He, boron trifluoride gas is corrosive, and a much higher voltage is required than what is used with ^{3}He detectors.

A.4 Some other types of neutron detectors

A.4.1 Fission Chambers

Fission chambers are a variation of the gas-filled counters previously described. They detect neutrons that induce fissions in fissionable material, coated on the inner walls of the chambers. Often the exterior appearance of fission chambers is quite similar to that of other gas counters, although they are also available in smaller diameters or in other shapes. The fissionable material is usually uranium highly enriched in ^{235}U. A very thin layer (0.02 to 2 mg/cm^2 surface thickness) is electroplated (sometimes evaporated or painted) on the inner walls. The thin layer is directly exposed to the detector gas. After a fission event, the two fission fragments travel in nearly opposite directions. The ionization caused by the fission fragment that enters the gas is sensed by the detector, the fragment traveling in the opposite direction is absorbed in the detector walls. The two fragments share about 160 MeV of energy, but their range is quite short (for uranium

the average fission fragment range is only about 7 μm, equivalent to about 13 mg/cm^2 of coating thickness). Consequently, fission fragments that are produced at a depth of more than 7 μm in the detector wall cannot reach the gas to cause ionization. Furthermore, most fragments exit at a grazing angle, so that their path length is longer than the minimum needed to escape. Because the coating must be kept thin to allow the fission fragments to enter the gas, the fission chamber uses only a small quantity of fissionable material and has a low detection efficiency. For thermal neutrons, the intrinsic efficiency is typically 0.5 to 1%. Fast neutrons can also be detected, but with even lower efficiency. A mixture of 90% argon and 10% methane is a common fill gas, the voltage applied is in the + 200 to 600 V range.

Because of the large quantity of energy deposited by the fission fragments, fission chambers have the highest sensitivity to γ rays (roughly 10^6R/h) of any of the neutron detectors. Also, an alpha particle background is present at low energies because nearly all fissionable material contains α-emitting isotopes. The α-particle energy is typically 5 MeV, whereas the fission fragment energy is an order of magnitude larger. Thus the threshold setting of the counting electronics can be set above the α-induced signal. At this threshold setting, some of the low-energy fission-fragment pulses will be lost. Plutonium has a much higher alpha activity than uranium; as a consequence more alpha pulses pile up and the threshold for plutonium-lined fission chambers must be set higher than for uranium-lined chambers.

However, despite of its disadvantages, they are the only detectors capable of direct unshielded neutron measurement of spent reactor fuel. This passive measurement feature applies to both high neutron and γ-ray fluxes. The inherently low efficiency of fission chambers is compensated for by the large number of neutrons available for counting [168].

A.4.2 ^{10}B-Lined Detectors

Detectors lined with ^{10}B lie between ^{3}He and BF_3 proportional counters and fission chambers in terms of neutron detection efficiency and γ-ray insensitivity. Structurally, ^{10}B-lined detectors are similar to fission chambers with the neutron-sensitive material, boron, plated in a very thin layer (about 0.2 mg/cm^2) on the walls of the detector and rely on Equation 3.2 to detect a neutron. Either the α particle or the lithium nucleus enters the detection gas (not both, since they are emitted back to back), and the detection process is initiated. Because the range of the alpha particle is about 1mg/cm^2 in boron, the plating must be thin and the detection efficiency is lower than for BF_3 gas-filled counters. However, since the nuclear reaction does not take place

in the fill gas, the gas can be optimized for fast timing. Argon at 0.25 atm pressure, with a small admixture of CO_2, is one common choice. The counter is operated in the proportional mode at a voltage of +600 to 850 V. The ^{10}B-lined counter can detect thermal neutrons with moderate efficiency and fast neutrons with low efficiency. It is mostly used for applications where it is necessary to detect neutrons in the presence of high γ-ray fields. With proper electronics, the detector can be operated in a γ-ray flux as high as 1000 R/h.

A.4.3 Plastic and liquid scintillators

Fast neutrons interact in scintillators through elastic scattering with the nuclei present (mostly carbon and hydrogen). Most of the useful scintillator light comes from recoiling hydrogen nuclei (protons) because a neutron can transfer 100% of its energy in an elastic scattering interaction to a recoiling proton but only 28% can be transferred to a recoiling ^{12}C nucleus. The kinetic energy of the recoiling protons is absorbed by the scintillator and is ultimately converted to heat and visible light. The visible light can be collected in a photomultiplier tube optically coupled to the scintillator and converted to an electronic pulse whose magnitude is related to the kinetic energy of the recoiling proton.

These detectors are completely described elsewhere [168]. Since the experiments were performed using the gas neutron detectors there is no need to consider in details all the nuances of the scintillators detectors. However, it becomes useful to highlighted its major advantages and drawbacks to justify the choice of the gas-filled detectors for our studies.

Plastic and liquid (organic) scintillators are often used for fast-neutron detection because of their fast response which is particularly beneficial for coincidence counting applications. Although organic scintillators have response times of a few nanoseconds, the coincidence resolving time is usually dictated by neutron flight time (tens of nanoseconds) from the sample to the detectors. In thermal neutron detectors the resolving times is dominated by moderation time (tens of microseconds) requires to slow a fast neutron prior to the detection. The major disadvantage of organic scintillators is their high γ-ray sensitivity. Detection probabilities for neutrons and γ-rays are comparable, and the pulse-height spectra resulting from mono energetic radiation of both types are broad and overlapping. Hence, pulse height alone yields little information about particle type. In certain organic scintillators, however, electronic pulse-shape discrimination techniques can be used to effectively distinguish between neutron and γ-ray interactions.

That is why the application of the gas-filled detectors and scintillator based detectors doesn't overlap in physics. As it has been considered above, ^{3}He detectors have higher

efficiency and better γ-discrimination properties. This make it the best tool to study β-delayed neutron emission. β-delayed neutrons are not energetic and neutron flux is kept relatively low. In studying properties for β-decay of neutron rich nuclei it is probable that the yield of the neutron rich isotope of interest is extremely low. That is why to perform an experiment in a reasonable beam time a neutron detector of high-efficiency is required. Proper shielding and identification of the isotopes makes it possible to carry out even coincide β-decay experiments [61]. The serious problem for any scintillators in comparison to gas detectors is the cross-talk effect (see the next § A.5). Nowadays there are a few scintillator neutron detector arrays: LAND [178], TONNERe [179], VANDALE [87] and others of different physics interest.

A.5 Multiple neutron emission and cross-talk effect

When it comes to studying neutron-neutron correlations and multiplicity of neutrons (emission of few neutrons per decay i.e. per β-decay or per spontaneous fission), ^{3}He detectors strongly favored over scintillator detectors. Due to the nuclear reaction taking place in the gas ($^3He + n \rightarrow^3 H +^1 H + 765keV$), a neutron is consumed. This fact naturally eliminates the cross talk effect. Crosstalk happens in multi detector systems when a neutron which gives a signal in one detector is scattered into another detector where it again gives a signal. Thus, one neutron appears to be two. This phenomenon leads to an overestimation of the total number of neutrons emitted from the target. The ratio of cross-talk events to real two neutron events varies with neutron energy and with detector configuration and could be very significant [180, 181].

Another important effect for the scintillators, diaphony, occurs when the incoming neutron is detected only by the second detector, then, in this case, two problems will affect the measurements: the detected angles will be incorrect, and the velocity of the neutron, deduced either from the time of flight or from the light deposit will be underestimated. Definitely, there are methods described elsewhere ([180, 181] etc) how to anticipate or significantly decrease the effect of the process described. They are all based either on sophisticated mathematical algorithms or complicity of a devoted electronics system devoted. Also one can perform an estimation in various computer codes: Monte-Carlo N Particle code [88] or others. Therefore, for study of neutron multiplicity an application of ^{3}He detectors seems to be more appropriate.

A.6 Measurement of (delayed) neutron energy spectra. Angular correlations.

As noted in A.3.2, passive neutron assays are usually based on counting neutrons without regard to their energy. This is because **(1)** - radioactive materials emit neutrons with broad energy spectra that are very similar from one isotope to another and **(2)** - neutron detection is an indirect process that preserves little information about the incident neutron energy. In this chapter it has been shown that neutron detection usually produces a broad spectrum of events that are only indirectly related to the neutron energy. A partial exception is found in the case of recoil detectors such as ^{4}He gas-filled counters and plastic scintillators. However, none of the detectors described can distinguish nuclear isotopes on the basis of their neutron energy [61]. As a consequence, passive neutron assay usually is based on the counting of thermal or fast neutrons, with perhaps some tailoring of the detector or its surroundings to favor a particular broad energy interval. Detectors are also chosen on the basis of their ability to produce fast (10 to 100 ns) or slow (10 to 100 μs) output signals for coincidence counting. Some detectors are also designed to have a detection efficiency that is nearly independent of neutron energy.

Although measurement of neutron energy spectra is not necessary for passive neutron assay, it is sometimes important for research or instrument development activities. Such a measurement is difficult, but possible by a variety of techniques. These techniques include *proton recoil spectrometers*, *neutron time-of-flight measurements*, and ^{3}*He spectrometers*.

The ^{3}He spectrometer developed by *Shalev and Cuttler* [182] was used to measure delayed neutron energy spectra. The spectrometer is a gas-filled proportional counter containing ^{3}He, argon, methane. Neutrons are detected via the ^{3}He(n,p)^{3}H reaction in the energy range of 20 keV to 2 MeV. In this energy range the reaction cross section is smooth and nearly flat. To detect fast neutrons the tube is not enclosed in moderating material; rather, it is wrapped in cadmium and boron sheets to reduce the contribution of the much stronger thermal ^{3}He(n,p) reaction (5330 b). Also, a lead shield is often added to reduce the effects of γ-ray pile-up on the neutron energy resolution. The intrinsic efficiency is low, on the order of 0.1%.

The energy spectrum of a ^{3}He spectrometer includes a full energy peak at the neutron energy E_n + 765 keV, a thermal neutron capture peak at 765 keV, and a ^{3}He(n,n) elastic scattering recoil spectrum with a maximum at 0.75E_n. To emphasize the full energy peak at E_n + 765 keV, long charge collection time constants of 5 to 8 μs are used. This favors the slower proton signals from the (n,p) reaction over the faster signals

from recoiling ^{3}He nuclei. It is also helpful to collect data in a two-dimensional array of charge collected vs signal rise time in order to obtain more pulse shape discrimination. In this way a neutron energy spectrum can be obtained, although it must be carefully unfolded from the data measured.

Delayed neutron spectra obtained with the ^{3}He spectrometers were measured, as an example, in [72, 183, 184].

The geometrical arrangements of tubes of a neutron detector gives an opportunity to measure the average neutron energy from a source as well as to obtain the angular distribution of the neutrons emitted. The idea is simple enough - if a neutron source is surrounded by layers of ^{3}He counters, the less-energetic neutrons will be registered by the first (inner) ring; whereas neutrons with higher energy touch the outer ring. The use of independent banks of counters embedded in polyethylene to correlate count rate ratios with neutron energies was discussed by *East and Walton* [185]. If the efficiency versus neutron energy curve of one bank of counters is quite different from the efficiency versus neutron energy curve of another bank of counters, the ratio of counts in the two banks will be a function of neutron energy. The method based on counting rate ratios of rings of neutron counter tubes in a block of polyethylene to allow measurements both on nuclides with very low P_n and on nuclides with very low fission yield as is described in [74].

To obtain information on the angular characteristics of the neutrons emitted the ancestor of TETRA consisted of 300 neutron counters. The angular resolution achieved is about 20% [69].

Appendix B

Examples of program/calculation files

Contents

B.1 Solution of Bateman Equations in Wolfram Mathematica

```
(*****Solving the D.E.s*****)
Clear["Global`*"]
InBeamSolution = DSolve[{
    y1'[t]/y1[t] == (-1)\[Lambda]1 + \[CapitalPhi]1/y1[t],(*84Ga*)
    y2'[t]/y2[t] == (-1)\[Lambda]2 + (1 - Pn1)*\[Lambda]1*y1[t]/y2[t],(*84Ge*)
    y3'[t]/y3[t] == (-1)\[Lambda]3 + (1 - Pn2)*\[Lambda]2*y2[t]/y3[t],(*84As*)
    y4'[t]/y4[t] == (-1)\[Lambda]4 + Pn1*\[Lambda]1*y1[t]/y4[t],(*83Ge*)
    y5'[t]/y5[t] == (-1)\[Lambda]5 + Pn2*\[Lambda]2*y2[t]/y5[t]
                                    + \[Lambda]4*y4[t]/y5[t],(*83As*)
     y1[0] == 0, y2[0] == 0, y3[0] == 0, y4[0] == 0, y5[0] == 0},
     {y1, y2, y3, y4, y5}, t];
f1[x_] = y1[x] /. InBeamSolution[[1]];
f2[x_] = y2[x] /. InBeamSolution[[1]];
f3[x_] = y3[x] /. InBeamSolution[[1]];
f4[x_] = y4[x] /. InBeamSolution[[1]];
f5[x_] = y5[x] /. InBeamSolution[[1]];
OutBeamSolution = DSolve[{
    z1'[t]/z1[t] == (-1)*\[Lambda]1,
    z2'[t]/z2[t] == (-1)*\[Lambda]2 + (1 - Pn1)*\[Lambda]1*z1[t]/z2[t],
    z3'[t]/z3[t] == (-1) \[Lambda]3 + (1 - Pn2)*\[Lambda]2*z2[t]/z3[t],
    z4'[t]/z4[t] == (-1) \[Lambda]4 + Pn1*\[Lambda]1*z1[t]/z4[t],
    z5'[t]/z5[t] == (-1) \[Lambda]5 +
      Pn2*\[Lambda]2*z2[t]/z5[t] + \[Lambda]4*z4[t]/z5[t],
    z1[0] == f1[Tbeam], z2[0] == f2[Tbeam], z3[0] == f3[Tbeam],
    z4[0] == f4[Tbeam], z5[0] == f5[Tbeam]}, {z1, z2, z3, z4, z5},t];
fz1[x_] = z1[x] /. OutBeamSolution[[1]];
fz2[x_] = z2[x] /. OutBeamSolution[[1]];
```

```
fz3[x_] = z3[x] /. OutBeamSolution[[1]];
fz4[x_] = z4[x] /. OutBeamSolution[[1]];
fz5[x_] = z5[x] /. OutBeamSolution[[1]];

(*****Setup funtcions*****)
fAct1[x_] := \[Lambda]1*f1[x];
fAct2[x_] := \[Lambda]2*f2[x];
fAct3[x_] := \[Lambda]3*f3[x];
fAct4[x_] := \[Lambda]4*f4[x];
fAct5[x_] := \[Lambda]5*f5[x];

fAct1z[x_] := \[Lambda]1*fz1[x];
fAct2z[x_] := \[Lambda]2*fz2[x];
fAct3z[x_] := \[Lambda]3*fz3[x];
fAct4z[x_] := \[Lambda]4*fz4[x];
fAct5z[x_] := \[Lambda]5*fz5[x];

FAct1[x_] := \[Piecewise]{{0, x == 0}, {fAct1[x], 0 < x <= Tbeam},
              {fAct1z[x - Tbeam], x > Tbeam}}
FAct2[x_] := \[Piecewise]{{0, x == 0}, {fAct2[x], 0 < x <= Tbeam},
              {fAct2z[x - Tbeam], x > Tbeam}}
FAct3[x_] := \[Piecewise]{{0, x == 0}, {fAct3[x], 0 < x <= Tbeam},
              {fAct3z[x - Tbeam], x > Tbeam}}
FAct4[x_] := \[Piecewise]{{0, x == 0}, {fAct4[x], 0 < x <= Tbeam},
              {fAct4z[x - Tbeam], x > Tbeam}}
FAct5[x_] := \[Piecewise]{{0, x == 0}, {fAct5[x], 0 < x <= Tbeam},
              {fAct5z[x - Tbeam], x > Tbeam}}

fActBeta[x_] := fAct1[x] + fAct2[x] + fAct3[x] + fAct4[x] + fAct5[x];
FActBeta[x_] := FAct1[x] + FAct2[x] + FAct3[x] + FAct4[x] + FAct5[x];

Fneutron1[x_] := neutronEff*FAct1[x]*Pn1
Fneutron2[x_] := neutronEff*FAct2[x]*Pn2
Fneutronsum[x_] :=  Fneutron1[x] + Fneutron2[x]
```

B.2 A sample input file for MCNP

```
CONFIGURATION TETRA BEDO                                          v.20FEB12
c ------------------------------------------------------------------------
c AUTOMATICALLY GENERATED FILE
c ------------------------------------------------------------------------
c CELL #500 volume for 3He gas for U=5,6,50,52,55,5xx
c ------------------------------------------------------------------------
c
c <<<Gas Volume>>>
501 0 7 -8 -25 u=5 imp:n=1
521 like 501 but u=52 mat=2 rho=-0.00116535 imp:n=1 $ 7 bar, orsay
c
c <<<Gas Boders >>>
502 0 35 -36 25 -24 u=5 imp:n=1
522 like 502 but u=52 mat=2 rho=-0.00116535 $ 2 -0.00116535 40 -41  25 -22 u=52 imp:n
c
c <<<Stll Tibes>>
503 0 7 -8 24 -27 u=5 imp:n=1 $ walls of counter
523 like 503 but u=52 mat=4 rho=-7.9
c
c <<<Moderator around>>
504 0 27 7 -8 u=5 imp:n=1
514 like 504 but u=50 mat=3 rho=-0.93
524 like 514 but u=52 $moderator
c 534 like 514 but u=51
c 534 like 514 but u=51 mat=6 rho=-1.005
534 like 514 but u=54 mat=3 rho=-0.93
544 like 514 but u=53 mat=6 rho=-1.005
554 like 514 but u=51 mat=3 rho=-0.93
c
c <<<Holes filled with CH2>>
506 0 7 -8 -27 u=6 imp:n=1 $ hole
516 like 506 but u=54  mat=3 rho=-0.93
526 like 506 but u=51  mat=8 rho=-7.92
c <<<Universes>>
505 0 -17 16 20 -21 18 -19 u=55 lat=2 imp:n=1
c ------------------------------------------------------------------------
525 like 505 but u=520 fill=-3:3 -3:3 0:0
c     1   2   3   4   5   6   7
      520 520 520 520 050 050 050 $1
      520 520 050 052 052 052 050 $2
```

```
     520 050 052 050 050 052 050 $3
     050 052 050 520 051 051 051 $4
     050 052 050 050 052 050 520 $5
     050 052 052 052 050 520 520 $6
     520 050 050 050 520 520 520 $7
c ------------------------------------------------------------------------
535 like 505 but u=530 fill=-4:4 -4:4 0:0
c    1   2   3   4   5   6   7   8   9
     530 530 530 530 050 050 050 050 530 $1
     530 530 530 050 052 052 052 052 050 $2
     530 530 050 052 050 050 050 052 050 $3
     530 050 052 050 530 530 050 052 050 $4
     050 052 050 530 530 530 051 051 051 $5
     050 052 050 530 530 050 052 050 530 $6
     050 052 050 050 050 052 050 530 530 $7
     050 052 052 052 052 050 530 530 530 $8
     530 050 050 050 050 530 530 530 530 $9
c ------------------------------------------------------------------------
545 like 505 but u=540 fill=-5:5 -5:5 0:0
c     1   2   3   4   5   6   7   8   9   0   1
     540 540 540 540 540 050 050 050 050 050 540 $1
     540 540 540 540 050 052 052 052 052 052 050 $2
     540 540 540 050 052 050 050 050 050 052 050 $3
     540 540 050 052 050 540 540 540 050 052 050 $4
     540 050 052 050 540 540 540 540 050 052 050 $5
     050 052 050 540 540 540 540 540 051 051 051 $6
     050 052 050 540 540 540 540 050 052 050 540 $7
     050 052 050 540 540 540 050 052 050 540 540 $8
     050 052 050 050 050 050 052 050 540 540 540 $9
     050 052 052 052 052 052 050 540 540 540 540 $0
     540 050 050 050 050 050 540 540 540 540 540 $1
c ------------------------------------------------------------------------
555 like 505 but u=550 fill=-6:6 -6:6 0:0
c     1   2   3   4   5   6   7   8   9   0   1   2   3
     550 550 550 550 550 550 050 050 050 050 050 050 550 $1
     550 550 550 550 550 050 052 052 052 052 052 052 050 $2
     550 550 550 550 050 052 050 050 050 050 050 052 050 $3
     550 550 550 050 052 050 550 550 550 550 050 052 050 $4
     550 550 050 052 050 550 550 550 550 550 050 052 050 $5
     550 050 052 050 550 550 550 550 550 550 050 052 050 $6
     050 052 050 550 550 550 550 550 550 550 051 051 051 $7
     050 052 050 550 550 550 550 550 550 050 052 050 550 $8
     050 052 050 550 550 550 550 550 050 052 050 550 550 $9
     050 052 050 550 550 550 550 050 052 050 550 550 550 $0
     050 052 050 050 050 050 050 052 050 550 550 550 550 $1
     050 052 052 052 052 052 052 050 550 550 550 550 550 $2
     550 050 050 050 050 050 050 550 550 550 550 550 550 $3$3
c ------------------------------------------------------------------------
565 like 505 but u=560 fill=-7:7 -7:7 0:0
c     1   2   3   4   5   6   7   8   9   0   1   2   3   4   5
     560 560 560 560 560 560 560 051 051 051 051 051 051 051 560 $1
     560 560 560 560 560 560 051 051 051 051 051 051 051 051 051 $2
     560 560 560 560 560 051 054 051 051 051 051 051 051 054 051 $3
     560 560 560 560 051 051 051 560 560 560 560 560 051 051 051 $4
     560 560 560 051 051 051 560 560 560 560 560 560 051 051 051 $5
     560 560 051 051 051 560 560 560 560 560 560 560 051 051 051 $6
     560 051 054 051 560 560 560 560 560 560 560 560 051 054 051 $7
     051 051 051 560 560 560 560 560 560 560 560 560 051 051 051 $8 center
     051 054 051 560 560 560 560 560 560 560 560 051 054 051 560 $9
     051 051 051 560 560 560 560 560 560 560 051 051 051 560 560 $0
     051 051 051 560 560 560 560 560 560 051 051 051 560 560 560 $1
     051 051 051 560 560 560 560 560 051 051 051 560 560 560 560 $2
     051 054 051 051 051 051 051 051 054 051 560 560 560 560 560 $3
     051 051 051 051 051 051 051 051 051 560 560 560 560 560 560 $4
     560 051 051 051 051 051 051 051 560 560 560 560 560 560 560 $5
c ------------------------------------------------------------------------
c CELL #600 volume for 3He gas for U=6,62,620
c ------------------------------------------------------------------------
c
c <<<Holes for Cabales>>>
c 601 0 -7 23 -27 u=6 imp:n=1
601 0 23 -22 -27 u=6 imp:n=1
621 like 601 but u=61 mat=9 rho=-1.2
c
c <<<Moderator around holes>>
c 604 0 -7 23 27 u=6 imp:n=1
604 0 23 -22 27 u=6 imp:n=1
624 like 604 but u=61 mat=6 rho=-1.005
c 624 like 604 but u=61 mat=3 rho=-0.93
c
```

```
c <<<Universes>>
605 like 505 but fill=61 u=610
c
c ---------------------------------------------------------------------
c CELLs #500
c ---------------------------------------------------------------------
c
500 0 -45 7 -8 imp:n=1
c 510 0 -10 9 13 -14 11 -12 45 7 -8 imp:n=1 $ 1 layer
510 3 -0.93 -10 9 13 -14 11 -12 45 7 -8 imp:n=1 $ 1 layer
520 0 -50 49 53 -54 51 -52 (10:-9:-13:14:-11:12) 7 -8  fill=520 imp:n=1 $ 2 layer
530 0 -60 59 63 -64 61 -62 (50:-49:-53:54:-51:52) 7 -8 fill=530 imp:n=1 $ 3 layer
540 0 -70 69 73 -74 71 -72 (60:-59:-63:64:-61:62) 7 -8 fill=540 imp:n=1 $ 4 layer
550 0 -80 79 83 -84 81 -82 (70:-69:-73:74:-71:72) 7 -8 fill=550 imp:n=1 $ 5 layer
560 0 -90 89 93 -94 91 -92 (80:-79:-83:84:-81:82) 7 -8 fill=560 imp:n=1 $ 6 layer
c 570 0 5 -6 -2 1 3 -4 (90:-89:-93:94:-91:92) 7 -8 imp:n=1 $ 7 layer
570 6 -1.005 5 -6 -2 1 3 -4 (90:-89:-93:94:-91:92) 7 -8 imp:n=1 $ 7 layer
c 570 3 -0.93 5 -6 -2 1 3 -4 (90:-89:-93:94:-91:92) 7 -8 imp:n=1 $ 7 layer
c
c ---------------------------------------------------------------------
c CELLs #500/600/900
c ---------------------------------------------------------------------
c 610 0 5 -6 -2 1 3 -4 8 -22 45 imp:n=1
610 6 -1.005 5 -6 -2 1 3 -4 (10:-9:-13:14:-11:12) 8 -22 imp:n=1 $ front
c 610 3 -0.93 5 -6 -2 1 3 -4 (10:-9:-13:14:-11:12) 8 -22 imp:n=1 $ front
620 0 -90 89 93 -94 91 -92 (10:-9:-13:14:-11:12) -7 23 fill=610 imp:n=1 $ back
c 630 0 5 -6 -2 1 3 -4 -7 23 (90:-89:-93:94:-91:92) imp:n=1
630 6 -1.005 5 -6 -2 1 3 -4 (90:-89:-93:94:-91:92) -7 23 imp:n=1 $ back
c 630 3 -0.93 5 -6 -2 1 3 -4 (90:-89:-93:94:-91:92) -7 23 imp:n=1 $ back
c
c 901 0 -1: 2: -3: 4: -5: 6: -23: 22 imp:n=0 $ no sphere
910 0 -10 9 13 -14 11 -12 8 -22 imp:n=0 $ for cell 610
920 0 -10 9 13 -14 11 -12 -7 23 imp:n=0 $ for cell 620
c ---------------------------------------------------------------------
c Cells 7xx, 9xx, walls and outer world
c ---------------------------------------------------------------------
701 0 -998 (-1: 2: -3: 4: -5: 6: -23: 22) -22 23 imp:n=1
702 0 -707 703 705 -706 -702 701 (998: 22: -23) imp:n=1
703 7 -7.92 707 -717 -22 23 1 -2 imp:n=1 $table plate
704 0 707 -704 701 -702 705 -706 (-707: 717: 22: -23: -1: 2) imp:n=1
705 7 -2.25 711 -712 713 -714 715 -716 (-701: 702: -703: 704: -705: 706) imp:n=1 $wal
901 0 -999 (-711: 712: -713: 714: -715: 716) imp:n=0
c 901 0 -999 (-701: 702: -703: 704: -705: 706) imp:n=1
902 0 999 imp:n=0
c ---------------------------------------------------------------------
c ---------------------------------------------------------------------
c SURFACES of the setup
c ---------------------------------------------------------------------
1 PZ -43.5
2 PZ 43.5
3 P 1.33974963E-01 0 0.5 -43.5
4 P 1.33974963E-01 0 0.5 43.5
5 P 1.33974963E-01 0 -0.5 -43.5
6 P 1.33974963E-01 0 -0.5 43.5
c Cylinder
45 CY 6.5
c ---------------------------------------------------------------------
c SURFACES the Central Hall/First Layer
c ---------------------------------------------------------------------
9 PZ -6.5
10 PZ 6.5
11 P 1.33974963E-01 0 0.5 -6.5
12 P 1.33974963E-01 0 0.5 6.5
13 P 1.33974963E-01 0 -0.5 -6.5
14 P 1.33974963E-01 0 -0.5 6.5
c ---------------------------------------------------------------------
c SURFACES the Second Layer
c ---------------------------------------------------------------------
49 PZ -10.9
50 PZ 10.9
51 P 1.33974963E-01 0 0.5 -10.9
52 P 1.33974963E-01 0 0.5 10.9
53 P 1.33974963E-01 0 -0.5 -10.9
54 P 1.33974963E-01 0 -0.5 10.9
c ---------------------------------------------------------------------
c SURFACES the Third Layer
c ---------------------------------------------------------------------
59 PZ -15.3
60 PZ 15.3
```

```
61 P 1.33974963E-01 0 0.5 -15.3
62 P 1.33974963E-01 0 0.5 15.3
63 P 1.33974963E-01 0 -0.5 -15.3
64 P 1.33974963E-01 0 -0.5 15.3
c ------------------------------------------------------------------------
c SURFACES the Forth Layer
c ------------------------------------------------------------------------
69 PZ -19.7
70 PZ 19.7
71 P 1.33974963E-01 0 0.5 -19.7
72 P 1.33974963E-01 0 0.5 19.7
73 P 1.33974963E-01 0 -0.5 -19.7
74 P 1.33974963E-01 0 -0.5 19.7
c ------------------------------------------------------------------------
c SURFACES the Fiths Layer
c ------------------------------------------------------------------------
79 PZ -24.1
80
 PZ 24.1
81 P 1.33974963E-01 0 0.5 -24.1
82 P 1.33974963E-01 0 0.5 24.1
83 P 1.33974963E-01 0 -0.5 -24.1
84 P 1.33974963E-01 0 -0.5 24.1
c ------------------------------------------------------------------------
c SURFACES the Sixth Layer (Boders of the detector)
c ------------------------------------------------------------------------
89 PZ -28.5
90 PZ 28.5
91 P 1.33974963E-01 0 0.5 -28.5
92 P 1.33974963E-01 0 0.5 28.5
93 P 1.33974963E-01 0 -0.5 -28.5
94 P 1.33974963E-01 0 -0.5 28.5
c ------------------------------------------------------------------------
c SURFACES the Seventh Layer
c ------------------------------------------------------------------------
c 29 PZ -40
c 30 PZ 40
c 31 P 1.33974963E-01 0 0.5 -40
c 32 P 1.33974963E-01 0 0.5 40
c 33 P 1.33974963E-01 0 -0.5 -40
c 34 P 1.33974963E-01 0 -0.5 40
c ------------------------------------------------------------------------
c SURFACES Small Hexagon
c ------------------------------------------------------------------------
16  PX   -2.5
17  PX    2.5
18  P     0.5 0 -1.33974963E-01 -2.5
19  P     0.5 0 -1.33974963E-01  2.5
20  P    -0.5 0 -1.33974963E-01 -2.5
21  P    -0.5 0 -1.33974963E-01  2.5
c ------------------------------------------------------------------------
c SURFACES General dimensions
c ------------------------------------------------------------------------
7  PY -25 $ total length of counter
8  PY  25 $ total length of counter
22 PY 35  $ total length of the setup
23 PY -35  $ total length of the setup
24 CY 1.5 $ gas volume radius
25 CY 1.5 $ gas volume radius
26 CY 1.6 $ outer radius
27 CY 1.6 $ outer radius
35 PY -25
36 PY 25
c ------------------------------------------------------------------------
c SURFACES [29-34] hex PZ reserved
c ------------------------------------------------------------------------
c 29 PZ -29.5
c 30 PZ 29.5
c 31 P 1.33974963E-01 0 0.5 -29.5
c 32 P 1.33974963E-01 0 0.5 29.5
c 33 P 1.33974963E-01 0 -0.5 -29.5
c 34 P 1.33974963E-01 0 -0.5 29.5
c 38 SO 70
c 39 SO 71
c ------------------------------------------------------------------------
c SURFACES [700] walls
c ------------------------------------------------------------------------
701 PY -200 $floor
702 PY 200 $roof
703 PX -200
704 PX 200
705 PZ -200
706 PZ 200
707 PX 50.24 $table plate
```

```
711 PY -220 $floor
712 PY 220 $roof
713 PX -220
714 PX 220
715 PZ -220
716 PZ 220
717 PX 51.74 $table plate
c ---------------------------------------------------------------------
c SURFACES [900] outer stuff
c ---------------------------------------------------------------------
c 998 SO 62
998 CY 50.23
999 SO 500
c ---------------------------------------------------------------------
c Sources
c ---------------------------------------------------------------------
c SDEF SUR=999 NRM=-1
c ---------------------------------------------------------------------
c Maxwellian 252 Cf
c ---------------------------------------------------------------------
sdef erg=d2 pos 0 0 0
sp1 -1 5.5
c ---------------------------------------------------------------------
c Mono energetic
c ---------------------------------------------------------------------
c sdef erg=4 par=n pos 0 0 0
c
c ---------------------------------------------------------------------
c Sphere
c ---------------------------------------------------------------------
c sdef erg=4 par=n cell=902 rad=d1 wgt=200
c si1 71.1
c
c ---------------------------------------------------------------------
c Tallies
c ---------------------------------------------------------------------
c <<<Flux avarage a cell F4: 3He >>>
c ---------------------------------------------------------------------
f524:n (521>525>520)
fm524:n 0.000233931 2 103 $7 bar, orsay
fc524 dUmon This is Tally 524
f534:n (521>535>530)
fm534:n 0.000233931 2 103 $7 bar, orsay
fc534 dUmon This is Tally 534
f544:n (521>545>540)
fm544:n 0.000233931 2 103 $7 bar, orsay
fc544 dUmon This is Tally 544
f554:n (521>555>550)
fm554:n 0.000233931 2 103 $7 bar, orsay
fc554 dUmon This is Tally 554
f54:n (521>(525 535 545 555)>(520 530 540 550))
fm54:n 0.000233931 2 103 $7 bar, orsay
fc54 dUmon This is Tally 54
c ---------------------------------------------------------------------
c     MATERIALS
c ---------------------------------------------------------------------
c     He3,  p=0.00086 g/cm^3
m2    3002 -1.
c ---------------------------------------------------------------------
c     polyathilen, p=0.93 g/cm^3
c     CH2
m3    1001 -.14372 6012 -.85628
c ---------------------------------------------------------------------
c     steel, light  p=7.9 g/cm^3
c     C      %     Mn      %      Ni      %     Si      %    Cr      %
m4    1260 -.0007   25055 -0.0029  28058 -.0912  14000 -.0047 24052 -.1880 &
c     Ti       %     Fe       %      Al      %
      22000 -.0038  26056 -.7081   13027  -0.0006
c ---------------------------------------------------------------------
c     Borated polyathilen, 5%, rho=1.005 g/cm^3
c     C            H2         B10        B11
m6    1260 -.3166 1001 -.6334 5010 -.0098 5011 -.0402
c ---------------------------------------------------------------------
c     Stainless steel 304, p=7.92 g/cc
c     Fe           Cr          Ni          Mn
m7    26056 -.695 24052 -.190 28058 -.095 25055 -0.020
c ---------------------------------------------------------------------
c    Concrete LA (MCNP) Mix 2.25g/cc
c     H            O          Si              AL              Na
m8    1001 -.00453 8016 -.5126  14028 -.36036 13027 -.03555  11023 -.01527 &
c     Ca           Fe
      20040 -.05791 26056 -.01378
```

```
c ---------------------------------------------------------------------
c     plexiglas p=1.2 g/cm^3
c     C5H8O2
m9    1001 8 1260 5 8016 2
c ---------------------------------------------------------------------
c number of histories
nps 1000000
```

Appendix C

TETRA: Getting ready to work

Contents

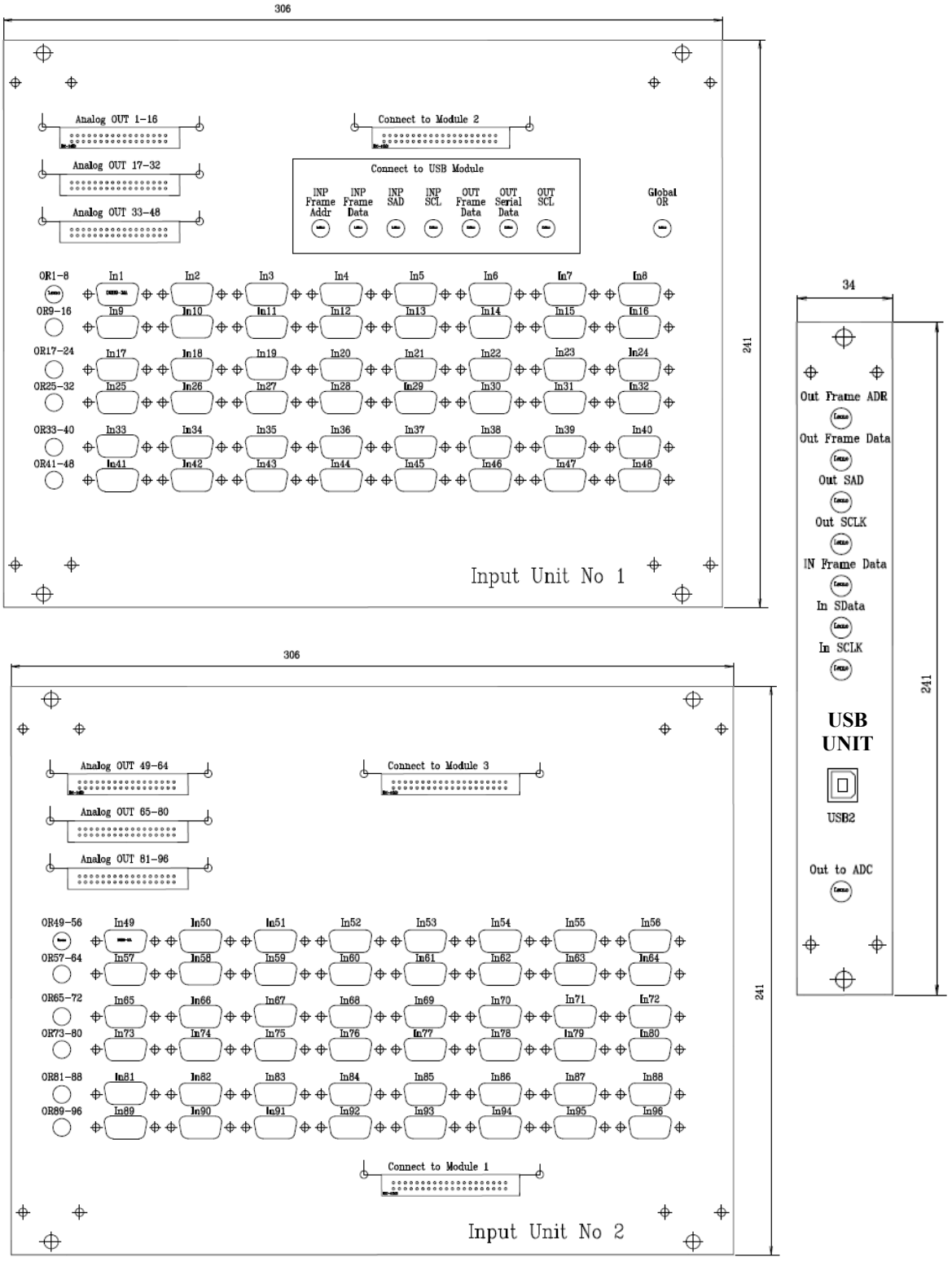

FIGURE C.1: Electronic Input Modules, schematical view

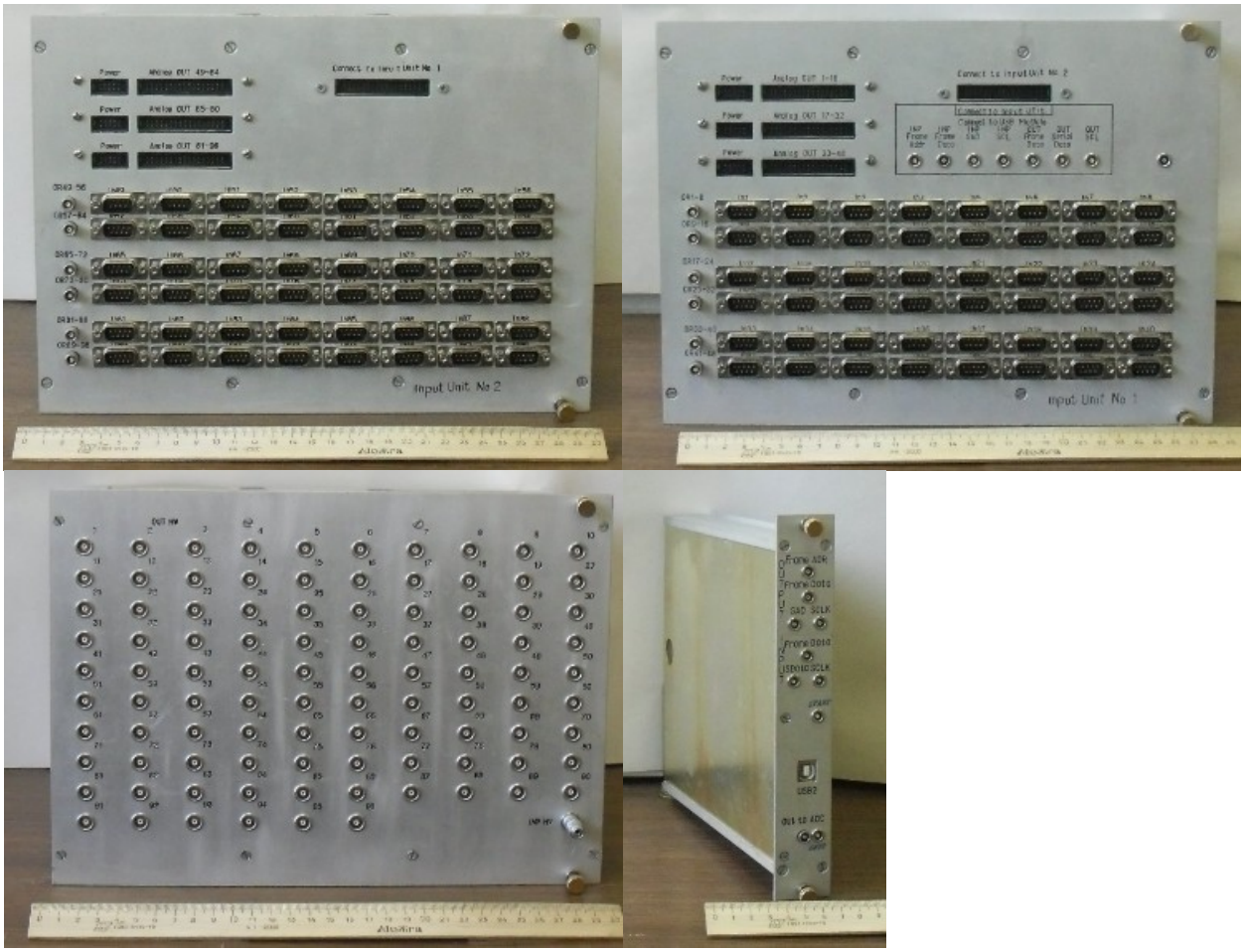

FIGURE C.2: Electronic Input Modules, photo

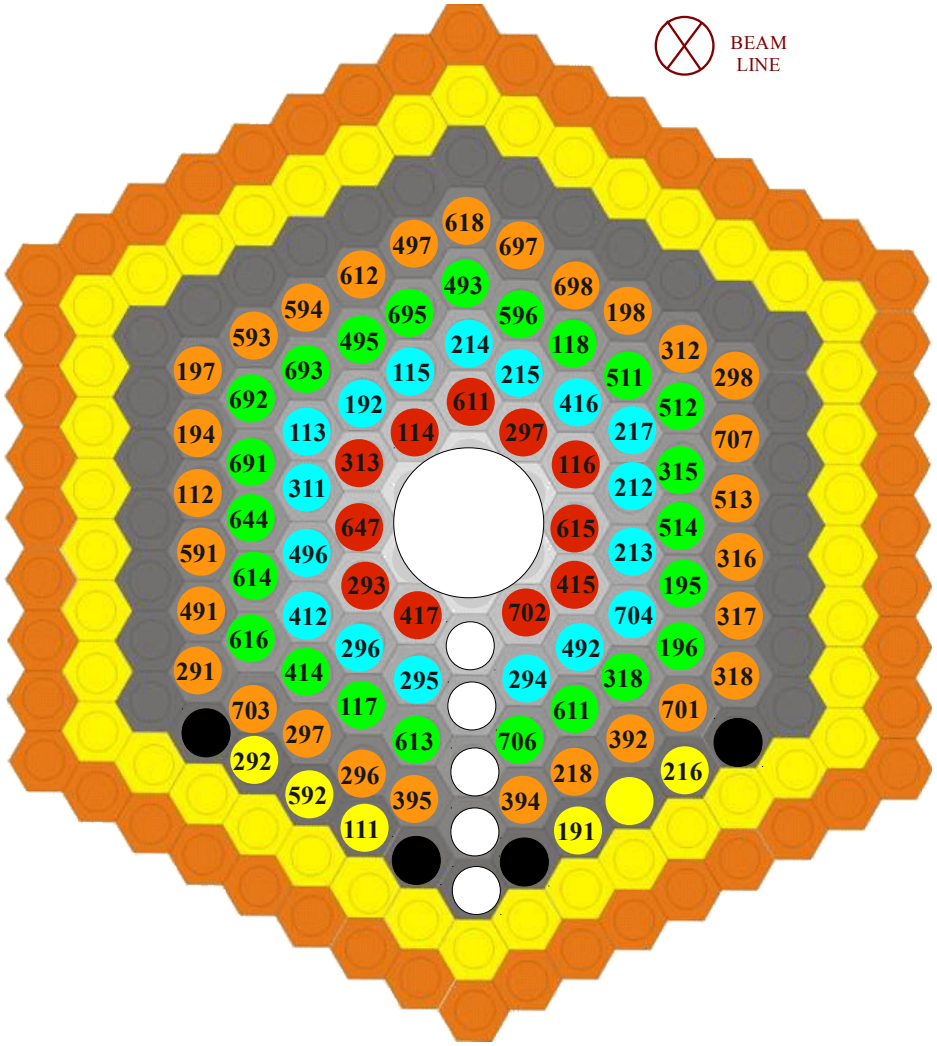

FIGURE C.3: Position of counters inside TETRA

FIGURE C.4: Electronic channels of TETRA

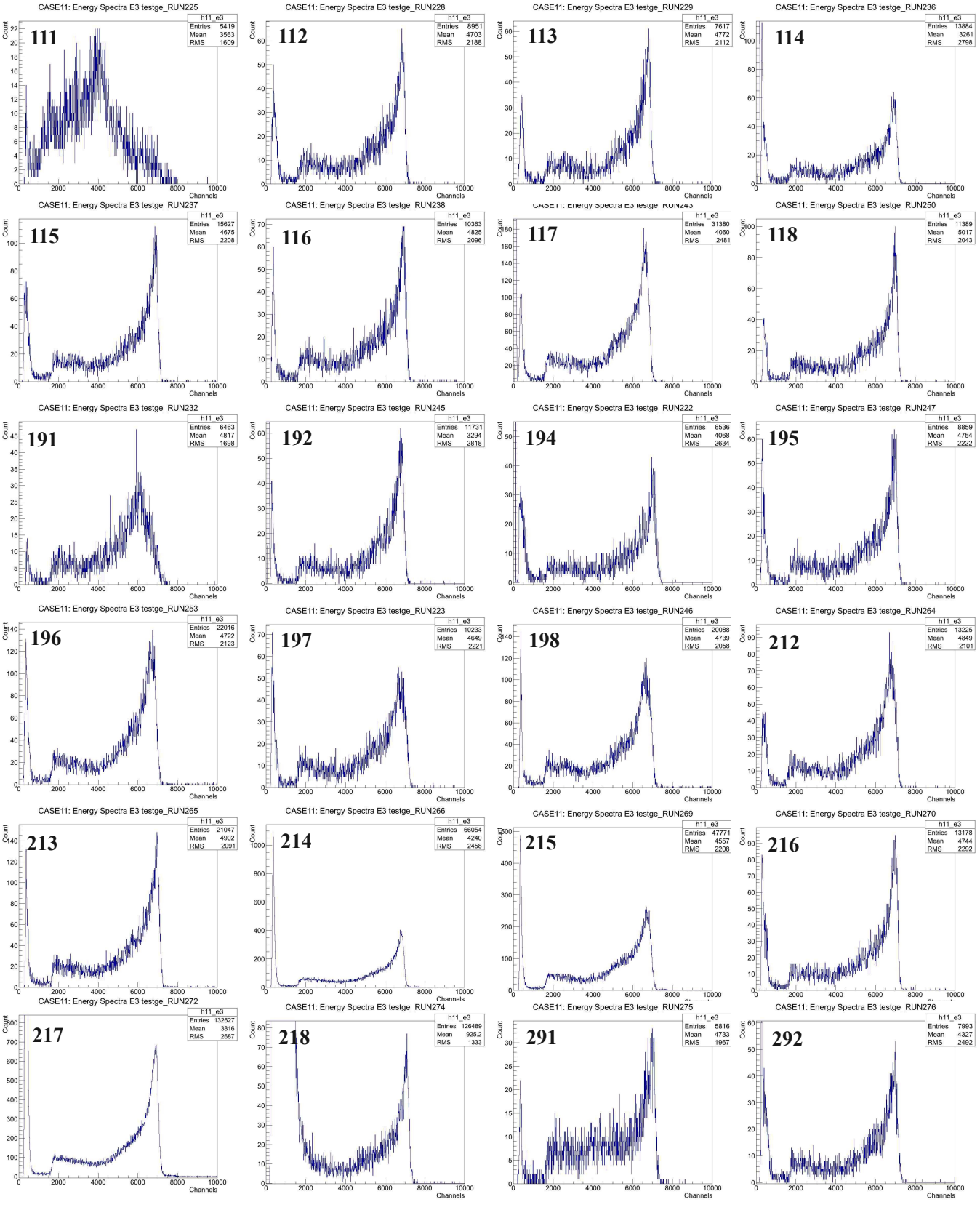

FIGURE C.5: Pulse height spectra

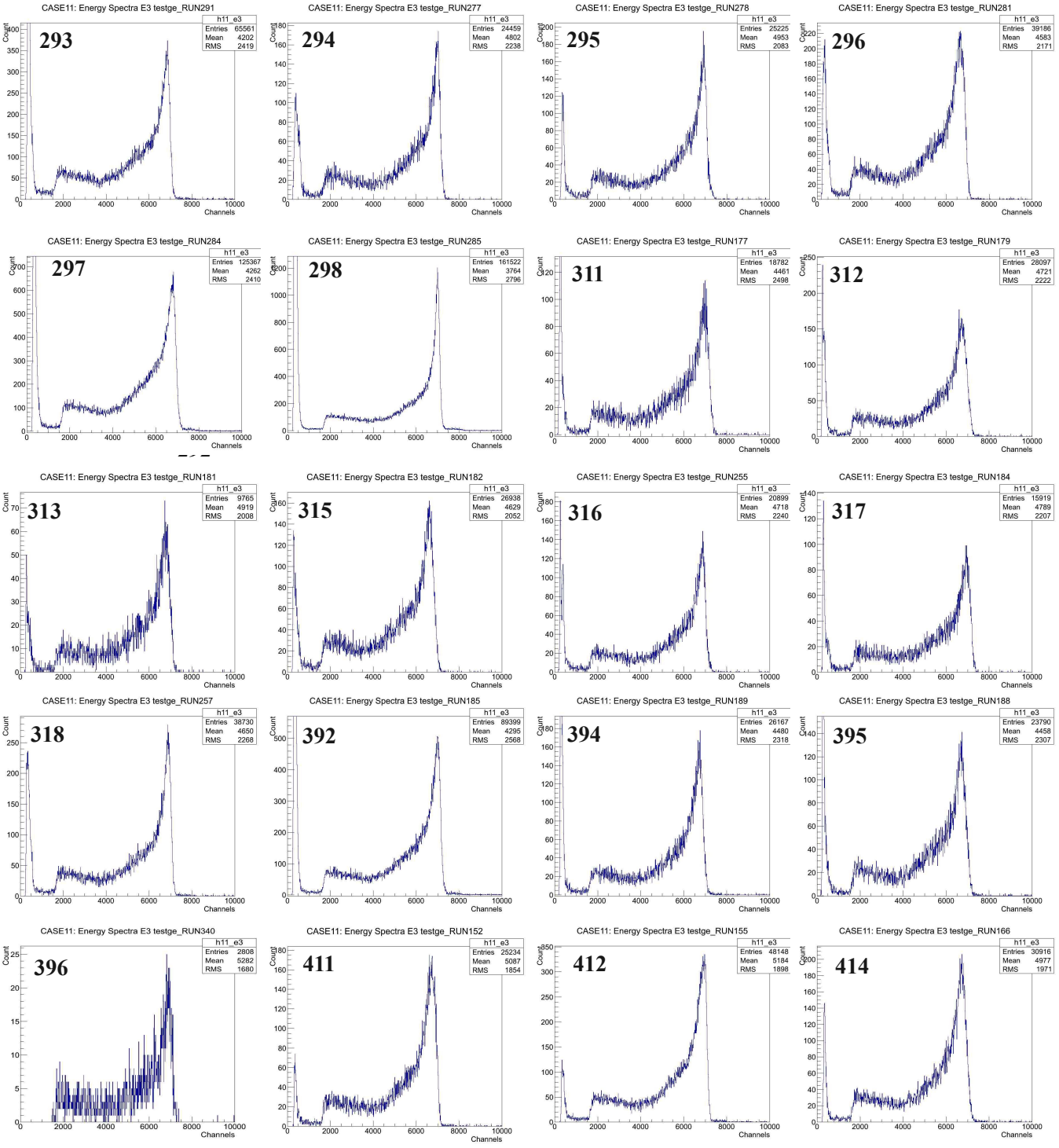

FIGURE C.6: Pulse height spectra

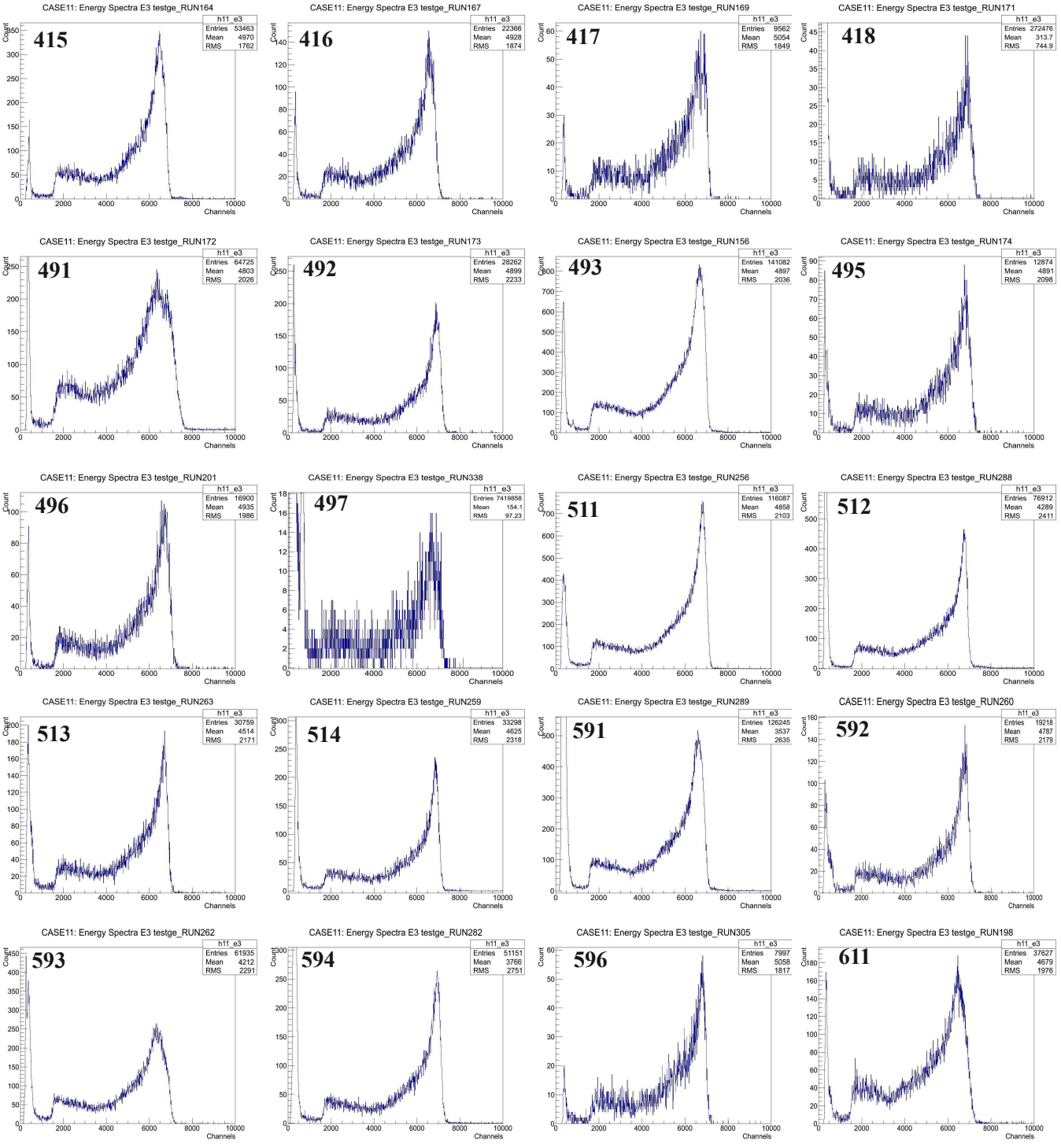

FIGURE C.7: Pulse height spectra

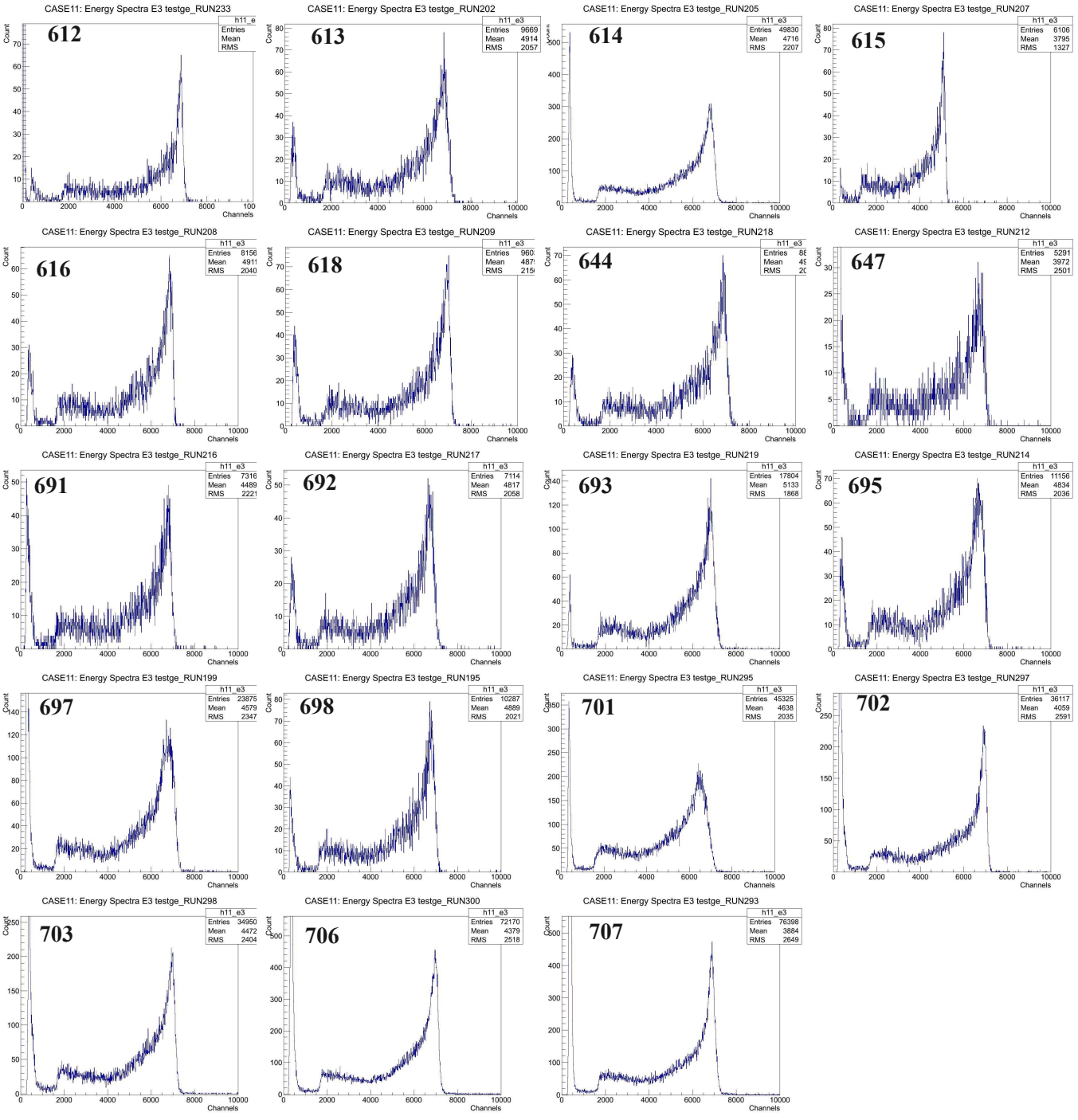

FIGURE C.8: Pulse height spectra

Sheet1

HEX	V	HEX	V	HEX	V	HEX	V	HEX	V	HEX	V
8	0.04219	38	0.29531	68	0.54844	98	0.8015625	C8	1.05469	F8	1.3078125
9	0.04746	39	0.30059	69	0.55371	99	0.8068359	C9	1.05996	F9	1.3130859
A	0.05273	3A	0.30586	6A	0.55898	9A	0.8121094	CA	1.06523	FA	1.3183594
B	0.05801	3B	0.31113	6B	0.56426	9B	0.8173828	CB	1.07051	FB	1.3236328
C	0.06328	3C	0.31641	6C	0.56953	9C	0.8226563	CC	1.07578	FC	1.3289063
D	0.06855	3D	0.32168	6D	0.57480	9D	0.8279297	CD	1.08105	FD	1.3341797
E	0.07383	3E	0.32695	6E	0.58008	9E	0.8332031	CE	1.08633	FE	1.3394531
F	0.07910	3F	0.33223	6F	0.58535	9F	0.8384766	CF	1.09160	FF	1.3447266
10	0.08438	40	0.3375	70	0.59063	A0	0.84375	D0	1.09688	100	1.35
11	0.08965	41	0.34277	71	0.59590	A1	0.8490234	D1	1.10215	101	1.3552734
12	0.09492	42	0.34805	72	0.60117	A2	0.8542969	D2	1.10742	102	1.3605469
13	0.10020	43	0.35332	73	0.60645	A3	0.8595703	D3	1.11270	103	1.3658203
14	0.10547	44	0.35859	74	0.61172	A4	0.8648438	D4	1.11797	104	1.3710938
15	0.11074	45	0.36387	75	0.61699	A5	0.8701172	D5	1.12324	105	1.3763672
16	0.11602	46	0.36914	76	0.62227	A6	0.8753906	D6	1.12852	106	1.3816406
17	0.12129	47	0.37441	77	0.62754	A7	0.8806641	D7	1.13379	107	1.3869141
18	0.12656	48	0.37969	78	0.63281	A8	0.8859375	D8	1.13906	108	1.3921875
19	0.13184	49	0.38496	79	0.63809	A9	0.8912109	D9	1.14434		
1A	0.13711	4A	0.39023	7A	0.64336	AA	0.8964844	DA	1.14961		
1B	0.14238	4B	0.39551	7B	0.64863	AB	0.9017578	DB	1.15488		
1C	0.14766	4C	0.40078	7C	0.65391	AC	0.9070313	DC	1.16016		
1D	0.15293	4D	0.40605	7D	0.65918	AD	0.9123047	DD	1.16543		
1E	0.15820	4E	0.41133	7E	0.66445	AE	0.9175781	DE	1.17070		
1F	0.16348	4F	0.41660	7F	0.66973	AF	0.9228516	DF	1.17598		
20	0.16875	50	0.42188	80	0.675	B0	0.928125	E0	1.18125		
21	0.17402	51	0.42715	81	0.68027	B1	0.9333984	E1	1.18652		
22	0.17930	52	0.43242	82	0.68555	B2	0.9386719	E2	1.19180		
23	0.18457	53	0.43770	83	0.69082	B3	0.9439453	E3	1.19707		
24	0.18984	54	0.44297	84	0.69609	B4	0.9492188	E4	1.20234		
25	0.19512	55	0.44824	85	0.70137	B5	0.9544922	E5	1.20762		
26	0.20039	56	0.45352	86	0.70664	B6	0.9597656	E6	1.21289		
27	0.20566	57	0.45879	87	0.71191	B7	0.9650391	E7	1.21816		
28	0.21094	58	0.46406	88	0.71719	B8	0.9703125	E8	1.22344		
29	0.21621	59	0.46934	89	0.72246	B9	0.9755859	E9	1.22871		
2A	0.22148	5A	0.47461	8A	0.72773	BA	0.9808594	EA	1.23398		
2B	0.22676	5B	0.47988	8B	0.73301	BB	0.9861328	EB	1.23926		
2C	0.23203	5C	0.48516	8C	0.73828	BC	0.9914063	EC	1.24453		
2D	0.23730	5D	0.49043	8D	0.74355	BD	0.9966797	ED	1.24980		
2E	0.24258	5E	0.49570	8E	0.74883	BE	1.0019531	EE	1.25508		
2F	0.24785	5F	0.50098	8F	0.75410	BF	1.0072266	EF	1.26035		
30	0.25313	60	0.50625	90	0.75938	C0	1.0125	F0	1.26563		
31	0.25840	61	0.51152	91	0.76465	C1	1.0177734	F1	1.27090		
32	0.26367	62	0.51680	92	0.76992	C2	1.0230469	F2	1.27617		
33	0.26895	63	0.52207	93	0.77520	C3	1.0283203	F3	1.28145		
34	0.27422	64	0.52734	94	0.78047	C4	1.0335938	F4	1.28672		
35	0.27949	65	0.53262	95	0.78574	C5	1.0388672	F5	1.29199		
36	0.28477	66	0.53789	96	0.79102	C6	1.0441406	F6	1.29727		
37	0.29004	67	0.54316	97	0.79629	C7	1.0494141	F7	1.30254		

Page 1

(A) Low Threshold

Sheet1

HEX	V								
FF	3.78516	CF	3.07266	9F	2.36016	6F	1.6476563	3F	0.93516
FE	3.77031	CE	3.05781	9E	2.34531	6E	1.6328125	3E	0.92031
FD	3.75547	CD	3.04297	9D	2.33047	6D	1.6179688	3D	0.90547
FC	3.74063	CC	3.02813	9C	2.31563	6C	1.603125	3C	0.89063
FB	3.72578	CB	3.01328	9B	2.30078	6B	1.5882813	3B	0.87578
FA	3.71094	CA	2.99844	9A	2.28594	6A	1.5734375	3A	0.86094
F9	3.69609	C9	2.98359	99	2.27109	69	1.5585938	39	0.84609
F8	3.68125	C8	2.96875	98	2.25625	68	1.54375	38	0.83125
F7	3.66641	C7	2.95391	97	2.24141	67	1.5289063	37	0.81641
F6	3.65156	C6	2.93906	96	2.22656	66	1.5140625	36	0.80156
F5	3.63672	C5	2.92422	95	2.21172	65	1.4992188	35	0.78672
F4	3.62188	C4	2.90938	94	2.19688	64	1.484375	34	0.77188
F3	3.60703	C3	2.89453	93	2.18203	63	1.4695313	33	0.75703
F2	3.59219	C2	2.87969	92	2.16719	62	1.4546875	32	0.74219
F1	3.57734	C1	2.86484	91	2.15234	61	1.4398438	31	0.72734
F0	3.5625	C0	2.85	90	2.1375	60	1.425	30	0.7125
EF	3.54766	BF	2.83516	8F	2.12266	5F	1.4101563	2F	0.69766
EE	3.53281	BE	2.82031	8E	2.10781	5E	1.3953125	2E	0.68281
ED	3.51797	BD	2.80547	8D	2.09297	5D	1.3804688	2D	0.66797
EC	3.50313	BC	2.79063	8C	2.07813	5C	1.365625	2C	0.65313
EB	3.48828	BB	2.77578	8B	2.06328	5B	1.3507813		
EA	3.47344	BA	2.76094	8A	2.04844	5A	1.3359375		
E9	3.45859	B9	2.74609	89	2.03359	59	1.3210938		
E8	3.44375	B8	2.73125	88	2.01875	58	1.30625		
E7	3.42891	B7	2.71641	87	2.00391	57	1.2914063		
E6	3.41406	B6	2.70156	86	1.98906	56	1.2765625		
E5	3.39922	B5	2.68672	85	1.97422	55	1.2617188		
E4	3.38438	B4	2.67188	84	1.95938	54	1.246875		
E3	3.36953	B3	2.65703	83	1.94453	53	1.2320313		
E2	3.35469	B2	2.64219	82	1.92969	52	1.2171875		
E1	3.33984	B1	2.62734	81	1.91484	51	1.2023438		
E0	3.325	B0	2.6125	80	1.9	50	1.1875		
DF	3.31016	AF	2.59766	7F	1.88516	4F	1.1726563		
DE	3.29531	AE	2.58281	7E	1.87031	4E	1.1578125		
DD	3.28047	AD	2.56797	7D	1.85547	4D	1.1429688		
DC	3.26563	AC	2.55313	7C	1.84063	4C	1.128125		
DB	3.25078	AB	2.53828	7B	1.82578	4B	1.1132813		
DA	3.23594	AA	2.52344	7A	1.81094	4A	1.0984375		
D9	3.22109	A9	2.50859	79	1.79609	49	1.0835938		
D8	3.20625	A8	2.49375	78	1.78125	48	1.06875		
D7	3.19141	A7	2.47891	77	1.76641	47	1.0539063		
D6	3.17656	A6	2.46406	76	1.75156	46	1.0390625		
D5	3.16172	A5	2.44922	75	1.73672	45	1.0242188		
D4	3.14688	A4	2.43438	74	1.72188	44	1.009375		
D3	3.13203	A3	2.41953	73	1.70703	43	0.9945313		
D2	3.11719	A2	2.40469	72	1.69219	42	0.9796875		
D1	3.10234	A1	2.38984	71	1.67734	41	0.9648438		
D0	3.0875	A0	2.375	70	1.6625	40	0.95		

Page 2

(B) Upper Threshold

FIGURE C.9: Values of low/upper discriminator threshold indexes

sea print

eff	F1/F2	F1/F3	F2/F3	F2/F	F3/F4
0.01	62.47	7070	113.18	21169	187.0
0.02	31.06	1749	56.3	5240	93.07
0.03	20.59	769	37.34	2305	61.74
0.04	15.36	428	27.86	1284	46.08
0.05	12.22	271	22.17	813.27	36.68
0.06	10.12	186	18.38	559.02	30.42
0.07	8.63	135	15.67	406.5	25.94
0.08	7.51	102	13.64	308.02	22.59
0.09	6.63	79.98	12.06	240.86	19.98
0.1	5.93	64.05	10.79	193.06	17.89
0.11	5.36	52.34	9.76	157.88	16.18
0.12	4.89	43.48	8.9	131.26	14.75
0.13	4.48	36.62	8.17	110.66	13.55
0.14	4.14	31.21	7.54	94.39	12.52
0.15	3.84	26.87	7	81.34	11.62
0.16	3.58	23.34	6.53	70.72	10.84
0.17	3.35	20.43	6.11	61.96	10.15
0.18	3.14	18	5.73	54.66	9.53
0.19	2.96	15.96	5.4	48.52	8.98
0.2	2.79	14.23	5.1	43.3	8.49
0.21	2.64	12.75	4.83	38.84	8.04
0.22	2.5	11.47	4.58	34.99	7.63
0.23	2.38	10.37	4.36	31.65	7.26
0.24	2.26	9.4	4.15	28.73	6.92
0.25	2.16	8.55	3.96	26.18	6.61
0.26	2.06	7.81	3.79	23.92	6.32
0.27	1.97	7.15	3.62	21.92	6.05
0.28	1.89	6.56	3.47	20.15	5.8
0.29	1.81	6.03	3.33	18.56	5.57
0.3	1.74	5.56	3.2	17.13	5.35
0.31	1.67	5.14	3.08	15.85	5.15
0.32	1.61	4.76	2.96	14.7	4.96
0.33	1.55	4.41	2.85	13.65	4.78
0.34	1.49	4.1	2.75	12.7	4.62
0.35	1.44	3.81	2.66	11.84	4.46
0.36	1.39	3.55	2.56	11.05	4.31
0.37	1.34	3.32	2.48	10.33	4.17
0.38	1.29	3.1	2.4	9.67	4.03
0.39	1.25	2.9	2.32	9.06	3.91
0.4	1.21	2.72	2.25	8.5	3.78
0.41	1.17	2.55	2.18	7.98	3.67
0.42	1.13	2.39	2.11	7.51	3.56
0.43	1.1	2.25	2.04	7.07	3.46
0.44	1.06	2.11	1.98	6.66	3.36
0.45	1.03	1.99	1.93	6.28	3.26
0.46	1	1.87	1.87	5.93	3.17
0.47	0.97	1.76	1.82	5.6	3.08
0.48	0.94	1.66	1.77	5.29	3
0.49	0.92	1.57	1.72	5.01	2.92
0.5	0.89	1.48	1.67	4.74	2.84

eff	F1/F2	F1/F3	F2/F3	F2/F	F3/F4
0.51	0.86	1.4	1.62	4.49	2.77
0.52	0.84	1.33	1.58	4.26	2.69
0.53	0.82	1.25	1.54	4.04	2.63
0.54	0.79	1.19	1.5	3.83	2.56
0.55	0.77	1.12	1.46	3.64	2.5
0.56	0.75	1.06	1.42	3.45	2.43
0.57	0.73	1.01	1.38	3.28	2.37
0.58	0.71	0.96	1.35	3.12	2.32
0.59	0.69	0.91	1.31	2.97	2.26
0.6	0.67	0.86	1.28	2.82	2.21
0.61	0.65	0.82	1.25	2.69	2.15
0.62	0.64	0.77	1.22	2.56	2.1
0.63	0.62	0.74	1.19	2.44	2.05
0.64	0.6	0.7	1.16	2.32	2.01
0.65	0.59	0.66	1.13	2.21	1.96
0.66	0.57	0.63	1.1	2.11	1.92
0.67	0.56	0.6	1.07	2.01	1.87
0.68	0.54	0.57	1.05	1.92	1.83
0.69	0.53	0.54	1.02	1.83	1.79
0.7	0.51	0.51	1	1.74	1.75
0.71	0.5	0.49	0.97	1.66	1.71
0.72	0.49	0.46	0.95	1.59	1.67
0.73	0.47	0.44	0.93	1.51	1.64
0.74	0.46	0.42	0.9	1.45	1.6
0.75	0.45	0.4	0.88	1.38	1.56
0.76	0.44	0.38	0.86	1.32	1.53
0.77	0.42	0.36	0.84	1.26	1.5
0.78	0.41	0.34	0.82	1.2	1.46
0.79	0.4	0.32	0.8	1.14	1.43
0.8	0.39	0.3	0.78	1.09	1.4
0.81	0.38	0.29	0.76	1.04	1.37
0.82	0.37	0.27	0.74	0.99	1.34
0.83	0.36	0.26	0.72	0.95	1.31
0.84	0.35	0.24	0.71	0.9	1.28
0.85	0.34	0.23	0.69	0.86	1.25
0.86	0.33	0.22	0.67	0.82	1.22
0.87	0.32	0.21	0.65	0.78	1.2
0.88	0.31	0.19	0.64	0.75	1.17
0.89	0.3	0.18	0.62	0.71	1.15
0.9	0.29	0.17	0.6	0.68	1.12
0.91	0.28	0.16	0.59	0.64	1.09
0.92	0.27	0.15	0.57	0.61	1.07
0.93	0.26	0.14	0.56	0.58	1.05
0.94	0.25	0.14	0.54	0.55	1.02
0.95	0.24	0.13	0.53	0.53	1
0.96	0.23	0.12	0.51	0.5	0.97
0.97	0.22	0.11	0.5	0.47	0.95
0.98	0.21	0.1	0.48	0.45	0.93
0.99	0.2	0.1	0.47	0.42	0.91

Page 1

FIGURE C.10: Efficiency as function of multiplicity ratios

Bibliography

[1] W. B.Rubidio, "The euroschool lectures on physics with exotic beams; vol. iii," (Springer, 2009) pp. 99–152.

[2] R. Azuma, T. Bjrnstad, H. Gustafsson, P. Hansen, B. Jonson, S. Mattsson, G. Nyman, A. Poskanzer, and H. Ravn, Phys. Lett. B **96**, 31 (1980).

[3] R. E. Azuma, L. C. Carraz, P. G. Hansen, B. Jonson, K. L. Kratz, S. Mattsson, G. Nyman, H. Ohm, H. L. Ravn, A. Schröder, and W. Ziegert, Phys. Rev. Lett. **43**, 1652 (1979).

[4] C. Detraz, M. Epherre, D. Guillemaud, P. Hansen, B. Jonson, R. Klapisch, M. Langevin, S. Mattsson, F. Naulin, G. Nyman, A. Poskanzer, H. Ravn, M. de Saint-Simon, K. Takahashi, C. Thibault, and F. Touchard, Phys. Lett. B **94**, 307 (1980).

[5] P. L. Reeder, R. A. Warner, T. R. Yeh, R. E. Chrien, R. L. Gill, M. Shmid, H. I. Liou, and M. L. Stelts, Phys. Rev. Lett. **47**, 483 (1981).

[6] B. Jonson, H. Gustafsson, P. Hansen, P. Hoff, P. Larsson, S. Mattsson, G. Nyman, H. Ravn, and D. Schardt, Proc.Int.Conf.Nuclei Far from Stability, Helsingor, Denmark **1**, 265 (1981), cERN 81-09.

[7] K. Miernik, K. P. Rykaczewski, C. J. Gross, R. Grzywacz, M. Madurga, D. Miller, J. C. Batchelder, I. N. Borzov, N. T. Brewer, C. Jost, A. Korgul, C. Mazzocchi, A. J. Mendez, Y. Liu, S. V. Paulauskas, D. W. Stracener, J. A. Winger, M. Wolinska-Cichocka, and E. F. Zganjar, Phys. Rev. Lett. **111**, 132502 (2013).

[8] P. Möller, J. Nix, and K.-L. Kratz, ADNDT **66**, 131 (1997).

[9] Y. Lyutostansky and I. Panov, Z. Phys. A **313**, 235 (1983).

[10] M. Arnould, S. Goriely, and K. Takahashi, Physics Reports **450**, 97 (2007).

[11] M. Madurga, R. Surman, I. N. Borzov, R. Grzywacz, K. P. Rykaczewski, C. J. Gross, D. Miller, D. W. Stracener, J. C. Batchelder, N. T. Brewer, L. Cartegni, J. H. Hamilton, J. K. Hwang, S. H. Liu, S. V. Ilyushkin, C. Jost, M. Karny, A. Korgul, W. Królas, A. Kuźniak, C. Mazzocchi, A. J. Mendez, K. Miernik, S. W. Padgett, S. V. Paulauskas, A. V. Ramayya, J. A. Winger, M. Woli ńska Cichocka, and E. F. Zganjar, Phys. Rev. Lett. **109**, 112501 (2012).

[12] P. Möller, B. Pfeiffer, and K.-L. Kratz, Phys. Rev. C **67**, 055802 (2003).

[13] I. Borzov, Nucl. Phys. A **777**, 645 (2006), special Isseu on Nuclear Astrophysics.

[14] I. N. Borzov, Phys. Rev. C **67**, 025802 (2003).

[15] S. Goriely, Private Communications (2013).

[16] J. Dobaczewski, I. Hamamoto, W. Nazarewicz, and J. A. Sheikh, Phys. Rev. Lett. **72**, 981 (1994).

[17] B. Bastin, S. Grévy, D. Sohler, O. Sorlin, Z. Dombrádi, N. L. Achouri, J. C. Angélique, F. Azaiez, D. Baiborodin, R. Borcea, C. Bourgeois, A. Buta, A. Bürger, R. Chapman, J. C. Dalouzy, Z. Dlouhy, A. Drouard, Z. Elekes, S. Franchoo, S. Iacob, B. Laurent, M. Lazar, X. Liang, E. Liénard, J. Mrazek, L. Nalpas, F. Negoita, N. A. Orr, Y. Penionzhkevich, Z. Podolyák, F. Pougheon, P. Roussel-Chomaz,

M. G. Saint-Laurent, M. Stanoiu, I. Stefan, F. Nowacki, and A. Poves, Phys. Rev. Lett. **99**, 022503 (2007).
[18] K. Sieja and F. Nowacki, Phys. Rev. C **81**, 061303 (2010).
[19] D. Verney, Habilitation diriger de la recherche, Manuscript, University Paris Sud (2013).
[20] O. Perru, O. Sorlin, S. Franchoo, F. Azaiez, E. Bouchez, C. Bourgeois, A. Chatillon, J. M. Daugas, Z. Dlouhy, Z. Dombrádi, C. Donzaud, L. Gaudefroy, H. Grawe, S. Grévy, D. Guillemaud-Mueller, F. Hammache, F. Ibrahim, Y. Le Coz, S. M. Lukyanov, I. Matea, J. Mrazek, F. Nowacki, Y.-E. Penionzhkevich, F. de Oliveira Santos, F. Pougheon, M. G. Saint-Laurent, G. Sletten, M. Stanoiu, C. Stodel, C. Theisen, and D. Verney, Phys. Rev. Lett. **96**, 232501 (2006).
[21] J. Leske, K.-H. Speidel, S. Schielke, O. Kenn, D. Hohn, J. Gerber, and P. Maier-Komor, Phys. Rev. C **71**, 034303 (2005), ref only.
[22] P. T. Hosmer, H. Schatz, A. Aprahamian, O. Arndt, R. R. C. Clement, A. Estrade, K.-L. Kratz, S. N. Liddick, P. F. Mantica, W. F. Mueller, F. Montes, A. C. Morton, M. Ouellette, E. Pellegrini, B. Pfeiffer, P. Reeder, P. Santi, M. Steiner, A. Stolz, B. E. Tomlin, W. B. Walters, and A. Wöhr, Phys. Rev. Lett. **94**, 112501 (2005).
[23] S. Wanajo, M. Tamamura, N. Itoh, K. Nomoto, Y. Ishimaru, T. C. Beers, and S. Nozawa, The Astrophysical Journal **593**, 968 (2003).
[24] M. Terasawa, K. Sumiyoshi, T. Kajino, G. J. Mathews, and I. Tanihata, The Astrophysical Journal **562**, 470 (2004).
[25] O. Perru, D. Verney, F. Ibrahim, O. Bajeat1, C. Bourgeois, F. Clapier, E. Cottereau, C. Donzaud, S. Du, M. Ducourtieux, S. Essabaa, S. Gales, D. Guillemaud-Mueller, O. Hubert, C. Lau, H. Lefort, F. L. Blanc, A. Mueller, J. Obert, N. Pauwels, J. Potier, F. Pougheon, J. Proust, B. Roussiere, J. Sauvage, and O. Sorlin, Eur. Phys. J **28**, 307 (2006).
[26] D. Verney, F. Ibrahim, C. Bourgeois, S. Essabaa, S. Galès, L. Gaudefroy, D. Guillemaud-Mueller, F. Hammache, C. Lau, F. L. Blanc, A. C. Mueller, O. Perru, F. Pougheon, B. Roussière, J. Sauvage, and O. Sorlin (PARRNe Collaboration), Phys. Rev. C **76**, 054312 (2007).
[27] J. A. Winger, K. P. Rykaczewski, C. J. Gross, R. Grzywacz, J. C. Batchelder, C. Goodin, J. H. Hamilton, S. V. Ilyushkin, A. Korgul, W. Królas, S. N. Liddick, C. Mazzocchi, S. Padgett, A. Piechaczek, M. M. Rajabali, D. Shapira, E. F. Zganjar, and J. Dobaczewski, Phys. Rev. C **81**, 044303 (2010).
[28] C. Gross, J. Winger, S. Ilyushkin, K. Rykaczewski, S. Liddick, I. Darby, R. Grzywacz, C. Bingham, D. Shapira, C. Mazzocchi, S. Padgett, M. Rajabali, L. Cartegni, E. Zganjar, A. Piechaczek, J. Batchelder, J. Hamilton, C. Goodin, A. Korgul, and W. Krlas, ACTA PHYSICA POLONICA B **40**, 447 (2008).
[29] K. Kolos, *Probing the nuclear structure in the vicinity of 78Ni via beta decay spectroscopy of 84Ga*, Ph.D. thesis, University Paris Sud 11 (2012).
[30] K. Kolos, D. Verney, F. Ibrahim, F. Le Blanc, S. Franchoo, K. Sieja, F. Nowacki, C. Bonnin, M. Cheikh Mhamed, P. V. Cuong, F. Didierjean, G. Duchêne, S. Essabaa, G. Germogli, L. H. Khiem, C. Lau, I. Matea, M. Niikura, B. Roussière, I. Stefan, D. Testov, and J.-C. Thomas, Phys. Rev. C **88**, 047301 (2013).
[31] K.-L. Kratz, B. Pfeiffer, O. Arndt, S. Hennrich, A. Wöhr, t. ISOLDE/IS333, and I. Collaborations, The European Physical Journal A - Hadrons and Nuclei **25**, 633 (2005).
[32] K.-L. Kratz, B. Pfeiffer, F.-K. Thielemann, and W. Walters, Hyperfine Interactions **129**, 185 (2000).

[33] I. Dillmann, K.-L. Kratz, A. Wöhr, O. Arndt, B. A. Brown, P. Hoff, M. Hjorth-Jensen, U. Köster, A. N. Ostrowski, B. Pfeiffer, D. Seweryniak, J. Shergur, and W. B. Walters (the ISOLDE Collaboration), Phys. Rev. Lett. **91**, 162503 (2003).
[34] T. Kautzsch, W.B. Walters, M. Hannawald, K.-L. Kratz, V.I. Mishin, V.N. Fedoseyev, W. Böhmer, Y. Jading, P. Van Duppen, B. Pfeiffer, A. Wöhr, P. Möller, I. Klöckl, V. Sebastian, U. Köster, M. Koizumi, J. Lettry, H.L. Ravn, and the ISOLDE Collaboration, Eur. Phys. J. A **9**, 201 (2000).
[35] I. N. Borzov and S. Goriely, Phys. Rev. C **62**, 035501 (2000).
[36] I. N. Borzov, Phys. Rev. C **71**, 065801 (2005).
[37] I. N. Borzov, EPJ Web of Conferences **38**, 12002 (2012).
[38] P. Gilbert Gedeon, *Reactor Kinetics and Operation. Course No: N03-002.* (CED, 2009).
[39] H.V.Klapdor and C. Wene, Journal of Physics G: Nuclear Physics **6**, 1061 (1980).
[40] K.Muhin, *Experimental Nuclear Physics* (Moscow, EnergoAtomIzdat, 2009).
[41] K. Heyde, *Basic Ideas and Concepts in Nuclear Physics*, 2nd ed. (Institute of Physics publishing Bristol and Philadelphia, 1999).
[42] S. Raman and N. B. Gove, Phys. Rev. C **7**, 1995 (1973).
[43] F.Didierjean and G. Walter, CRN **84**, 487 (1998).
[44] B. Singh, J. Rodriguez, S. Wong, and J. Tuli, Nuclear Data Sheets **94**, 1 (1994).
[45] C. Duke, P. Hansen, O. Nielsen, and G. Rudstam, Nucl. Phys. A **151**, 609 (1970).
[46] T. Tachibana, M. Yamada, and Y. Yoshida, Prog. Ther. Phys. **84**, 641 (1990).
[47] K.-L. Kratz and G. Herrmann, Z. Phys. A **263**, 435 (1973).
[48] B. Pfeiffer, K.-L. Kratz, and P. Möller, Progress in Nuclear Energy **41**, 39 (2002).
[49] K. Takahashi and M. Yamada, Prog. Ther. Phys. **41**, 1470 (1969).
[50] http://wwwndc.jaea.go.jp/nucldata/, (10/2013).
[51] H. Homma, E. Bender, M. Hirsch, K. Muto, H. V. Klapdor-Kleingrothaus, and T. Oda, Phys. Rev. C **54**, 2972 (1996).
[52] B. Brown, Nucl. Phys. A **704**, 11 (2002), rIKEN Symposium Shell Model 2000.
[53] B. Brown and B. Wildenthal, ADNDT **33**, 347 (1985).
[54] M. Hino, K. Muto, and T. Oda, Phys. Rev. C **37**, 1328 (1988).
[55] P. Möller and J. R. Nix, ADNDT **26**, 165 (1981).
[56] P. Möller, J. Nix, W. Myers, and W. Swiatecki, ADNDT **59**, 185 (1995).
[57] J. A. H. Sr. and R. A. Sorensen, Nuclear Physics A **98**, 542 (1967).
[58] Y. Aboussir, J. Pearson, A. Dutta, and F. Tondeur, ADNDT **61**, 127 (1995).
[59] I. Borzov, S. Fayans, E. Krmer, and D. Zawischa, Z. Phys. A **355**, 117 (1996).
[60] P. Möller, J. Nix, W. D. Myers, and W. J. Swiatecki, Nucl. Phys. A **536**, 61 (1992).
[61] T. Crane and M. Baker, "Neutron detectors. chap. 13, passive nondestructive assay of nuclear materials," (Los Alamos National Laboratory, 1991).
[62] "Korea atomic energy research institute nuclear data evaluation laboratory," (2007).
[63] G. Ter-Akopian, A. Popeko, E. Sokol, L. Chelnokov, V. Smirnov, and V. Gorshkov, Nucl. Instr&Meth. **190**, 119 (1981).
[64] A. Yeremin, A. Belozerov, M. Chelnokov, V. Chepigin, V. Gorshkov, A. Kabachenko, O. Malyshev, A. Popeko, R. Sagaidak, A. Shutov, E. Sokol, and A. Svirikhin, Nucl. Instr&Meth. A **539**, 441 (2005).
[65] A. Svirikhin, C. Briançon, S. Dmitriev, Y. Oganessian, E. Sokol, D. Testov, and A. Yeremin, AIP Conf. Proc. **1175**, 297 (2009).
[66] A. Svirikhin, A. Isaev, A. Yeremin, A. Kuznetsov, O. Malyshev, A. Popeko,

E. Sokol, M. Chelnokov, and V. Chepigin, Instruments and Experimental Techniques **54**, 644 (2011).
[67] D. Testov, C. Brianon, S. Dmitriev, A. Yeremin, Y. Penionzhkevich, Y. Pyatkov, and E. Sokol, Physics of Atomic Nuclei **72**, 1 (2009), 10.1134/S1063778809010013.
[68] Y. Pyatkov, D. Kamanin, W. Oertzen, A. Alexandrov, I. Alexandrova, O. Falomkina, N. Jacobs, N. Kondratjev, E. Kuznetsova, Y. Lavrova, V. Malaza, Y. Ryabov, O. Strekalovsky, A. Tyukavkin, and V. Zhuchko, The European Physical Journal A **48**, 1 (2012).
[69] E. Sokol, V. Smirnov, S. Lukyanov, and Y. Penionzhkevich, Nucl. Instr&Meth. A **400**, 96 (1997).
[70] J. Cerny, Z. Dlouhy, Z. Dolezal, M. Ivanov, P. Kubik, E. Kuznetsova, Y. Penionzkevich, E. Sokol, J. Svejda, and I. Wilhelm, Nucl. Instr&Meth. A **540**, 430 (2005).
[71] S. Shalev and G. Rudstam, Phys. Rev. Lett. **28**, 687 (1972).
[72] S. Shalev and G. Rudstam, Nucl. Phys. A **230**, 153 (1974).
[73] H. Franz, J. V. Kratz, K. L. Kratz, W. Rudolph, G. Herrmann, F. M. Nuh, S. G. Prussin, and A. A. Shihab-Eldin, Phys. Rev. Lett. **33**, 859 (1974).
[74] P. L. Reeder, J. F. Wright, and L. J. Alquist, Phys. Rev. C **15**, 2098 (1977).
[75] P. Hoff, Nucl. Phys. A **359**, 9 (1981).
[76] A. T. Reed, O. Tarasov, R. D. Page, D. Guillemaud-Mueller, Y. E. Penionzhkevich, R. G. Allatt, J. C. Angélique, R. Anne, C. Borcea, V. Burjan, W. N. Catford, Z. Dlouhý, C. Donzaud, S. Grévy, M. Lewitowicz, S. M. Lukyanov, F. M. Marqués, G. Martinez, A. C. Mueller, P. J. Nolan, J. Novák, N. A. Orr, F. Pougheon, P. H. Regan, M. G. Saint-Laurent, T. Siiskonen, E. Sokol, O. Sorlin, J. Suhonen, W. Trinder, and S. M. Vincent, Phys. Rev. C **60**, 024311 (1999).
[77] D. Testov, S. Ancelin, F. Ibrahim, M. Niikura, Y. Penionzhkevich, V. Smirnov, E. Sokol, B. Tastet, and D. Verney, AIP Conf. Proc. **1224**, 568 (2010).
[78] D. Testov, E. Kuznetcova, and J. Wilson, Preprint JINR **15** (2013).
[79] D. Testov, J. Wilson, D. Verney, J. Bettane, E. Sokol, Y. Penionzhkevich, E. Kuznetsova, M. Niikura, S. Ancelin, G. Mavilla, K. Kolos, F. Ibrahim, and V. Smirnov, "First delayed neutron emission measurements at alto with the neutron detector tetra," in *Exotic Nuclei*, Chap. 47, pp. 365–372.
[80] E. J. Axton, A. G. Bardell, S. J. Felgate, and E. M. R. Long, Metrologia **21**, 181 (1985).
[81] M. Dakowski, Y. Lazarev, V. Turchin, and L. Turovtseva, Nucl. Instr&Meth. **113**, 195 (1973).
[82] A. S. Vorobyev, V. N. Dushin, F.-J. Hambsch, V. A. Jakovlev, V. A. Kalinin, A. B. Laptev, B. F. Petrov, and O. A. Shcherbakov, AIP Conf. Proc. **769**, 613 (2005).
[83] R. J. Tuttle, in *Consultants' Meeting on Delayed Neutron Properties*, Vol. INDC(NDS)-107 (1979) 29, IAEA, Vienna, Austria. (1979) pp. 26–30.
[84] J. W. Meadows, Phys. Rev. **157**, 1076 (1967).
[85] M. Gòmez-Hornillos, J. Rissanen, J. Tain, A. Algora, D. Cano-Ott, J. Agramunt, V. Gorlychev, R. Caballero, T. Martnez, L. Achouri, J. ysto, G. Corts, V. Elomaa, T. Eronen, A. Garca, J. Hakala, A. Jokinen, P. Karvonen, V. Kolhinen, I. Moore, M. Parlog, H. Penttil, Z. Podolyak, C. Pretel, M. Reponen, V. Sonnenschein, and E. Valencia, Journal of Physics Conference Series **312**, 052008 (2010).
[86] J. Pereira, P. Hosmer, G. Lorusso, P. Santi, A. Couture, J. Daly, M. D. Santo, T. Elliot, J. Grres, C. Herlitzius, K.-L. Kratz, L. Lamm, H. Lee, F. Montes, M. Ouellette, E. Pellegrini, P. Reeder, H. Schatz, F. Schertz, L. Schnorrenberger, K. Smith, E. Stech, E. Strandberg, C. Ugalde, M. Wiescher, and A. Whr, Nucl.

Instr&Meth. A **618**, 275 (2010).
[87] A. J. Mendez, S. Ilyushkin, D. W. Bardayan, B. Manning, M. Madurga, R. Grzywacz, W. A. Peters, M. Wolinska-Cichocka, M. E. Howard, L. Cartegni, A. Ratkiewicz, K. Rykaczewski, M. Al-Shudifaft, J. C. Batchelder, K. T. Schmitt, C. J. Gross, C. Rasco, J. A. Cizewski, D. Miller, M. Matos, K. Miernik, J. C. Blackmon, S. V. Paulauskas, and F. Sarazin, "Performance of vandle measuring beta-delayed neutron spectra of fission fragments," in *Fission and Properties of Neutron-Rich Nuclei* (World Scientific, 2012) Chap. 79, pp. 472–472.
[88] X-5, Monte, Carlo, and Team, *LA-UR-03-1987, MCNP A General Monte Carlo N-Particle Transport Code, Version 5* (2003).
[89] C., K. Guardiolaa, F. Amgaroub, C. F. Garcac, D. Quiriona, and M. Lozanoa, Journal of Instrumentation **6**, 1 (2011).
[90] J. Shultis and R. Faw, *An MCNP Primer* (2011).
[91] R. Brewer, *Criticality Calculations with MCNP5: A Primer* (2009).
[92] J. P. Lestone and A. Gavron, Phys. Rev. C **49**, 372 (1994).
[93] N. Pauwels, Ph.D. thesis, University Paris Sud 11 (1998).
[94] W. T. Diamond, Nucl. Instr&Meth. A **432**, 471 (1999).
[95] Y. Oganessian, S. Dmitriev, J. Kliman, O. Maslov, G. Starodub, A. Belov, and S. Tretiakova, Nucl. Phys. A **701**, 87 (2002), 5th International Conference on Radioactive Nuclear Beams.
[96] M. Lebois, *Structure des noyaux de Germanium et de Gallium riches en neutrons au-delà de N=50 â ALTO*, Ph.D. thesis, University Paris Sud 11 (2008).
[97] B. Tastet, *Structure des noyaux de gallium, de germanium et d'arsenic riches en neutrons autour de N=50 et développement d'une source d'ionisation laser á ALTO*, Ph.D. thesis, University Paris Sud 11 (2011).
[98] M. C. Mhamed, S. Essabaa, C. Lau, M. Lebois, B. Roussire, M. Ducourtieux, S. Franchoo, D. G. Mueller, F. Ibrahim, J. LeDu, J. Lesrel, A. Mueller, M. Raynaud, A. Said, D. Verney, and S. Wurth, Nucl. Instr&Meth. B **266**, 4092 (2008).
[99] F. Clapier, A. C. Mueller, J. Obert, O. Bajeat, M. Ducourtieux, A. Ferro, A. Horbowa, L. Kotfila, C. Lau, H. Lefort, S. Kandri-Rody, N. Pauwels, J. C. Potier, J. Proust, J. C. Putaux, C. F. Liang, P. Paris, A. C. C. Villari, R. Lichtenthäler, L. Maunoury, and J. Lettry, Phys. Rev. ST Accel. Beams **1**, 013501 (1998).
[100] H. Ravn and B. Allardyce, *Treatise on Heavy Ion Science* (Plenum Press, New York, 1989).
[101] K. Perjrvi, U. Bergmann, V. Fedoseyev, A. Joinet, U. Kster, C. Lau, J. Lettry, H. Ravn, and M. Santana-Leitner, Nucl. Instr&Meth. B **204**, 272 (2003), 14th International Conference on Electromagnetic Isotope Separators and Techniques Related to their Applications.
[102] B. Roussire, F. Ibrahim, J. Sauvage, O. Bajeat, N. Barr, F. Clapier, E. Cottereau, C. Donzaud, M. Ducourtieux, S. Essabaa, D. Guillemaud-Mueller, C. Lau, H. Lefort, C. Liang, F. L. Blanc, A. Mueller, J. Obert, N. Pauwels, J. Potier, F. Pougheon, J. Proust, O. Sorlin, D. Verney, and A. Wojtasiewicz, Nucl. Instr&Meth. B **194**, 151 (2002).
[103] B. Roussire, O. Bajeat, N. Barr, C. Bourgeois, F. Clapier, E. Cottereau, C. Donzaud, M. Ducourtieux, S. Essabaa, D. Guillemaud-Mueller, F. Ibrahim, C. Lau, F. L. Blanc, H. Lefort, C. Liang, A. Mueller, J. Obert, N. Pauwels, J. Potier, F. Pougheon, J. Proust, J. Sauvage, O. Sorlin, D. Verney, and A. Wojtasiewicz, Nucl. Instr&Meth. B **246**, 288 (2006).
[104] P. Van Duppen, in *The Euroschool Lectures on Physics with Exotic Beams, Vol. II*, Lecture Notes in Physics, Vol. 700, edited by J. Al-Khalili and E. Roeckl (Springer

Berlin Heidelberg, 2006) pp. 37–77.
[105] R. Kirchner, Nucl. Instr&Meth. B **204**, 179 (2003), 14th International Conference on Electromagnetic Isotope Separators and Techniques Related to their Applications.
[106] S. Sundell and H. Ravn, Nucl. Instr&Meth. B **70**, 160 (1992).
[107] W. P. Jesse and J. Sadauskis, Phys. Rev. **100**, 1755 (1955).
[108] G. S. Hurst, M. G. Payne, S. D. Kramer, and J. P. Young, Rev. Mod. Phys. **51**, 767 (1979).
[109] H. Friedrich, *Theoretical Atomic Physics* (Springer, 1998).
[110] R. Radziemski, *Reference data on atoms* (Springer, 1985).
[111] R. Li and S. Franchoo, in *1st Topical Workshop on Laser Based Particle Sources, 1st Topical Workshop on Laser Based Particle Sources* (2013).
[112] http://isolde-project-rilis.web.cern.ch/isolde-project rilis/elements.html, (2013).
[113] P. Paris, C. Liang, D. Lecouturier, M. Arianer, J. Obert, A. Caruette, A. Ferro, J. Fournet, J. Putaux, and J. Sarrouy, Nucl. Instr&Meth. **186**, 91 (1981).
[114] C. Lau, *Etude de la production de faisceaux riches en neutrons par fission induite par neutrons rapides*, Ph.D. thesis, University Paris Sud 11 (2000).
[115] http://http://www.nndc.bnl.gov, (08/2013).
[116] D. Abriola, B. Singh, and I. Dillmann, *Summary Report of Consultants' Meeting on Beta-delayed neutron emission evaluation*, Tech. Rep. (International Atomic Energy Agency, Vienna, Austria, 2011).
[117] http://root.cern.ch/drupal/, .
[118] D. Verney, B. Tastet, K. Kolos, F. Le Blanc, F. Ibrahim, M. Cheikh Mhamed, E. Cottereau, P. V. Cuong, F. Didierjean, G. Duchêne, S. Essabaa, M. Ferraton, S. Franchoo, L. H. Khiem, C. Lau, J.-F. Le Du, I. Matea, B. Mouginot, M. Niikura, B. Roussière, I. Stefan, D. Testov, and J.-C. Thomas, Phys. Rev. C **87**, 054307 (2013).
[119] P. Hoff and B. Fogelberg, Nucl. Phys. A **368**, 210 (1981).
[120] G. Rudstam, K. Aleklett, and L. Sihver, ADNDT **53**, 1 (1993).
[121] P. Reeder, R. Warner, M. Edminston, R. Gill, and A. Pietrowski, Proc. Am. Soc. Nucl. Chem. Meeting Chicago , 171 (1985).
[122] P. L. Reeder, R. A. Warner, G. P. Ford, and H. Willmes, Radiation Effects **94**, 93 (1986), http://www.tandfonline.com/doi/pdf/10.1080/00337578608208362 .
[123] E. Lund, P. Hoff, K. Aleklett, O. Glomset, and G. Rudstam, Z. Phys. A **294**, 233 (1980).
[124] J. A. Winger, J. C. Hill, F. K. Wohn, R. Moreh, R. L. Gill, R. F. Casten, D. D. Warner, A. Piotrowski, and H. Mach, Phys. Rev. C **36**, 758 (1987).
[125] K.-L. Kratz, H. Gabelmann, P. Möller, B. Pfeiffer, H. Ravn, and A. Whr, Z. Phys. A **340**, 419 (1991).
[126] C. M. Baglin, Nuclear Data Sheets **109**, 2257 (2008).
[127] C. M. Baglin, Nuclear Data Sheets **79**, 447 (1996).
[128] J. Katz, H. Franz, N. Kaffrel, and G. Herrmann, **250**, 13 (1975).
[129] H. Gausemel, K. A. Mezilev, B. Fogelberg, P. Hoff, H. Mach, and E. Ramström, Phys. Rev. C **70**, 037301 (2004).
[130] J. S. Thomas, D. W. Bardayan, J. C. Blackmon, J. A. Cizewski, U. Greife, C. J. Gross, M. S. Johnson, K. L. Jones, R. L. Kozub, J. F. Liang, R. J. Livesay, Z. Ma, B. H. Moazen, C. D. Nesaraja, D. Shapira, and M. S. Smith, Phys. Rev. C **71**, 021302 (2005).
[131] J. S. Thomas, G. Arbanas, D. W. Bardayan, J. C. Blackmon, J. A. Cizewski, D. J. Dean, R. P. Fitzgerald, U. Greife, C. J. Gross, M. S. Johnson, K. L. Jones,

R. L. Kozub, J. F. Liang, R. J. Livesay, Z. Ma, B. H. Moazen, C. D. Nesaraja, D. Shapira, M. S. Smith, and D. W. Visser, Phys. Rev. C **76**, 044302 (2007).

[132] M. Lebois, D. Verney, F. Ibrahim, S. Essabaa, F. Azaiez, M. C. Mhamed, E. Cottereau, P. V. Cuong, M. Ferraton, K. Flanagan, S. Franchoo, D. Guillemaud-Mueller, F. Hammache, C. Lau, F. Le Blanc, J. F. Le Du, J. Libert, B. Mouginot, C. Petrache, B. Roussière, L. Sagui, N. de Séréville, I. Stefan, and B. Tastet, Phys. Rev. C **80**, 044308 (2009).

[133] J. A. Winger, S. V. Ilyushkin, K. P. Rykaczewski, C. J. Gross, J. C. Batchelder, C. Goodin, R. Grzywacz, J. H. Hamilton, A. Korgul, W. Królas, S. N. Liddick, C. Mazzocchi, S. Padgett, A. Piechaczek, M. M. Rajabali, D. Shapira, E. F. Zganjar, and I. N. Borzov, Phys. Rev. Lett. **102**, 142502 (2009).

[134] G. Rudstam and E. Lund, Phys. Rev. C **13**, 321 (1976).

[135] O. Perru, F. Ibrahim, O. Bajeat, C. Bourgeois, F. Clapier, E. Cottereau, C. Donzaud, M. Ducourtieux, S. Gals, D. Guillemaud-Mueller, C. Lau, H. Lefort, F. Blanc, A. Mueller, J. Obert, N. Pauwels, J. Potier, F. Pougheon, J. Proust, B. Roussire, J. Sauvage, O. Sorlin, and D. Verney, Physics of Atomic Nuclei **66**, 1421 (2003).

[136] J. A. Winger, S. V. Ilyushkin, C. J. Gross, K. P. Rykaczewski, D. Shapira, R. Grzywacz, S. N. Liddick, S. Padgett, M. M. Rajabali, J. C. Batchelder, A. Korgul, W. Krolas, C. Mazzocchi, A. Piechaczek, E. F. Zganjar, C. Goodin, and J. H. Hamilton, in *Proc.4th.Intern.Conf.Fission and Properties of Neutron-Rich Nuclei* (2008).

[137] P. L. Reeder, R. A. Warner, and R. L. Gill, Phys. Rev. C **27**, 3002 (1983).

[138] F. Montes, A. Estrade, P. T. Hosmer, S. N. Liddick, P. F. Mantica, A. C. Morton, W. F. Mueller, M. Ouellette, E. Pellegrini, P. Santi, H. Schatz, A. Stolz, B. E. Tomlin, O. Arndt, K.-L. Kratz, B. Pfeiffer, P. Reeder, W. B. Walters, A. Aprahamian, and A. Wöhr, Phys. Rev. C **73**, 035801 (2006).

[139] H. Huck, A. Jech, G. Marti, M. L. Perez, J. J. Rossi, and H. M. Sofia, Phys. Rev. C **40**, 1384 (1989).

[140] V. Fedoseyev, Y. Jading, O. Jonsson, R. Kirchner, K.-L. Kratz, M. Krieg, E. Kugler, J. Lettry, T. Mehren, V. Mishin, H. Ravn, T. Rauscher, F. Scheerer, O. Tengblad, P. Duppen, and A. Whr, Z. Phys. A **353**, 9 (1995).

[141] J. C. Hill, F. K. Wohn, Z. Berant, R. L. Gill, R. E. Chrien, C. Chung, and A. Aprahamian, Phys. Rev. C **29**, 1078 (1984).

[142] M. L. Gartner and J. C. Hill, Phys. Rev. C **18**, 1463 (1978).

[143] H. Gktrk, B. Ekstrm, E. Lund, and B. Fogelberg, Zeitschrift fr Physik A Atomic Nuclei **324**, 117 (1986).

[144] T. Kautzsch, A. Wöhr, W. B. Walters, K. L. Kratz, B. Pfeiffer, M. Hannawald, J. Shergur, O. Arndt, S. Hennrich, S. Falahat, T. Griesel, O. Keller, A. Aprahamian, B. A. Brown, P. F. Mantica, M. A. Stoyer, H. L. Ravn, the ISOLDE IS333, and R. C. Collaborations, Eur. Phys. J. A **25**, s1.117 (2005).

[145] G. Rudstam, P. Aagaard, P. Hoff, B. Johansson, and H. U. Zwicky, Nucl.Instrum.Methods **186**, 365 (1981).

[146] H. Gausemel, B. Fogelberg, T. Engeland, M. Hjorth-Jensen, P. Hoff, H. Mach, K. A. Mezilev, and J. P. Omtvedt, Phys. Rev. C **69**, 054307 (2004).

[147] B. Fogelberg and P. Carl, Nuclear Physics A **323**, 205 (1979).

[148] B. Grapengiesser, E. Lund, and G. Rudstam, Journal of Inorganic and Nuclear Chemistry **36**, 2409 (1974).

[149] E. Lund and G. Rudstam, Phys. Rev. C **13**, 1544 (1976).

[150] G. Engler and E. Ne'Eman, Nuclear Physics A **367**, 29 (1981).

[151] J. Hakala, S. Rahaman, V.-V. Elomaa, T. Eronen, U. Hager, A. Jokinen, A. Kankainen, I. D. Moore, H. Penttilä, S. Rinta-Antila, J. Rissanen, A. Saastamoinen, T. Sonoda, C. Weber, and J. Äystö, Phys. Rev. Lett. **101**, 052502 (2008).
[152] S. Baruah, G. Audi, K. Blaum, M. Dworschak, S. George, C. Guénaut, U. Hager, F. Herfurth, A. Herlert, A. Kellerbauer, H.-J. Kluge, D. Lunney, H. Schatz, L. Schweikhard, and C. Yazidjian, Phys. Rev. Lett. **101**, 262501 (2008).
[153] G. Audi, F. Kondev, M. Wang, B. Pfeiffer, X. Sun, J. Blachot, and M. MacCormick, Chinese Physics C **36**, 1157 (2012).
[154] http://www.nndc.bnl.gov/nudat2/, (08/2013).
[155] B. Fogelberg, A. Bcklin, and T. Nagarajan, Physics Letters B **36**, 334 (1971).
[156] M. Hannawald, K.-L. Kratz, B. Pfeiffer, W. B. Walters, V. N. Fedoseyev, V. I. Mishin, W. F. Mueller, H. Schatz, J. Van Roosbroeck, U. Köster, V. Sebastian, and H. L. Ravn (ISOLDE Collaboration), Phys. Rev. C **62**, 054301 (2000).
[157] M. Hannawald, V. Fedoseyev, U. Kster, K.-L. Kratz, V. Mishin, W. Mueller, H. Ravn, J. V. Roosbroeck, H. Schatz, V. Sebastian, and W. Walters, Nucl. Phys. A **688**, 578 (2001).
[158] A. C. Pappas and G. Rudstam, Nuclear Physics **21**, 353 (1960).
[159] J.-P. Gautheron, *Contribution a l'etude des precurseurs de neutrons retardes de fission*, Ph.D. thesis, L'universite Scientifique et Medicale de Grenoble (1974).
[160] C. D. Coryell, Annual Review of Nuclear Science **2**, 305 (1953), http://www.annualreviews.org/doi/pdf/10.1146/annurev.ns.02.120153.001513 .
[161] http://http://www.nndc.bnl.gov, (01/2014).
[162] S. Amiel and H. Feldstein, Physics Letters B **31**, 59 (1970).
[163] H. Mach, R. L. Gill, D. D. Warner, A. Piotrowski, and R. Moreh, Phys. Rev. C **34**, 1117 (1986).
[164] E. Amaldi and E. Fermi, Phys. Rev. **50**, 899 (1936).
[165] E. Amaldi, L. R. Hafstad, and M. A. Tuve, Phys. Rev. **51**, 896 (1937).
[166] A. O. Hanson and J. L. McKibben, Phys. Rev. **72**, 673 (1947).
[167] C. L. Bailey, W. E. Bennett, T. Bergstralth, R. G. Nuckolls, H. T. Richards, and J. H. Williams, Phys. Rev. **70**, 583 (1946).
[168] *Engineering Data Sheets 1.21 and 1.22 for BF3 Proportional Counters*, Tech. Rep. (1979).
[169] D. Beddingfield, H. Menlove, and N. Johnson, Nucl. Instr&Meth. A **422**, 35 (1999).
[170] T. L. AtWell and H. O. Menlove, *Measurement of the Time Resolution of Several 4He and CH4 Proportional Counters*, Tech. Rep. (Los Alamos National Laboratory, 1974).
[171] A. Lintereur, K. Conlin, J. Ely, L. Erikson, R. Kouzes, E. Siciliano, D. Stromswold, and M. Woodring, Nucl. Instr&Meth. A **652**, 347 (2011), ¡ce:title¿Symposium on Radiation Measurements and Applications (SORMA) XII 2010¡/ce:title¿.
[172] D. Beddingfield, N. Johnson, and H. Menlove, Nucl. Instr&Meth. A **455**, 670 (2000).
[173] C. T. W, *Shielding for 3He Detectors*, LA-6675-PR (Los Alamos National Laboratory, 1976).
[174] A. E. Evans, H. O. Menlove, R. B. Walton, and D. B. Smith, Nucl. Instr&Meth. **133**, 577 (1976).
[175] R. Kouzes, *The 3He Supply Problem*, Tech. Rep. PNNL-18388 (2009).

[176] R. Kouzes, *Status Summary of 3He and Neutron Detection Alternatives for Homeland Security*, Tech. Rep. PNNL-19360 (2010).
[177] K. A. Nelson, S. L. Bellinger, B. W. Montag, J. L. Neihart, T. A. Riedel, A. J. Schmidt, and D. S. McGregor, Nucl. Instr&Meth. A , (2011).
[178] http://www land.gsi.de, (2013).
[179] A. Bu, T. Martin, C. Timi, N. Achouri, J. Anglique, C. Borcea, I. Cruceru, A. Genoux-Lubain, S. Grvy, M. Lewitowicz, E. Linard, F. Marqus, F. Negoi, F. de Oliveira, N. Orr, J. Pter, and M. Sandu, Nucl. Instr&Meth. A **455**, 412 (2000).
[180] J. Wang, A. Galonsky, J. Kruse, P. Zecher, F. Deak, A. Horvath, A. Kiss, Z. Seres, K. Ieki, and Y. Iwata, Nucl. Instr&Meth. A **397**, 380 (1997).
[181] P. Dsesquelles, A. Cole, A. Dauchy, A. Giorni, D. Heuer, A. Lleres, C. Morand, J. Saint-Martin, P. Stassi, J. Viano, B. Chambon, B. Cheynis, D. Drain, and C. Pastor, Nucl. Instr&Meth. A **307**, 366 (1991).
[182] S. Shalev and J. M. Cuttler, Nuclear Science and Engineering **51** (1973).
[183] H. Franz, W. Rudolph, H. Ohm, K.-L. Kratz, G. Herrmann, F. Nuh, D. Slaughter, and S. Prussin, Nucl. Instr&Meth. **144**, 253 (1977).
[184] K.-L. Kratz, A. Schröder, H. Ohm, M. Zendel, H. Gabelmann, W. Ziegert, P. Peuser, G. Jung, B. Pfeiffer, K. Wnsch, H. Wollnik, C. Ristori, and J. Cranon, Z. Phys. A **306**, 239 (1982).
[185] L. East and R. Walton, Nucl. Instr&Meth. **72**, 161 (1969).